Effect of Fatigue Crack Surface Oxidation on Reliability of Non Destructive Testing Techniques

A THESIS SUBMITTED

To the University of Hyderabad in partial fulfillment of

The award of the degree of

DOCTOR OF PHILOSOPHY

In

MATERIALS ENGINEERING

By

Vamsi Krishna Rentala

Reg. No. 12ETMM10

Under the supervision of

Dr. Jai Prakash Gautam
Professor, SEST, UoH

Dr. M.Phani Surya Kiran
Scientist 'E', NDTG, DMRL

School of Engineering Sciences and Technology

University of Hyderabad, Hyderabad, India

October 2020

Declaration

I, **Vamsi Krishna Rentala**, declare that this thesis work entitled **"Effect of Fatigue Crack Surface Oxidation on Reliability of Non Destructive Testing Techniques"**, submitted in partial fulfillment of the requirement for the award of Doctor of Philosophy (Materials Engineering) in the School of Engineering Sciences and Technology, University of Hyderabad is completely my work except for those referenced. This work was done under the supervision of **Dr.Jai Prakash Gautam, Professor, School of Engineering Sciences and Technology, University of Hyderabad** and **Dr.M.Phani Surya Kiran, Scientist 'E', Non-Destructive Testing Group, Defence Metallurgical Research Laboratory.** This thesis is a record of the bonafide research work carried out by me. The results incorporated in this thesis have not been reproduced/copied from any source. This work has not been submitted to any other University or Institution for the award of any other degree or equivalent.

Vamsi Krishna Rentala
Reg. No. 12ETMM10
Int. M.Tech/Ph.D Materials Engineering
School of Engineering Sciences and Technology
University of Hyderabad
Official Email Id: vamsikrishnarentala@uohyd.ac.in
Personal Email Id: vamsi.pec@gmail.com

CERTIFICATE

This is to certify that the thesis work entitled "**Effect of Fatigue Crack Surface Oxidation on Reliability of Non Destructive Testing Techniques**", submitted by **Vamsi Krishna Rentala** bearing Reg. No. 12ETMM10 in partial fulfilment of the award of the degree of Doctor of Philosophy in Materials Engineering is a bonafide record of research work that has been carried out by him at **Defence Metallurgical Research Laboratory,** Hyderabad and **School of Engineering Sciences and Technology, University of Hyderabad,** under our guidance and supervision. The content of this thesis has not been submitted earlier, as a whole or in part, to this or any other University/Institution for the award of any degree or equivalent.

Thesis Supervisor

Dr. Jai Prakash Gautam
Professor
School of Engineering Sciences and Technology
University of Hyderabad
Hyderabad

Dr. JAI PRAKASH GAUTAM
Professor
School of Engineering Sciences & Technology
University of Hyderabad
Hyderabad-500 046.

Thesis Co-Supervisor

Dr. M.Phani Surya Kiran
Scientist "E"
Non Destructive Testing Group
Defence Metallurgical Research Laboratory
Hyderabad

Dr. M. PHANI SURYA KIRAN
Scientist
Defence Metallurgical Research Laboratory
Kanchanbagh, Hyderabad.

Approved by

7/8/20

Prof. Dibakar Das
Dean
School of Engineering Sciences and Technology
University of Hyderabad
Hyderabad

Prof. Dibakar Das
DEAN
School of Engineering Sciences and Technology
University of Hyderabad 500 046.

CERTIFICATE

This is to certify that the thesis entitled **Effect of Fatigue Crack Surface Oxidation on Reliability of Non Destructive Testing Techniques** Submitted by **Vamsi Krishna Rentala** bearing registration number **12ETMM10** (Int. M.Tech./Ph.D. Materials Engineering) in partial fulfillment of the requirements for award of Doctor of Philosophy in the School of Engineering Sciences and Technology is a bonafide work carried out by him under my supervision and guidance.

This thesis is free from plagiarism and has not been submitted previously in part or in full to this or any other University or Institution for award of any degree or diploma.

Parts of this thesis have been published in the following peer reviewed journal publications:

1. ***Vamsi Krishna Rentala***, *Phani Mylavarapu, Jai Prakash Gautam, "Issues in Estimating Probability of Detection of NDT Techniques – A Model Assisted Approach", (Elsevier)* ***Ultrasonics*** *87 (2018) 59–70.*

2. ***Vamsi Krishna Rentala***, *Phani Mylavarapu, Jai Prakash Gautam, Vikas Kumar, "Generation of POD Curves in the Absence of Service Induced Cracked Components- An Experimental Approach ",* ***Insight-Nondestructive testing and condition monitoring****, Vol.61, No 1, January 2019, pp. 28-34(7).*

3. ***Vamsi Krishna Rentala***, *Phani Mylavarapu, J.P.Gautam, Gp.Capt.B.V.N.Shiva, K.Gopinath, Vikas Kumar, "Physical Manifestation of $a_{90/95}$ in Remnant Life Revision Studies of Aero-engine Components",* ***Procedia Structural Intergrity*** *(Elsevier), Volume 14, 2019, Pages 597-604.*

Further, the student has passed the following courses towards fulfilment of coursework requirement for Ph.D.

Course Code	Name	Credits	Pass/Fail
AC801	Research Methodology	4	Pass

and was exempted from doing coursework (recommended by Doctoral Committee) on the basis of the following courses passed during his M.Tech. program (in Int. M.Tech./Ph.D. program) and the M.Tech. degree was awarded:

Course Code	Name	Credits	Pass/Fail
MT401	Thermodynamics and Phase Equilibria	4	Pass
MT402	Characterization of Materials	4	Pass
MT403	Advanced Engineering Mathematics	4	Pass
MT404	Seminar	2	Pass
MT405	Mechanical Behavior of Materials/Selection of Materials	4	Pass
MT406	Concepts of Materials Science	4	Pass
MT407	Materials Processing and Characterization Laboratory	4	Pass
MT408	Dislocation and Plasticity	2	Pass
MT451	Materials & Technologies for Energy Systems	4	Pass
MT452	Diffusion and Kinetics	2	Pass
MT453	Modeling and Simulation	4	Pass
MT454	Powder Metallurgy and Ceramics	4	Pass
MT455	Surface Engineering	4	Pass
MT456	Metal Forming Science and Technology	4	Pass
MT457	Laboratory	4	Pass
MT458	Seminar	2	Pass
MT500	Dissertation	18	Pass

Supervisor

Dr. JAI PRAKASH GAUTAM
Professor
School of Engineering Sciences & Technology
University of Hyderabad
Hyderabad-500 046.

Dean of School

Prof. Dibakar Das
DEAN
School of Engineering Sciences and Technology
University of Hyderabad 500 046.

Acknowledgements

Firstly, I would like to express my deep gratitude and sincere thanks to my thesis co-supervisor from DMRL, Dr.M.Phani Surya Kiran, Scientist 'E', NDTG for encouraging and inspiring me to pursue Ph.D after the completion of M.Tech thesis work under his supervision. I am deeply indebted to his patience in training me not only on the scientific and technical aspects but also in making me a capable person in various aspects of life. The joy and enthusiasm he has for research were contagious and motivational for me. His guidance helped me at all times of my research and writing of this thesis. Needless to say that none of this would have been possible without his dedicated mentorship. I could not have imagined having a better advisor and mentor for my Ph.D study. Secondly, I express my sincere gratitude to my thesis supervisor Dr. Jai Prakash Gautam, Professor, School of Engineering Sciences and Technology, University of Hyderabad for providing me with the opportunity to do Ph.D. under his supervision. I am extremely thankful for his guidance, encouragement, continuous support and patience during my PhD study. His immense knowledge and plentiful experience have encouraged me in all the time of my academic research and daily life.

I would like to thank my doctorial review committee members, Dr.-Ing. V. V. S. S. Srikanth, Professor, School of Engineering Sciences and Technology (SEST), UoH and Dr. Swati Gosh Acharya, Associate Professor, SEST, UoH for their valuable suggestions and comments which have helped to improve the quality of my thesis work. I am thankful to Prof. Dibakar Das, Dean and all faculty members of SEST for their support. I would also like to express my sincere thanks to Prof.M.Sundararaman, former Dean (currently in IIT Madras), for his support and motivation while doing this work as well as during the course work. I also thank all the lab technicians and non-teaching staff, SEST, UoH, for their timely help.

I would like to extend my sincere thanks to Dr.Vikas Kumar, Ex-Director, DMRL for his support during my entire Ph.D work at DMRL. My special thanks to Gp.Capt.BVN Shiva, Indian Air Force, for providing the aero-engine turbine discs required for extracting samples for my experimental work. I am also grateful to Dr. Gopinath, Scientist 'G', Group Head, NDTG, DMRL for his support in facilitating Gleeble thermo-mechanical simulator for carrying out high temperature POD studies and also for his critical review of my articles before submitting to journals for publication. Many thanks to Dr.T.Jayakumar, DRDO Chair, DMRL for his ideas and suggestions during the completion of high temperature part of the thesis work. Special thanks to Dr. Ashok Kaul, CEO, LPTI Inc., Canada for critical

discussions which helped in identifying the high temperature POD problem. Special thanks are also extended to Prof. Hara Gopal, BITS-Hyderabad for providing his share of knowledge required for overcoming the statistical difficulties involved in plotting POD curves.

I thank Mr.Siva Koti, TO 'A', MBG, DMRL and Mr.Lambodar Sahoo, STA 'B', NDTG, DMRL for their help in carrying out room temperature and high temperature fatigue tests, respectively. I would like to acknowledge the assistance provided by Mr.Chandra Mohan, TO 'A', ETC, DMRL during fluorescent penetrant non-destructive inspection facility. In addition, I would like to thank all members of MBG, NDTG, ETC, EMG, Metallography, Mechanical workshop groups of DMRL for the help provided to me during the experimental part of this program.

I am very much thankful to the Council of Scientific and Industrial Research (CSIR), Govt. of India for providing me the financial support in the form of Senior Research Fellowship (ACK. No.: 141308/2k15/1, File No.:09/414(1124)/2016 EMR-I). Heartfelt thanks are also extended to Science and Engineering Research Board (SERB) – International Travel grant Scheme (ITS) by Department of Science and Technology (DST), Government of India for providing the Financial Assistance (File Number: ITS/2019/005225) for participating in "11th International Symposium on NDT in Aerospace, France (13 November, 2019 to 15 November, 2019)". I also thank Mr.Devender, Fellowship and Scholarship section, UoH for providing me the timely information and support regarding the CSIR-SRF fellowship administrative formalities.

Huge thanks to Dr.Pardhu Yella, Assistant Professor, MGIT for the stimulating scientific and technical discussions which helped in keeping things in perspective. Thanks are also extended to Dr.K.V.Srinivasulu for consistently inspiring and motivating me to pursue Ph.D at any cost. I thank my friends P.Sunil Kumar, Suresh Beera (currently in M/s. Kajaria ceramics Ltd, Hyderabad), S.Janakiram for all the technical support provided during experimental tasks of my Ph.D work and also for all the fun due course. In addition, I thank the M.Tech project students of DMRL Mr.Yateesh (currently in M/s. Vestas Ltd, Chennai), Mr.Sandeep (M/s. Hyundai Motor Company, Hyderabad), Mr.Phani Karthick (currently as SRF in ARCI, Hyderabad), Mr.Chinmaya (Currently Ph.D scholar, Taiwan university, Taiwan), Mr.Manoj (M.Tech, NITK) and Mr.Satish Kumar (STA 'B', NDTG, DMRL) for sharing the best moments spent during my Ph.D work in DMRL.

I wish to express my most profound gratitude and reverence to my parents Mr.R.Shankaraiah and Mrs. R.Sobha who sacrificed every comfort of their life to give a better life for me and for their epitome of patience in allowing me to choose the career of my interest. I also thank my in laws Mr.B.Yesuraju and Mrs.B.Achutamba for all the moral support. I feel great to acknowledge my dear wife Mrs.Sridevi Vamsi Krishna, Dy.EE, GHMC for putting up with my craziness, for showering all the unconditional love and always being so encouraging and supportive. I should definitely say that I am blessed to have her in my life. I also thank my elder brother Major.Dr.R.Siva Prasad, Indian Army and his family (wife- Dr.Nirisha & son- R.Sharvanth) and my younger brother Dr.R.Mallikarjuna for their support and encouragement.

Above all, I would like to convey my devotional gratitude to all the Gods for giving me the strength, knowledge, ability and opportunity to undertake this research study and complete it satisfactorily. Without their blessings, this achievement would not have been possible.

Vamsi Krishna Rentala

List of Publications

Journal Publications

1. **Vamsi Krishna Rentala**, Phani Mylavarapu, Jai Prakash Gautam, "Issues in Estimating Probability of Detection of NDT Techniques – A Model Assisted Approach", (Elsevier) Ultrasonics, Volume 87, Pages 59–70, February 2018. https://doi.org/10.1016/j.ultras.2018.02.012
2. **Vamsi Krishna Rentala**, Phani Mylavarapu, Jai Prakash Gautam, Vikas Kumar, "Generation of POD Curves in the Absence of Service Induced Cracked Components- An Experimental Approach ", Insight-Nondestructive testing and condition monitoring, Volume 61, Issue Number 1, Pages 28-34(7), January 2019. https://doi.org/10.1784/insi.2019.61.1.28
3. **Vamsi Krishna Rentala**, Phani Mylavarapu, J.P.Gautam, Gp.Capt.B.V.N.Shiva, K.Gopinath, Vikas Kumar, "Physical Manifestation of $a_{90/95}$ in Remnant Life Revision Studies of Aero-engine Components", Procedia Structural Intergrity (Elsevier), Volume 14, Pages 597-604, 2019. https://doi.org/10.1016/j.prostr.2019.05.073
4. **Vamsi Krishna Rentala**, Phani Mylavarapu, Atul Kumar, Jai Prakash Gautam, Gopinath Kakkropath, T. Jaya Kumar, "POD of NDT Techniques Using High Temperature Oxidized Fatigue Cracks in an Aero Engine Alloy". (To be submitted).

Conference Proceedings

5. **Vamsi Krishna Rentala**, Phani Mylavarapu, J.P.Gautam, Vikas Kumar, "NDE Reliability using Natural Fatigue cracks", 7th European-American Workshop on NDE Reliability,Sep'17, Potsdam, Germany. Published in e-Journal of NDT (ndt.net), (More information about this article: http://www.ndt.net/?id=21793).
6. **Vamsi Krishna Rentala**, Phani Mylavarapu, Gopinath, J.P.Gautam, Vikas Kumar, "Model Assisted Probability of Detection for Lognormally Distributed Defects", 8th International Symposium on NDT in Aerospace, Nov'2016, published in e-Journal of NDT (ndt.net), (More information about this article: http://www.ndt.net/?id=20615).
7. **Vamsi Krishna Rentala**, Phani Mylavarapu, K.Gopinath, J.P.Gautam, Vikas Kumar, " Effect of Elliptical Crack Aspect Ratio on POD" , NDE-2016, published in e-Journal of NDT (ndt.net), (More information about this article: http://www.ndt.net/?id=21213).

Indian- Defence Research and Development Organisation (DRDO)-Technical Reports

8. Phani Surya Kiran Mylavarapu, **Vamsi Krishna Rentala**, M. Sundaraman, Hina Gokhale,Vikas Kumar, "Sensitivity Evaluation of NDT Techniques on Naturally Initiating Fatigue Cracks – An Experimental Approach for a POD Framework", DRDO-DMRL-NDTG-083-2015, March 2015.
9. Phani Surya Kiran Mylavarapu, **Vamsi Krishna Rentala**, Jai Prakash Gautam, K.Gopinath, Vikas Kumar, "Challenges in POD of Ultrasonic testing", DRDO-DMRL-NDTG-169-2017, August 2017.

Conference Presentations

International Conferences

1. **Vamsi Krishna Rentala**, Phani Mylavarapu, Atul Kumar, Jai Prakash Gautam, B.V.N.Shiva, K.Gopinath, T.Jayakumar and Vikas Kumar, Effect of High Temperature Oxidation of Fatigue Cracks in Aero-Engine Components on POD of NDT Techniques, 11th international symposium on NDT in Aerospace, November 13-15, 2019 at Paris, France. (Oral)
2. **Vamsi Krishna Rentala**, Atul Kumar, Phani Mylavarapu, Jai Prakash Gautam, B.V.N.Shiva, T.Jayakumar, K.Gopinath and Vikas Kumar, EBSD Characterization of Oxidized High Temperature Fatigue Cracks Generated in a Nickel based Superalloy using Gleeble® Test System, ADMAT-2019, September 23-25, Hyderabad. (Poster)
3. **Vamsi Krishna Rentala**, Phani Mylavarapu, J.P.Gautam, Gp.Capt.B.V.N.Shiva, K.Gopinath, Vikas Kumar, "Physical Manifestation of $a_{90/95}$ in Remnant Life Revision Studies of Aero-engine Components", SICE-2018, Hyderabad, India
4. **Vamsi Krishna Rentala**, Phani Mylavarapu, Jai Prakash Gautam, Vikas Kumar, "NDE Reliability using Natural Fatigue cracks", 7th European-American Workshop on NDE Reliability, September 2017, Potsdam, Germany. (Oral)
5. **Vamsi Krishna Rentala**, Phani Mylavarapu, Gopinath, Jai Prakash Gautam, Vikas Kumar, "Model Assisted Probability of Detection for Lognormally Distributed Defects", 8th International Symposium on NDT in Aerospace, November 2016, Bangalore, India. (Oral)
6. **Vamsi Krishna Rentala**, Jai Prakash Gautam and Phani Mylavarapu,"Microstructure Evaluation on Naturally initiating fatigue cracks of a Nickel based superalloy used in aero-engines,", EMSI-2016, 30 May-01 June 2016, IIT-BHU Varanasi, India. (Poster)

National Conferences

7. **Vamsi Krishna Rentala**, Phani Mylavarapu, Jai Prakash Gautam, Gp. Capt. B.V.N. Shiva, Vikas Kumar, "Issues in POD estimation of Qualitative NDT Techniques", NDE-2017, Dec 14-16 2017, Chennai, India. (Oral)
8. **Vamsi Krishna Rentala**, Phani Mylavarapu, K.Gopinath, Jai Prakash Gautam, Vikas Kumar, "Effect of Elliptical Crack Aspect Ratio on its Probability of Detection", NDE-2016, 15-17 Dec 2016, Thiruvananthapuram, India. (Poster)

9. **Vamsi Krishna Rentala**, Phani Mylavarapu, Jai Prakash Gautam and Vikas kumar, "Challenges in Model-assisted Probability of Detection (POD) of Ultrasonic Testing- A Modeling Approach," NDE-2015, 26-28 November 2015, Hyderabad, India. (Oral)
10. **Vamsi Krishna Rentala**, Phani Surya Kiran Mylavarapu, M.Sundararaman, Vikas Kumar, "Sensitivity Evaluation of Non-destructive techniques on naturally initiating fatigue cracks- An experimental approach for a POD framework," NDE-2014, 4-6 Dec'14, Pune, India. (Poster)

Table of Contents

Acknowledgements iv

List of Publications vii

Conference Presentations ix

Table of Contents xi

List of Figures xvi

List of Tables xxi

Abstract xxii

1. INTRODUCTION 1

1.1 History of aircraft failures and possible reasons 1

1.2 Metal fatigue 3

1.2.1 High temperature fatigue cycling 5

1.3 Lifing methodologies 6

1.3.1 Infinite-life design 6

1.3.2 Safe-life design 6

1.3.3 Fail-safe design 7

1.3.4 Damage tolerance design 7

1.4 Non-destructive testing 9

1.4.1 Liquid Penetrant Technique (LPT) 9

1.4.1.1. Reliability aspects of LPT 10

1.4.2 Eddy Current Technique (ECT) 11

1.4.2.1. Coil impedance and impedance plane 12

1.4.2.2. Lift-off 12

1.4.2.3. Skin Depth 13

1.4.2.4. Reliability aspects of ECT technique 15

1.4.3. Ultrasonic Testing (UT) 15

1.4.3.1. Wave propagation 17

1.4.3.2. Attenuation of the wave 18
1.4.3.3. Reliability aspects of ultrasonic inspection technique 18
1.5 Probability of detection (POD)- indicator of reliability of NDT techniques 19
1.5.1. Model-assisted POD 22
1.5.1.1 Modeling and Simulation 24
1.5.1.2 Censoring of data 25
1.5.1.3 Noise 25
1.6 Reasons for NDE variability and the requirement for POD 25
1.7 Objectives of the thesis work 28
1.8 Organization of thesis 28
References 30
2. LITERATURE REVIEW 33
2.1 Experimental POD studies 33
2.2 Modeling based POD studies 37
2.3 Multi-parameter POD studies 38
2.4 POD studies using transfer function approaches 41
2.5 Importance of probability distributions and statistics in POD studies 42
References 46
3. EXPERIMENTAL POD PROCEDURE 54
3.1 Material 54
3.2 Room temperature fatigue cycling 55
3.3 High temperature fatigue cycling 57
3.3.1 Specimen geometry 57
3.3.2 Optimization of load for fatigue cycling 58
3.3.3 Fatigue cycling in Gleeble system 58
3.4 Crack size measurements using Scanning Electron Microscope (SEM) 59
3.5 NDT inspection of fatigue cracks 60

3.5.1 Eddy current technique (ECT) 61
3.5.2 Fluorescent liquid penetrant technique (FLPT) 62
3.6 Theory and Procedure for plotting the POD curves 63
3.6.1. POD using HIT/MISS NDT data 63
3.6.1.1. HIT/MISS POD approaches for multiple cracks at a site 64
3.6.2. POD using â (signal response) NDT data 66
3.6.2.1 Maximum Likelihood Estimators (MLE) 67
References 69
4. MODEL BASED POD PROCEDURE 71
4.1. MAPOD work flowchart 71
4.2 Experimental ultrasonic testing for calibration and validation 72
4.3. Development of mathematical model 74
4.4. Generation of random crack sizes 76
4.4.1. Random crack sizes by lognormal distribution 76
4.5. POD from lognormally distributed crack sizes 77
References 78
5. RESULTS AND DISCUSSION 80
5.1. Part I - NDT response data generation using experimental POD work 80
5.1.1. Details of surface fatigue crack sizes generated 80
5.1.1.1. Room temperature cracks 80
5.1.1.2. High temperature cracks 82
5.1.2. Observations from SEM micrographs 84
5.1.2.1. Room temperature cracks 84
5.1.2.2. High temperature cracks 85
5.1.3. NDT inspection of fatigue cracks 91
5.1.3.1 FLPT 91
5.1.3.1.1 Room temperature cracks 91

5.1.3.1.2. High temperature cracks 93
5.1.3.2. ECT inspection 94
5.1.3.2.1. ECT inspection of EDM notches 94
5.1.3.2.2. ECT Inspection of high temperature fatigue cracks 95
5.1.3.2.3. ECT inspection of room temperature fatigue cracks 99
5.2. Part II-NDT response data generation using model based POD procedures 103
5.2.1 Validation of mathematical model 103
5.2.2 Generation of NDT response data from physics based numerical model 103
5.3. Part III - Statistical analysis of NDT response data 104
5.3.1. Statistical analysis for â vs. a data 104
5.3.1.1. POD using model based NDT data 104
5.3.1.1.1. Estimation of best linear fit between â vs. a 104
5.3.1.1.2. Regression with censoring data 105
5.3.1.1.3. Effect of $\hat{a}_{dec}$ (decision threshold) on $a_{90/95}$ values 109
5.3.1.2. POD using experimental data 111
5.3.1.2.1. POD curves using higher number of random crack depth sizes 113
5.3.2. Statistical analysis using HIT/MISS data 117
5.3.2.1. FLPT data of room temperature cracks 117
5.3.2.2. ECT inspection data 119
5.3.3. Summary of $a_{90/95}$ values obtained 123
5.4. Part IV - Remnant life calculations using DT methodology 124
5.4.1 Theory on remnant life calculations using deterministic fracture mechanics approach 124
5.4.2 Procedure for remnant life calculations 126
5.4.3 Remnant life calculations using deterministic fracture mechanics approach 127
References 129
6. CONCLUSIONS 133

Appendix-I: Statistical analysis of HIT/MISS data using Minitab 136

Appendix- II – Statistical analysis for â vs. a data using Minitab 143

Appendix- III – Matlab program for automatic defect identification using Hilbert transform from numerical A-scan signals 150

List of Figures

Figure 1: Aircraft failure modes [4] 3
Figure 2: Fatigue stress cycles (a) Reversed (b) Repeated and (c) Irregular [7] 4
Figure 3: Effect of frequency on fatigue life at constant elevated temperature [7] 5
Figure 4: Fatigue design methodologies (a) Infinite life (b) Safe life (c) Fail safe 8
Figure 5: Schematic representation of damage tolerance methodology 8
Figure 6: Typical steps involved in liquid penetrant inspection process. 9
Figure 7: Schematic of eddy current testing [17] 11
Figure 8: Impedance plane diagram [19] 12
Figure 9: Impedance plane with lift-off and signals of surface notches of sizes (a) 0.04 inch (b) 0.02 inch and (c) 0.008 inch obtained from eddy current inspection of aluminium 7075 defect calibration block. 13
Figure 10: Variation of eddy current density with respect to depth [16] 14
Figure 11: Eddy current depth of penetration with respect to frequency, conductivity and permeability [19] 15
Figure 12: Schematic of Ultrasonic testing [20] 16
Figure 13: Vibration of particles in longitudinal and shear waves [21] 17
Figure 14: The drop in signal amplitude with multiple backwalls due to attenuation in the material [21] 18
Figure 15: Realistic vs Idealized POD curve for any technique [22] 19
Figure 16: Typical POD curve indicating a_{50}, a_{90} and $a_{90/95}$ [23] 20
Figure 17: Flow chart of model assisted POD [24] 23
Figure 18: Equipment to Equipment variability in POD 26
Figure 19: Technique-Technique Variability in POD 26
Figure 20: Operator- operator variability in POD 27
Figure 21: Workflow in POD activity 28
Figure 22: Reliability index of dye penetrant inspection of fatigue cracks in Aluminium cylinders [1] 34
Figure 23: POD curve plotted for dye penetrant inspection of fatigue cracks in a service expired aero-engine compressor disc [6] 35
Figure 24: Eddy current response for EDM notches and Fatigue cracks in complex engine components [15] 37
Figure 25: Comparison of MAPOD curve with experimental POD curve [51] 38

Figure 26: Different categories of influential parameters [65]. 40
Figure 27: Multi-parameter POD curves (a) as a function of flaw length for different flaw depths and (b) as a function of flaw area and comparison with conventional POD procedure [56] 40
Figure 28: Schematic of transfer function approach based POD curve estimation for cracks in a desired geometry using notches and cracks response from a flat plate [66] 41
Figure 29: Fatigue cracks following lognormal distribution [77] 42
Figure 30: Censored data regression with (a) OLS (b) MLE [81] 43
Figure 31: Example of regression between â vs. a using (a) natural logarithm [83] (b) logarithm to the base 10 [25] 44
Figure 32: A portion of turbine disc exposed to 3000 hours of service life that is used for extraction of samples (a) Before and (b) After 54
Figure 33: Multiple fatigue cracks emanating from bolt hole locations of an aero-engine disc [3]. 55
Figure 34: Specimen design showing loading point and supports 56
Figure 35: Experimental set up of 3-point bend fatigue testing 56
Figure 36: Specimen design used for fatigue cycling in Gleeble® system 57
Figure 37: (a) Sample with thermocouples welded at the center (b) Blocks used for holding sample (c) Sample in the blocks (d) Specimen chamber with sample in the blocks 59
Figure 38: SEM equipped with EDS and EBSD detectors 60
Figure 39: Nickel based superalloy material with 0.6 mm to 1.0 mm deep EDM notches. 61
Figure 40: (a) Samples with penetrant and (b) developer applied during FLPT inspection 62
Figure 41: Flowchart of POD statistical procedure using Hit/Miss NDT data. 64
Figure 42: An example of multiple flaws at a site [16] 65
Figure 43: Flowchart of POD statistical procedure using signal response NDT data. 69
Figure 44: MAPOD work flowchart followed in this study 71
Figure 45: Ultrasonic Inspection (a) Experimental Setup (b) Sample (Ti-6Al-4V Block) with dimensions 72
Figure 46: A-scan signal of Ti-6Al-4V block indicating the FBH response. 73
Figure 47: Experimental A-scan signal of contact ultrasonic testing showing 4 back wall echoes 73
Figure 48: (a) 2-D axisymmetric model of Ti-6Al-4V block with FBH and (b) its representative 3-D model for understanding 74

Figure 49: (a) Input waveform signal used for 5MHz (b) Frequency content of input waveform signal 75
Figure 50: A-scan signal of 2-D axisymmetric model showing 4 back wall echoes. 76
Figure 51: Histogram of 40 crack sizes along with lognormal distribution fit 77
Figure 52: Histogram of room temperature fatigue crack lengths generated (a) lognormal distribution fit (b) results of goodness of fit test 81
Figure 53: (a) Goodness of fit test result highlighting lognormal distribution (b) Histogram of surface fatigue crack length sizes with lognormal distribution fit 83
Figure 54: (a) Micrographs of one of the room temperature tested samples with crack lengths indicated (0.95 mm and 0.56 mm) (b) its EBSD grain boundary map 84
Figure 55: Service induced fatigue cracks [5, 6] 85
Figure 56: High temperature multiple fatigue cracks at (a) single notch location (b) crack 1 filled with oxides (c) crack 2 filled with oxides and (d) two cracks at notch location in zoomed view 85
Figure 57: Oxidized fatigue crack micrograph showing cracking of material surface due to oxidation and crack branching along with slip band oxidation in figure insets. 86
Figure 58: EDS results confirming the presence of oxides in (a) Crack surface oxidation (b) Slip band oxidation 87
Figure 59: EDAX analysis results of material surface oxidation and oxide induced cracking confirms the presence of oxides. 87
Figure 60: (a) Fractured samples indicating notch region (b) fractograph of the crack surface from the fracture samples indicating direction of crack propagation (c) zoomed view of fracture surface indicating bright and dark regions 88
Figure 61: SEM micrograph and EDAX spectrum of (a) bright region and (b) dark region of the fracture surface. 89
Figure 62: Micrograph of Fatigue crack in a sample tested under vacuum at 650°C 90
Figure 63: EDS analysis of fatigue crack generated in vacuum tested sample 91
Figure 64: FLPT results captured under UV light in dark room. 94
Figure 65: (a) ECT setup for inspection of calibration sample (b) Impedance plane of the EDM notches in calibration sample. 95
Figure 66: Linear regression of ECT amplitude data vs. EDM notch depth sizes. 95
Figure 67: ECT impedance map 1 mm size defect (a) EDM notch (b) oxidized fatigue crack 96

Figure 68: Histogram of equivalent crack depth sizes along with log-normal distribution fit. 98
Figure 69: ECT impedance map 1 mm size defect (a) EDM notch (b) oxidized or high temperature fatigue cracks and (c) non-oxidized or room temperature fatigue crack. 101
Figure 70: Histogram with lognormal distribution fit of equivalent crack depths of room temperature fatigue cracks 102
Figure 71: Linear regression of (a) â vs. ln(a) (b) ln(â) vs. ln(a) (c) â vs. a and (d) ln(â) vs. a 105
Figure 72: Regression Table 106
Figure 73: (a)POD vs. ln(a) for 40 lognormally distributed crack sizes indicating $a_{90/95}$ = 0.80 mm (b) POD vs. flaw size (a) indicating a_{50}, a_{90} and $a_{90/95}$ as 0.5 mm, 0.73 mm and 0.80 mm, respectively. 107
Figure 74: (a) POD vs. $\log_{10}$(a) plot for 40 lognormally distributed crack sizes indicating $a_{90/95}$ = 0.83 mm and (b) POD vs. flaw size plot indicating a_{50}, a_{90} and $a_{90/95}$ as 0.74 mm, 0.88 mm and 0.91 mm, respectively. 108
Figure 75: POD vs. flaw size plots for (a) 50 and (b) 500 lognormally distributed crack sizes indicating $a_{90/95}$ values as 0.79 and 0.72 mm, respectively. 109
Figure 76: $a_{90/95}$ vs. $\hat{a}_{dec}$ values for different number of FBH defects 110
Figure 77: log-log plot with linear regression of ECT signal amplitude and the corresponding equivalent crack depth sizes data of high temperature oxidized fatigue cracks. 112
Figure 78: Regression with censored data using MLE method in Minitab statistical software 112
Figure 79: POD vs. equivalent crack depth for (a) oxidized cracks indicating a_{90} = 0.45 mm and (b) non-oxidized cracks indicating a_{90} = 0.58 mm.....113
Figure 80: Histogram with lognormal distribution fit of 50 random crack sizes generated ..114
Figure 81: POD vs. 50 random crack depths generated according to the probability distribution parameters of (a) oxidized cracks indicating a_{90} = 0.45 mm and $a_{90/95}$ = 0.60 mm and (b) non-oxidized cracks indicating a_{90} = 0.58 mm and $a_{90/95}$ = 0.75 mm.....115
Figure 82: Histogram with lognormal distribution fit of 500 random crack sizes generated 116
Figure 83: POD vs. 500 random crack depths generated according to the probability distribution parameters of (a) oxidized cracks indicating $a_{90/95}$ = 0.45 mm and (b) non-oxidized cracks indicating $a_{90/95}$ = 0.58 mm. 116
Figure 84: POD curves using three approaches for multiple cracks at a site for FLPT with (a) Type 1; (b) Modified Type 1 and (c) Type 2 approaches indicating $a_{90/95}$ values. 118

Figure 85: POD curves indicating a_{90} and $a_{90/95}$ values of FLPT data with (a) 52 cracks and (b) 17 cracks. 119
Figure 86: Binary logistic regression performed in Minitab software. 120
Figure 87: POD vs. surface crack length for (a) oxidized cracks indicating a_{90} = 0.41 mm and $a_{90/95}$ = 0.45 mm (b) non-oxidized cracks indicating a_{90} = 0.75 mm and $a_{90/95}$ = 1.12 mm ... 120
Figure 88: POD vs. equivalent crack depth for (a) oxidized cracks indicating a_{90} = 0.32 mm and $a_{90/95}$ = 0.35 mm (b) non-oxidized cracks indicating a_{90} = 0.70 mm and $a_{90/95}$ = 0.76 mm ... 121
Figure 89: Schematic along with nomenclature of single edge notched bend (SENB) specimen [32] ... 126
Figure 90: Effect of $a_{90/95}$ on remnant fatigue cycles ... 129
Figure 91: Screenshot showing the binary logistic regression option in Minitab software ... 137
Figure 92: Screenshot showing the pop-up window of binary logistic regression ... 138
Figure 93: Result of the binary logistic regression performed between log(crack sizes) and HIT/MISS response data ... 138
Figure 94: Screenshot showing the scatter plot option in Minitab software ... 140
Figure 95: Screenshot showing the various modes of plotting scatter plot in Minitab software ... 141
Figure 96: Screenshot showing the selection of x and y variables for plotting POD curves. 141
Figure 97: POD curve of FLPT inspection of room temperature cracks indicating a_{50}, a_{90} and $a_{90/95}$ values ... 142
Figure 98: Screenshot showing regression with life data option in Minitab software ... 144
Figure 99: Screenshot showing the variables and model with distribution in Minitab software ... 145
Figure 100: Result of the regression with life data analysis ... 145
Figure 101: Screenshot showing the option for plotting CDF of lognormal distribution in Minitab software ... 147
Figure 102: Screenshot showing the plotting of CDF of log-normal distribution function ... 148
Figure 103: POD curve of 40 lognormally distributed crack sizes indicating a90/95 = 0.8 mm ... 149
Figure 104: Generating initial signal in time domain ... 150
Figure 105: Generating 5 MHz signal ... 151

List of Tables

Table 1: Typical chemical composition of Turbine Disc Material ~ Nimonic 80A in wt%....54
Table 2: Details of surface fatigue crack width dimensions obtained in room temperature tested samples. 82
Table 3: Details of surface fatigue crack width dimensions obtained in high temperature tested samples. 83
Table 4: Crack Dimensions along with FLPT HIT/MISS indications....91
Table 5: Details of inspection site number, number of flaws at a site and the corresponding flaw sizes along with FLPT indications....93
Table 6: ECT signal response data of all high temperature tested samples....98
Table 7: ECT signal response data of all room temperature tested samples 101
Table 8: Peak to peak amplitudes of successive back wall echoes and the corresponding time difference and amplitude ratios of both experimental and modeling A-scan signals. 103
Table 9: Representative NDT Response data generated using physics based numerical model 104
Table 10: â vs. a data along with left censoring (L) and right censoring (R) 105
Table 11: Number of censored and uncensored data with respect to the number of defect sizes 109
Table 12: Values of $a_{90/95}$ for various number of defects with different decision threshold levels 110
Table 13: Summary of $a_{90/95}$ values obtained using FLPT and ECT inspection of room temperature and high temperature cracks. 124
Table 14: Effect of $a_{90/95}$ on remnant life calculations 128
Table 15: FLPT HIT/MISS response of room temperature crack length data....136
Table 16: Probabilities along with 95% confidence intervals of all the crack sizes inspected using FLPT....139
Table 17: Lognormally distributed 40 FBH sizes and the corresponding ultrasonic signal amplitudes of defects 143
Table 18: Probabilities and 95% lower confidence probabilities obtained from the CDF of log-normal distribution 149

Abstract

Conventionally, under the concept of safe life methodology for aero-engines, the components after reaching the original equipment manufacturer (OEM) specified life are retired from service. Therefore, safe life is a highly conservative methodology and does not fully utilize the materials' potential. In order to overcome this conservative approach, advanced lifing methodologies such as damage tolerance (DT) are currently being explored. Remnant life assessment (RLA) of the aero-engine components is the major idea behind the life extension programs carried out under the DT concept. In order to estimate the remnant life of a component using fracture mechanics, knowledge about the initial crack size present in the component and the critical crack size at which the component fails are mainly required. The critical crack size at which the component fails can be calculated using fracture mechanics based approaches considering the information on the material, design, loading conditions, etc. However, the size of the initial crack present in the component can only be estimated using Non-Destructive Testing (NDT) Techniques. Hence, assessment of the reliability of NDT techniques is essential and plays a significant role in precise estimation of the remnant life of a component. The capability or the reliability of the NDT techniques is in general estimated by plotting probability of detection (POD) curves. These POD curves yield $a_{90/95}$ (detecting a crack with 90% probability and 95% confidence) value for use in remnant life calculations. A typical experimental POD procedure requires several safe life expired aero-engine components containing numerous fatigue cracks. However, the requirement of a large number of in-service failed components with numerous initiating fatigue cracks makes POD a cost-intensive methodology. Hence, laboratory samples with electrical discharge machined (EDM) notches representing fatigue cracks have also been used for NDT reliability studies. However, probability of detection (POD), a measure of NDT reliability, is usually a function of several material and crack parameters rather than only crack dimensions. This limits the applicability of EDM notches (with a minimum width of notch ~0.25 mm) as artificial fatigue cracks for POD studies. Therefore, the current study initially demonstrates the methodology of generating natural fatigue cracks mimicking in-service conditions under room temperature conditions in nickel-based superalloy samples extracted from aero-engine turbine disc. However, fatigue cracks which are generated at room temperature conditions does not represent the effects of higher engine service operating conditions such as oxidation, etc.,. As the engine operates at high temperatures, oxidation effects on fatigue cracks are predominant. This results in the formation of oxidized fatigue cracks at high stress

concentration locations of the turbine components. In order to mimic the real service fatigue cracks to the best possible extent possible, it is essential to generate fatigue cracks at high temperature oxidizing conditions (service temperature ~ 650°C) for use in NDT reliability studies. Hence, in the current study, efforts are also made to generate oxidized surface fatigue cracks using Gleeble system. These cracks are inspected using fluorescent liquid penetrant technique (FLPT) and eddy current technique (ECT). Compared to FLPT inspection of room temperature cracks, FLPT inspection of high temperature oxidized fatigue cracks suffered from poor detectability due to crack closure with oxides. However, ECT has detected most of the cracks resulting in the generation of both HIT/MISS and â (ECT signal amplitude) vs. a (crack size) data. This NDT inspection data is statistically processed for obtaining POD curves and the $a_{90/95}$ value. In all the cases, the $a_{90/95}$ values of high temperature cracks are sensitive compared to that of room temperature cracks due to the higher detectability of oxide cracks. Further, these $a_{90/95}$ values are incorporated into the damage tolerance based life calculations for estimating the remnant fatigue cycles the component can withstand before failure. Due to ECT technique's higher sensitivity, it is observed that NDT with ECT technique will result in the higher number of remnant cycles compared to the FLPT technique.

Moreover, estimation of the reliable $a_{90/95}$ value of an NDT technique is dependent on various parameters such as the material, geometry of the component, type of crack, size and shape of crack, environment, etc. Hence, it is essential for reliability to be estimated for all materials, defects, geometries, etc., making POD an extremely laborious, cost intensive and time consuming task. Therefore, model based POD studies (MAPOD) studies have also been developed. MAPOD studies involves in using a physics based numerical model for collecting the NDT response of a designed defect in a designed geometrical component. Further processing the signal response data and the crack sizes simulated using appropriate statistical techniques would result in plotting the POD curves. Even though POD studies are initiated since early 1970's, several existing issues in POD studies resulted in some ambiguity about the statistical procedures and challenges involved. In this study, MAPOD approaches are demonstrated by addressing various issues related to selection of crack sizes distribution, challenges involved in censoring and regression, estimation of distribution parameters, etc. Ultrasonic testing on volumetric defects has been identified as a platform to discuss the challenges involved. A COMSOL Multiphysics based FEM numerical model developed to simulate ultrasonic response from a Ti-6Al-4V cylindrical block has been validated experimentally. Further, the individual ultrasonic response from various Flat Bottom Hole

(FBH) defects following lognormal distribution has been generated using the numerical model. $a_{90/95}$ value obtained from POD curve showed that the POD value increased with an increase in decision threshold.

1. INTRODUCTION

During the recent years, life extension studies of service expired engine components is attaining higher prominence in the field of aero-industry. As part of the advanced life extension methodologies, damage tolerance technique plays a vital role in the aero-industry. Damage tolerance technique relies on the safe NDT inspection intervals which are deduced from the reliability of the NDT techniques used for inspection. Hence, estimating the reliability of the NDT techniques plays a prominent role in the successful implementation of damage tolerance methodology for aero-engines. As the current work is based on estimating the reliability of NDT techniques in inspecting fatigue cracks using experimental and model based POD studies, brief introduction to these concepts is provided in the current chapter. The major topics that are briefly discussed are various modes of aircraft failures, fatigue of engine components, fatigue life design methodologies, reliability aspects of different NDT techniques mostly used in the aero-industry and reliability or POD curves of NDT techniques using both experimental and model assisted methods.

1.1 History of aircraft failures and possible reasons

Aviation accidents are being considered as the most fatal incidents involving very less chances of life survival. The worst crash of Japan Airlines Flight 123 in 1985 occurred due to improper repair of in-flight structural component resulting in highest number (520) of fatalities ever reported under a single aircraft incident [1]. Ever since, major technological developments in areas related to design (against corrosion and widespread metal fatigue damages), aero-engine materials (for usage in both structural and engine components), technologies related to collision avoidance and better air traffic control systems, advanced non-destructive inspection methods, avoidance of electrical spark eliminations and real-time flight tracking, etc., are continuously being pursued. In spite of all these advancements, aircraft accidents similar to the recent Southwest airlines flight 1380 accident of April 17, 2018 continue to happen due to a undetected crack in a fan blade even after NDT inspection [2]. According to the Boeing's statistical summary of commercial jet airplane accidents, a total of 1989 accidents occurred worldwide resulting in 31,042 fatalities between1959 to 2017 [3].

All these accidents are reported to have occurred due to various aircraft failure modes that need basic understanding. Figure 1 shows the various modes of aircraft failures obtained from U.S Airforce statistical database [4]. From Figure 1, it can be observed that the pilot

error and lack of stringent logistics individually contribute 43% each to aircraft failures. Some of the notable accidents due to pilot errors include, accidents of Air Canada Flight 621 in 1970, American Airlines Flight 587 in 2001 and Adam Air Flight 574 in 2007 [5]). The remaining 14% of aircraft failures are attributed to the weather conditions (for example BOAC Flight 911 incident in 1966 [5]) and miscellaneous accounts. Amongst these errors, the errors arising from the pilot side can be overcome by imparting required rigorous training procedures. Moreover, developments of pilot less flight systems or automation of piloting systems could also help in avoiding pilot error. Further comparing the failures occurred due to logistics (Figure 1), it can be observed that the majority (37%) of those are from the aero-engine side (for example accidents of American Airlines Flight 191 in 1979, Lauda Air Flight 004 in 1991, Kongolo Antonov An-32B crash in 2007 and Airlines PNG Flight 1600 in 2011 [5]). Additionally, landing gears failure (United Airlines Flight 173 [5]) contributes to 20% of the failures occurring due to logistics. Furthermore, flight controls and electrical issues (United Airlines Flight 811 [5]) contribute to 13% each in failures due to the logistics. Moreover, fuel issues (Ex: TWA Flight 800 [5]) and airframe structures (Ex: Alaska Airlines Flight 261 [5]) contribute to 9% and 8% of logistics, respectively. Flight controls, fuel and electrical issues and airframe structures which contribute to the remaining errors due to logistics can be rectified with suitable efforts. Therefore, amongst the failures due to logistics, as aero-engine contributes to the maximum, due care should be undertaken for understanding the causes of occurrence.

Aero-engine containing approximately 25000 numerous parts made with different materials is considered as the most complicated machine that has ever been invented [6]. Aero-engines use gas turbines as the power houses operating on Brayton cycle process. Aero-engines/turbojet engines basically consists of several cold section and hot section components such as the air inlet section, compressor, combustion chamber, turbine and exhaust. All these components work under high temperature conditions undergoing service degradation. They are prone to various failure mechanisms such as the fatigue (high cycle fatigue and low cycle fatigue), creep, corrosion, mechanical damage such as foreign object damage or a bird hit, or due to flaws occurring from the manufacturing procedures of aero-engine components [7]. Among the various failure mechanisms occurring in the aero-engines, metal fatigue contributes to 49% and is thus considered as the predominant cause of failure (Ex: Accidents of Aloha Airlines Flight 243 in 1988 and China Airlines Flight 611 in 2002 [5]). Turbine discs, blades and vanes are the most common parts that undergo severe metal fatigue damage

[8]. Hence, these components are to be designed against metal fatigue damage. Brief information on fatigue is provided in the next section.

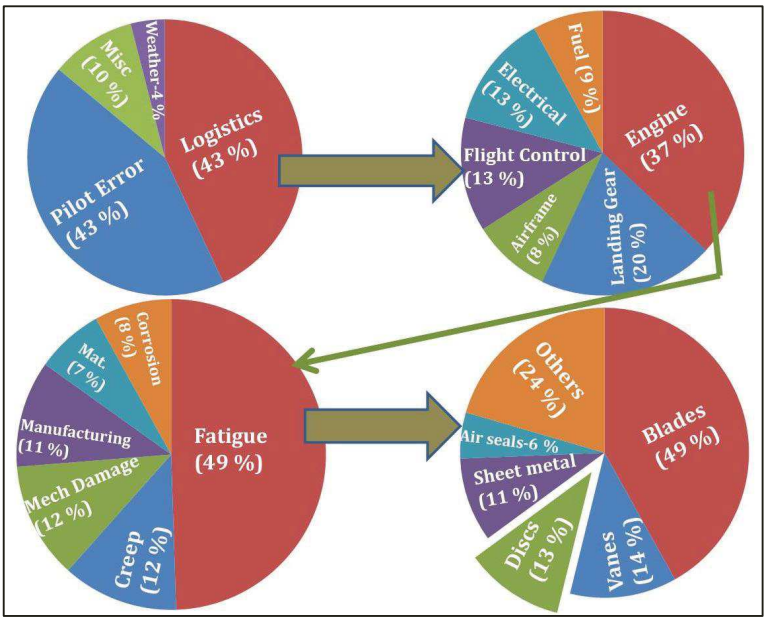

Figure 1: Aircraft failure modes [4]

1.2 Metal fatigue

Metals subjected to fluctuating stresses tend to fail at stresses lower than that are required to cause fracture on a single application of loads. Typically, metals used in applications involving repeated loading and vibration are subjected to fatigue failures. 90% of service failures due to mechanical causes are mainly because of fatigue [7]. Three different types of fluctuating stress cycles which can cause fatigue failures are, 1. Reversed stress cycle 2. Repeated stress cycle 3. Irregular stress cycle. Figure 2 [7] shows a pictorial description of the three fatigue stress cycles. In reversed stress cycle (Figure 2(a)), applied loads fluctuate between tensile and compressive whereas, in repeated stress cycle (Figure 2(b)), fluctuating loads are either fully tensile or compressive in nature. Moreover, in the irregular stress cycle, the loads are completely random in nature. From Figure 2(a) & (b), it can be observed that the maximum and minimum stresses are equal for the reversed kind of fatigue stress cycle unlike for the repeated stress cycle. From Figure 2(c), it can be observed that the third type of stress cycle which is entirely random can be correlated to the real engine cycles. The nomenclatures σ_{max}, σ_{min}, σ_m, σ_a and σ_r used in the Figure 2 accounts for the maximum stress, minimum stress, mean stress, alternating stress and range of stress, respectively. From Figure

2, it can be observed that range of stress (σ_r) is the difference between the maximum and minimum stresses in a cycle and alternating stress (σ_a) is equal to half of the stress range and mean stress (σ_m) is the algebraic mean of the maximum and minimum stresses in a cycle. Apart from these notations, two general ratios, namely, stress and amplitude ratios are used in representing fatigue data and are defined as, Stress ratio, R = $\frac{\sigma_{min}}{\sigma_{max}}$ and Amplitude ratio, A = $\frac{\sigma_a}{\sigma_m} = \frac{1-R}{1+R}$

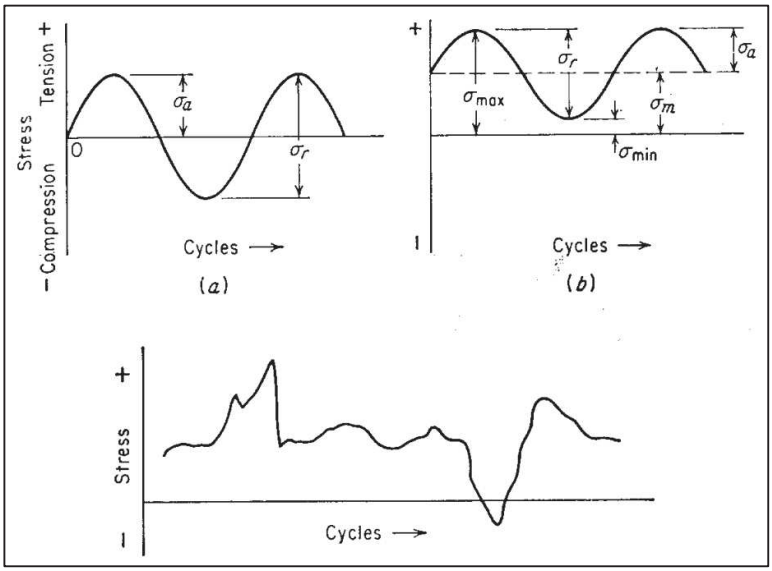

Figure 2: Fatigue stress cycles (a) Reversed (b) Repeated and (c) Irregular [7]

Fatigue data is usually represented in the form of S (stress) – N (number of cycles to failure) curves. Based on the number of cycles to failure, N, and the type of fatigue test i.e., either stress control or strain control, fatigue is classified into High Cycle Fatigue (HCF) and Low Cycle Fatigue (LCF). In general, HCF is a stress controlled fatigue test which usually results in $N>10^5$ cycles whereas, LCF is a strain controlled fatigue test having $N<10^4$ or 10^5 cycles. Either for HCF or LCF, fatigue failure occurs by means of a crack initiation, crack propagation and sudden fracture. These cracks usually initiate at a point of stress concentration such as notches or geometrical sharp corners or metallurgical inclusions. In addition to the basic factors such as higher stresses, large number of cycles and stress concentrations, fatigue is also controlled by various other factors such as residual stresses, combined stresses, metallurgical variables, corrosion and temperature. Even though fatigue depends on all these variables, as the current study deals only with room temperature and high temperature fatigue tests, the following discussion would be related to high temperature fatigue only.

1.2.1 High temperature fatigue cycling

As the majority of aero-engine turbine disc components are made up of nickel based superalloys, discussion on the high-temperature fatigue is restricted to the behavior of nickel based superalloys, only. In general, increase in temperatures above the ambient conditions would result in the decrease of the fatigue strength of metals. As the temperatures are greater than half the melting point of the material, creep becomes the predominant cause of failure [7]. Fatigue tests performed at higher temperatures would result in formations of oxide scales and aluminium scales on the surface and sub-surface, respectively [9]. In addition, high temperature fatigue tests also results in the formation of grain boundary oxidation due to which the strengthening precipitates or carbides along the grain boundary oxidize [9]. Further, these oxides contribute to the fatigue crack initiation and would also result in the increase of fatigue crack propagation rates [9]. It is well known that a fine grain structure is more suitable to resist fatigue fracture at room temperatures. However, with an increase in the test temperature, minor difference in the fatigue properties of coarse and fine grain structures of materials is observed. Unlike the room temperature fatigue cycling, at higher temperatures frequency plays an important role in the fatigue damage mechanism.

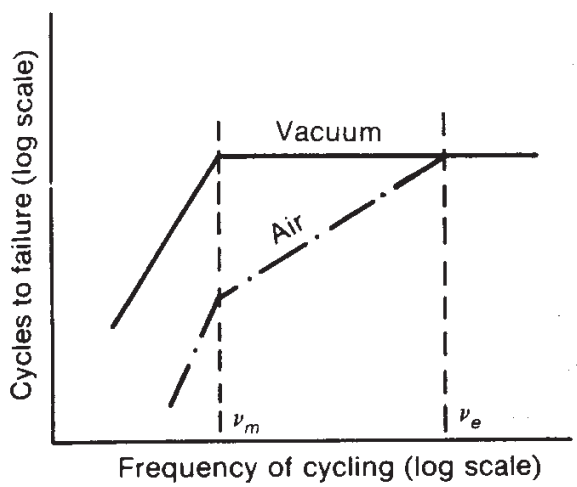

Figure 3: Effect of frequency on fatigue life at constant elevated temperature [7]

Figure 3 [7] shows the effect of frequency at higher temperatures on fatigue life. From Figure 3, it can be observed that at higher operating frequencies i.e., after v_e (higher frequency), as there is no change in the number of cycles to failure the fatigue damage mechanisms are independent of frequency. In addition, the failure occurs by the usual transgranular mode of fracture. However, at the intermediate range under the air

environment, i.e., between v_e and v_m (lower frequency), sufficient time is available for oxidation resulting in the transition of the fracture mode from transgranular to intergranular. Moreover, at lower frequencies, the intergranular fracture modes may occur [7]. In addition, at higher temperature conditions, microstructure of the material plays a key role in undergoing different mechanisms of fatigue.

Depending on the type of application, modern engineering structures employed in critical service industries such as defence, space and atomic energy undergo complex thermal and structural loads during their intended service resulting in room or high temperature fatigue/creep, etc. Considering the high cost and human risk involved in the operation of engineering structures, there is a growing demand for higher reliability. Therefore, life expectancy of the structures proposed to be established will be estimated at the design and deployment stage. Considering the safety factor, the life declared by original equipment manufacturer (OEM) is of highly conservative in nature and often results in life revision studies at the end of intended life or also during service [10]. Some of the current lifing methodologies incorporated on fatigue limited structures such as aero-engine components are described further.

1.3 Lifing methodologies

As fatigue is the predominant failure mechanism of aero-engine and its components, stringent designs against fatigue failure have been developed from the past many years [11]. The most common and distinct design philosophies against fatigue failure are:

1.3.1 Infinite-life design

This is the earliest design philosophy made against fatigue failure. In this design criterion, the operating stresses which are kept below the fatigue limit of the material would never result in failure of the component. Figure 4(a) shows the concept of infinite life design technique. From Figure 4(a), it can be observed that, infinite number of cycles to failure exist when stresses are applied below the fatigue limit of the material and vice versa. This kind of design philosophy is suitable for the parts subjected to very large cycles of uniform stresses. However, infinite-life design would limit the materials potential. Periodic inspection is not necessary in this type of design philosophy.

1.3.2 Safe-life design

Safe-life design is based on the primary assumption that the part/component is initially flaw-free and a crack once initiated, needs a finite life to develop into a critical crack

[7]. Components will be retired from service when they reach the safe declared life. Therefore, this finite life time is specified by the designer of the component or the part accompanied by a safety factor. Typically, a component will be defined a safe life of $1/n^{th}$ of the full-scale fatigue life demonstrated under ideal conditions as shown in Figure 4(b). This factor of safety, n, a value typically between 3-8 is used to account for environmental effects, differences in the manufactured product quality and material property variations. This is the most common design philosophy that is being followed in the aero-engine industry.

1.3.3 Fail-safe design

This design criterion assumes that the fatigue cracks which may be initiated in the parts or components are expected to be detected and repaired even before they lead to catastrophic failures. This lifing methodology which was also developed by Aero-engine industry tolerates the weight penalty neither by using higher safety factors nor the associated danger due to lower safety factors [7]. Muliple- load paths i.e., if a primary load path is failed, the load will be picked up by an alternative load path are employed in this design philosophy and the failure of the component will be prevented. Figure 4(c) shows the concept of fail-safe design technique. From Figure 4(c), it can be observed that fail-safe design technique is capable of increasing very small amount of life by suitably incorporating alternatives/repairs to primary load path failures. Detection and inspection of cracks is very important in this methodology.

1.3.4 Damage tolerance design

This design philosophy is the latest and the modified version of fail-safe design philosophy. Damage tolerance (DT) design philosophy assumes that every component consists of cracks which are expected to grow during the service. In simple words, DT concept is about tolerating the component even under the presence of damage/cracks. This concept is the basis for the U.S Air Force Airframe Structural Integrity Program (ASIP) [12] and Engine Structural Integrity Program (ENSIP) [13, 14]. The remaining fatigue cycles required for the crack to grow from an initial size to dysfunction size (usually $2/3^{rd}$ of critical crack size) can be calculated using fracture mechanics. Further, using the remnant fatigue cycles of the component, the safe inspection intervals (SII) are estimated. Moreover, these SII predictions are strongly influenced by the initial crack size and dysfunction crack size. During these safe inspection intervals, if a disc is found to contain a crack of size reliably detectable by the NDT technique, the disc is retired from the service (Figure 5). The dysfunction crack sizes are established analytically based on the best estimates of service

loads and material properties. However, the initial crack size present in the component is the reliably detectable crack size by non-destructive testing (NDT). This initial crack size is thus dependent on the reliability of the NDT technique used. Reliability of finding initial crack size by a non-destructive testing (NDT) technique is quantified through a parameter with statistical significance termed as "Probability of Detection (POD)". POD is a function of material used, surface conditions, type of cracks, orientation of cracks along with its length and width, etc. For the sake of completeness, brief introduction of most common NDT techniques typically used in the aero-engine industry are discussed in further sections.

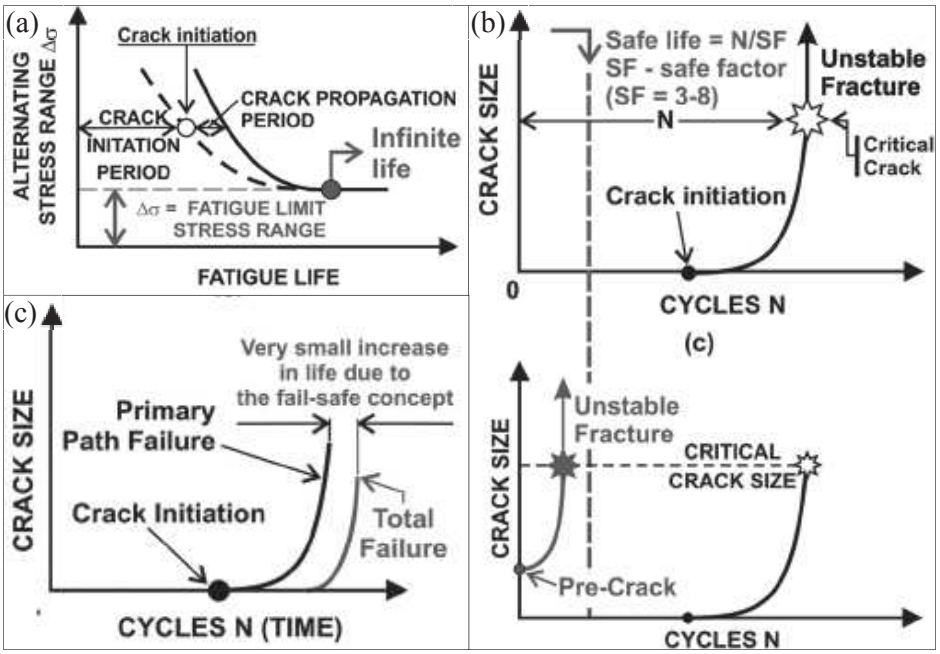

Figure 4: Fatigue design methodologies (a) Infinite life (b) Safe life (c) Fail safe

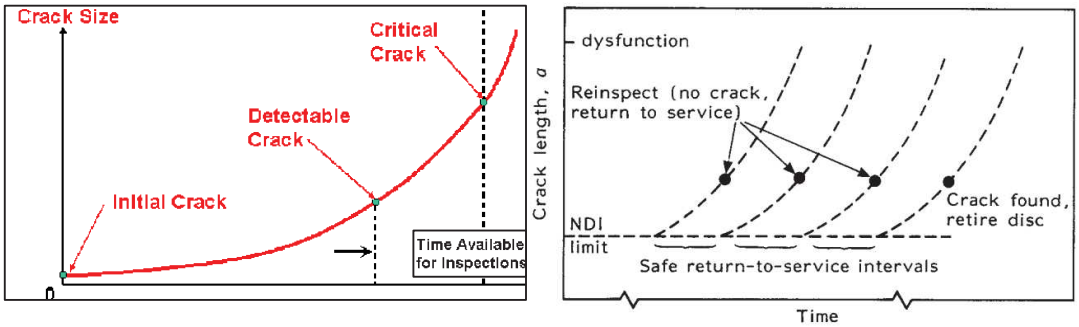

Figure 5: Schematic representation of damage tolerance methodology

1.4 Non-destructive testing

According to the American Society of Non-destructive Testing (ASNT), Nondestructive testing (NDT) is the process of inspecting, testing, or evaluating materials, components or assemblies for discontinuities, or differences in characteristics without destroying the serviceability of the part or system. In other words, the part can still be used even after the completion of NDT inspection or test. Most common NDT techniques that are frequently used for the inspection of aero-engine components in the base repair depots of the aero-industry are only discussed below

1.4.1 Liquid Penetrant Technique (LPT)

Liquid penetrant inspection technique is one of the oldest and most widely used nondestructive testing (NDT) methods. It is one of the simplest NDT methods used to inspect parts ranging from common automobile spark plugs to critical aircraft engine components. Figure 6 shows the liquid penetrant inspection process. In this inspection method, a penetrant liquid is applied to the surface of the part to be inspected. Due to capillary action, the penetrant is drawn in to the surface breaking defects. Further, liquid penetrant applied on the surface is only removed leaving the penetrant entered in to the surface breaking defects. With the application of developer on the surface, the penetrant entered into the defects is drawn out, resulting in an indication. In addition, based on the type of the penetrant dye used in the inspection process, LPT is classified as visible dye (can be seen in ambient light) penetrant inspection and fluorescent dye (requires the use of ultra-violet light or black light to inspect) penetrant inspection.

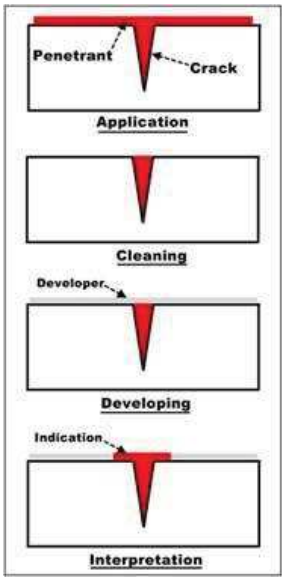

Figure 6: Typical steps involved in liquid penetrant inspection process.

More detailed information about the pre-cleaning, penetrant application procedure and developing action in LPT can be found elsewhere [15, 16].As the current study is mainly focused on the estimation of the reliability of various NDT techniques used in the aero-industry, some of the reliability aspects of the LPT techniques are discussed.

1.4.1.1. Reliability aspects of LPT

1. Properties of penetrants such as surface energy, density, viscosity, colour brightness, etc. and the properties of developers such as permeability, porosity, dispersity, particle size, effects of liquid carrier etc. should meet the LPT requirements. If the properties of the penetrants and developers used do not meet the requirements, the process of dye to penetrate in to defects and the subsequent developing actions will be poor resulting in the lower reliability of the technique.
2. Depending on the type of dye penetrant used i.e., visible dye or fluorescent dye, the LPT inspection should be suitably carried out. For visible dye penetrant inspection, experiments should be carried out under sufficient day light. However, for the case of fluorescent dye penetrant, inspections are to be carried out in completely dark room under the usage of black light or UV light.
3. Regardless of the type of penetrant used, the pre-cleaning of the part has to be performed with extreme care by the operator. In the absence of proper cleaning, any impurities or dust particles present on the surface can block the penetrant from entering in to the defects open to surface.
4. The extent of penetrant dwell time is a critical parameter depending on the type of the defects. For example, inspection of tight fatigue cracks needs higher dwell time for allowing the penetrant to enter in to the crack when compared with moderate dwell times while inspecting EDM induced notches.
5. The surface roughness of the part subjected for inspection is also an important requirement for carrying out LPT. As the surface is irregular, pre-cleaning and excess penetrant removal procedures would be inaccurate. This result in the presence of dust particles or excess penetrant on the sample surface and thus possess higher chances of masking the actual defects present on the surface.
6. Nature of the defect being inspected such as the type of defect (round defects or linear defects), size of defect (defect volume), etc., are also important. In general, crack length on the sample surface is used to quantify the size of the defect.

However, width and depth of the cracks are also essential and hence, volume of the defect becomes prominent in LPT inspection procedures. However, if multiple parameters of the crack such as length, width and depth are accounted, then multi-parameter POD curves or POD vs. volume of the defect curves should be adopted.

1.4.2 Eddy Current Technique (ECT)

ECT is the one of the most frequently used NDT techniques for inspection of aero-engine components in the aero-industry. In ECT, an alternating current is made to flow in a coil (also called as probe) which, in turn, produces an alternating magnetic field around it. Due to electromagnetic induction, this coil when brought close to an electrically conducting surface of a metallic material induces an eddy current flow in the material. These eddy currents are generally parallel to the coil winding. The presence of any defect or discontinuity in the material disturbs the eddy current flow and in turn, generate an alternating magnetic field (in opposite direction) (Figure 7 [17]) which may be detected either as a voltage across a second coil or by the perturbation of the impedance of the original coil. Changes in the eddy current field/density are recorded by means of plotting impedance planes. Variations in the impedance maps due to the discontinuities are detected and are used to characterize the defect. ECT technique is mainly used for detection and characterization of surface and sub-surface defects.

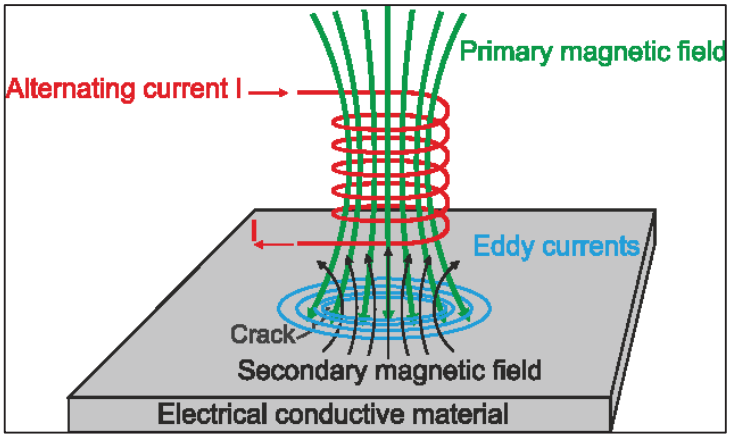

Figure 7: Schematic of eddy current testing [17]

The principal operating variables in eddy current inspection include, coil impedance, electrical conductivity, magnetic permeability, lift-off and skin effect [18]. As the electrical conductivity and magnetic permeability are the material properties of the part being

inspected, brief information on coil impedance, impedance plane, lift-off and skin depth are provided for completeness.

1.4.2.1. Coil impedance and impedance plane

In the case of direct current flowing in a coil, the resistance to the flow of electric current is purely due to the electrical resistance (R). However, when alternating current (AC) is flowing in a coil, the resistance to the flow of electric current is due to two aspects of the coil i.e., electric and magnetic. The first one is the AC resistance (R) of the coil and the other is the inductive reactance, X_L. The electrical resistance (R) is the measure of the opposition to the flow of electric current in an electrical circuit. Inductive reactance, is the combined effect of coil inductance and test frequency. Hence, the total resistance to the flow of alternating current in a coil is known as impedance, Z, which comprises of both AC resistance, R, and inductive reactance, X_L. The impedance can be expressed as $Z = \sqrt{R^2 + X_L^2}$, where $X_L = 2\pi f L_o$, f is the test frequency in Hz and L_o is the coil inductance in henrys. The resistance, inductive reactance and the impedance are all expressed in ohms. Impedance is usually plotted on an impedance-plane diagram as shown in Figure 8 [19]. From Figure 8, it can be observed that the resistance is plotted along the x-axis whereas the inductive reactance is plotted along the y-axis. The impedance plane diagram is a very useful way of displaying eddy current signal response data.

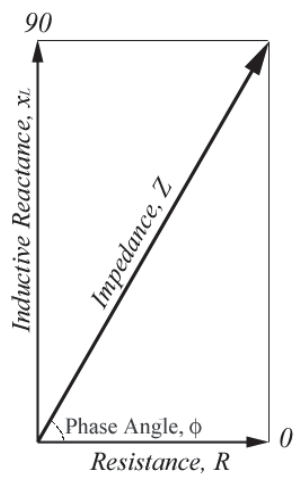

Figure 8: Impedance plane diagram [19]

1.4.2.2. Lift-off

When an eddy current probe connected to an eddy current inspection instrument is placed in air, few signal indications are displayed even in the absence of a conductive

material in the vicinity of the probe. This initial signal indication obtained from air point changes as the coil is moved closer to a metallic conductor. Due to the strongest field of the coil, the indicated change in the impedance plane continues to increase at a more rapid rate until the coil is directly on the conductor. These changes in signals indications with respect to the changes in spacing between the coil and the metallic conductor being inspected are known as lift-off signals. In simpler words, the distance between the probe and the metallic conductor being inspected is called as lift-off. Figure 9 shows the impedance plane of aluminium 7075 standard defect calibration block containing lift-off signal. As the lift-off increases the eddy current density in the material and subsequently decreases the impedance change in the probe, it is always desirable to set lift-off as minimum as possible as shown in Figure 9. Even though, lift-off signals are not desired during routine defect detection process, they aid in identifying the thickness of non-conducting coatings such as paints on non-ferromagnetic and ferromagnetic materials.

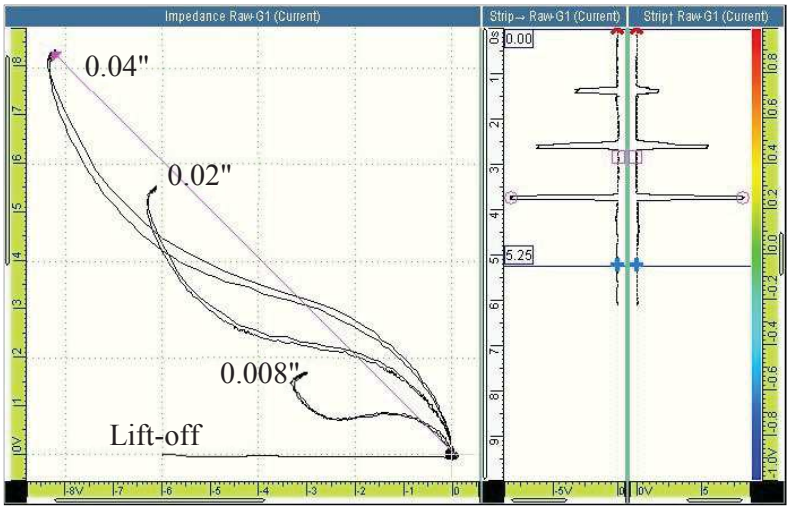

Figure 9: Impedance plane with lift-off and signals of surface notches of sizes (a) 0.04 inch (b) 0.02 inch and (c) 0.008 inch obtained from eddy current inspection of aluminium 7075 defect calibration block.

1.4.2.3. Skin Depth

In general, eddy currents are not uniformly distributed throughout the thickness of a sample being inspected with being denser on the surface and become progressively less dense with increasing distance below the surface. This phenomenon is known as the skin effect and the maximum depth these eddy currents penetrate in the material is known as skin depth. In case of thicker samples, eddy currents are induced only up to a certain depth below the surface. Figure 10 shows variation of eddy current density as a function of depth below the

surface [16]. The depth at which the density of the eddy current is reduced to a level about 37% of the density at the surface is defined as the standard depth of penetration. This depth depends on the probe frequency, electrical conductivity and magnetic permeability of the material. Depth of penetration decreases with an increase in the conductivity, permeability, and probe frequency as shown in Figure 11 [19]. The standard skin depth of penetration can be estimated using Equation 1 [16].

$$\text{Standard skin depth in mm, } \delta = 50\left[\sqrt{\left(\frac{\rho}{f\mu_r}\right)}\right] \quad (1)$$

where, ρ = electrical resistivity, μΩ-cm

f = frequency, Hz

μ_r = relative magnetic permeability

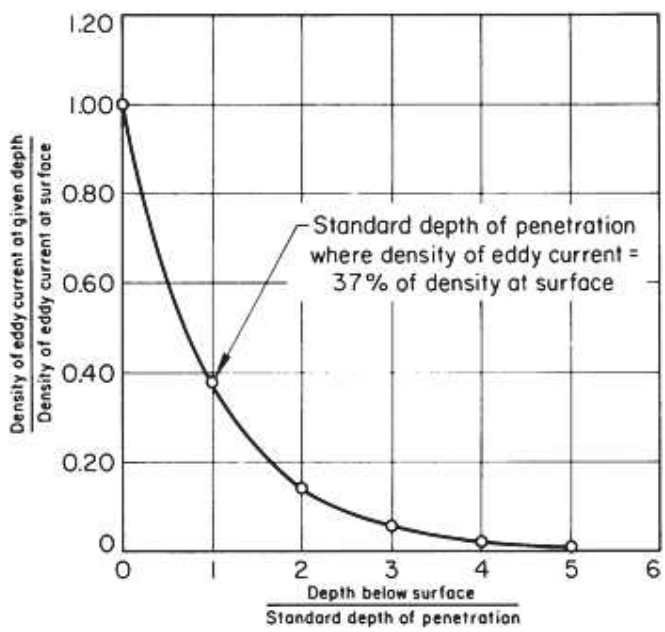

Figure 10: Variation of eddy current density with respect to depth [16]

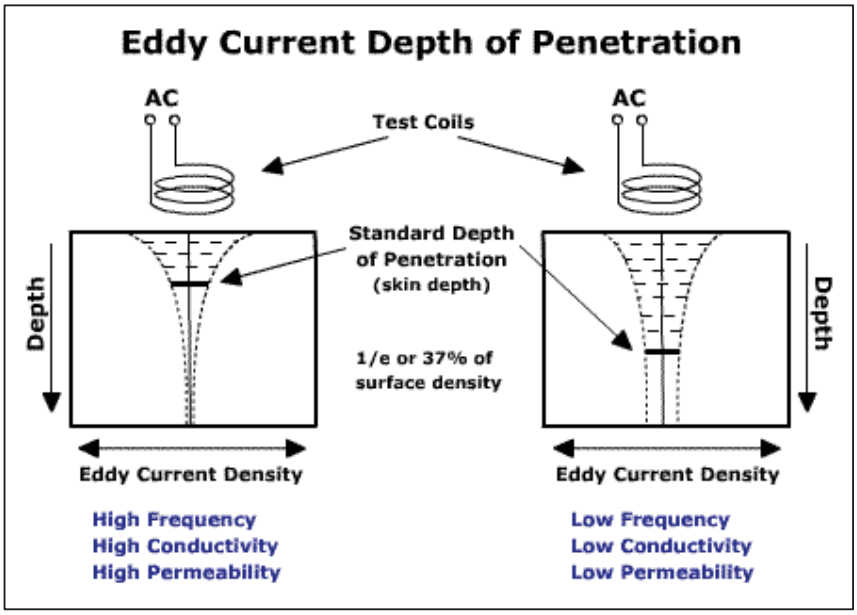

Figure 11: Eddy current depth of penetration with respect to frequency, conductivity and permeability [19]

More information about the eddy current inspection technique and its detailed procedure can be found elsewhere [15, 16]. Some of the reliability aspects of eddy current testing are:

1.4.2.4. Reliability aspects of ECT technique

1. Suitable reference standards have to be used for carrying out eddy current inspection technique.
2. As the POD is a function of many parameters, selection of the right frequency probe and the type of probe (absolute or differential) are essential for better sensitivity of the ECT technique.
3. Especially in the case of conductivity measurements using eddy current testing, the surface of the part for inspection has to be completely clean and even paint on the part surface should be completely removed for reliable results.

1.4.3. Ultrasonic Testing (UT)

Ultrasonic testing and evaluation of materials is performed by using ultra-high frequency (above 20 kHz) sound waves. Ultrasonic testing unit mainly comprises of pulser/receiver, ultrasonic probe and a display device as shown in Figure 12 [20]. In this technique, ultrasonic waves transmitted in to the material are reflected back to the transducer when hit by a discontinuity. In general, any change in the propagation medium for the

acoustic wave results in reflection and transmission of the wave at the boundary due to impedance mismatch. The resistance offered to the propagation of an ultrasonic wave by a material is known as the acoustic impedance. The acoustic impedance can be estimated by multiplying the density of the material with the velocity of sound in the material. The amount of energy reflected and transmitted depends on the acoustic impedance values of the media through which ultrasonic waves propagate. The transmission of sound waves and the receiving of the reflected signals are possible with the help of an electronic device called as a probe. Ultrasonic probes are made of piezoelectric materials which convert an electrical signal into high frequency mechanical waves and vice-versa. In addition, as ultrasonic waves require a medium to travel, coupling medium or the contact between probe and component plays a dominant role in testing.

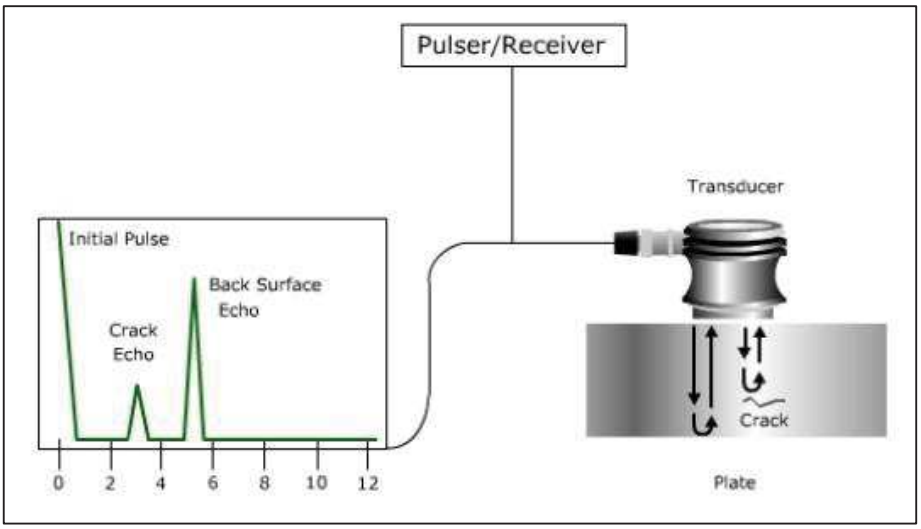

Figure 12: Schematic of Ultrasonic testing [20]

Ultrasonic techniques can be classified as contact and immersion techniques. In contact technique, the region of interest on the specimen is scanned by placing probe directly on the surface of the specimen with a coupling fluid in between. Immersion technique is developed so as to minimize the transmission loss of acoustic energy. In this technique, both the specimen and probe are immersed in the water. Ultrasonic tests can be carried out using either normal incidence or angle probes depending upon accessibility, test requirements and object conditions. Ultrasonic techniques are also classified depending on the location of probes, into, pulse-echo and through-transmission techniques. Pulse-echo method uses a single probe to transmit ultrasonic waves into the specimen at regular intervals. Coupling of the probe to specimen surface can be achieved by contact or immersion technique. If

transmitted wave encounters a discontinuity, some amount of energy will be returned to the probe. Analysis of signal acquired results in understanding about the discontinuity size and its location. Through-transmission technique includes two probes for transmitting and receiving of the high frequency waves on either side of the testing component. Both sides of the components should be accessible in through-transmission technique. The difference in the energy at transmitting side to the receiving side should be analyzed to characterize the component [15].

1.4.3.1. Wave propagation

Ultrasonic waves are mechanical or stress waves which propagate in an elastic medium by localized vibrations. Depending on the oscillation of material, waves are classified as longitudinal and shear waves. Longitudinal waves are the type of waves that propagates along the movement of material. These waves can be generated in solids, fluids and gases. Transverse or shear waves propagate perpendicular to the material movement direction as shown in Figure 13 [21]. Unlike longitudinal waves, transverse waves can only be propagated in solids.

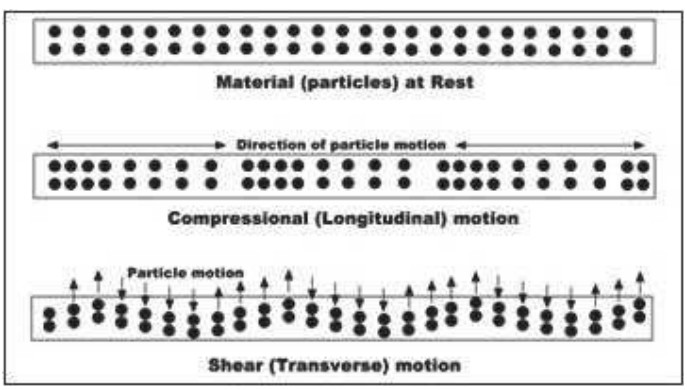

Figure 13: Vibration of particles in longitudinal and shear waves [21]

The wavelength (λ) of the wave is directly proportional to the velocity (v) of the wave in the material and inversely proportional to the frequency (*f*) of the wave. These three parameters are related as shown in Equation 2 [16].

$$\lambda = \frac{v}{f} \tag{2}$$

1.4.3.2. Attenuation of the wave

During wave propagation, the intensity of the wave reduces with the distance travelled through a medium due to attenuation. In material, attenuation is primarily due to the scattering and absorption of the wave. Scattering is the loss due to reflection of the wave whereas, absorption is the conversion of sound energy into other forms of energy. A typical reduction in wave amplitude due to attenuation while propagating through a medium is as shown in Figure 14 [21]. As shown in Figure 14, the amplitude of successive back wall reflections reduces compared to the first backwall reflection. More information about the ultrasonic inspection technique and its detailed procedure can be found elsewhere [15,16].

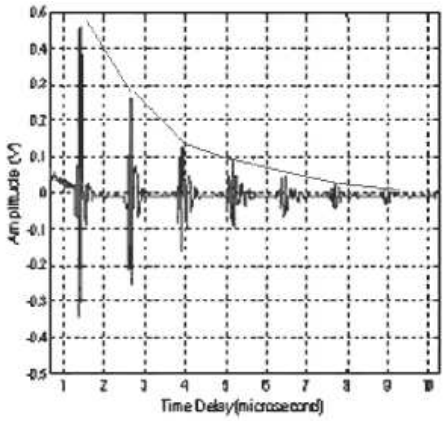

Figure 14: The drop in signal amplitude with multiple backwalls due to attenuation in the material [21]

1.4.3.3. Reliability aspects of ultrasonic inspection technique

1. Improper coupling medium on the sample surface results in the loss of sound energy transmission and could sometimes mislead the reliability estimation studies.
2. Care has to be taken while performing ultrasonic inspection of rough surfaces. In addition, if the parts that are being inspected are irregular in shape, ultrasonic inspection technique has a huge limitation in performing the task.
3. It is also important to select the suitable probe type for ultrasonic inspection of defects. For example, selection of angular probes in the cases where linear defect exists parallel to the incoming sound beam.

Considering various factors which affect the NDT signal, estimating the reliability of the NDT technique is of paramount importance. Brief introduction to the concepts of POD which quantify the reliability of NDT technique are given below.

1.5 Probability of detection (POD)- indicator of reliability of NDT techniques

Conventionally, non-destructive testing (NDT) occupies a pioneering role in the field of defect detection in materials and structures used in aviation, automobile and nuclear industries. Of all these industries, defect detection in aviation and nuclear industries occupies a more prominent role due to the high human and capital risk involved. In aero-engine structures, knowing the "largest anomaly missed" by an NDT procedure is essential than the "smallest anomaly ever detected'. This requirement has led National Aeronautics and Space Administration (NASA) in 1969 to initiate a program for identifying the largest anomaly missed for the materials and NDT procedures that were to be used in the design and production of the space shuttle system. The result of this work was the generation of a large volume of experimental data along with the initial concept, use, and presentation in the form of a probability of detection (POD) plot. Figure 15 shows the idealized and realistic POD curves drawn with respect to the flaw size, 'a' [22]. It is generally believed that a flaw size > a_{NDE} is expected to have 100% probability of detection and a flaw size below a_{NDE}, 0% POD. However, each and every flaw size has its own probability of detection. Subsequently, the POD method of analysis has been refined and improved upon and is now considered to be a "standard" method for quantitative NDT process capabilities assessment. Its use has been expanded to include, (1) NDT procedure validation; (2) NDT personnel proficiency demonstration and qualification; (3) comparative analysis of NDT processing materials, equipment and procedures; and (4) automated NDT systems qualification.

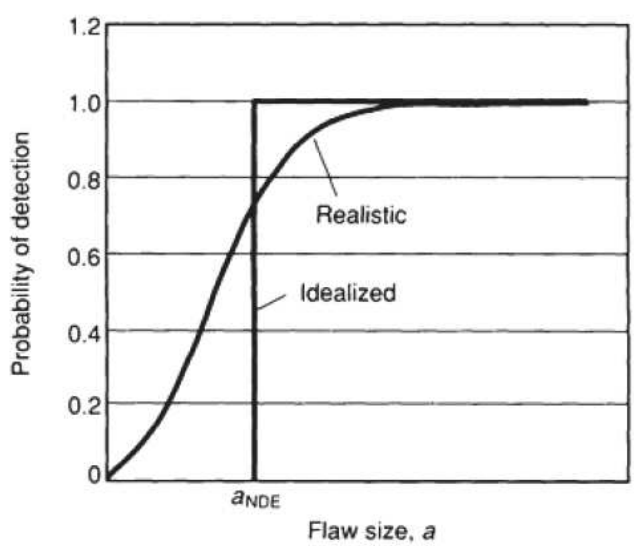

Figure 15: Realistic vs Idealized POD curve for any technique [22]

According to Berens, the POD(a) is defined as "the proportion of all cracks of size 'a' that ***will be detected*** in a particular application of an NDE system". This definition is later redefined in MIL-HDBK 1823 (2009) as "The fraction of targets of nominal size, 'a', ***expected to be found*** given their existence". This is normally expressed as a ratio of a probability of detecting a discontinuity with a confidence level of 90/95, 90/90, 90/75 or 90/50, depending on the requirements of the application. The first number in the series denotes the probability (given as a percentage) that the anomaly will be detected. The second number denotes the confidence level for detecting the anomaly. This information is usually represented as a graph. The probability of detection is plotted as a function of anomaly size for a fixed confidence level (more commonly 95% lower confidence bound). Figure 16 shows a POD curve with 90/95 lower bound along with flaw size at 50% and 90% probability levels [23].

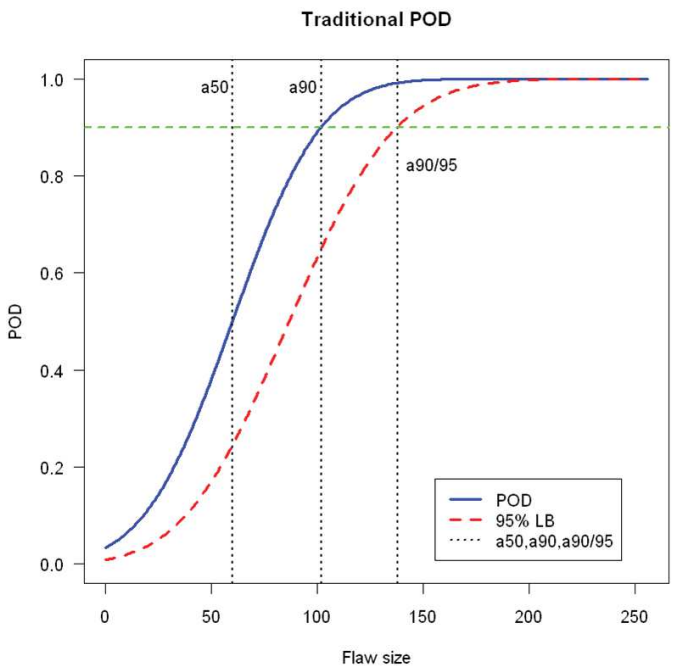

Figure 16: Typical POD curve indicating a_{50}, a_{90} and $a_{90/95}$ [23]

Estimation of POD of any NDT technique can be obtained by both experimental and model assisted methods as per MIL-HDBK 1823A (2009) standard [24]. MIL-HDBK 1823A (2009) describes the procedure to be adopted along with the sample shape, size and defect classification to be considered for generating POD curves. POD data generation is usually carried out either using "HIT (defect detected)/MISS (defect undetected)" approach for qualitative NDT outcome or "â (NDT signal response for a defect) vs. a (defect size)"

approach for quantitative NDT outcome. Qualitative techniques deal with only defect identification. However, quantitative techniques deal with identification and sizing of cracks. Therefore, out of the available NDT techniques, visual testing, fluorescent dye penetrant inspection and visible dye penetrant inspection fall into the qualitative techniques whereas, ultrasonic testing, eddy current testing and magnetic particle inspection fall under the quantitative techniques of NDT.

Hit/Miss POD approach is applied for the qualitative NDT techniques and the NDT outcome is indicated as "H" for hit for a defect detected and "M" means miss for a defect not detected. In the case of quantitative NDT techniques, â vs. a methodology is used. In this methodology, signal response from a discontinuity which is directly related to the flaw size is denoted as "â" and the discontinuity size is denoted as "a". NDT signal response "â" is measured in different ways depending on the NDT method and instrument being used. The quantity "â" is the signal feature of interest, such as signal amplitude (e.g., ultrasonic), phase-angle (e.g., eddy current), or the number of events (e.g., acoustic emission). For example, in the case of liquid penetrant and fluorescent penetrant inspection, POD data is usually generated as HIT/MISS as no quantitative defect size can be determined. Similarly, for ultrasonic testing, eddy current inspection, etc., size of the defect can be quantified and hence, the POD approach usually adopted is â vs. a.

As per MIL-HDBK 1823A (2009), a minimum of 60 and 40 flawed sites have to be considered for POD data generation using HIT/MISS method and â vs. a, respectively. In addition, the ratio of flawed: unflawed locations (inspection sites where there is probability for detecting cracks) for POD data generation should be at least 1:3. For example, in the case of a aero-engine disk, assuming that there will be one defect per bolt hole, a minimum of 40 bolt holes with cracks and 120 bolt hole locations without cracks have to be considered for POD curve generation using "â vs. a" approach. Assuming that there are 8 bolt holes per disc and only one crack per bolt hole, a minimum of 20 disks will be required to meet the requirement of inspecting 160 bolt holes. If 40 cracks could not be found in 20 disks, higher number of disks will be required. It also suggested that the flaw sizes should be uniformly distributed on a log scale covering the expected range of increase of the POD function. These entire requirements pose several challenges for carrying out experimental studies and hence, model assisted POD (MAPOD) have been developed.

1.5.1. Model-assisted POD

Model-assisted probability of detection (MAPOD) research addresses the development of stochastic methods with NDE models to mitigate the high cost and further enhance the quality of NDE technique validation studies. It helps in determining the relation between detectability and physical characteristics of the target. Figure 17 shows the flowchart of MAPOD as described in MIL HDBK-1823(2009) [24]. In the current study, procedure for establishing POD curves for quantitative NDE techniques is established for ultrasonic testing using model assisted methods. Hence, MAPOD is discussed in the context of ultrasonic inspection procedure.

In cases where defective components are available, POD can directly be computed by means of statistical analysis of the NDT data obtained. However, in the case of MAPOD, controlling factors are to be defined and separated into experimentally measured and theoretically predicted factors (Figure 17). Amongst the controlling factors, factors such as multiple inspectors, sensor changes, loading and unloading of specimens, calibration repetition, inspection repetition, surface roughness, grain noise etc., can be classified under experimentally assessed whereas, sample size, geometry, etc. can be classified under theoretically assessed.

Further, finding controlling factors by experimental assessment requires carefully designed experiments with required test specimens. In addition, all these factors are mainly dependent on human and environmental factors and hence, it is important to estimate these factors. However, human and environmental factors are usually estimated using either human reliability data, in-service inspection data, or Monte Carlo simulation models. Moreover, simulation methods for estimating human and environmental factors are particularly useful for image-based NDE methods (for example X-Ray- radiography testing) [25]. As the MAPOD work in this study proposed to be carried out on ultrasonic inspection (signal based) does not come under image-based NDE methods, it is not possible to include the human factors in to the MAPOD curve using simulation based methods. In order to consider the in-service inspection data or using human reliability models, a round robin study is basically envisaged. The current work only describes the framework involved in estimating effect of theoretically assessed controlling factors. Theoretical assessment of controlling factors requires developing representative physics based model, identifying input parameters to the model and validating the model. In the case of ultrasonic testing, this will also involve incorporating the effect of signal and grain noise parameters.

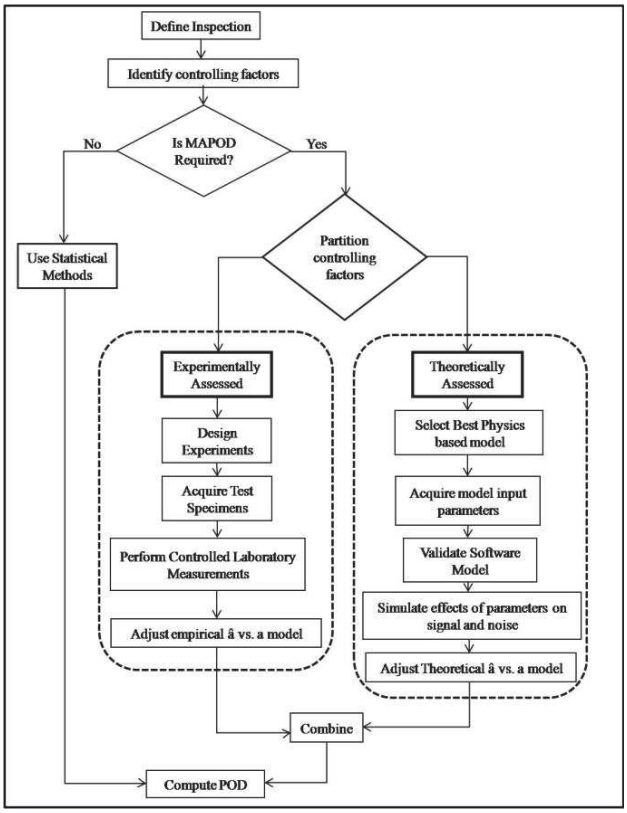

Figure 17: Flow chart of model assisted POD [24]

In addition, in the case of experimental POD, crack size ranges for each and every material proposed to be studied with the crack type should be available for generation of POD curve. However, in the case of MAPOD, these features can be incorporated in to the model and a modified MAPOD curve can be arrived at. Compared to conventional POD studies, MAPOD procedures have the potential to evaluate the reliability of an NDT technique at a lower cost [24]. However, before MAPOD curve reaches a possibility of replacing experimentally generated POD curve along with its validity for various materials, validation of the MAPOD curve has to be performed by using experimental POD curve (at least for one material) [26, 27]. This poses challenges as experimental creation of flat bottom holes or notches, in the case of ultrasonic inspection as accurate as model generated notches is difficult. Also, as mentioned above, generation of MAPOD curve is dependent on partitioned controlling factors which are experimentally and theoretically assessed. Therefore, considering the challenges involved in estimating experimentally assessed factors effect on POD curve, the current study, only discusses the MAPOD curve by incorporating

theoretically assessed factors. Carrying out MAPOD studies are only possible by means of modeling and simulation and hence are discussed below.

1.5.1.1 Modeling and Simulation

Efficiency of NDT system response can be effectively improved with the help of modeling and simulation. In NDT domain, modeling is broadly defined as identifying the optimal measurement parameters such as probe frequency, probe diameter and location so as to effectively detect the defects in the component. In addition, simulation is broadly defined as estimating the predictive NDT response for a given classification of defects in a component. Even though modeling and simulation differ in definition; both are performed using numerical tools either commercially available or custom developed for a specific application.

Either in modeling or simulation, a NDT system model basically comprises of a source, a sample, and a receiver. The source component usually defines the incident field in the sample through representation of the input signal, source hardware, electrical connection, source transducer and the transducer interface condition with the sample. Given the incident field, the output characteristics can be estimated with the help of material properties, sample geometry and discontinuity (often cracks or corrosion) characteristics. Depending on the measurement technique, significant material properties can include elastic properties, electrical conductivity, magnetic permeability, dielectric permittivity, thermal conductivity and density. Discontinuity characteristics include, type (cracks, voids, porosity, corrosion etc.), geometry, and condition (such as the interface condition between crack faces).

The model is typically developed in order to provide the most accurate representation of a measurement technique [28]. Models can produce significant benefits at several stages of the NDT technique development process. Firstly, models can be used to aid in the interpretation of raw measurement data. With this understanding, modelling can be beneficial in selecting the appropriate features of the measurement for evaluation and classification. Probe design and optimization, and/or ultrasonic transducer characteristics or eddy current coil parameters, can greatly benefit from parametric studies using accurate measurement models. For the development of automated inspection techniques, models can augment the training data set, thus reducing sample costs. Moreover, censoring and noise analysis occupy an important role in â vs. a type NDT data. General introduction to censoring and noise analysis are given below.

1.5.1.2 Censoring of data

An observation is considered as censored if the possible range of the value is only known rather than its exact value. Signal response data is usually censored as left censoring and right censoring. For example, the observed data cannot be greater than 100 % of screen height as well as cannot be lower than the noise level. For very small cracks, the response signal is usually mixed up in the noise signal and hence the data is left-censored, whereas for very large cracks, the response signal is saturated at 100 % of the screen height and thus it is right-censored. In either of the cases, â vs. a is no longer linear and hence, is an indication of the noise and saturation of the signals.

1.5.1.3 Noise

Noise is defined as signal responses that contain no useful target characterization information [29]. Any experiment is prone to noise and hence should be considered in any POD analysis. In general, the non-linearity of the â vs. a in the presence of noise is usually observed for very small crack sizes. Noise is a combination of both electronic noise and material noise (grain noise in the case of ultrasonics). Since noise is a signal with no information about the target, it is easy to collect noise data by performing the inspection in a structurally similar, unflawed region of test piece. A rule of thumb is to collect at least three times noise information as target information. In some inspections the background noise is low and thus more difficult to quantify. Having a great deal of noise data mitigates this problem. Since it is difficult (or impossible) to duplicate the initial test environment after completion of experiment, noise must be collected concurrently with the target response data.

1.6 Reasons for NDE variability and the requirement for POD

Generally, it is assumed that a properly trained operator working with a calibrated instrument would eventually detect all defects present in any system. It is also assumed that any error in reliability would only occur due to type of crack or its location. However, a recent work by Sandia National Laboratories, USA, [30] demonstrated the effect of variability in operator, equipment and technique on defect detectability as shown in Figures 18-20. From Figures 18-20, the variability in defect response with each of the factors, i.e, equipment, technique and operator can be understood. Even though this effort was carried out on composite laminates with various defects, similar results are also anticipated in the case of metals. Hence, it is imperative for any organization to estimate the reliability of the equipment present within along with operator's reliability. To summarize, the common causes of variability in NDT response are:

1. Flaws of same size- Possibility of variation in signal level
2. NDE output –Different over wide range of flaw sizes
3. Human Operator effect
4. NDE Procedures vary

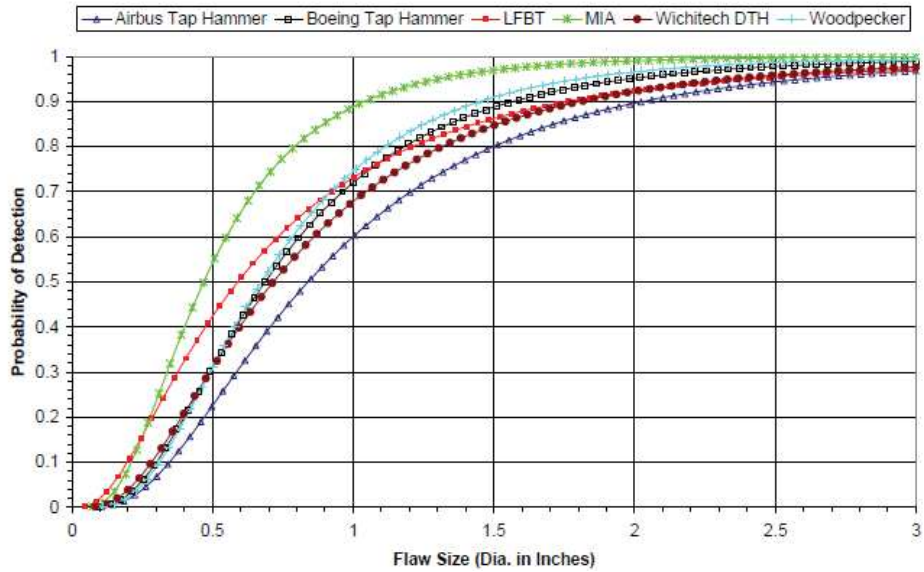

Figure 18: Equipment to Equipment variability in POD

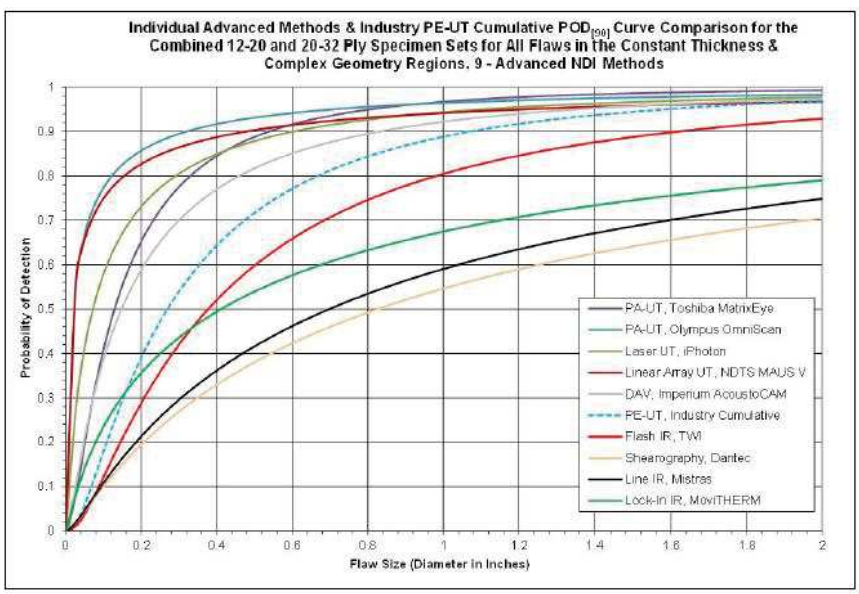

Figure 19: Technique-Technique Variability in POD

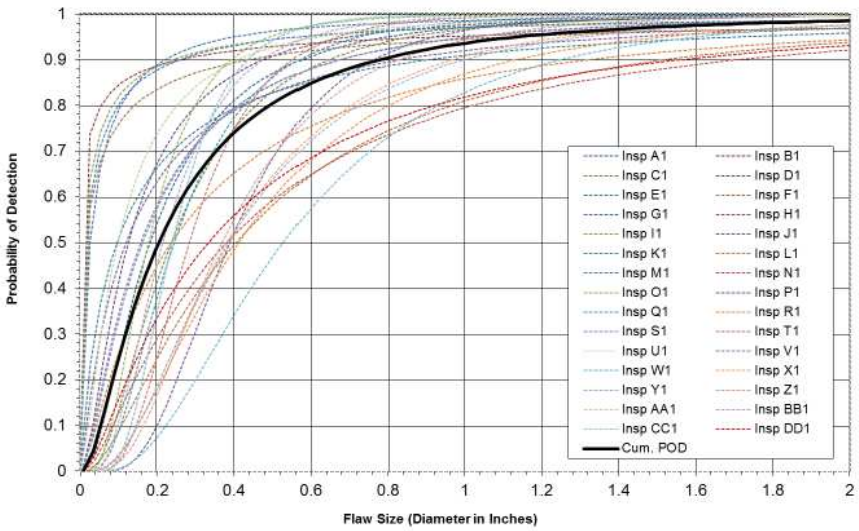

Figure 20: Operator- operator variability in POD

Even though Western countries were successful enough to generate POD curves for damage tolerance assessment from the early 1970's, no such effort was in place in India even till 2013. Considering the extreme importance of this procedure on life revision studies, an indigenous effort for understanding the various POD approaches currently being followed and generate POD curves for the different systems, equipment's and aero-engine materials was initiated at Defence Metallurgical Research Lab (DMRL), a premier metallurgical lab under Defence Research and Development Organization (DRDO) in 2013. This thesis work discusses the efforts undertaken for achieving the generation of representative service fatigue cracks for use in NDT reliability studies.

Figure 21 shows the typical workflow in POD activity. As shown in Figure 21, POD curves can be broadly generated using either experimental or modeling based approaches. In either of the approaches, statistical analysis of the NDT response data does not differ and does only depend upon whether the response is binomial in nature (qualitative NDT techniques) or signal response (quantitative NDT techniques). Detailed description about the experimental protocols to be incorporated for generating experimental defect response will be discussed in Chapter 3. Modeling assisted studies to simulate NDT defect response will be discussed in Chapter 4. Chapter 5 deals with the results on NDT response data generated, different statistical approaches to be followed for varying NDT response classification along with the impact of POD on life revision calculations under DT methodology.

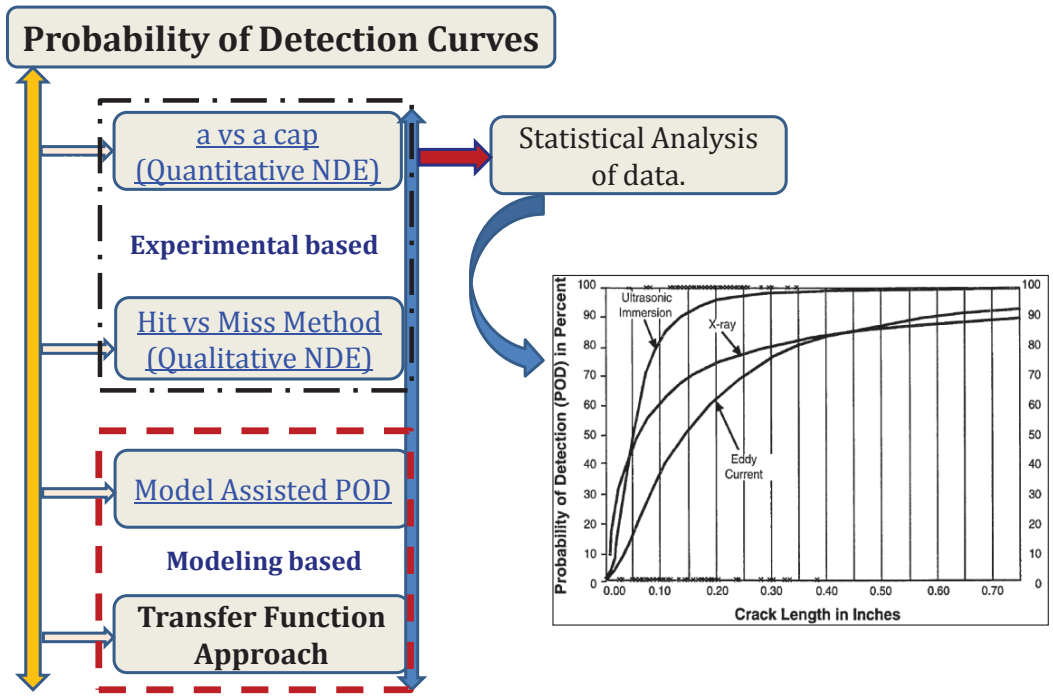

Figure 21: Workflow in POD activity

1.7 Objectives of the thesis work

1. To carry out experimental POD studies using laboratory induced natural fatigue cracks with morphological features mimicking service induced aero-engine cracks.
2. To study the effect of oxidized fatigue cracks on NDT signal response data and in turn on the POD curves.
3. To develop and validate physics based numerical models for ultrasonic inspection of defects and address various issues involved in the statistical procedures of model based POD approaches.
4. To calculate the remnant fatigue life and safe NDT inspection intervals of aero-engine components by estimating the reliability of the currently practiced NDT techniques in the aero-industry.

1.8 Organization of thesis

As the current thesis work is based on estimating the reliability of the NDT techniques currently practiced in the aero-industry, Chapter 1 briefly provides the introduction to certain topics relevant for understanding the current work. Further, Chapter 2 provides the complete literature review on both experimental and model assisted POD activities carried out

worldwide. Furthermore, Chapter 3 provides the complete experimental details on POD studies carried in the current work. Chapter 4 provides the detailed procedure followed in developing and validating physics based numerical models for use in model based POD studies. Moreover, Chapter 5 provides the results and discussions from the current study in three parts. Part 1 discusses the complete results obtained from the generation of NDT signal response data using experimental POD studies (both at room temperature and high temperature conditions) and from model based POD studies. Part 2 discusses the results of statistical analysis of NDT signal response data i.e., hit/miss and â vs. a POD data obtained from experimental and model based POD studies, respectively. Part 3 discusses the results obtained from remnant life calculations performed using Deterministic Fracture Mechanics (DFM) approaches under Damage Tolerance (DT) lifing methodology using the POD data obtained from Part 2. Moreover, Chapter 6 and chapter 7 provide the conclusions made from the current work and the scope of future studies on POD activities, respectively.

Chapter 3, Chapter 4 and Chapter 5 are mainly based on the journal papers published from the current work. The published papers are

1. Vamsi Krishna Rentala, Phani Mylavarapu, Jai Prakash Gautam, "Issues in Estimating Probability of Detection of NDT Techniques – A Model Assisted Approach", (Elsevier) Ultrasonics 87 (2018) 59–70. https://doi.org/10.1016/j.ultras.2018.02.012
2. Vamsi Krishna Rentala, Phani Mylavarapu, Jai Prakash Gautam, Vikas Kumar, "Generation of POD Curves in the Absence of Service Induced Cracked Components- An Experimental Approach ", Insight-Nondestructive testing and condition monitoring, Vol 61, No 1, January 2019, pp. 28-34(7). https://doi.org/10.1784/insi.2019.61.1.28
3. Vamsi Krishna Rentala, Phani Mylavarapu, J.P.Gautam, Gp.Capt.B.V.N.Shiva, K.Gopinath, Vikas Kumar, "Physical Manifestation of a90/95 in Remnant Life Revision Studies of Aero-engine Components", Procedia Structural Intergrity (Elsevier), Volume 14, 2019, Pages 597-604. https://doi.org/10.1016/j.prostr.2019.05.073
4. Vamsi Krishna Rentala, Phani Mylavarapu, Atul Kumar, Jai Prakash Gautam, Gopinath Kakkropath, T. Jaya Kumar, "POD of NDT Techniques Using High Temperature Oxidized Fatigue Cracks in an Aero Engine Alloy". (to be submitted).

References

1. "Aviation Safety Network Safety Database". Aviation Safety Network. June 2013.
2. News in ASM International, 18th April 2018. Web Link: https://www.asminternational.org/home/-/journal_content/56/10192/33512518/NEWS (Last accessed on Nov 2018).
3. Statistical Summary of Commercial Jet Airplane Accidents Worldwide Operations | 1959 – 2017, Prepared by Boeing, 2018.
4. U.S Air Force statistical data base. Web Link: https://www.afhistory.af.mil/USAF-STATISTICS (Last accessed: Nov 2018)
5. List of aircraft structural failures, Wikipedia. Web link: https://en.wikipedia.org/wiki/List_of_aircraft_structural_failures (Last accessed: Nov 2018)
6. Moxon, Julian. How Jet Engines Are Made. Threshold Books, 1985.
7. George E.Dieter, "Mechanical Metallurgy", Third edition, Mc Graw Hill Publishers, 2013.
8. A.K.Koul , W. Beres , P. Au , A. Fahr and W. Wallace: "Life Cycle Management Strategies for Aging Engines", Defence Technical Information Center, pp:1-17 (2001).
9. Andre Pineau, Stephen D. Antolovich, "High temperature fatigue of nickel-base superalloys – A review with special emphasis on deformation modes and oxidation", Engineering Failure Analysis 16 (2009) 2668–2697.
10. Veronica Fornlöf, "Improved Remaining Useful Life Estimations for On-Condition Parts in Aircraft Engines", Licentiate Dissertation, university of skovde.
11. F.C.Campbell: "Elements of metallurgy and engineering alloys", ASM International, pp: 262-263, (2008).
12. Military Standard, "Aircraft Structural Integrity Program," Airplane Requirements, Mil-STD-1530 (USAF), Sept. (1972).
13. W.D. Cowie, "Turbine Engine Structural Integrity Program (ENSIP)", J. Aircraft, Vol. 12, pp: 366-369 (1975).
14. United States Air Force, "Engine Structural Integrity Program", Military Standard 1783, Aeronautical Systems Division, Wright-Patterson Air Force Base, OH, 1984.
15. Baldev Raj, T.Jayakumar and M.Thavasimuthu: "Practical Non-Destructive testing", second edition, pp: 1-55, (2005).

16. Metals Handbook, “Non-destructive Evaluation and Quality Control”, ASM International, 9th edition, Vol.17 (1992).
17. Javier García-Martín, Jaime Gómez-Gil and Ernesto Vázquez-Sánchez, “Review on Non-Destructive Techniques Based on Eddy Current Testing”, Sensors 2011, 11, 2525-2565
18. Mark Willcox and George Downes: “A Brief Description of NDT Techniques”, NDT equipment limited, pp: 17-20, (2003).
19. NDT Resource center, NDT course material, Eddy current testing, link: https://www.nde-ed.org/ (Accessed on August 2020).
20. K.K. Singh, N. Mondal, C. Mandal, R.R. Prasad, P.P. Sengupta, “Application of Ultrasonic and Eddy Current Testing for Inspection of Rolls”, ndt.net, More Info at Open Access Database www.ndt.net/?id=15142
21. Abbas Fahr, “Aeronautical Applications of Non-destructive testing” chapter 7, 196-198, 2014.
22. ASM Handbook, Volume 17: Nondestructive Evaluation of Materials, ISBN: 978-1-62708-152-8, 2018.
23. W.Q.Meeker: “R.B.Thompson’s contribution to model assisted probability of detection,” AIP Conf. Proceedings, 1430, pp.83-94, (2012)
24. Department of Defense handbook, “Non-destructive evaluation system reliability assessment”, MIL-HDBK-1823A (USA), April 2009.
25. M Wall, S Burch and J Lilley, “Human Factors in POD modeling and use of trial data”, Insight, Vol 51, No 10, October 2009.
26. Michele Carboni, Stefano Cantini, “A “Model Assisted Probability of Detection” approach for ultrasonic inspection of railway axles”, 18th World Conference on Nondestructive Testing, 16-20 April 2012.
27. Michele CARBONI, Stefano CANTINI, Cristina GILARDONI, “Validation of the Rotating UT Probe for In Service Inspections of Freight Solid Axles by Means of the MAPOD Approach”, 5th European-American Workshop on Reliability of NDE – Lecture 14, 2013.
28. T. A. Gray, F. Amin, and R. B. Thompson, “Application of Ultrasonic Pod Models”, Technical Paper, Iowa State University, pp: 1737-1744.
29. Luca Gandossi and Charles Annis, “Probability of detection curves- statistical best practices”, ENIQ TGR Technical document, ENIQ Report no. 41, EUR 24429 EN, 2010.

30. Dennis P. Roach and Thomas M. Rice, “A quantitative assessment of advanced nondestructive inspection techniques for detecting flaws in composite laminate aircraft structures”, DOT/FAA/TC-15/4, March 2016.

2. LITERATURE REVIEW

Successful implementation of the advanced lifing methodology such as a damage tolerance design depends on the estimation of the reliably detectable crack size by an NDT technique. In order to estimate the reliable crack size detected by the NDT technique, statistical procedures also called as probability of detection (POD) studies has to be carried out. General introduction to POD i.e., minimum number of defects required, flawed:unflawed ratio, different approaches such as HIT/MISS and â vs. a, etc., is already discussed in Chapter 1. Hence, the current chapter reviews various work carried out on POD activities worldwide. Considering the extensive literature available in the field of POD, an attempt is made to segregate studies on POD in to experimental and model based POD approaches. This chapter mainly focuses on the conventional experimental POD approaches adopted using service expired components and model based POD approaches. Under the experimental POD approaches, various alternative approaches for generating cracked samples in the absence of service expired components are also discussed whereas model based POD approaches adopted were discussed along with some advances in the field of POD such as multi-parameter and transfer function POD approaches. In addition, challenges associated in carrying out statistical analysis of NDT outcome data in POD studies were also discussed.

2.1 Experimental POD studies

The first attempt in estimating the reliability of the NDT techniques was made by Packman et.al., [1] in the year 1968 as part of an Air Force Materials Laboratory project. In order to assess the applicability of a fracture mechanics and nondestructive testing design criterion (damage tolerance design criterion), efforts were made to identify reliably detectable crack size by NDT techniques. Four different NDT techniques such as penetrant inspection, radiography, ultrasonic and magnetic particle inspections were used for inspection of fatigue cracks in 7075 Aluminium cylinders and 4330V modified steel cylinders. All the crack sizes present in these cylinders were grouped in to crack size ranges i.e., (0.001-0.050, 0.051-0.100, 0.101-0.150, 0.151-0.200, etc., inches). After completion of NDT inspections, probabilities were estimated as the ratio of the number of cracks detected to the total number of cracks present in the particular range of sizes. Further, probabilities for each range of crack sizes were plotted against the actual crack sizes resulting in the NDT reliability curves. Earlier works on NDT reliability studies considered the probabilities according to the range of crack sizes indicated in terms of reliability index. Reliability index is similar to probability

and ranges from 0 to 1. Figure 22 shows the reliability index vs. actual crack length of dye penetrant inspection of fatigue cracks in aluminium cylinders. From the available literature on POD, it can be confirmed that this was the first POD curve ever plotted. From Figure 22, it can be observed that the maximum reliability obtained by the technique was only 85% for the range between 0.25-0.30 inches of crack sizes. However, it can also be noted that the probability for crack sizes between 0.30-0.40 inches falls below 85% and further increases for the remaining crack sizes. This procedure of plotting POD curves is called as the empirical POD method. However, this way of estimating the probabilities does not account for various critical parameters as mentioned in MIL-HDBK such as the requirement of minimum number of defects, flawed : unflawed ratio, etc.

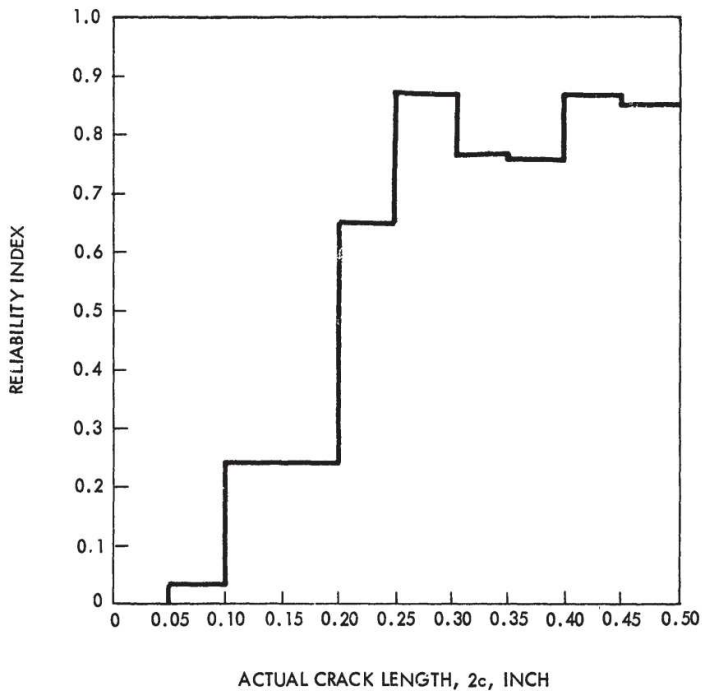

Figure 22: Reliability index of dye penetrant inspection of fatigue cracks in Aluminium cylinders [1]

Further reliability studies were carried out by using different statistical procedures so as to account for majority of the parameters in a systematic way. The reliability index curve shown in Figure 22 was further fitted with a suitable cumulative distribution function resulting in the POD vs. flaw size curves. Subsequently, POD curves for NDT techniques were plotted considering variety of specimen configurations and flaw types for several projects at U.S Air Force and NASA [2-5]. In majority of the reliability studies, service expired components containing several discontinuities or fatigue cracks are used. Further, the data on number of cracks detected by the NDT techniques is obtained and was cross verified

with actual number of defects identified by characterizing destructive sections of the component under microscope. Several researchers [6-8] have carried out the NDT reliability procedures on various service expired components obtained from aero-industry, railways, nuclear industries, etc. A typical POD curve obtained for dye penetrant inspection of fatigue cracks in service expired compressor disc is shown in Figure 23. From Figure 23, it can be observed that the $a_{90/95}$ value obtained for dye penetrant inspection was approximately 3 mm. This POD curve was plotted for dye penetrant HIT/MISS data by following the standard log-logistic distribution function. Considering the laborious nature of sample preparation with numerous cracks for POD assessments, Advisory Group for Aerospace Research and Development (AGARD) has initiated a round robin NDI demonstration program amongst the "The North Atlantic Treaty Organization (NATO)" countries. In round robin inspection procedures, the samples/service expired components used for POD studies were subjected to NDT inspections across various industries/laboratories [9]. This program basically accounted for variability "between equipment to equipment" and "between instrumental settings" even for the same NDT technique. In addition, an attempt to account for different environmental aspects, operator errors/human factors, etc. was also considered in the AGARD program.

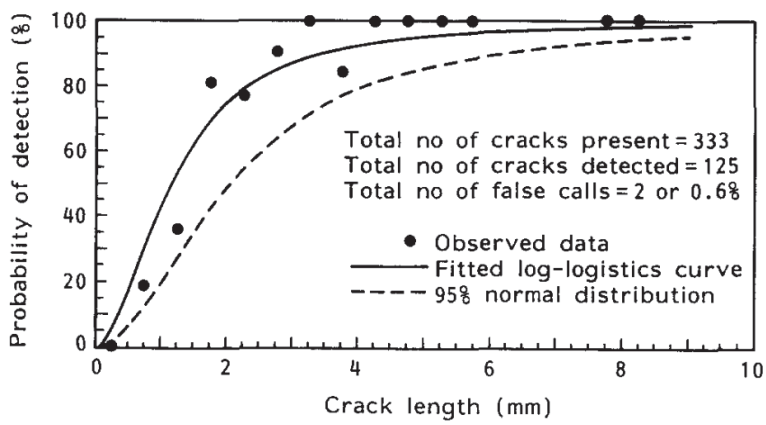

Figure 23: POD curve plotted for dye penetrant inspection of fatigue cracks in a service expired aero-engine compressor disc [6]

In addition, capabilities of the NDT techniques can also be estimated by processing the NDT field inspection data [10, 11]. Across various industries, inspections are usually carried out at various stages such as at the manufacturing stage, in-service operated conditions, periodic inspection intervals, etc. During these various stages, NDT data generated can be properly segregated according to the type of component, material, geometry and size of the defect as well as the NDT technique used for inspection. This segregated data can further be processed using relevant statistical procedures for plotting POD curves.

However, proper care has to be adopted during the segregation and processing stage as mixing of the data may lead to erroneous results.

Broadly, it can be understood that the POD generation procedures using experimental procedures can be carried out using service expired components and analyzing NDT field inspection data. However, these procedures are subjected to various challenges such as availability of service expired components and time constraints when round robin inspections are planned. Moreover, usage of NDT field inspection needs careful attention while collecting and processing the data.

Alternatively, under the absence of safe life expired components, POD studies are also being carried out using various sample generation methodologies. Several studies were performed by generation of POD samples with Electric Discharge Machining (EDM) notches representing fatigue cracks. EDM notches are created in samples with varying dimensions and are being inspected using various NDT techniques for carrying out POD studies [12-14]. However, due to the constant width of the EDM wire diameter (0.2 mm - 0.3 mm), notches made using EDM cannot exactly replicate the tight fatigue cracks induced during service. It is well known that the POD studies are not only dependent on crack length but also on other crack dimensions such as width and depth. In addition, unlike EDM cuts, real fatigue cracks are not perfectly straight. Short fatigue cracks are in general more tight and tortuous in nature. Eventually, the variation in crack morphology between EDM notches and in-service fatigue cracks will affect NDT response [15, 16] and hence, EDM notches should be avoided. Moreover, if the POD studies are being carried out for a specific type of crack generating from specific locations in a component (for example: bolt hole cracks in a turbine disc), the randomized nature of crack initiation is lost and hence, these EDM cuts cannot be a suitable option. Instead of directly considering EDM notches as cracks, researchers also used EDM notches (as suggested in MIL-HDBK-1823A [17]) as starter defects to guide crack generation under fatigue loading conditions. Nevertheless, the randomized location of the crack in an aero-engine disc is compromised with the help of a small EDM starter notch. This would also compromise the quality of POD data obtained using these cracks emanating from EDM notches. Figure 24 shows the signal response vs. flaw size of eddy current inspection of same sizes of EDM notches and fatigue cracks in complex engine components. From Figure 24, it can be observed that the eddy current response is higher for EDM notches compared to fatigue cracks. Hence, it can be understood that POD curves plotted using EDM notches and fatigue cracks are not similar.

Recently, alternative mechanisms of defect production techniques on real and unused components are also being explored with the help of advanced fatigue testing facilities such as controlled thermal fatigue damage mechanism, rotating bending fatigue testing and hemispherical dimple based cyclic fatigue [18-20]. Several researchers have used these mechanisms in creating real fatigue cracks in the actual components. However, the implementation of this alternative mechanism in carrying out POD studies depends on the availability of specialized experimental facilities for crack generation.

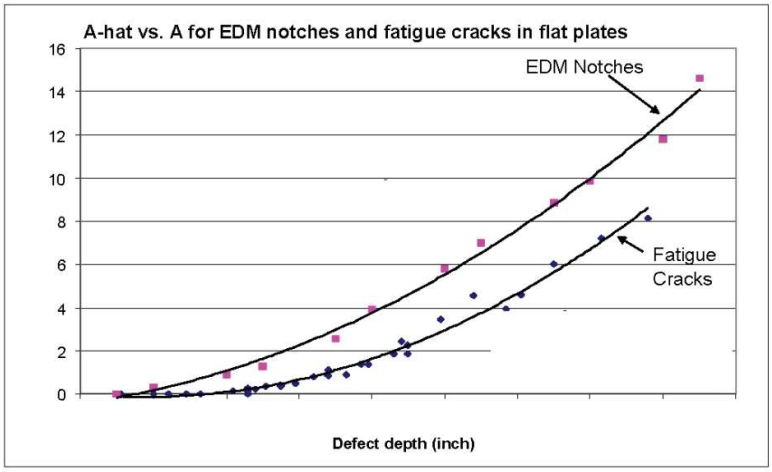

Figure 24: Eddy current response for EDM notches and Fatigue cracks in complex engine components [15]

2.2 Modeling based POD studies

Even though, the procedure adopted by researchers used service expired components in estimating POD, severe requirements of time as well as components with existing cracks limit its application across industries. Moreover, a laborious, time consuming and cost intensive approach of generating individual POD curves for all the materials and the crack types is extremely essential for implementing DT methodology. This has led several researchers [21-36] to explore the feasibility of using model assisted POD. Thompson [27] has reviewed the early usage of physics based models for the estimation of POD to implement the damage tolerant design. Li et al. [28] have described a set of physical model-assisted analyses for studying the POD of two different ultrasonic inspection methods in detecting synthetic hard alpha inclusion and flat bottom hole defects in a titanium disk. Amin et al. [29] and Thompson et al. [37] have developed MAPOD models for ultrasonic inspection considering focused probes and internal defects, respectively. Several researchers have also used in-built modules of various NDT techniques such as ultrasonic, radiography

and eddy current inspection techniques in CIVA software for carrying out simulation based POD studies [33, 38-48]. Carvalho et al. [34] used Monte Carlo simulation technique to develop POD curves for ultrasonic testing. In addition, a model developed by Ogilvy et al. [49] for the scattering of ultrasound by well-oriented planar defects is combined with noise theory to produce a calculated capability of detection. Moreover, the POD curves obtained from the physics based models were also found to be in good agreement with the experimentally generated POD curves [50-53]. Figure 25 shows the comparison of POD curves plotted using both experimental and model based approaches. From Figure 25, it can be observed that the model based POD curve (MAPOD) exactly matches with the experimental POD curve. Hence, MAPOD studies are capable of replacing the conventional way of conducting experimental POD studies.

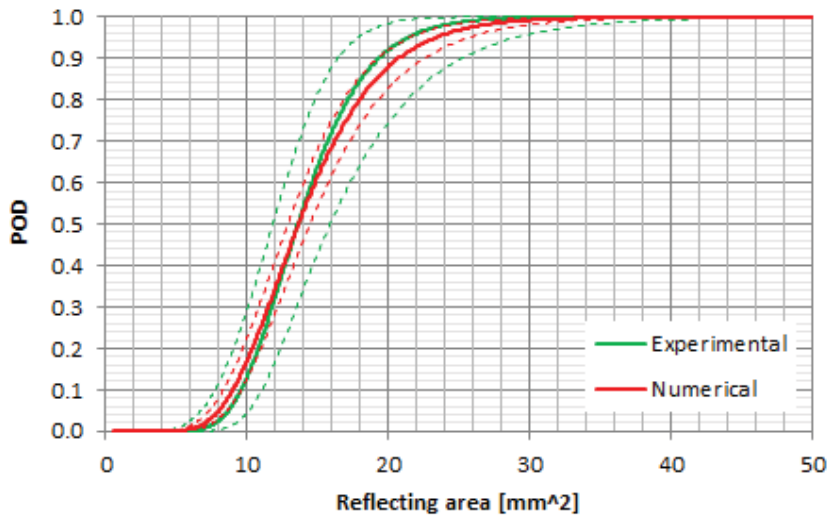

Figure 25: Comparison of MAPOD curve with experimental POD curve [51]

2.3 Multi-parameter POD studies

Conventionally, POD curves of the NDT techniques are produced only as a function of one defect parameter such as crack length. However, for many of the quantitative NDT techniques the defect response is often a function of multiple defect parameters. For example, in the case of ultrasonic inspection of fatigue cracks, the crack orientation plays a vital role in estimating the POD of the technique. If the crack orientation is parallel to the incoming sound beam, the amplitude of the reflections of the waves is smaller when compared to the perpendicular orientation of the crack. Accordingly, the resulting POD of the technique could be higher or lower. In addition, for the cases where defect length alone does not correspond to the defect severity, the POD of the NDT technique cannot be determined only as a function

of defect length. Hence, estimating the POD as a function of defect length alone is not a reliable estimate in cases where other defect parameters such as width, depth, orientation etc., have large influence on the POD. If the POD was estimated as a function of crack length alone even under the influence of various defect parameters, there might be a risk in accepting a component with a critical defect or rejecting a component with a defect which is not critical for the application. Figure 26 shows the different categories of influential parameters. Examples of typical input parameters include, component based such as internal structure, temperature in case of ECT and defect based such as dimensions, orientations, etc. Examples of parameters from ECT inspection procedures include, type of probe used, frequency, scan speed, recording criterion, data analysis methods, etc. whereas, equipment parameters (ex. ECT) include, transmitter, receiver, analog to digital converters, scan devices, etc. However, in practical scenarios, while carrying out POD studies all these parameters cannot be accounted and hence majority of the researchers [54-64] had worked only on defect parameters based multi-parameter approaches. Pavlovic et al., [55] have incorporated multi-parameter POD approaches in accessing the capability of ultrasonic phased array inspection of canister components which are used for nuclear waste disposals. They conducted their studies with the help of flat bottom holes (FBH) manufactured of varying sizes, depths and orientations. They were successful in showing the effect of FBH size, depth and orientation on multi-parameter based volumetric POD curves. Pavlovic et al., [56] have studied the effect of depth and length of surface broken semi-elliptical crack similar to flaws in cast iron components on the POD analysis of ultrasonic inspection technique using both experimental and model based signal response approaches. In another study, Kanzler et al., [57] have estimated multi-parameter POD curve of low-frequency eddy current inspection of canister components with the help of artificial defects. Instead of using numerical approaches to study signal response analysis, analytical approaches for studying non-linear signal response analysis especially encountered with low-frequency eddy current testing were established. Few researchers [58, 62] have even developed novel methods using artificial defects inspected by eddy current inspection procedures to study multi-parameter based POD approaches. In multi-parameter based POD approaches, POD curves are plotted as a function of defect area or defect volume usually called as area POD curve or volume POD curve, respectively. Figure 27 shows the POD curves plotted using multi-parameter approaches [65]. From Figure 27, it can be observed that the POD curves vary with changes in any one of the flaw dimensions and cannot match with the single parameter POD approaches. Even though the importance of multiple influencing parameters on POD curves have been identified, all of

the literature studies on multi-parameter POD approaches available till today are only carried out using standard defects or artificial defects such as flat bottom holes, EDM notches, semi-elliptical notches, etc. Performing multi-parameter based POD studies for real cracks are extremely essential in ensuring the structural integrity of the components.

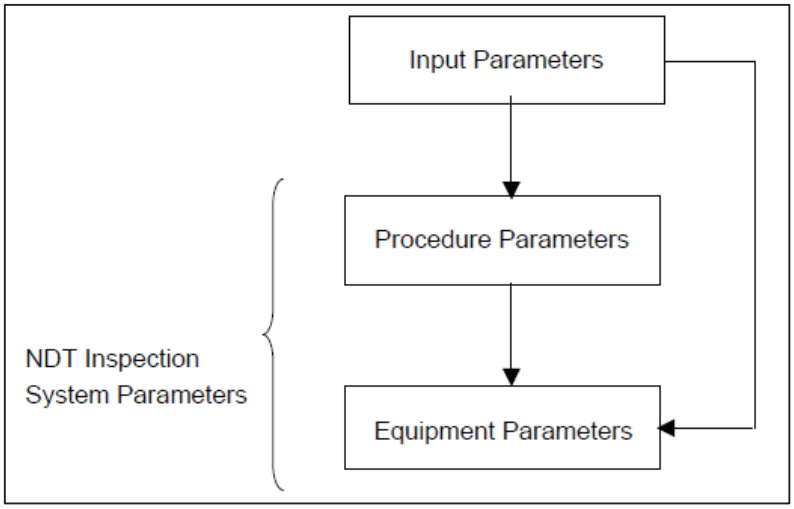

Figure 26: Different categories of influential parameters [65].

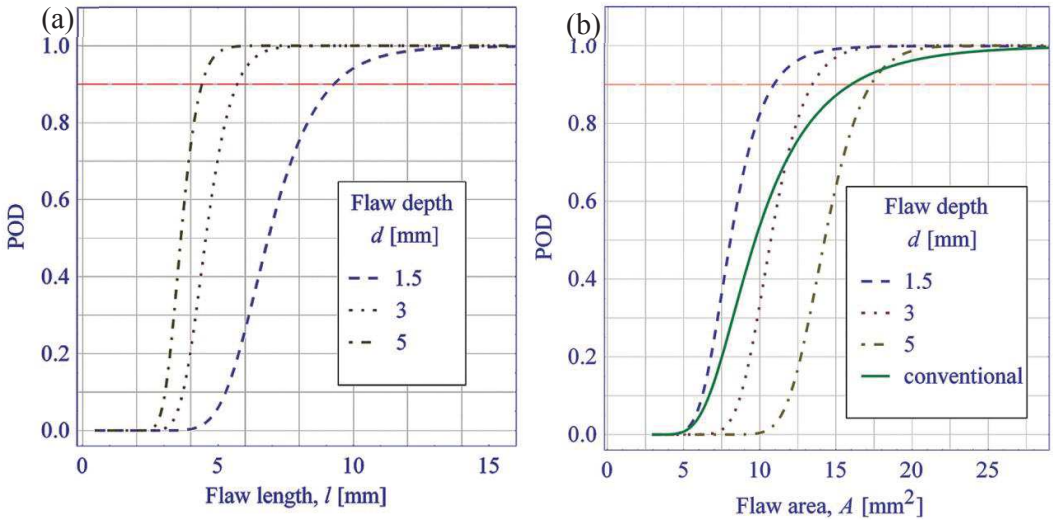

Figure 27: Multi-parameter POD curves (a) as a function of flaw length for different flaw depths and (b) as a function of flaw area and comparison with conventional POD procedure [56]

2.4 POD studies using transfer function approaches

As discussed earlier, POD is broadly a function of three main parameters, namely, the material used, geometry of the component and the type of defect. Hence, POD studies are to be carried out for each and every material, component and the type of defect and which makes POD procedures laborious, time consuming and cost intensive in nature. Smith [66] discussed the potential of carrying out transfer function based POD approaches with MAPOD working group in 2005. He proposed an idea of estimating the POD of cracks in a desired geometry by identifying the relationship between artificial flaws and cracks in a flat plate inspected using experimental techniques. Further, identifying the response of artificial flaws in the geometry of interest, POD of cracks in the desired geometry can be generated. Figure 28 shows the POD estimation of cracks in a desired geometry using notches and cracks response from a flat plate. This idea of transfer function based POD approach was purely experimental. Further, Thompson [67] developed a unified approach integrating both experimental and simulation strategies in performing transfer function based POD approaches. Subsequently, very few researchers [68-70] have carried out POD studies using transfer function approaches by combining both experimental and modeling signal responses. Using transfer function approaches, POD curves can be transferred from one material to other material and from one defect geometry to other geometry. Recently, Subhair et al., [71] have proposed a signal noise based transfer function approach for transferring POD curves among materials with different signal to noise ratio (SNR) values. This approach is capable of producing transferred POD curves with the help of limited experimental data.

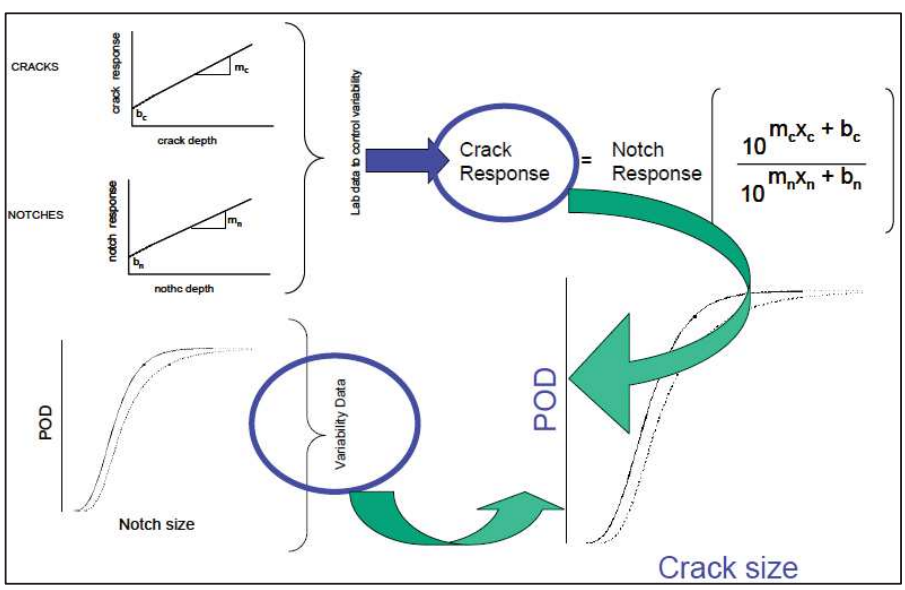

Figure 28: Schematic of transfer function approach based POD curve estimation for cracks in a desired geometry using notches and cracks response from a flat plate [66]

2.5 Importance of probability distributions and statistics in POD studies

Reliability studies of NDT techniques involves in inspections of samples containing numerous defects at random locations and statistical analysis of the NDT response data. It is well known that depending on the type of the NDT technique i.e., either qualitative or quantitative, the outcome of the NDT is either HIT/MISS or 'â vs. a'. However, this NDT outcome data has to be processed with the correct statistical procedures in order to avoid erroneous results. Prior to that, the distribution of defect sizes is extremely important in further processing of the NDT inspection data. In the studies mentioned above, statistical analysis of the cracks obtained as well as generation of POD curves has been performed either from an experiment or modeling data with a fixed statistical distribution. Even though, MIL-HDBK 1823A suggest that the logarithm of assumed crack sizes should be uniformly distributed, Safizadeh et al. [72] have commented that a Rayleigh statistical distribution of log of flaw sizes is required to generate a POD curve with maximum number of cracks in transition zone. Also, unlike in the case of experimental POD curve generation, distribution of crack sizes has to be assumed for MAPOD and is usually dependent on the distribution of service induced fatigue cracks. In general, fatigue cracks originating from in-service aero-engine turbine discs follow log-normal distribution [73-80]. Hence, in the current study, statistical procedures were only developed considering log-normal distribution. Figure 29 shows the lognormal distribution of fatigue cracks.

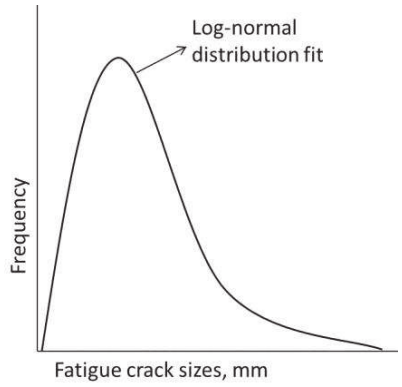

Figure 29: Fatigue cracks following lognormal distribution [77]

Moreover, identification of the noise/decision thresholds and signal saturation levels plays a vital role in NDT inspection procedures. However, these thresholds have to be effectively incorporated in the statistical analysis of the NDT outcome data. This is in general carried out by censoring the data according to the decision thresholds and signal saturation levels identified. Further, the censored data and the uncensored data are to be properly

processed using various regression analysis methods described in the literature. The two most common regression methods are identified as the ordinary least square method (OLS) and the maximum likelihood estimators (MLE) method. Usage of ordinary least squares (OLS) regression for censored data would result in a much skewed result as shown in Figure 30 [81]. Annis et al., [81] have commented about the appropriateness of the POD curve using regression parameters estimated by OLS method. In their study, they have concluded that the OLS method applied on censored data changes the shape of POD curve. However, as POD curve is dependent on the censored data, Maximum likelihood estimation (MLE) method has been recommended. MLE considers the censored data by estimating the likelihoods unlike throwing away the censored data as in the case of OLS method. Using MLE, Annis et al., [81] observed that the POD curve shape stayed the same by considering the estimates of the censored data.

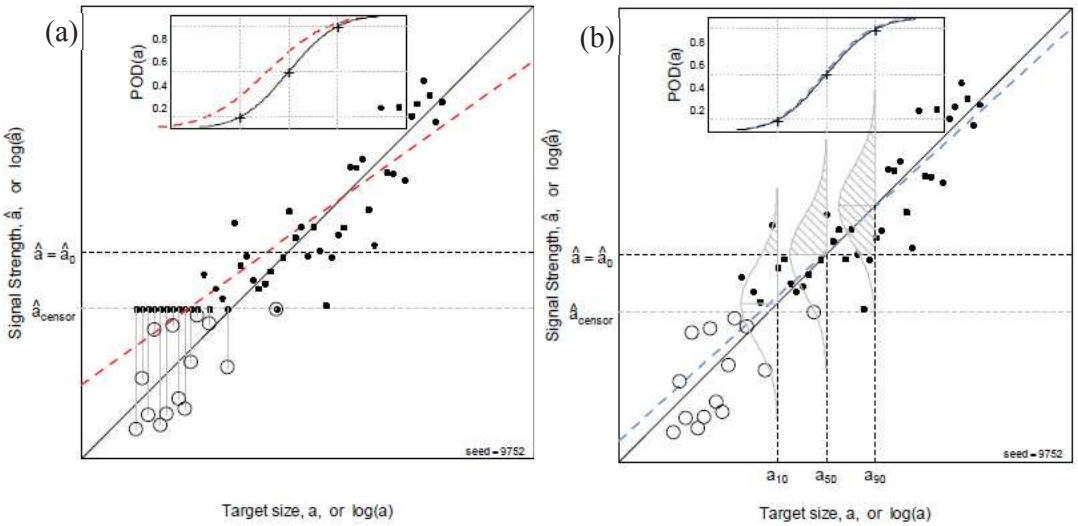

Figure 30: Censored data regression with (a) OLS (b) MLE [81]

Further, the parameters obtained from the regression analysis are to be used in generating POD data according to the parent distribution of defects sizes which are inspected by the NDT techniques. Moreover, MIL-HDBK 1823 explains that the regression between 'â' vs. 'a' has to be performed for the best possible combination of linear fit. In the studies discussed above, POD curves were plotted either by using commercial software's such as CIVA or using the statistical tool available with MILHDBK 1823. This has resulted in some ambiguity about the statistical procedures and challenges involved. To the best of the author's knowledge, some of the major issues which are still not clear for a new user of POD curves include, selection of defects distribution, challenges involved in censoring and regression,

estimation of distribution parameters [82], etc. In addition, another point of concern in plotting POD curves is to decide whether to opt for regression equation between natural logarithms of â and a [83] or between logarithm to the base 10 of â and a [25, 84]. Figure 31 shows the examples of regression plots performed using both natural logarithms and logarithms to the base 10 in carrying out POD statistical analysis. Therefore, it is important to address all these issues involved in the statistical study of POD.

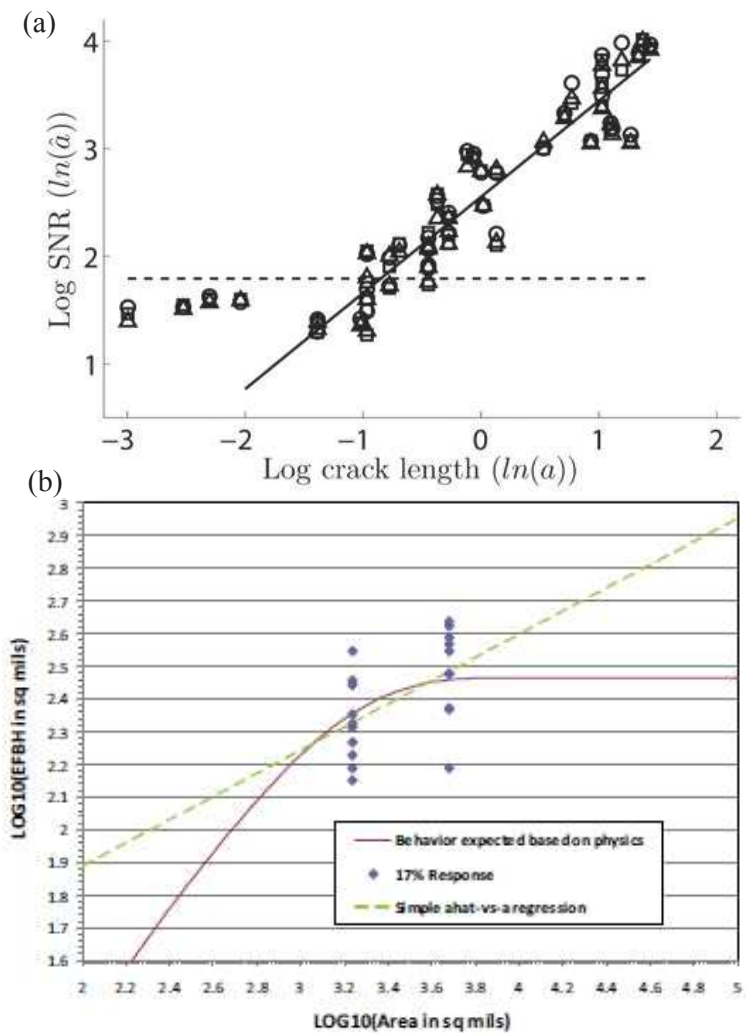

Figure 31: Example of regression between â vs. a using (a) natural logarithm [83] (b) logarithm to the base 10 [25]

From all the studies discussed above, it can be understood that POD studies can be carried out either by using experimental or modeling approaches. Under experimental POD studies, service expired component or NDT field inspection data are used for estimating the

reliability of NDT techniques. However, in the absence of service expired components, researchers have used various EDM induced notches, starter defects for guiding crack initiations and even advanced defect production technologies. These methods are helpful to some extent and possess certain drawbacks. Moreover, inspecting samples with induced cracks does not include the effects of service conditions such as oxidized fatigue cracks, NDT signal response variations due to oxides and oxide scale presenting on the actual service expired components. It is well known from various literature studies that the NDT signal responses not only depends only on the crack parameters but also on the microstructural variations such as oxide induced effects. For example, the NDT signal response amplitude from a crack of size 2 mm in a virgin sample will be different compared to similar crack in a service expired component. Hence, it can be understood that if the NDT signal response varies with respect to the microstructural variations, the corresponding POD obtained for the techniques also varies. These variations in the reliably detectable crack sizes by NDT techniques can strongly effect the damage tolerance based lifing calculations and the corresponding safe inspection intervals. However, several studies carried out in the literature are on laboratory grown fatigue cracks in room temperature conditions and thus does not include these factors. Moreover, it is also known that if the POD studies are planned for a specific component and from a specific location, cracks grown using EDM notches does not take in to account the actual stress concentration present near the critical location in a component. Moreover, all the studies available on generating cracks representing in-service degradation were on steels. In addition, multiple cracks at the same location which is a commonly observed phenomenon in fatigue cracks are not considered. Therefore in the current study, efforts were made to generate natural fatigue cracks in high strength nickel based superalloys with possibility of multiple cracks from a single location along with crack branching phenomenon. Also, condition of true geometric stress concentration factor present near bolt hole in a turbine disc is maintained during the study. These cracks are generated under both room temperature and high temperature fatigue testing conditions. Further, more details about the experimental POD procedures and the development of model based POD procedures by addressing the above mentioned issues are given in chapter 3 and chapter 4, respectively. Finally the results obtained from both the experimental and model based POD studies along with the damage tolerance based lifing calculations were discussed in detail in chapter 5.

References

1. Packman, P. F., Pearson, H. S., Marchese, G. B., and Owens, J. S., "The Applicability of a Fracture Mechanics- Nondestructive Testing Design Criterion," AFML-TR-68-32 (1968).
2. Lord, R. J., "Evaluation of the Reliability and Sensitivity of NDI Methods for Titanium Alloys," AFML-TR-703-107, Vol, II, June 1974.
3. Southworth, H. L., et al., "Practical Sensitivity Limits of Production Nondestructive Testing Methods in Aluminum and Steel," AFML-TR-74-241, March 1975.
4. Yee, B. G. W., et al., "Assessment of NDE Reliability Data," NASA CR-134991, October 1976.
5. W. H. LEWIS et al., "Reliability Of Nondestructive Inspections", Lockheed-Georgia technical report, December 1978.
6. A K Koul, N C Bellinger and A Fahr, 'Damage-tolerance-based life prediction of aeroengine compressor discs: I. A deterministic fracture mechanics approach', Int J Fatigue, Vol 12, No 5, pp 379-387, 1990.
7. M Şimşir and A Ankara, 'Comparison of two non-destructive inspection techniques on the basis of sensitivity and reliability', Mater & Design, Vol 28(5), pp 1433-1439, 2007.
8. B Sasi, B P C Rao and T Jayakumar, 'Dual-frequency eddy current non-destructive detection of fatigue cracks in compressor discs of aero engines', Defence Science J, Vol 54(4), pp 563, 2004.
9. A.Fahr, D. Forsyth, M. Bullock, W. Wallace, POD Assessment of NDI Procedures-Results of a Round Robin Test, in: D.O. Thompson, D.E. Chimenti (Eds.) Rev. Prog. Quant. Nondestruct. Eval. Vol. 14, Springer US, Boston, MA, (1995), pp. 2391-2398.
10. J.H. Heida and F.P. Grooteman, "Airframe inspection reliability using field inspection data", National Aerospace Laboratory, NLR-TP-98144, March 1998.
11. D.S. Forsyth, A. Fahr, D.V. Leemans, K.I. McRae, S. Kallsen, C. Nessa, D.O. Thompson, D.E. Chimenti, L. Poore, Development of POD from in-service NDI data, AIP Conference Proceedings, 509 (2000) 2167-2174.
12. S K Nath, K Balasubramaniam and C V Krishnamurthy, 'Reliability assessment of manual ultrasonic time of flight diffraction (TOFD) inspection for complex geometry components', NDT&E Int, Vol 43, pp 152–162, 2010.

13. J H Kurz, A Jüngert and C Boller, 'Reliability considerations of NDT by probability of detection (POD) determination using ultrasound phased array', Eng Failure Analysis, Vol 35, pp 609–617, 2013.
14. A A Carvalho, J Rebello, R R Silva and L Sagrilo, 'Reliability of the manual and automatic ultrasonic technique in the detection of pipe weld defects', Insight, Vol 48, No 11, pp 649-654(6), November 2006.
15. M Carboni, 'A critical analysis of ultrasonic echoes coming from natural and artificial flaws and its implications in the derivation of probability of detection curves', Insight, Vol 54, No 4, pp 208-216(9), April 2012.
16. M Yanishevsky, M Martinez and D Backman, 'Artificial seeding of fatigue cracks in NDI reference coupons', Insight, Vol 52, No 12, pp 664-671(8), December 2010.
17. Department of Defense handbook, "Non-destructive evaluation system reliability assessment", MIL-HDBK-1823A (USA), April 2009.
18. M Kemppainen, I Virkkunen and H Hänninen, 'Advanced flaw production method for in-service inspection qualification mock-ups', Nuclear Eng and Design, Vol 224(1), pp 105-117, 2003.
19. Carboni M and Cantini S, 'Advanced ultrasonic ''Probability of Detection'' curves for designing in-service inspection intervals', Int J Fatigue, Vol 86, pp 77-87, May 2016.
20. B Weekes, D P Almond and T Barden, 'Eddy-current induced thermography—probability of detection study of small fatigue cracks in steel, titanium and nickel-based superalloy', NDT&E Int, Vol 49, pp 47–56, 2012.
21. R B Thompson, L J Brasche, D S Forsyth, E Lindgren,P Swindell and W Winfree, 'Recent advances in model-assisted probability of detection', Proceedings of the 4th European-American Workshop on the Reliability of NDE, Berlin, Germany, 2009.
22. S.N. Rajesh, L. Udpa, S.S. Udpa, Estimation of Eddy Current Probability of Detection (POD) Using Finite Element Method, in: D.O. Thompson, D.E. Chimenti (Eds.) Rev. Prog. Quant. Nondestruct. Eval. Vol. 12A and 12B, Springer US, Boston, MA, (1993), pp. 2365-2372, https://doi.org/10.1007/978-1-4615-2848-7_304
23. W.Q. Meeker, S.-L. Jeng, C.-P. Chiou, R.B. Thompson, Improved Methodology for Inspection Reliability Assessment for Detecting Synthetic Hard Alpha Inclusions in Titanium, in: D.O. Thompson, D.E. Chimenti (Eds.) Rev. Prog. Quant. Nondestruct. Eval. Vol. 17A, Springer US, Boston, MA, (1998), pp. 2061-2068. https://doi.org/10.1007/978-1-4615-5339-7_267

24. M. Li, W.Q. Meeker, R.B. Thompson, D.O. Thompson, D.E. Chimenti, Physical Model Assisted Probability Of Detection In Nondestructive Evaluation, AIP Conference Proceedings, 1335 (2011) 1541-1548. http://dx.doi.org/10.1063/1.3592113
25. R.B. Thompson, W.Q. Meeker, L.J.H. Brasche, D.O. Thompson, D.E. Chimenti, Pod Of Ultrasonic Detection Of Synthetic Hard Alpha Inclusions In Titanium Aircraft Engine Forgings, AIP Conference Proceedings, 1335 (2011) 1533-1540. https://doi.org/10.1063/1.3592112
26. P. Sarkar, W.Q. Meeker, R.B. Thompson, T.A. Gray, W. Junker, Probability of Detection Modeling for Ultrasonic Testing, in: D.O. Thompson, D.E. Chimenti (Eds.) Rev. Prog. Quant. Nondestruct. Eval. Vol. 17A, Springer US, Boston, MA, (1998), pp. 2045-2052, https://doi.org/10.1007/978-1-4615-5339-7_265
27. R.B. Thompson, D.O. Thompson, D.E. Chimenti, Early Work On The Use Of Models In The Determination Of Pod/Inspection Reliability In The Us And Uk, AIP Conference Proceedings, 1335 (2011) 1581-1588. http://dx.doi.org/10.1063/1.3592118
28. M. Li, W.Q. Meeker, R.B. Thompson, D.O. Thompson, D.E. Chimenti, Physical Model Assisted Probability Of Detection In Nondestructive Evaluation, AIP Conference Proceedings, 1335 (2011) 1541-1548. http://dx.doi.org/10.1063/1.3592113
29. F. Amin, T. A. Gray, F.J. Margetan, Ultrasonic Pod Model Validation And Development For Focused Probes, in: Rev. Prog. Quant. Nondestruct. Eval., (1990). https://doi.org/10.1007/978-1-4684-5772-8_110
30. M. Li, W.Q. Meeker, P. Hovey, D.O. Thompson, D.E. Chimenti, Using A Bayesian Model To Jointly Estimate The Flaw Size Distribution And The Pod Function, AIP Conference Proceedings, 1211 (2010) 687-694, http://dx.doi.org/10.1063/1.3362461
31. Adam C. Cobb, J. Fisher, Model-Assisted Probability of Detection for Ultrasonic Structural Health Monitoring, in: 4th European-American Workshop on Reliability of NDE, Berlin, (2009). www.ndt.net/index.php?id=8333 (Last accessed: February 2018)
32. S.N. Rajesh, L. Udpa, S.S. Udpa, Numerical model based approach for estimating probability of detection in NDE applications, IEEE Transactions on Magnetics, 29 (1993) 1857-1860. 10.1109/20.250768.
33. Jonne Haapalainen, E. Leskelä, Probability of Detection Simulations for Ultrasonic Pulse-echo Testing, in: 18th World Conference on Nondestructive Testing, Durban,South Africa, (2012). http://www.ndt.net/article/wcndt2012/papers/258_wcndtfinal00258.pdf (Last accessed: February 2018)

34. A.A. Carvalho, R.R. Silva, L.V.S. Sagrilo, J.M.A. Rebello, Reliability of the ultrasonic inspection by numerical simulation technique, Insight - Non-Destructive Test. and Cond. Monitoring. 53 (2011) 603-609. https://doi.org/10.1784/insi.2011.53.11.603
35. M. Wall, S.F. Burch, J. Lilley, Review of models and simulators for NDT reliability (POD), Insight - Non-Destructive Test. and Cond. Monitoring. 51 (2009) 612-619, https://doi.org/10.1784/insi.2009.51.11.612
36. R.B. Thompson, D.O. Thompson, D.E. Chimenti, Use of Physics-Based Models in the Determination of POD for 3D Defects, AIP Conference Proceedings 760 (2005) 1917-1924, https://doi.org/10.1063/1.1916904
37. R.B. Thompson, D.O. Thompson, D.E. Chimenti, Use of Physics-Based Models in the Determination of POD for 3D Defects, AIP Conference Proceedings 760 (2005) 1917-1924, https://doi.org/10.1063/1.1916904
38. P. Calmon, S. Mahaut, S. Chatillon, R. Raillon, CIVA: An expertise platform for simulation and processing NDT data, Ultrasonics 44 (2006) 975–979. https://doi.org/10.1016/j.ultras.2006.05.218
39. Philippe Dubois, Sébastien Lonne, Frédéric Jenson, Steve Mahaut, Simulation of Ultrasonic, Eddy Current and Radiographic Techniques Within The Civa Software Platform, ECNDT (2010). http://www.extende.com/files/extende/publications/2010_ECNDT_Dubois_Civa10_EN.pdf (Last accessed: February 2018)
40. Professor Robert A Smith, Development of a protocol for acceptance of new NDT capability in the air domain, Military Aircraft Structures Airworthiness Advisory Group, Paper 122, (2014).
41. Nicolas Dominguez, Damien Rodat, Frank Guibert, Aurélien Rautureau, Pierre Calmon, POD Evaluation Using Simulation: Progress and Perspectives regarding Human Factor, 19th World Conference on Non-Destructive Testing 2016. http://ndt.net/?id=19531. (Last accessed: February 2018)
42. J. Moysan, M.A. Ploix, G. Corneloup, A. Le Brun, Analysis of a Multiple-Operators Database for MAPOD Study of Ultrasonic Pulse-Echo Response from Side-Drilled Holes, 4th Eur. Am. Work. Reliab. NDE www.ndt.net/index.php?id=8366. (Last accessed: February 2018)
43. Nicolas Dominguez, Frédéric Reverdy, POD evaluation using simulation: Progress, practice and perspectives, AIP Conference Proceedings 1706, 200007 (2016). doi: 10.1063/1.4940651.

44. M. S. Mohammed, Kim Ki Seong, Probability of Detection Simulations to Study the Influence of Surface Roughness on the Reliability of Ultrasonic Testing System, Russian J. Nondestructive Test. 50 (2014) 239–247. https://doi.org/10.1134/S1061830914040056
45. D. Tisseur, M. Costin, POD Calculation on a Radiographic Weld Inspection with Civa 11 Rt Module. www.ndt.net/?id=18474. (Last accessed: February 2018)
46. Guillemette Ribay, Xavier Artusi, Frédéric Jenson, Christopher Reece, and Pierre-Emile Lhuillier, Model-based POD study of manual ultrasound inspection and sensitivity analysis using metamodel, AIP Conference Proceedings 1706, 200006 (2016). doi: 10.1063/1.4940650
47. F. Jenson, S. Mahaut, P. Calmon, C. Poidevin, Simulation Based Pod Evaluation Of Ndi Techniques, ECNDT (2010). http://idspektr.ru/10_ECNDT/reports/4_05_22.pdf (Last accessed: February 2018)
48. Charles R A Schneider, Ruth M Sanderson, Capucine Carpentier, Lu Zhao, Channa Nageswaran, Estimation of probability of detection curves based on theoretical simulation of the inspection process, BINDT Annual Conf. (2012).
49. J.A. Ogilvy, Model for predicting ultrasonic pulse-echo probability of detection, NDT & E Int. 26 (1993) 19-29. https://doi.org/10.1016/0963-8695(93)90160-V
50. L.J. Meyer RM, Crawford SL, A. MT, Review of literature for model assisted probability of detection, in: PNNL-23714, 2014. https://www.pnnl.gov/main/publications/external/technical_reports/PNNL-23714.pdf (Last accessed: February 2018)
51. Michele Carboni, S. Cantini, A Model Assisted Probability of Detection" approach for ultrasonic inspection of railway axles, in: 18th World Conference on Nondestructive Testing, South Africa, 2012. http://www.ndt.net/article/wcndt2012/papers/200_wcndtfinal00200.pdf (Last accessed: February 2018)
52. K. Smith, B. Thompson, B. Meeker, T. Gray, L. Brasche, D.O. Thompson, D.E. Chimenti, Model-Assisted Probability of Detection Validation for Immersion Ultrasonic Application, AIP Conference Proceedings, 894 (2007) 1816-1822. https://doi.org/10.1063/1.2718184
53. J.S. Knopp, J.C. Aldrin, E. Lindgren, C. Annis, Investigation Of A Model-Assisted Approach To Probability Of Detection Evaluation (Preprint), AFRL-ML-WP-TP-2006-494, 2006. http://www.dtic.mil/dtic/tr/fulltext/u2/a464706.pdf (Last accessed: February 2018)

54. Mato Pavlovic, Kazunori Takahashi, Christina Müller, Reliability in non-destructive testing (NDT) of the canister components, SKB Rapport R-08-129, (2008). http://www.iaea.org/inis/collection/NCLCollectionStore/_Public/40/057/40057523.pdf (Last accessed: February 2018)
55. Mato Pavlovic, Kazunori Takahashi, Ulf Ronneteg, Christina Müller, Multi-Parameter Influence on the Response of the Flaw to the Phased Array Ultrasonic NDT System. The Volume POD, 4th European-American Workshop on Reliability of NDE, (2009). www.ndt.net/index.php?id=8336. (Last accessed: February 2018)
56. M Pavlović , K Takahashi, C Müller, Probability of detection as a function of multiple influencing parameters, Insight 54 (2012). DOI: 10.1784/insi.2012.54.11.606.
57. D Kanzler, C Müller, J Pitkänen, Probability of detection for surface-breaking holes with low-frequency eddy current testing – a non-linear multi-parametric approach, Insight 56 (2014). DOI: 10.1784/insi.2014.56.12.664.
58. Noritaka Yusa, Jeremy S. Knopp, Evaluation of probability of detection (POD) studies with multiple explanatory variables, J Nucl Sci Technol 53 (2016) 574–9. http://dx.doi.org/10.1080/00223131.2015.1064332.
59. Andrea Gianneo, Michele Carboni, Marco Giglio, Feasibility study of a multi-parameter probability of detection formulation for a Lamb waves–based structural health monitoring approach to light alloy aeronautical plates, Structural Health Monitoring (2016). DOI: 10.1177/1475921716670841.
60. Andrea Gianneo, Michele Carboni, Marco Giglio, Reliability Aspects and Multi-Parameter POD Formulation for Guided Wave Based SHM Techniques, 19th World. Conf. Non-Destructive Testing (2016). http://ndt.net/?id=19534 (Last accessed: February 2018)
61. A. Gianneo, M. Carboni, M. Giglio, A preliminary study of multi-parameter POD curves for a guided waves based SHM approach to lightweight materials, AIP Conference Proceedings , 1706, 030018 (2016). http://dx.doi.org/10.1063/1.4940490.
62. NoritakaYusa, WeixiChen, Hidetoshi Hashizume, Demonstration of probability of detection taking consideration of both the length and the depth of a flaw explicitly, NDT E Int. 81 (2016) 1–8. http://dx.doi.org/10.1016/j.ndteint.2016.03.001.
63. Nick Rothbart, Christiane Maierhofer, Matthias Goldammer, Probability of detection analysis of round robin test results performed by flash thermography, Quantitative Infrared Thermography J. (2016). http://dx.doi.org/10.1080/17686733.2016.1229246.

64. N Yusa, Probability of detection model for the non-destructive inspection of steam generator tubes of PWRs, IOP Conf. Series: Journal of Physics: Conf. Series 860 (2017) 012032. doi :10.1088/1742-6596/860/1/012032
65. ENIQ Recommended Practice 1: Influential/Essential Parameters, Issue 2, ENIQ Report nr. 24, June 2005.
66. K. Smith, "POD Transfer Function Approach," presented to the MAPOD Working Group at the February 4, 2005 meeting in Palm Springs, California.
67. R. Bruce Thompson, “A Unified Approach To The Model-Assisted Determination Of Probability Of Detection”, CP975, Review of Quantitative Nondestructive Evaluation Vol. 27, ed. by D. O. Thompson and D. E. Chimenti, 2008.
68. C.A. Harding, G.R. Hugo, S.J. Bowles, Application of model-assisted POD using a transfer function approach, in: D.O. Thompson, D.E. Chimenti, (Eds.), Rev. Prog. Quant. Nondestruct. Eval. vol. 1096, Chicago (Illinois): AIP Conf. Proc., 2009, pp.1792–1796.
69. M. Carboni, S.A. Cantini, “Model Assisted Probability of Detection” approach for ultrasonic inspection of railway axles, in: 18th World Conf. Nondestruct. Test. 2012 Conf. Durban, South Africa, 2012, pp. 16–20
70. S. Demeyer, F. Jenson, N. Dominguez, E. Iakovleva, Transfer function approach based on simulation results for the determination of pod curves, in: D.O. Thompson, D.E. Chimenti (Eds.), Rev. Prog. Quant. Nondestruct. Eval. AIP Conf. Proc., Burlington, VT, 2012, pp. 1757–1764.
71. Mohamed Subair Syed Akbar Alia, Anish Kumar, Prabhu Rajagopal, “Signal noise based transfer function approach for reliability estimation of ultrasonic inspection”, Ultrasonics, accepted article in press, available online 29 september 2018.
72. M.S. Safizadeh, D.S. Forsyth, A. Fahr, D.O. Thompson, D.E. Chimenti, C. Nessa, S. Kallsen, L. Poore, Recent Studies on the POD Analysis of “â vs. a” NDI Data, AIP Conference Proceedings, 657 (2003) 1846-1853. https://doi.org/10.1063/1.1570353
73. Phani Mylavarapu, Vamsi Krishna Rentala, M.Sundararaman, Vikas Kumar, H. Gokhale, Sensitivity evaluation of NDT techniques on naturally initiating fatigue cracks-An experimental approach for a POD framework, in: DRDO-DMRL-NDTG-083, DMRL Technical Report, Hyderabad, (2015).
74. Hina Gokhale, Shahnawaz, Raghu, V. Kumar, Probabilistic fatigue life assessment of gun barrels, in: DRDO-DMRL-034, DMRL Technical Report (2012).
75. D.A. Virkler, B.M. Hillberry, P.K. Goel, The Statistical Nature of Fatigue Crack Propagation, J. Engineering Mater. Technol. 101 (1979) 148-153. doi:10.1115/1.3443666.

76. Y. Liu, S. Mahadevan, Probabilistic fatigue life prediction using an equivalent initial flaw size distribution, Int. J. Fatigue 31 (2009) 476-487. https://doi.org/10.1016/j.ijfatigue.2008.06.005
77. A.Makeev, Y. Nikishkov, E. Armanios, A concept for quantifying equivalent initial flaw size distribution in fracture mechanics based life prediction models, Int. J. Fatigue 29 (2007) 141-145. https://doi.org/10.1016/j.ijfatigue.2006.01.018
78. J.N. Yang, G.C. Salivar, C.G. Annis, Statistical modeling of fatigue-crack growth in a nickel-base superalloy, Engineering Fracture Mechanics 18 (1983) 257-270. https://doi.org/10.1016/0013-7944(83)90137-6.
79. Phani Mylavarapu, Vamsi Krishna Rentala, M.Sundararaman, Vikas Kumar, H. Gokhale, Sensitivity evaluation of NDT techniques on naturally initiating fatigue cracks-An experimental approach for a POD framework, in: DRDO-DMRL-NDTG-083, DMRL Technical Report, Hyderabad, (2015).
80. Hina Gokhale, Shahnawaz, Raghu, V. Kumar, Probabilistic fatigue life assessment of gun barrels, in: DRDO-DMRL-034, DMRL Technical Report (2012).
81. Luca Gandossi and Charles Annis, “Probability of detection curves- statistical best practices”, ENIQ TGR Technical document, ENIQ Report no. 41, EUR 24429 EN, 2010.
82. D. S. Forsyth, A. Fahr, An Evaluation of POD statistics, in: RTO AVT Workshop on “Airframe Inspection Reliability under Field/Depot Conditions", Belgium, (1998).
83. B. Weekes, D.P. Almond, P. Cawley, T. Barden, Eddy-current induced thermography—probability of detection study of small fatigue cracks in steel, titanium and nickel-based superalloy, NDT E Int. 49 (2012) 47-56. https://doi.org/10.1016/j.ndteint.2012.03.009
84. M. Carboni, A critical analysis of ultrasonic echoes coming from natural and artificial flaws and its implications in the derivation of probability of detection curves, Insight - Non-Destructive Test. and Cond. Monitoring, 54 (2012) 208-216. https://doi.org/10.1784/insi.2012.54.4.208

3. EXPERIMENTAL POD PROCEDURE

As the NDT reliability or POD studies are depending on many factors, reliability of NDT techniques is usually measured using service expired discs with several fatigue cracks at critical locations such as bolt hole, fir tree, etc., [1]. Under the absence of service expired aero-engine components, laboratory induced cracks can be used for reliability measurement of NDT techniques [2]. In the current research work, representative service fatigue cracks have been generated under both room temperature and high temperature conditions for use in NDT reliability studies. This chapter provides the experimental POD work carried out for generation of fatigue cracks under room temperature and high temperature conditions.

3.1 Material

As the current work deals with service fatigue cracks originating from aero-engine turbine discs, samples for generation of room and high temperature fatigue cracks are extracted from an actual aero-engine turbine disc component (as shown in Figure 32). These samples are designed in such a way so as to generate fatigue cracks similar to the cracks originating from the bolt hole locations of a turbine disc, as shown in Figure 33 [3].This turbine disc is made up of Nickel based superalloy material similar to Nimonic 80A composition. Table 1 shows the typical chemical composition of the turbine disc material.

Table 1: Typical chemical composition of Turbine Disc Material ~ Nimonic 80A in wt%

C	Fe	Mn	Si	Ti	S	Cr	Pb	B	Cu	Ce	Al	Ni
0.04-0.08	1	0.4	0.6	2.65-2.9	0.007	19-22	0.001	0.01	0.07	0.02	0.7-1	Bal

Figure 32: A portion of turbine disc exposed to 3000 hours of service life that is used for extraction of samples (a) Before and (b) After

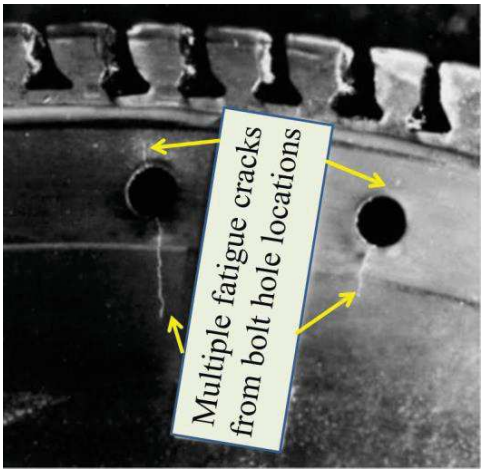

Figure 33: Multiple fatigue cracks emanating from bolt hole locations of an aero-engine disc [3].

The extracted blanks from the turbine disc material are used for fabricating specimens according to the sample design considered for carrying out room temperature and high temperature fatigue testing. The details regarding the specimen design, load optimization and fatigue testing procedures of room temperature and high temperature fatigue testing are provided in the next section. Further, the details of crack size analysis using microscopy techniques and NDT inspection procedures are also provided.

3.2 Room temperature fatigue cycling

Earlier studies performed during the M.Tech thesis work of Vamsi [4] provides the complete methodology of generating service induced fatigue cracks under room temperature fatigue testing conditions. However, for completeness, brief information on the specimen geometry, optimization of loading conditions and room temperature fatigue testing equipment are provided in the current section. Figure 34 shows the room temperature fatigue testing specimen design along with the loading point "P" and supports. This specimen design is prepared in order to generate representative fatigue cracks emanating from critical locations such as a bolt hole using three-point bend fatigue testing, as recommended in Appendix F of MIL-HDBK 1823A [2]. From Figure 34, it can be observed that the specimen length and span length between supports are 55 mm and 50 mm, respectively. The cross section of the sample is 10 mm X 10 mm. It can also be observed that the radius of the semi-circular notch which represents the stress concentration factor of a bolt hole in an aero-engine turbine disc is 2 mm.

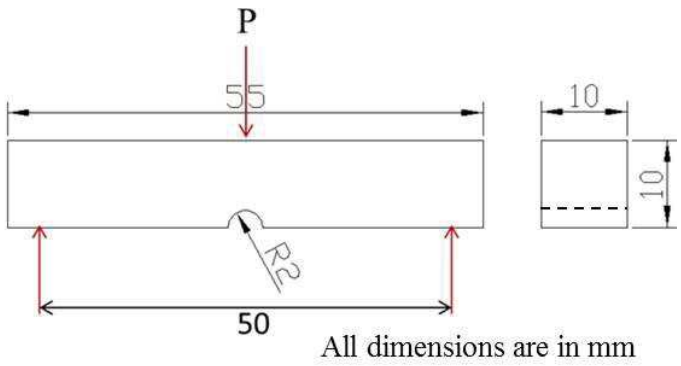

Figure 34: Specimen design showing loading point and supports

The fatigue loading conditions (Maximum load = -6.5 kN and stress ratio, R = 0.1) optimized from the M.Tech thesis work of Vamsi [4] are used for carrying out 3-point bend fatigue testing under room temperature conditions. A total of 21 identical samples obtained from a turbine disc were machined according to the specimen design. All the specimens are polished metallographically before fatigue testing. These samples are tested on frequency controlled servo-hydraulic fatigue test equipment with a three point bend fixture for initiating fatigue cracks (Figure 35). As the fatigue cracks in the aero-engine components experience constant number of loading cycles, the number of fatigue cycles for generation of fatigue cracks in the these samples is maintained constant at 1.05 x 10^5 cycles and the varying range of crack sizes are obtained due to the statistical nature of fatigue. All these fatigue cracks are then inspected using ECT and FLPT techniques for POD analysis.

Figure 35: Experimental set up of 3-point bend fatigue testing

3.3 High temperature fatigue cycling

3.3.1 Specimen geometry

As it is difficult to obtain components with service induced cracks, it is essential to evolve a methodology for generating high temperature fatigue cracks which are morphologically similar to the service induced fatigue cracks. While conventional high temperature fatigue test specimens interrupted at different fractions of lives would have many fatigue cracks of differing lengths, identifying and measuring the dimensions of smaller cracks of short crack regime under a microscope over the entire specimen gauge length is a cumbersome process and may not cover all the cracks and thus, end up being less reliable. This study demonstrates a first-of-its kind methodology adopted for generating oxidized cracks using Gleeble® test system. In order to generate fatigue cracks similar to that originating from the bolt hole location of a turbine disc under the operating temperature of ~650°C, a flat fatigue specimen containing a semi-circular edge notch of 2 mm radius is adopted. As Gleeble employs resistance (joule) heating, the notch helped not only in generating a stress concentration at the notch, but also in creating a zone of high current density. By choosing appropriate stainless steel grip sets, axial thermal gradient prevalent in Gleeble® environment is leveraged to maintain the test temperature to a narrow region at the notch. The rest of the parallel length region of the test specimen is maintained at much lower test temperatures which gradually reduced to room temperature at the gripped ends. Through imposition of repeated loading and unloading cycles imposed on a flat notched specimen, oxidized fatigue cracks, similar to those observed in service conditions, could be generated in the laboratory. Figure 36 shows the specimen design with 10 mm gauge width, 55.6 mm of gauge length and 4 mm thickness used for testing in Gleeble® system.

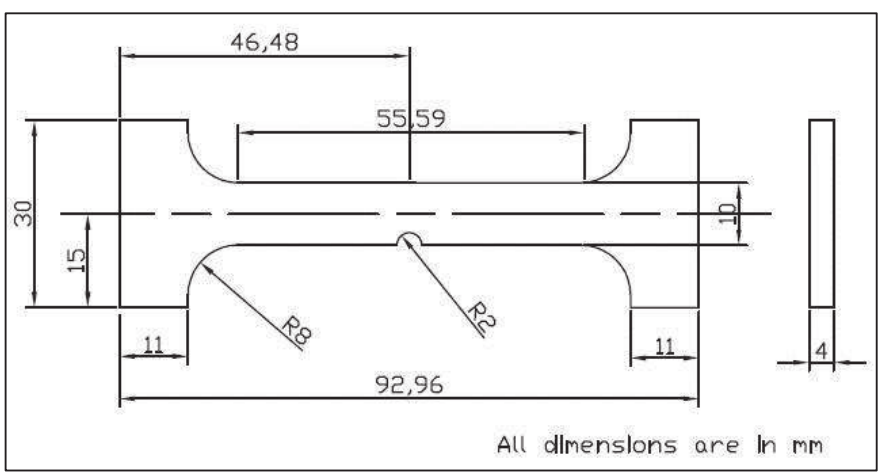

Figure 36: Specimen design used for fatigue cycling in Gleeble® system

3.3.2 Optimization of load for fatigue cycling

Similar to the optimization of fatigue loading conditions for room temperature samples tested during M.Tech thesis of Vamsi [4], the load corresponding to 80% of yield stress of the material is chosen for carrying out the high temperature fatigue cycling in Gleeble test system. The yield stress of the material at 650°C is 646 MPa and the load corresponding to 80% (516 MPa) of 646 MPa is equal to 21 kN (i.e., 516 MPa x 40 mm^2 (sample cross sectional area according to Figure 36)). Hence, a load of 21 kN is chosen for carrying out high temperature fatigue cycling in Gleeble® test system.

3.3.3 Fatigue cycling in Gleeble system

Using the calculated loading conditions equivalent to 80% of yield stress of the material, the specimen is tested under triangular waveform with a maximum load of 21 kN and a stress ratio of R = 0.1 typically used in fatigue tests conducted to represent aero-engine conditions [5-8]. As a thumb rule, it is believed that, at higher temperatures and at lower test frequencies of approximately less than 1 Hz, the chances of observing crack surface oxidation is predominant and hence, a frequency of 0.1 Hz is used in the current study [5]. As the disk experiences temperatures of approximately 650°C during service, the testing is also carried out at 650°C in air environment. In Gleeble® system, the sample is heated using resistance heating mechanism by controlling the temperature with the help of thermocouples spot welded at the center of the sample. Figure 37 shows (a) the sample with thermocouple attached to it, (b) grip sets used for holding the sample, (c) specimen fixed in grip sets and (d) the Gleeble® test chamber showing the gripped specimen as part of the load train. A total of 13 samples have been tested for generation of fatigue cracks using Gleeble® system. In order to optimize the number of fatigue cycles for initiation of the fatigue cracks, one sample is tested initially for fatigue cycling and interrupted after every 200 cycles until a crack at notch location is observed using optical microscope (M/s. Olympus, USA). In order to facilitate easy microscopic observation of fine fatigue cracks and measurement of crack dimensions, the region below the notch in every specimen is polished through standard metallographic procedure before subjecting them to high temperature fatigue cycling. Fatigue cycling in air environment is started after the specimen is heated to 650°C at a heating rate of 5°C/sec. All the tests are conducted in air environment. Once a crack is found to be initiated microscopically, the fatigue cycling is stopped and the corresponding number of fatigue cycles is fixed for carrying out the fatigue cycling of the remaining samples. For the first sample, the number of fatigue cycles for initiating a crack is found to be 2200 cycles. Hence, for all the remaining samples, the fatigue cycling is uninterruptedly continued till 2000 cycles

and checked for any crack initiation under the microscope. In the absence of crack initiation after 2000 cycles at the notch location, the test is further continued but with interruptions after every 100 cycles for microscopic inspections and stopped when cracks are observed to be initiated under the microscope. Both sides of the flat specimens are inspected for fatigue cracks. Because of the temperature and stress concentration imposed at the notch root region, locating fatigue cracks is relatively easy as cracks are always observed at that location. In addition, an attempt to understand the effect of oxidation under the high temperature air environment is carried out by performing fatigue testing of one sample under vacuum (~10^{-6} torr) under identical fatigue test conditions.

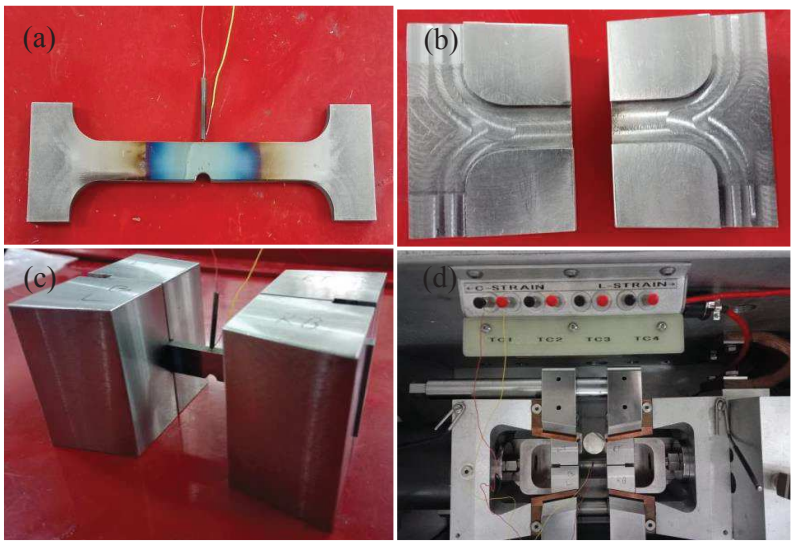

Figure 37: (a) Sample with thermocouples welded at the center (b) Blocks used for holding sample (c) Sample in the blocks (d) Specimen chamber with sample in the blocks

3.4 Crack size measurements using Scanning Electron Microscope (SEM)

After initial screening for confirmation of presence of cracks, all the tested samples were subjected to crack size measurements using Nova Nano SEM 450 FESEM system (M/s. FEI Technologies Inc., U.S.A) (Figure 38). Dimensions of the surface fatigue cracks are measured in both length and width directions. However, as the crack width is assumed to vary from the crack origin to the crack tip, crack width is calculated as an average of the measured dimensions at the crack origin, the crack middle and the crack tip locations. In addition, energy dispersive X-ray spectroscopy (EDS) is also performed for identifying the presence of oxides formed on both material and crack surfaces. Subsequently, all the samples

are non-destructively inspected using Eddy current technique (ECT) and Fluorescent liquid penetrant technique (FLPT).

Electron Backscattered Diffraction (EBSD) analysis

In order to understand the nature of fatigue crack i.e., either trans-granular or inter-granular and also for observing various microstructural features of the material, fatigue cracked samples are characterized using EBSD technique. Prior to placing the samples for EBSD characterization, samples are electro polished with A2 electrolyte (73.14 v% of ethanol, 10.02 v% of butoxy ethanol, 9.01 v% of distilled water and 7.81 v% of perchloric acid) at 20°C for 15 seconds at 25 V and a flow rate of 12 seconds. These electro polished specimens are used for EBSD characterization on M/s. FEI NOVA NANOSEM system. EBSD scans are performed on the fatigue crack location of the sample with a step size of 2 microns.

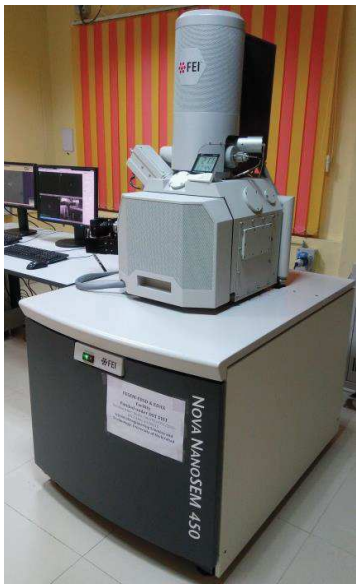

Figure 38: SEM equipped with EDS and EBSD detectors

3.5 NDT inspection of fatigue cracks

In the current study, two conventional NDT techniques, namely, eddy current technique (ECT) and fluorescent liquid penetrant technique (FLPT) are used for detection of room temperature (RT) and high temperature (HT) fatigue cracks. All the samples with cracks are initially inspected with ECT and followed by FLPT.

3.5.1 Eddy current technique (ECT)

In order to calibrate the eddy current testing procedure, EDM notches of different depths ranging from 0.1 mm to 1.0 mm are generated on two nickel based superalloy samples i.e., 0.1 mm to 0.5 mm deep EDM notches in 1 sample and 0.6 mm to 1.0 mm deep EDM notches in another sample. One of the nickel based superalloy samples with 0.6 mm to 1.0 mm deep EDM notches is shown in Figure 39. As the EDM wire diameter used is 0.25 mm, the width of all the EDM notches is maintained at 0.25 mm. With the help of the gain and rotation variation of the eddy current inspection process possible within the Omniscan ECT system (M/s. Olympus, U.S.A), the ECT signal of notch of largest depth i.e., 1 mm is adjusted to 80 % full screen height (FSH). All the inspections in this study are carried out using a straight pencil probe [9] (shielded coil based absolute probe of diameter 0.5 mm) designed to work with in a frequency range of 500 kHz to 1MHz. Further, the standard skin depth for 500 kHz and 1 MHz frequencies in nickel superalloy are calculated using Equation (1) [10]. By using the electrical (ρ = electrical resistivity = 126.772 $\mu\Omega$-cm) and magnetic properties (μ_r = relative magnetic permeability = 1.06) of nickel based superalloy [11] and the frequency value of 5,00,000 Hz, the standard skin depth values are estimated to be 0.78 mm and 0.54 mm for 500 kHz and 1 MHz frequencies, respectively.

Compared with the signal to noise ratio of ECT signals obtained for EDM notches when performed with 500 KHz frequency, signal to noise ratio of ECT signals obtained with 1 MHz frequency is found to be lower. Therefore, in this study, 500 kHz frequency is used for all defect types. In addition, it is also commonly known that surface cracks in low conductivity materials such as titanium or stainless steel are most popularly inspected using the frequency ranges 200 kHz to 500 kHz [11]. Hence, as the conductivity of nickel based superalloy (1.36 %IACS (international annealed copper standards)) is also similar to that of titanium (conductivity of Ti-6Al-4V = 1.01 %IACS) [11], in the current study, eddy current probe frequency of 500 kHz is considered for all inspections. Prior to the inspection of the sample with EDM notches, the pencil probe is balanced with the material and the lift-off is adjusted to be horizontal in the impedance plane. Eddy current response from the EDM notches is considered for estimating the equivalent crack depths of the cracks in both room temperature and high temperature fatigue tested samples.

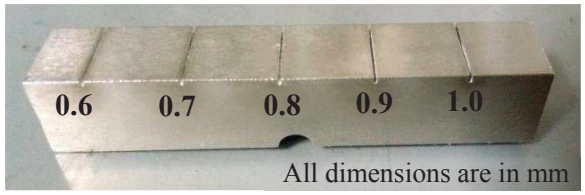

Figure 39: Nickel based superalloy material with 0.6 mm to 1.0 mm deep EDM notches.

3.5.2 Fluorescent liquid penetrant technique (FLPT)

Prior to inspection of fatigue cracks generated in specimens, FLPT procedure is calibrated using TAM panels [12]. Further, all the room temperature and high temperature tested specimens are cleaned with acetone for removing any dust present on the sample surface. This is similar to the surface cleaning adopted on components before FLPT. Sufficient care is taken while cleaning the samples with acetone such that the cleaning process does not remove any oxides (in the case of high temperature cracks) from the crack surfaces. Further, water washable penetrant is applied on all the samples as shown in Figure 40(a) and a dwell time of 15 minutes is provided for the penetrant to penetrate in to the cracks. After completion of the dwell time, the penetrant on the surface is washed with water and developer is applied as shown in Figure 40(b). Finally, all the samples are observed under fluorescent lamp for any crack indications.

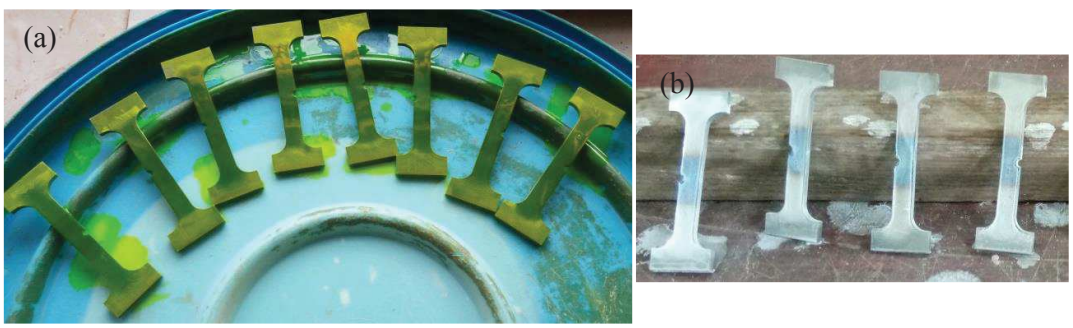

Figure 40: (a) Samples with penetrant and (b) developer applied during FLPT inspection

As the FLPT is qualitative in nature, data is recorded as a HIT or MISS i.e., if an indication is observed on a sample, then it is recorded as a HIT (defect detected) indication and otherwise as a MISS (defect undetected) indication. However, for ECT, inspection data is recorded in both $\hat{a}$ (ECT signal amplitude) and HIT/MISS type NDT assessment. During the ECT at a notch location containing fatigue crack, if a defect signal is observed in the impedance plane then the corresponding ECT signal amplitude for that notch location is noted as well as recorded as a HIT indication. Further, all the NDT inspection data from both the NDT techniques is statistically processed for plotting the POD curves.

3.6 Theory and Procedure for plotting the POD curves

Detailed discussion about the procedures to be adopted for plotting POD curves of HIT/MISS and $\hat{a}$ vs. a types of NDT data are given in MIL HDBK 1823A [2] . However, for completeness, the procedures are discussed briefly.

3.6.1. POD using HIT/MISS NDT data

Statistical analysis for determination of POD using qualitative or HIT/MISS type NDT data can be carried out using Berens approach of log-odds distribution function [2, 13, 14]. The functional form of the log-odds distribution function is as shown in Equation (3) [13].

$$P_i = \frac{e^{\left(f(a)\right)}}{1 + e^{\left(f(a)\right)}} \tag{3}$$

$$\text{where, } f(a) = \alpha + \beta.\ln\left(a_i\right) \tag{4}$$

P_i is the probability of detection for defect i, a_i is the size of defect i, α and β are regression parameters that define the binary logistic regression fit(as the NDT outcome of HIT/MISS is binary). By using a logit link function, binary logistic regression process is performed between NDT response (HIT or MISS) and the log(flaw size). The logit of a number P between 0 and 1 is given by Equation 5 [13]

$$Logit(P) = \log\left(\frac{P}{1-P}\right) \tag{5}$$

Figure 41 shows the flow chart of the statistical procedure followed for Hit/Miss NDT data using Minitab statistical software [15]. Step by step procedure to be adopted is shown in Appendix I. From the binary logistic regression analysis, the regression parameters α and β are obtained which are further used for calculating the probability of detecting each crack size using log-odds distribution function.

Substituting the crack sizes, in addition to obtaining the α and β values from the binary logistic regression analysis using the log-odds distribution function (Equation (3) and Equation (4) [13]), the corresponding probabilities for detecting each crack size by the NDT technique are obtained. In addition, the 95% lower confidence limits are also calculated using Equation (6) [5].

95% Lower Confidence Limit (LCL) of $\alpha = \alpha \pm \left(1.96 * \left(\frac{\beta}{\sqrt{n}}\right)\right)$ (6)

where, 'n' is the number of cracks.

By substituting the 95% lower confidence value of α and the original β value along with the crack sizes in the log-odds distribution function, the probabilities with 95% lower confidence are obtained. Further, POD curve is obtained by plotting probabilities versus crack sizes. From the POD curve, the intersection of 90% probability on the 95% lower confidence curve results in the identification of $a_{90/95}$ (flaw of size 'a' that can be detected with 90% probability at 95% confidence level) value.

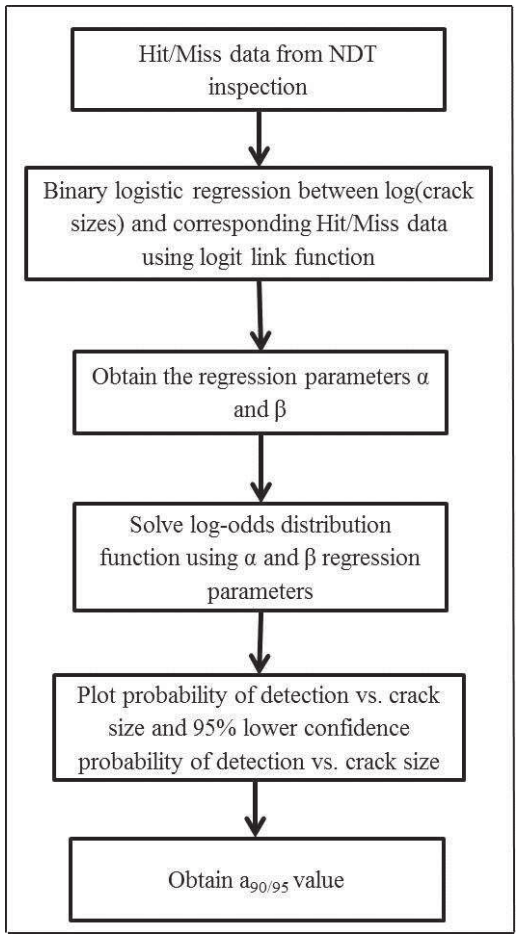

Figure 41: Flowchart of POD statistical procedure using Hit/Miss NDT data.

3.6.1.1. HIT/MISS POD approaches for multiple cracks at a site

As the $a_{90/95}$ value obtained from NDT reliability studies is used for remnant life estimation under damage tolerance lifing concept, estimation of $a_{90/95}$ value should be of highest accuracy. However, the qualitative NDT inspection data at a site containing multiple cracks (as

shown in Figure 42) results in ambiguity of POD approaches to be adopted for the estimation of $a_{90/95}$ values. Amongst several approaches attempted by researchers, the maximum flaw size approach (Type I) and the sum of flaw sizes approach (Type II) [16] happens to be the most common of all. In those cases, the $a_{90/95}$ values obtained will be different for different approach for the same NDT inspection data.

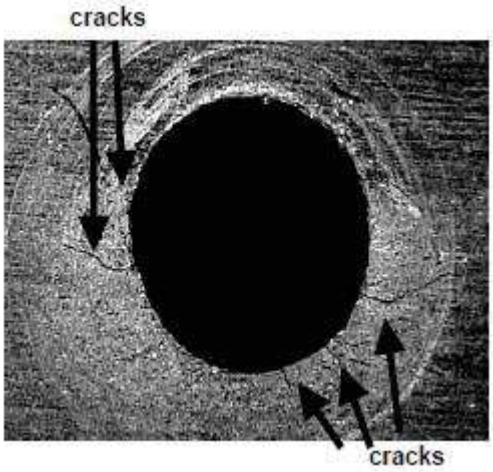

Figure 42: An example of multiple flaws at a site [16]

In order to perform the maximum flaw size (Type 1) and sum of flaw sizes (Type 2) approaches for POD analysis of multiple cracks at a site, the HIT/MISS NDT inspection data is segregated according to the number of flaws at an inspection site. Further, for a site containing multiple cracks, the NDT outcome is identified and the new NDT response is generated for each individual crack at that site according to the two POD approaches, namely maximum flaw size and sum of flaw sizes. For example, in maximum flaw size approach (Type 1), if the NDT response is HIT for a site containing multiple cracks, the maximum flaw size present at that site is considered to be HIT and the remaining flaws are marked as MISS. If the NDT response is a MISS indication at a site containing multiple cracks, all the individual cracks at that site are also considered to be MISS. In sum of flaw sizes approach (Type 2), if the NDT response is HIT for a site containing multiple cracks, the size corresponding to cumulative sum of flaws is considered to be HIT whereas for a MISS indication, the size corresponding to cumulative sum of flaws are considered to be missed. Hence, it can be understood that the FLPT inspection data is processed with both types of POD approaches whereas the ECT HIT/MISS data is only processed with Type 2. Along with Type 1, Type 2 is also applied for FLPT data because it is assumed that the FLPT indication

after a prolonged dwell time for developer indication will actually results in the cumulative sum of penetrant from all the cracks at that site. Further, the ECT inspection data is only processed with Type 2 approach as the ECT response is always the cumulative effect of all the cracks at a site and is difficult to resolve the response for each individual flaw at a site containing multiple cracks close to each other. In addition, the maximum flaw size approach is slightly modified and applied on the FLPT inspection data for POD analysis. In the modified Type 1 approach, if the FLPT outcome is HIT for a site containing multiple cracks, the maximum flaw at a site containing multiple cracks is marked as HIT and the remaining flaws are not considered in POD analysis. Similarly for the MISS indication at a site containing multiple cracks, the maximum flaw at a site containing multiple cracks is marked as MISS and the remaining flaws are not considered in POD analysis.

All the FLPT HIT/MISS data generated from all the three types i.e., Type 1, Modified Type 1 and Type 2 of POD approaches and ECT HIT/MISS data with Type 2 approach are processed using the standard log-odds distribution model for obtaining the POD curve. In addition, the 95 % lower confidence curves are also plotted in order to identify the $a_{90/95}$ value of all these techniques with different POD approaches.

3.6.2. POD using â (signal response) NDT data

In general, the reliability assessment using signal response based NDT data can be carried out using lognormal model for POD, as shown in Equation (7)- (9) [2]

$$POD(a) = 1-Q\left[\frac{\ln(a)-\mu}{\sigma}\right] \tag{7}$$

$$\text{where, mean, } \mu = \frac{\ln(y_{th})-\beta_0}{\beta_1} \tag{8}$$

$$\text{and standard deviation, } \sigma = \frac{\delta}{\beta_1} \tag{9}$$

where, POD(a) is the mean probability of detection of cracks of size, *a*

Q is the standard normal survivor function, and y_{th} is the value of the signal *â* at the decision threshold. According to MIL-HDBK1823A, decision threshold is defined [2] as the value of â above which the signal is interpreted as a HIT (defect detected) and below which the signal is interpreted as a MISS (defect not detected). Moreover, β_o and β_1 are the regression parameters obtained between ln(â) and ln(a) data from the regression equation shown in Equation 10 [2]:

$$\ln(\hat{a}) = \beta_o + \beta_1 \ln(a) + \varepsilon \quad (10)$$

where, ε denotes the residuals, normally distributed with zero mean and variance, σ^2. β_0 and β_1 are the regression parameters and δ is the standard error. Berens and Hovey [14] presented two approaches, namely, the Range Interval Method (RIM), which is also known as Regression Analysis, and the method of Maximum Likelihood Estimators (MLE) for estimating these constants. However, only MLE method was followed in the current study, as it is the most common method to estimate location and scale parameters as described in MIL-HDBK-1823A. Moreover, the MLE method does not require any information other than the actual inspection data. Hence, estimation of location and scale parameters of log-normal distribution by MLE method is discussed further.

3.6.2.1 Maximum Likelihood Estimators (MLE)

As described in MIL-HDBK-1823A, the most common method to estimate all of the coefficients (β_0, β_1, μ and σ) is to use maximum likelihood estimators. The likelihood L for a single observation is

$$L(Pi;ai,xi)=(P_i^{x_i}).(1-P_i)^{(1-x_i)} \quad (11)$$

where, Pi is the probability of detecting flaw i of size a_i and x_i is the inspection outcome, 0 for a "miss", and 1 for a "hit".

The overall likelihood of observing all the data is the product of their individual likelihoods. Thus, the likelihood of a series of independent inspections is the multiplication of the individual observations

$$L(Pi;ai,xi)=\left[\prod_{i=1}^{h} P_i\right]\left[\prod_{j=1}^{n-h}(1-P_i)\right] \quad (12)$$

where, L is the overall likelihood, n is the total number of flaws, h is the number of flaws detected, and n-h is the number of flaws missed. Also, probability of a miss = 1- probability of a hit. Generally, the hit and miss values are established by destructive verification tests or other acceptable means. By taking the logarithm of the Equation (12), the series of products become a series of sums, as shown in Equation 13.

$$\ln L(Pi;ai,xi)=\sum_{i=1}^{h} \ln P_i+\sum_{j=1}^{n-h} \ln P_j \quad (13)$$

The likelihood function shown in Equation 13 is applicable to both the log-logistic and log-normal distributions. The above equation is differentiated with respect to μ and σ and the

corresponding derivatives are set to zero and the resulting simultaneous equations are solved to provide estimates of μ and σ.

Similar to Figure 41, Figure 43 shows the flow chart of POD statistical procedure using signal response NDT data. Step by step procedure to be adopted is shown in Appendix II. From Figure 43, it can be observed that the $\hat{a}$ vs. a data obtained from NDT inspection is processed with regression with life data analysis option available in Minitab statistical software [15]. This regression process is performed between the suitable form of log-log data i.e., ln(â) vs. ln(a) or $\log_{10}$â vs. $\log_{10}$a. However, not all cracks are always detected by any NDT technique and hence, censoring of NDT signal response data is mandatory [2]. This censoring is generally carried out as upper and lower censoring. Upper censoring is usually performed for data above saturation level, whereas, lower censoring is performed to separate noise data. Further, assigning the censoring data, the decision threshold is selected considering the signal amplitudes below which would be recorded as noise. Furthermore, the regression of ln($\hat{a}$) vs. ln(a) data is performed using maximum likelihood estimator (MLE) method. After obtaining the regression parameters i.e., β_0 and β_1, the mean and standard deviation of the distributed data are calculated. Moreover, using the mean and standard distribution values, the cumulative distributive function (CDF) of lognormal distribution function for all the defect sizes used for NDT reliability studies is plotted resulting in POD curves. These POD curves yield the reliably detectable crack size detected by the NDT technique for use in remnant life calculations using deterministic fracture mechanics approaches.

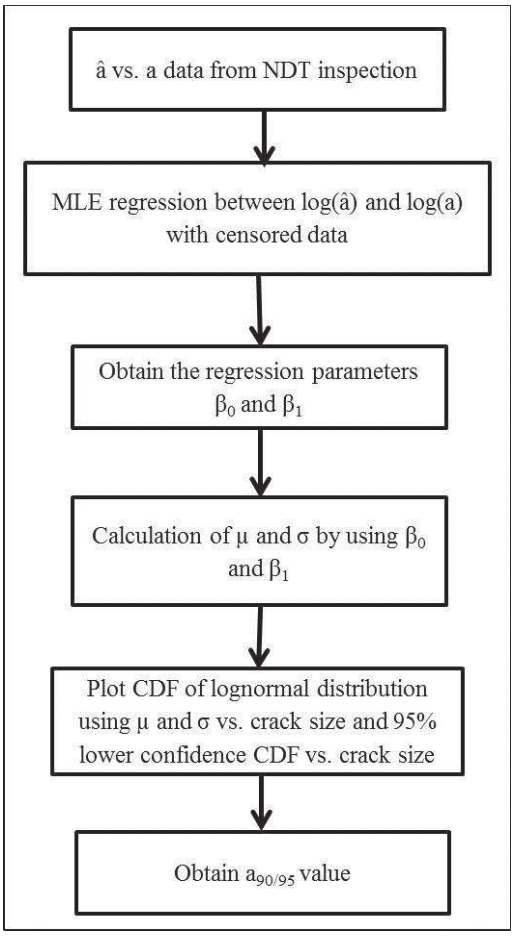

Figure 43: Flowchart of POD statistical procedure using signal response NDT data.

References

1. A.K. Koul, N.C. Bellinger and A. Fahr: "Damage-tolerance-based life prediction of aero-engine compressor discs: I. A deterministic fracture mechanics approach" J. Fatigue Vol.12, pp: 379-387(1990).
2. Department of Defense handbook, "Non-destructive evaluation system reliability assessment", MIL-HDBK-1823A (USA), April 2009.
3. W. Beres, A.K. Koul, "stress intensity factor calculations for cracks emanating from bolt holes in a jet engine compressor disc", ICAS2002 congress.
4. Vamsi Krishna Rentala, "Sensitivity Evaluation of NDT Techniques on Naturally Initiating Fatigue Cracks- an Experimental Approach for a POD Framework", M.Tech Thesis, University of Hyderabad, June 2014.

5. Garimella, L., Liaw, P.K. & Klarstrom, D.L. Fatigue behavior in nickel-based superalloys: A literature review. JOM 49, 67 (1997).
6. XinyueHuang, LiangWang, YunmingHu, GuangpingGuo, DavidSalmon, YingLi, WenxiaZhao, "Fatigue crack propagation behavior of Ni-based superalloys after overloading at elevated temperatures", Progress in Natural Science: Materials International, Volume 26, Issue 2, April 2016, Pages 197-203
7. M. Clavel And A. Pineau, Fatigue Behaviour of Two Nickel-base Alloys I: Experimental Results on Low Cycle Fatigue, Fatigue Crack Propagation and Substructures, Materials Science and Engineering, 55 (1982) 157 – 171.
8. R G Zhao, L Y Deng, Y F Liu, N Ji, C L Ren and X M Li, "Detection and analysis of high temperature fatigue fracture surface oxygen diffusion of GH4133B superalloy used in turbine disk of aero-engine", IOP Conf. Series: Materials Science and Engineering 531 (2019) 012021.
9. Olympus Material on Eddy current inspection- eddy current probes and accessories, EC_Probes_EN_200907.
10. Eddy Current Testing at Level 2: Manual for the Syllabi Contained IAEA-TECDOC-628/Rev. 2 'Training Guidelines for Non-Destructive Testing Techniques, Training Course Series No. 48, International Atomic Energy Agency, Vienna, 2011.
11. CSNDT compiled by eddy current technology incorporated, ASM metals handbook, vol 2, 10th edition, March 2002. www.nde.ed.org/generalresources/materialsproperties/ET/et_matlprop_index.htm
12. Volume 17, Nondestructive Evaluation and Quality Control. Metals Park, Ohio ASM International, 1989.
13. ASTM E2862-18, Standard Practice for Probability of Detection Analysis for Hit/Miss Data, ASTM International, West Conshohocken, PA, 2018, www.astm.org
14. Berens, A., 1992. NDE Reliability Data Analysis, in "ASM Metals handbook volume 17", non-destructive evaluation and quality control, ASM international, pp. 1437-1470.
15. Minitab 17 Statistical Software (2010).[Computer software]. State College, PA: Minitab, Inc. (www.minitab.com)
16. Spencer, F., 2006. Probability of detection estimation for hit/miss data when detection cannot be attributed to specific flaws: an exploratory data analysis, Review of QNDE, vol.25.

4. MODEL BASED POD PROCEDURE

Estimation of POD of any NDT techniques can be obtained by both experimental and model assisted methods. POD depends on many factors such as material, geometry, defect characteristics, inspection technique, etc. These requirements put enormous limitations on generating experimental POD curves and hence, Model Assisted Probability of Detection (MAPOD) curves are currently in vogue. In the current work on model based POD studies, MAPOD approaches are demonstrated by addressing various issues related to selection of crack sizes distribution, challenges involved in censoring and regression, estimation of distribution parameters, etc. Ultrasonic testing on volumetric defects has been identified as a platform to discuss the challenges involved. In the current chapter, the procedure carried out for obtaining POD curves using model based techniques is discussed.

4.1. MAPOD work flowchart

Figure 44 shows the MAPOD work flowchart followed in the current study. From Figure 44, it can be observed that, initially a physics based mathematical model is developed. Further, the model is validated with the experimentally obtained A-scan data and utilized for predicting the ultrasonic wave interaction with a statistically distributed random crack sizes. Moreover, the statistical analysis of the $\hat{a}$ vs. a data results in the POD curve.

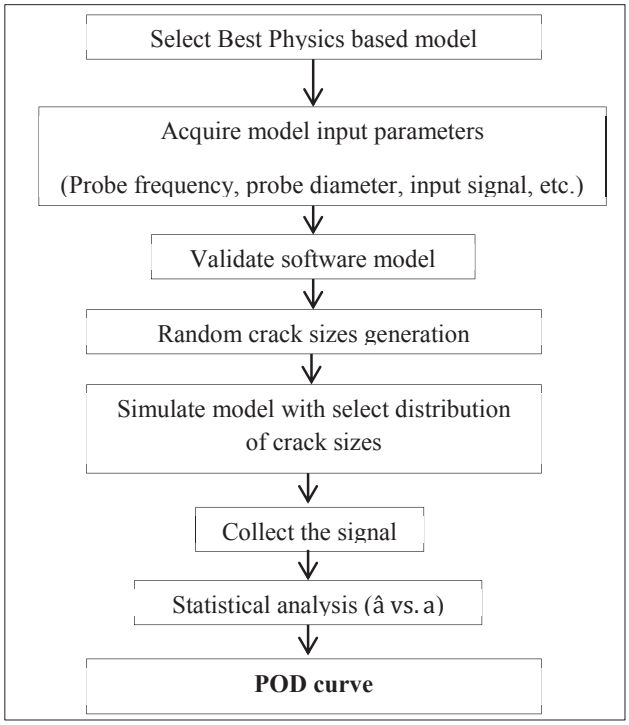

Figure 44: MAPOD work flowchart followed in this study

4.2 Experimental ultrasonic testing for calibration and validation

In order to develop numerical models to estimate the probability of detection of NDE techniques, physics based model simulating the NDE technique is an essential requirement. However, the physics based numerical model has to be validated before its utilization for generation of POD curve. Therefore in this study, experimental ultrasonic signals are generated in order to validate signals as observed from numerical modeling.

A Ti-6Al-4V cylindrical block with a diameter of 50 mm and height of 15 mm is considered for ultrasonic inspection. A flat bottom hole (FBH) of diameter 0.5 mm and a height of 5 mm present in the Ti-6Al-4V block is used as embedded defect representation. Hence, it can be understood that the depth of the FBH from the measuring surface or the transducer is 10 mm. Use of FBH represents the response from flat cracks at normal incidence. Even though the FBH in the block can be at any desired height, current study only deals with a height of 5 mm. Ultrasonic signals are captured using a single channel ultrasonic pulser receiver available in Omniscan MX portable instrument (M/s. Olympus In., USA) with a 5 MHz longitudinal probe (V110-RM from M/s Panametrics Inc., USA). Figure 45 shows the experimental setup along with the sample dimensions. Figure 46 shows the experimental A-scan signal obtained on the Ti-6Al-4V block. Ultrasonic inspection is initially calibrated for sound velocity in the block material with two different thicknesses and the corresponding ultrasonic longitudinal wave velocity in Ti-6Al-4v is measured to be 6000 m/s. From Figure 46, it can be observed that the defect/FBH echo at 25 % full screen height (FSH) is obtained by increasing the gain up to 27 dB. This increase in gain resulted in saturated backwall echoes and thus, eliminating possibility of using experimental signal as a validation for modeling signal.

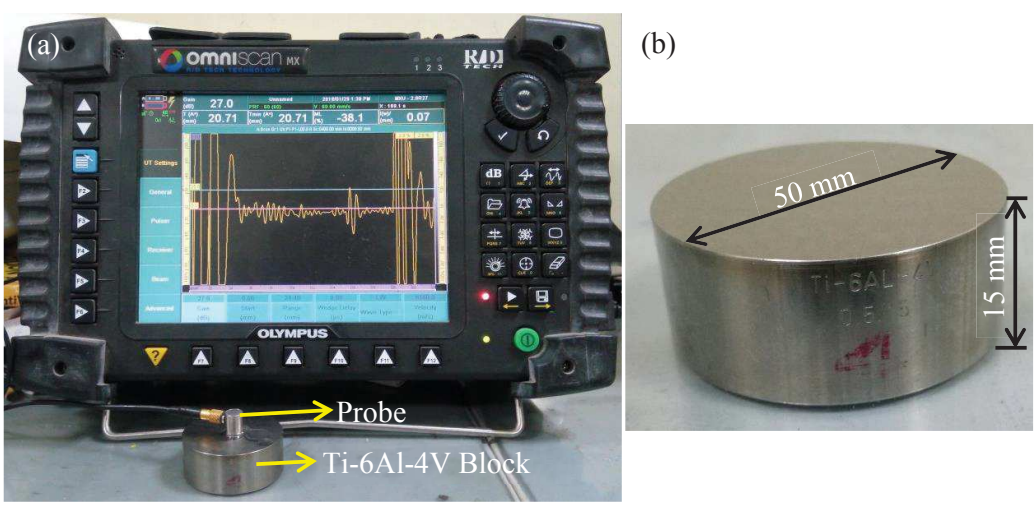

Figure 45: Ultrasonic Inspection (a) Experimental Setup (b) Sample (Ti-6Al-4V Block) with dimensions

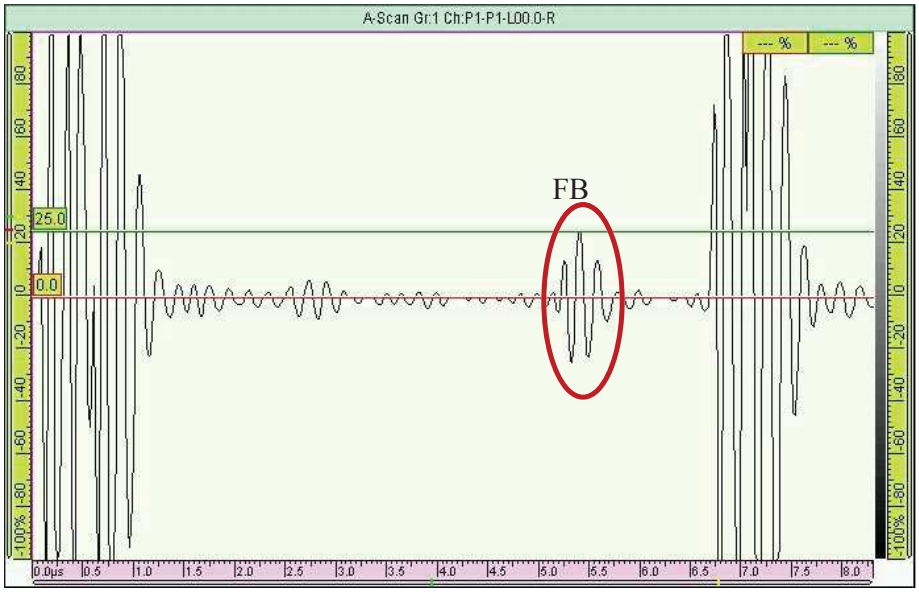

Figure 46: A-scan signal of Ti-6Al-4V block indicating the FBH response.

In the absence of any possibility to validate modeling signal using signals from FBH block, validation is further carried out by considering successive backwall echoes captured on a block without FBH. Hence, the experimental A-scan signals are recorded on a Ti-6Al-4V block with a height of 20 mm and without any FBH/defect containing in it as shown in Figure 47. It has to be noted that the diameter of the block is maintained at 50 mm, i.e., same as the block with FBH. The A-scan signal is recorded for 29 µs such that at least 4 successive back wall echoes are captured. Further, the peak to peak amplitude ratios and time of flight between successive back wall echoes are calculated and compared with that of the A-scan signals obtained from the numerical model.

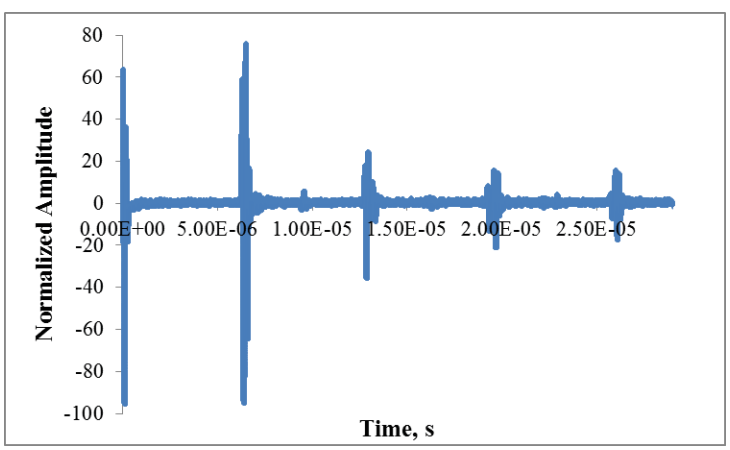

Figure 47: Experimental A-scan signal of contact ultrasonic testing showing 4 back wall echoes

4.3. Development of mathematical model

In the ultrasonic inspection of samples, ultrasonic waves which propagate into the material are originated from a cylindrical transducer. Due to the cylindrical shape of the transducer, spherical waves travel through the medium. In order to replicate this condition numerically, computational cost would be extremely higher. 2-D models simulating the actual wave propagation have been attempted by several researchers [1-4]. However, the accuracy of these models in predicting exact amplitude of the defect is limited [1]. In the case of geometrical domain symmetry (ex: cylindrical, square, rectangle) or in the case of defect symmetry (ex: flat bottom hole, spherical hole) 2-D axisymmetric models can predict the amplitude from defect and reduce the computation cost [3]. As the current study involves a flat bottom hole present in a cylindrical block, a 2-D axisymmetric model of wave propagation is developed for simulations. Transducer is assumed to be a line source in the 2-D axisymmetric model representing the cylindrical shape as in the case of 3-D. Fundamental details about the basis of selecting analytical model of signal, its frequency content, selection of time step, selection of mesh size and the study selected for performing simulation was discussed by Phani et al [5].

For generation of â response (ultrasonic signal response) required for POD analysis, a 2D-axisymmetric model of Ti-6Al-4V cylindrical block is created with dimensions of the block as well as FBH similar to that of used during experimental ultrasonic inspection as shown in Figure 48.

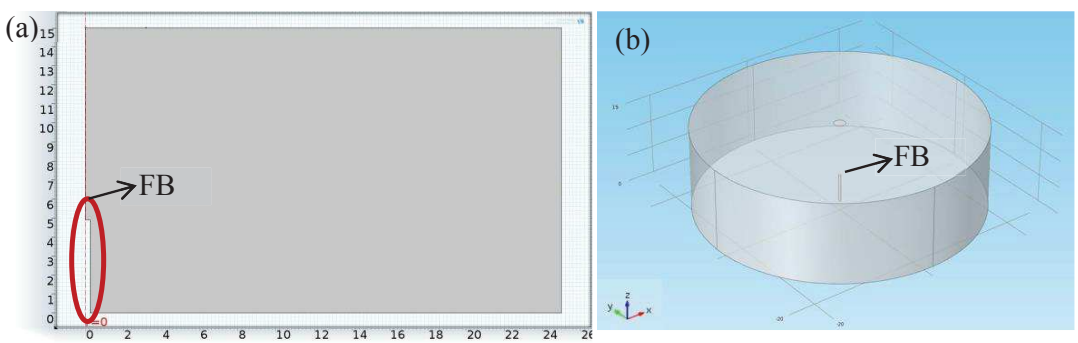

Figure 48: (a) 2-D axisymmetric model of Ti-6Al-4V block with FBH and (b) its representative 3-D model for understanding

As mentioned earlier, FBH represents flat cracks. However, the real cracks obtained in aero-engine discs can be in any orientation with respect to the measuring surface. In the current study, efforts are only made to study FBH representing flat cracks parallel to the surface. FEM modeling and simulation is performed in COMSOL Multiphysics package

ver.4.3a using structural mechanics module [6]. As the 5 MHz transducer probe diameter is 0.25 inch, the line source in the model is also created for a length of 6.35 mm. The model is meshed with an element size of λ/8 (i.e. 0.15 mm), where λ=1.2 mm (velocity of sound in Ti-6Al-4V material is considered as 6000 m/s). Time stepping is calculated at a Courant Friedrich Lewy number (CFL) of 0.15 and is found to be 3.6e-9 s. Further, the FEM model is solved for a total duration of 7 μs with a step size of 20 ns. Frequency content for 5 MHz probe is incorporated with an interpolation function from the 6.35 mm line source. Input signal and its frequency content are as shown in Figure 49(a) and 49(b).

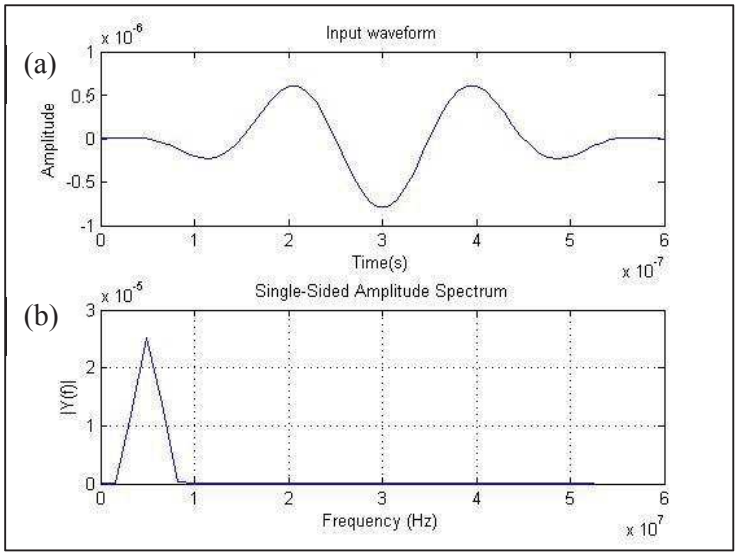

Figure 49: (a) Input waveform signal used for 5MHz (b) Frequency content of input waveform signal

In order to validate the physics based numerical model, as mentioned earlier, the geometry of the Ti-6Al-4V block is created with a diameter of 50 mm and height of 20 mm without any FBH/defect present in it as in the case of experimentally inspected block. All other FEM parameters are maintained similar to that of model with FBH. Further, the developed mathematical model is validated (results discussed in Section 5.2.1) by comparing the peak to peak amplitude ratios and time of flight between successive back wall echoes in A-scan signal obtained from both experimental ultrasonic testing and from mathematical model. Figure 50 shows the A-scan signal with four successive backwall echoes predicted using modeling.

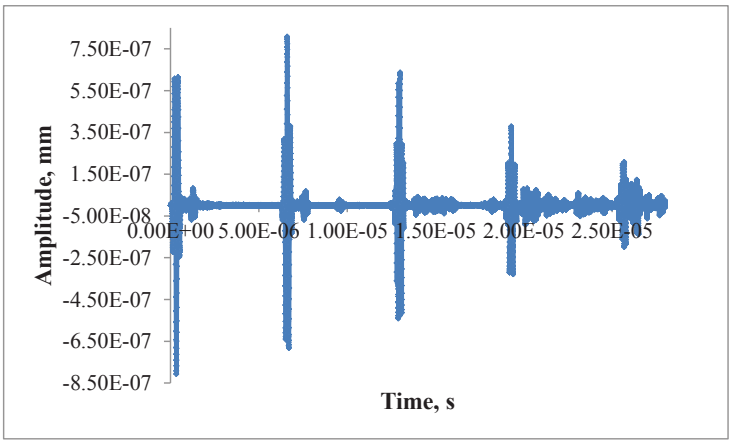

Figure 50: A-scan signal of 2-D axisymmetric model showing 4 back wall echoes.

4.4. Generation of random crack sizes

The developed FEM model after validating (discussed in Section 5.2.1) is used for simulating ultrasonic defect response signals for various crack sizes. Unlike in the case of experimental POD curve generation, distribution of crack sizes has to be assumed for MAPOD and is usually dependent on the distribution of service induced fatigue cracks. As discussed in the literature chapter (Section 2.5), fatigue cracks originating from in-service aero-engine turbine discs follow log-normal distribution [7-12]. Hence, in the current study, all the crack sizes are generated in lognormal distribution and the POD of all these cracks sizes is estimated for ultrasonic testing.

4.4.1. Random crack sizes by lognormal distribution

The probability density function of the lognormal distribution is expressed as shown in Equation 14:

$$f(x|\mu,\sigma) = \frac{1}{\sqrt{(2\pi)\sigma x}} exp^{\frac{-(ln(x)-\mu)^2}{2\sigma^2}} \quad (14)$$

where, μ and σ are location and scale parameters, respectively. As the material selected for ultrasonic inspection with a 5 MHz transducer probe is Ti-6Al-4V, the longitudinal velocity of the ultrasonic wave is approx. 6000 m/s and the corresponding wavelength is λ=velocity/frequency =1.2 mm. Therefore, approximately any cracks above λ/2=0.6 mm would be detectable using this technique. However, every crack either above or below λ/2 possesses a probability to be detected. Hence, in this study MAPOD is performed by considering crack sizes less than 0.6 mm and greater than 0.6 mm. For example, a crack size of less than 0.6 mm should have lesser probability of getting detected compared to a crack

size of greater than 0.6 mm. In order to generate this range of crack sizes following lognormal distribution, lognormal parameters, i.e., location of -0.3, scale of 0.3 and a threshold value of 0 are assumed. Using these parameters, initially, 40 crack sizes (as per the minimum number of required defects mentioned in MIL-HDBK 1823A) in the range of 0.36 mm to 1.37 mm following lognormal distribution are generated. Figure 51 shows the histogram of crack sizes along with lognormal distribution fit.

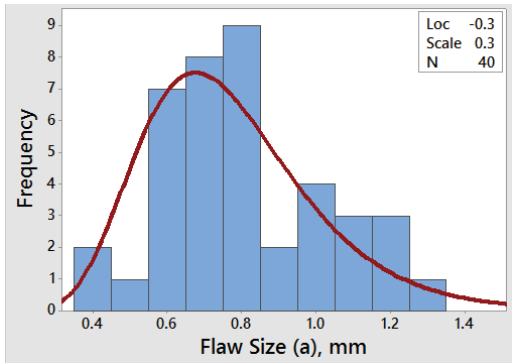

Figure 51: Histogram of 40 crack sizes along with lognormal distribution

4.5. POD from lognormally distributed crack sizes

From the numerically obtained A-scans, automatic defect echo identification has been carried out by applying a Hilbert transform to the signal in Matlab program (Appendix III). The actual FBH sizes are considered as 'a' whereas the ultrasonic signal amplitude from the defect echo is considered as 'â'. Similar to the experimental procedure adopted for generating A-scan signal from a 0.5 mm FBH, the defect echo response in modeling is also set to 25 % full screen height (FSH) and the defect echo amplitudes of the remaining defects have been scaled assuming vertical linearity. Statistical analysis of data for POD curve generation involves in estimation of best linear fit between â vs. a. Subsequently, the best linear fit data is used for regression with censored data. From the censored regression, all the regression parameters are estimated using Maximum Likelihood Estimators (MLE) method. Further, the parameters of the parent distribution are calculated and the corresponding Cumulative Distribution Function (CDF) is plotted resulting in the POD curve. For the POD curve, 95 % lower confidence curve is also plotted so as to estimate the exact reliability of the NDT system by considering the crack size with 90% probability and 95% confidence limit ($a_{90/95}$) value.

References

1. R. Ludwig, W. Lord, A finite-element formulation for the study of ultrasonic NDT systems, IEEE Trans. on Ultrasonics, Ferroelectrics, and Frequency Control, 35 (1988) 809-820. doi:10.1109/58.9338.
2. W. Lord, R. Ludwig, Z. You, Developments in ultrasonic modeling with finite element analysis, J. Nondestructive Evaluation, 9 (1990) 129-143. https://doi.org/10.1007/BF00566389
3. P. Stucky, W. Lord, Finite element modeling of transient ultrasonic waves in linear viscoelastic media, IEEE Trans. on Ultrasonics, Ferroelectrics, and Frequency Control, 48 (2001) 6-16. doi:10.1109/58.895895.
4. Z. You, M. Lusk, R. Ludwig, W. Lord, Numerical simulation of ultrasonic wave propagation in anisotropic and attenuative solid materials, IEEE Trans. on Ultrasonics, Ferroelectrics, and Frequency Control, 38 (1991) 436-445. doi:10.1109/58.84288.
5. Phani Surya Kiran Mylavarapu, S. Boddapati, A Numerical study on particle scattering of ultrasonic waves in syntactic foams-I, in: DRDO-DMRL-NDTG-043, DMRL Technical Report, Hyderabad,India, 2013.
6. Andreea-Manuela Zelenyak, Nora Schorer, Markus G.R. Sause, Modeling of ultrasonic wave propagation in composite laminates with realistic discontinuity representation, Ultrasonics 83 (2018) 103-113. http://dx.doi.org/10.1016/j.ultras.2017.06.014.
7. Phani Mylavarapu, Vamsi Krishna Rentala, M.Sundararaman, Vikas Kumar, H. Gokhale, Sensitivity evaluation of NDT techniques on naturally initiating fatigue cracks-An experimental approach for a POD framework, in: DRDO-DMRL-NDTG-083, DMRL Technical Report, Hyderabad, (2015).
8. Hina Gokhale, Shahnawaz, Raghu, V. Kumar, Probabilistic fatigue life assessment of gun barrels, in: DRDO-DMRL-034, DMRL Technical Report (2012).
9. D.A. Virkler, B.M. Hillberry, P.K. Goel, The Statistical Nature of Fatigue Crack Propagation, J. Engineering Mater. Technol. 101 (1979) 148-153. doi:10.1115/1.3443666.
10. Y. Liu, S. Mahadevan, Probabilistic fatigue life prediction using an equivalent initial flaw size distribution, Int. J. Fatigue 31 (2009) 476-487. https://doi.org/10.1016/j.ijfatigue.2008.06.005
11. Makeev, Y. Nikishkov, E. Armanios, A concept for quantifying equivalent initial flaw size distribution in fracture mechanics based life prediction models, Int. J. Fatigue 29 (2007) 141-145. https://doi.org/10.1016/j.ijfatigue.2006.01.018

12. J.N. Yang, G.C. Salivar, C.G. Annis, Statistical modeling of fatigue-crack growth in a nickel-base superalloy, Engineering Fracture Mechanics 18 (1983) 257-270. https://doi.org/10.1016/0013-7944(83)90137-6.

5. RESULTS AND DISCUSSION

This chapter discusses the results obtained on NDT reliability studies using both experimental and model assisted methods in the current research work. Results are classified into four different parts. Part I discusses NDT response data generation using experimental POD work, Part II discusses the NDT response data generation using model based POD procedures, Part III discusses statistical analysis of â vs. a and HIT/MISS NDT data for plotting POD curves and Part IV discusses damage tolerance remnant fatigue life calculations using deterministic fracture mechanics approaches.

5.1. Part I - NDT response data generation using experimental POD work

Details of fatigue crack sizes generated under both room temperature and high temperature fatigue testing conditions, scanning electron microscopy observations of fatigue cracks and the NDT response data obtained from the inspection of these cracks are discussed under this section.

5.1.1. Details of surface fatigue crack sizes generated

5.1.1.1. Room temperature cracks

Surface fatigue crack length measurements

As discussed in Section 3.2, 21 samples are subjected to room temperature fatigue testing at optimized loading conditions (obtained from Vamsi et al.[1]) required for inducing stresses corresponding to 80% of the material yield strength. Amongst these samples, 4 samples are found to not contain any fatigue cracks on either of the sides. In the remaining samples, 4 samples contain cracks initiated in only one side i.e., either side1 or side 2. Multiple cracks are found to be initiated in 13 samples. This kind of variation in the generation of fatigue cracks for the same loading conditions can be attributed to the random or statistical nature of fatigue. As cracks are not expected to be observed under service conditions at every bolt hole location, experimental conditions considered in this study, which resulted in randomized nature of fatigue cracks can be considered as representative true engine conditions. In total 52 fatigue cracks are identified from the 17 samples. These fatigue cracks are statistically processed using Minitab statistical software Ver. 17 for identifying the size distribution. Figure 52 shows the goodness of fit [2] test results along with histogram of log-normally distributed fatigue cracks. From Figure 52, it can be observed that the crack sizes are log-normally distributed as the P- value is found to be higher and the

corresponding Anderson-Darling (AD) statistic value is lower compared to all other distributions [2]. As discussed earlier, the distribution of fatigue cracks are similar to the log-normal distribution of fatigue cracks originating from in-service aero-engine turbine discs [3, 4]. The range of surface crack lengths obtained is from 0.06 mm to 1.66 mm.

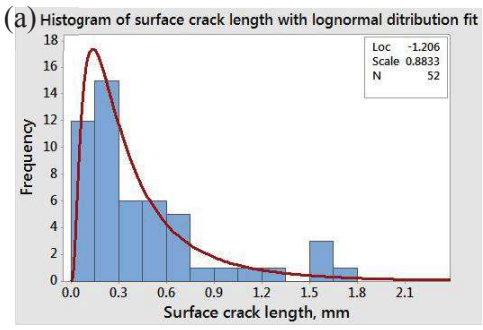

(b)

Goodness of Fit Test

Distribution	AD	P	LRT P
Normal	1.063	0.006	
Lognormal	0.136	0.971	
3-Parameter Lognormal	0.144	*	0.648
Exponential	0.602	0.349	
2-Parameter Exponential	0.206	>0.250	0.042
Weibull	0.341	>0.250	
3-Parameter Weibull	0.235	>0.500	0.204
Smallest Extreme Value	1.567	<0.010	
Largest Extreme Value	0.563	0.143	
Gamma	0.304	>0.250	
3-Parameter Gamma	0.287	*	0.633
Logistic	0.847	0.015	
Loglogistic	0.154	>0.250	
3-Parameter Loglogistic	0.155	*	0.458

Figure 52: Histogram of room temperature fatigue crack lengths generated (a) lognormal distribution fit (b) results of goodness of fit test

Fatigue crack width measurements

Crack width at a notch location in cases where multiple fatigue cracks are present is only measured for the crack possessing largest surface crack length. Further, as discussed in the experimental procedure (Section 3.4), the crack width dimensions are calculated as an average value of crack widths measured at the crack origin, the middle of the crack length and the crack tip location. Table 2 shows the crack width measurements of surface fatigue cracks obtained in all the room temperature tested samples. In Table 2, side 2 of samples 10 and 13 are indicated with an asterisk '*' mark. This denotes existence of multiple cracks at that location and the maximum crack length among the multiple cracks is less than 0.07 mm. Hence, due to the severe tightness of cracks, the crack widths at those locations could not be measured. From Table 2, it can be observed that the average crack width dimensions obtained range from 0.20 µm to 3.17 µm.

Table 2: Details of surface fatigue crack width dimensions obtained in room temperature tested samples.

Sample ID	Side 1				Side 2			
	Crack width, µm				Crack width, µm			
	Origin	Middle	Tip	Average	Origin	Middle	Tip	Average
Sample 2	2.13	0.89	0.28	**1.10**	2.52	1.91	0.52	**1.65**
Sample 3	No crack				0.82	0.63	0.59	**0.68**
Sample 4	No crack				0.92	0.74	0.62	**0.76**
Sample 5	2.71	0.91	0.34	**1.32**	1.02	0.63	0.33	**0.66**
Sample 6	3.91	2.23	1.81	**2.65**	5.81	3.35	0.35	**3.17**
Sample 7	3.13	1.54	0.70	**1.79**	No crack			
Sample 8	2.43	1.02	0.69	**1.38**	1.15	0.75	0.41	**0.77**
Sample 9	0.90	0.49	0.53	**0.64**	0.75	0.58	0.20	**0.51**
Sample 10	0.69	0.50	0.22	**0.47**	*			
Sample 12	0.53	0.29	-	**0.41**	0.95	0.39	0.25	**0.53**
Sample 13	0.44	-	-	**0.44**	*			
Sample 14	No crack				2.23	1.71	1.13	**1.69**
Sample 15	0.95	0.63	0.46	**0.68**	3.54	2.43	0.87	**2.28**
Sample 17	0.65	0.40	0.33	**0.46**	1.03	0.89	0.84	**0.92**
Sample 18	0.99	0.54	0.12	**0.55**	1.75	0.99	0.23	**0.99**
Sample 19	1.14	0.98	0.85	**0.99**	2.74	1.31	0.90	**1.65**
Sample 21	0.20	-	-	**0.20**	1.95	0.98	0.46	**1.13**

* Cracks of sizes < 0.07 mm are available at these locations. However, due to the tightness of cracks, it is not possible to measure crack widths.

5.1.1.2. High temperature cracks

Surface fatigue crack length measurements

High temperature fatigue cracks are initiated by subjecting samples to varying fatigue cycles from 2000 to 2500. Exact number of cycles required for each sample is identified by periodic monitoring of initiation of crack for every 100 cycles until a crack is observed using optical microscope. However, due to the statistical nature of the fatigue phenomenon, in two samples because of their early fracture, controlled crack initiation during high temperature fatigue testing in Gleeble® system could not be achieved. Also, because of the same reason, fatigue cracks of different sizes are generated in the remaining samples. In total, 69 cracks are identified from these 10 samples with surface crack lengths ranging from 0.01 mm to 1.16 mm. Figure 53 shows the goodness of fit [2] test results along with histogram of log-normally distributed fatigue cracks. From Figure 53, it can be observed that the crack sizes also follow log-normal distribution similar to the room temperature cracks.

(a)

Goodness of Fit Test

Distribution	AD	P	LRT P
Normal	6.167	<0.005	
Lognormal	0.280	0.633	
3-Parameter Lognormal	0.256	*	0.642
Exponential	1.492	0.031	
2-Parameter Exponential	1.048	0.087	0.026
Weibull	1.244	<0.010	
3-Parameter Weibull	1.005	0.014	0.053
Smallest Extreme Value	11.026	<0.010	
Largest Extreme Value	2.322	<0.010	
Gamma	1.095	0.009	
3-Parameter Gamma	0.986	*	0.209
Logistic	3.714	<0.005	
Loglogistic	0.160	>0.250	
3-Parameter Loglogistic	0.163	*	0.785

(b)

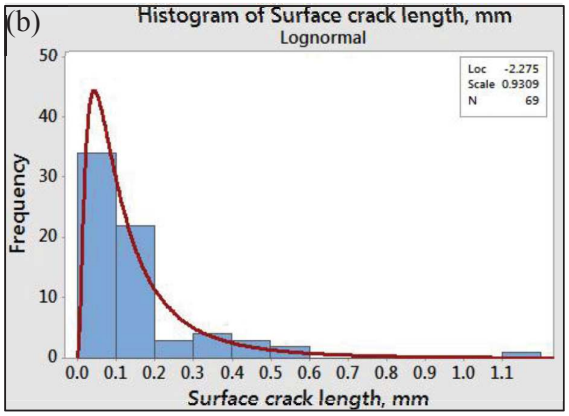

Figure 53: (a) Goodness of fit test result highlighting lognormal distribution (b) Histogram of surface fatigue crack length sizes with lognormal distribution fit

Fatigue crack width measurements

Table 3 shows the crack width measurements of surface fatigue cracks obtained in all the high temperature tested samples. From Table 3, it can be observed that the average crack width dimensions range from 0.35 µm to 3.38 µm.

Table 3: Details of surface fatigue crack width dimensions obtained in high temperature tested samples.

Sample ID	**Side 1**				**Side 2**			
	Crack width, µm				**Crack width, µm**			
	Origin	**Middle**	**Tip**	**Average**	**Origin**	**Middle**	**Tip**	**Average**
Sample 1	0.66	0.59	0.42	**0.56**	0.40	0.38	0.26	**0.35**
Sample 2	6.21	3.15	0.78	**3.38**	5.45	2.96	0.84	**3.09**
Sample 3	0.71	0.52	0.39	**0.54**	1.89	1.35	0.22	**1.15**
Sample 5	2.21	1.73	0.98	**1.64**	2.01	0.93	0.44	**1.13**
Sample 6	*				1.38	1.15	0.95	**1.16**
Sample 9	5.14	1.93	0.71	**2.59**	3.73	1.68	0.87	**2.09**
Sample 10	*				2.84	0.69	0.53	**1.36**
Sample 11	1.07	0.71	0.40	**0.73**	0.91	0.52	0.39	**0.60**
Sample 12	2.43	2.01	1.38	**1.94**	4.95	2.11	0.92	**2.66**
Sample 13	*				6.49	2.07	0.81	**3.12**
Sample tested in vacuum	No crack				0.72	0.48	-	**0.60**

* Cracks of sizes < 0.07 mm are available at these locations. However, due to the tightness of cracks, it is not possible to measure crack widths.

5.1.2. Observations from SEM micrographs

5.1.2.1. Room temperature cracks

Figure 54(a) shows the optical micrograph of room temperature fatigue cracks in one of the tested samples. From Figure 54(a), it can be observed that the fatigue cracks have initiated only from the circular notch (representing bolt hole) location of the sample. However, the location of initiation of cracks varied from sample to sample within the semi-circular notch. As 3-point bending setup is used as the loading fixture, maximum bending stress is localized at the center of the sample span i.e., at the center of the notch in the sample. Therefore, most of the cracks observed in this study are found to initiate closer to the center of the notch tip. However, crack branching phenomenon is also observed in the samples. Due to the presence of hard carbide/precipitate particles present in the nickel based superalloy materials [5, 6], cracks in samples are tortuous in nature (as shown in Figure 55). Figure 54(b) shows the EBSD grain boundary map indicating the location of cracks, grain boundaries and Σ3 twin boundaries. From Figure 54(b), it can be observed that the fatigue cracks in the sample are purely trans-granular in nature. Similar morphological behaviour of narrow fatigue cracks with crack branching in purely trans-granular fashion was reported in literature [7-9]. These fatigue cracks are also similar to the actual in-service fatigue cracks originating in engines [8, 9] and hence can be readily used for POD studies.

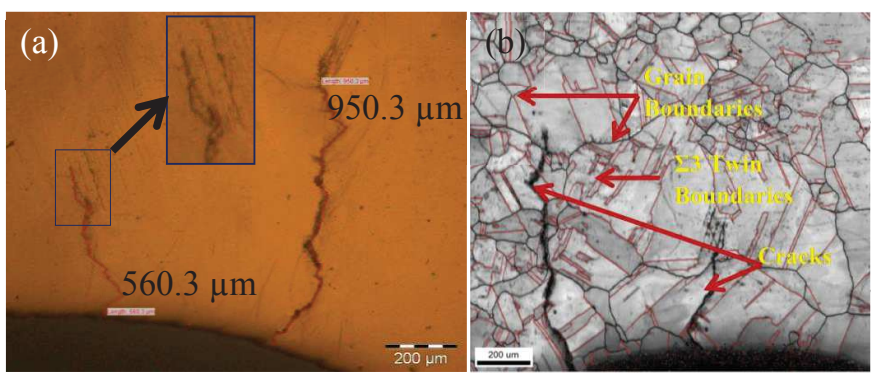

Figure 54: (a) Micrographs of one of the room temperature tested samples with crack lengths indicated (0.95 mm and 0.56 mm) (b) its EBSD grain boundary map

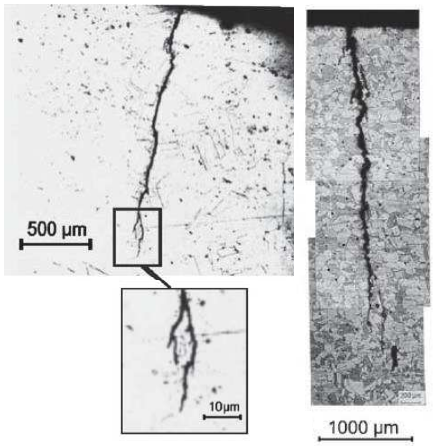

Figure 55: Service induced fatigue cracks [5, 6]

5.1.2.2. High temperature cracks

Figure 56(a) shows a typical micrograph of one of the fatigue cracked samples showing crack initiation at the notch. Similar cracks initiating from the notch are observed in all the test specimens. From Figure 56(a), it can be observed that two cracks (shown in Figure inset 56(b)) are initiated from the notch location due to the stress concentration at the circular notch. However, the two cracks initiated are much closer towards the middle of the circular notch. It can also be noted that the spatial distance between the two fatigue cracks is approximately 50 µm only. As mentioned earlier, the ECT probe diameter is 0.5 mm, which is far higher than the spatial distance between multiple cracks at a notch location, and hence, the ECT response at a notch location is considered as a response from cumulative sum of all cracks at that notch location. In addition, it can also be observed that the crack surfaces are fully oxidized (shown in Figure insets 56(c) and (d)) due to the high temperature fatigue cycling in air environment. This results in the filling of crack widths with oxides as shown in Figure 56 (c) & (d).

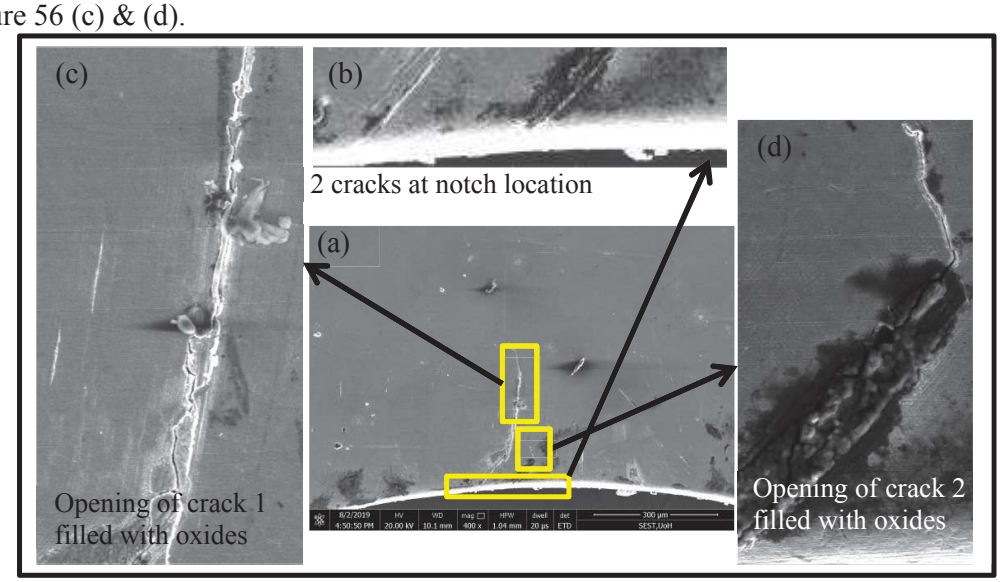

Figure 56: High temperature multiple fatigue cracks at (a) single notch location (b) crack 1 filled with oxides (c) crack 2 filled with oxides and (d) two cracks at notch location in zoomed view

In general, the material surface away from notch location would not crack during fatigue loading. In the current study, the cracking of material surface is observed (Figure 57). Due to the brittle nature of oxides, cracking of oxide layer takes place which eventually leads to the cracking of material surface [10-12]. Hence, it can be understood that these cracks on material surface are formed due to the oxidation of material surface. Figure 57 shows the micrograph of the specimen surface showing the material surface cracking due to oxidation (in Figure inset 57(b)) and crack branching along with slip band oxidation (in Figure inset 57(c)). From the insets of Figure 57, it can be observed that the crack shows certain in-service engine fatigue crack features such as crack branching [9, 13]. In addition, it can also be observed that the slip bands around the fatigue cracks as well as few selected locations of the material surface are oxidized. Moreover, the oxide induced cracking at slip bands (Figure 57(c)) is predominantly observed around the notch locations. These cracks on the material surface are due to the formation and cracking of oxides (which are brittle in nature) during loading. This oxide cracking results in the cracking of material surface during loading, leading to crack initiation and propagation.

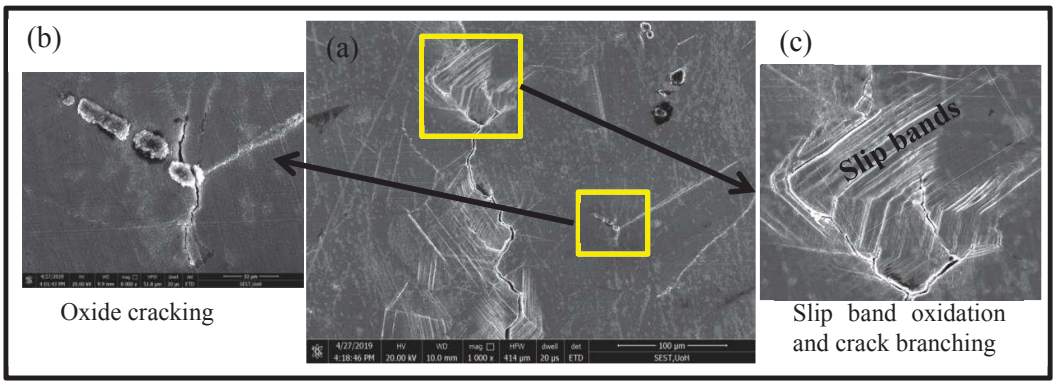

Figure 57: Oxidized fatigue crack micrograph showing cracking of material surface due to oxidation and crack branching along with slip band oxidation in figure insets.

EDAX analysis is also carried out to identify the presence of oxides in the crack surfaces. Figure 58 shows the results of the EDS analysis at both the crack surface and the slip bands. From Figure 58, it can be observed that both the crack surface and slip bands show the predominant presence of oxygen peaks indicating the formation of oxides during the high temperature fatigue loading.

In addition to the oxidation of the cracks and the slip bands, general oxidation of the specimen is also observed. Figure 59 shows the EDS results from the material surface after high temperature fatigue testing. From Figure 59, it can be observed that the material surface

also shows presence of oxygen. This phenomenon of oxidation of nickel based superalloys at higher temperatures is similar to that of observed in literature [14]. Considering (a) log-normally distributed crack sizes (b) narrow, tortuous and multiple fatigue cracks at a location and (c) formation of oxides in the fatigue crack surfaces, observed from this study, it can be concluded that the Gleeble® based novel methodology adopted for fatigue crack generation produces fatigue cracks similar to that of expected from in-service conditions [8, 9].

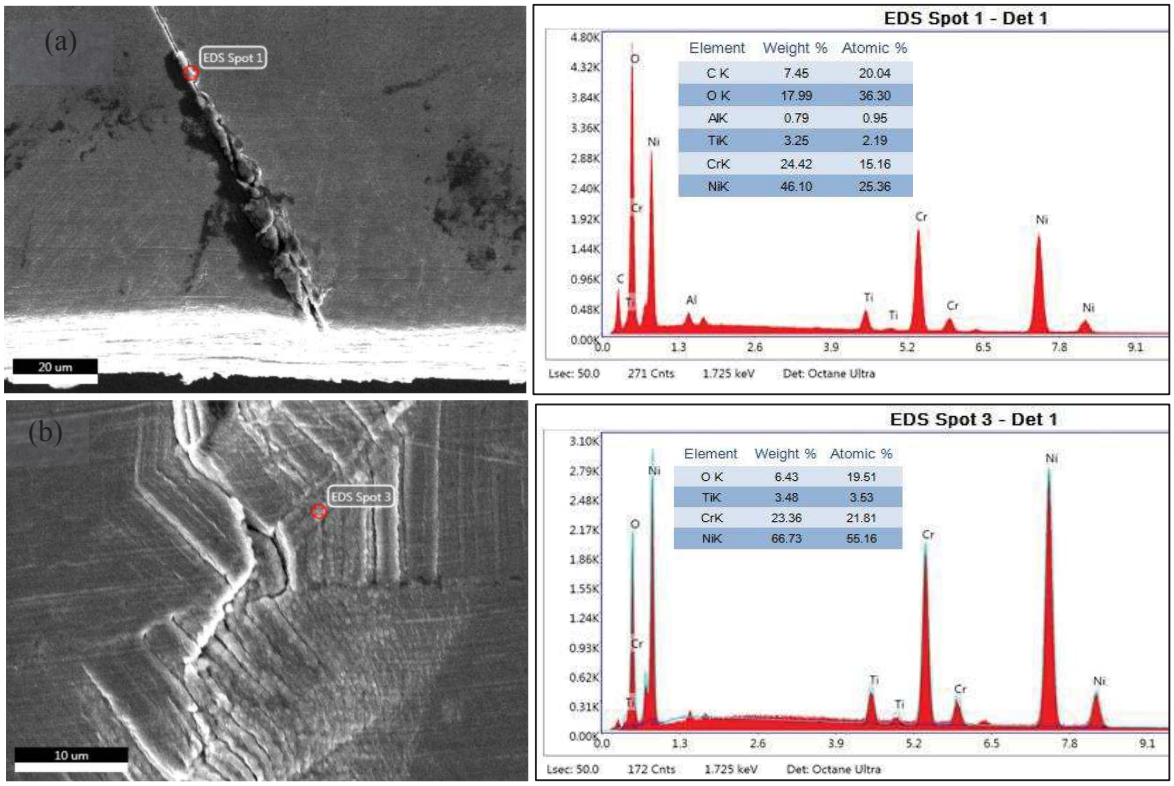

Figure 58: EDS results confirming the presence of oxides in (a) Crack surface oxidation (b) Slip band oxidation

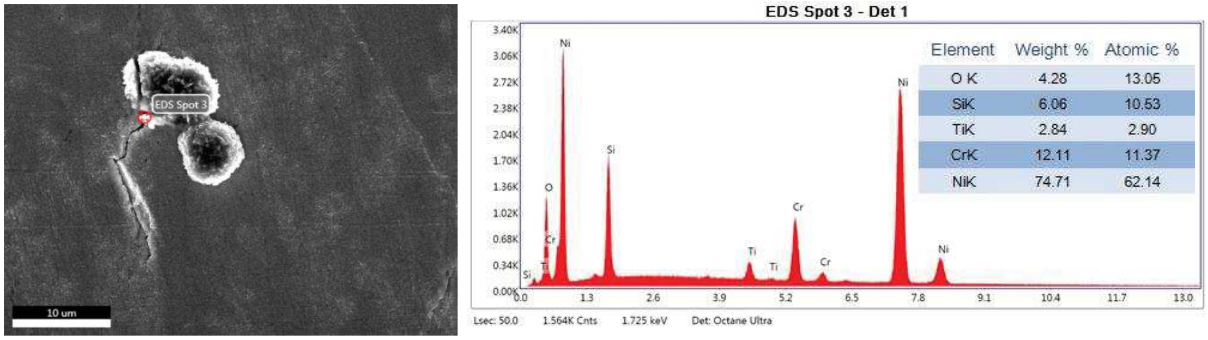

Figure 59: EDAX analysis results of material surface oxidation and oxide induced cracking confirms the presence of oxides

SEM and EDAX of fracture surface

Presence of oxides in the crack surface is further studied by performing SEM and EDAX analysis on the fracture surface of two samples fractured during the testing. As mentioned earlier, these samples fractured due to the statistical nature of the fatigue in spite of optimized loading conditions (so as to not fracture) adopted in the study. Figure 60(a) shows the fracture sample indicating notch region and fractograph of the crack surface from the fractured sample (shown in Figure inset 60(b)). Figure 60(b) also indicates the direction of crack propagation. Figure 60(c) shows the fracture surface consisting of bright and dark regions. In general, the dark region corresponds to crack propagation and bright regions correspond to overload fracture locations during room temperature fatigue testing. However, from the fractograph of the fracture surface, it can be observed that the bright region corresponds to crack propagation and the dark region corresponds to overload fracture location. In order to understand the disparity in bright and dark regions between room temperature and high temperature tested samples, EDS analysis is performed.

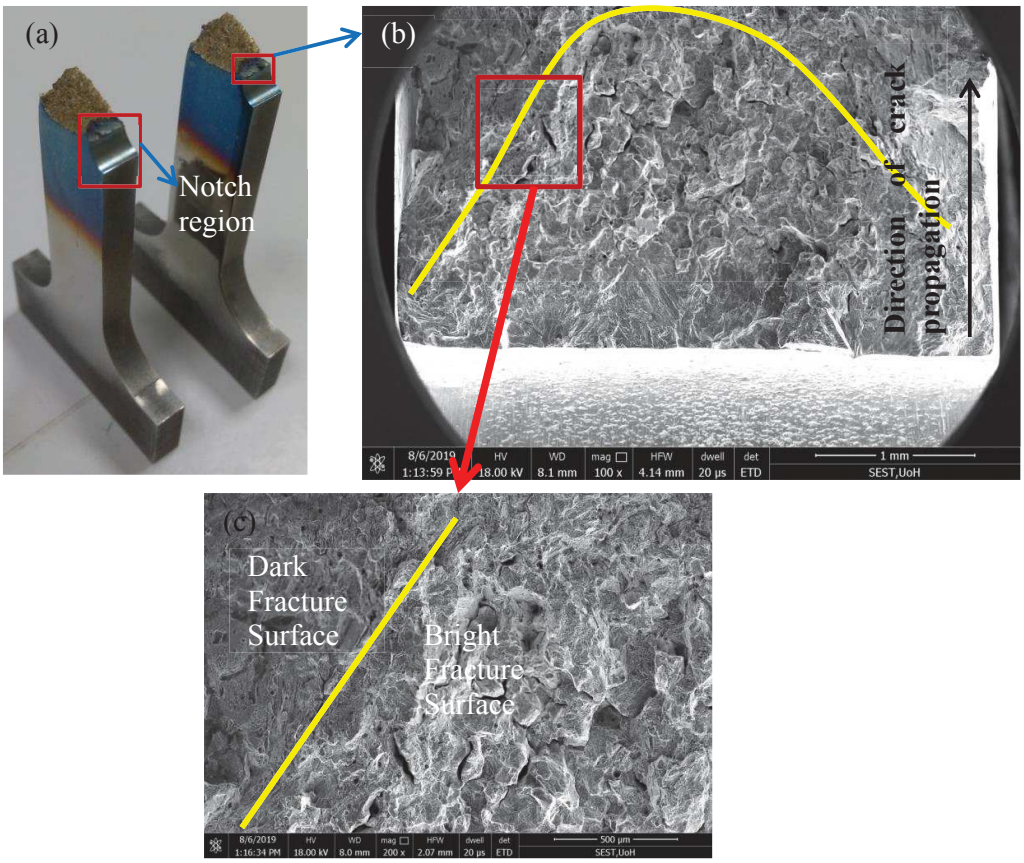

Figure 60: (a) Fractured samples indicating notch region (b) fractograph of the crack surface from the fracture samples indicating direction of crack propagation (c) zoomed view of fracture surface indicating bright and dark regions

Figures 61(a) and (b) show the results of EDAX analysis on the bright and dark regions of the fracture surface along with the corresponding energy spectrum for the fractograph shown in Figure 60. From Figures 61(a) and (b), it can be observed that the EDAX analysis of the bright region on the fracture surface results in the presence of oxides whereas, the dark region does not show presence of oxides. Hence, it can be clearly understood that the crack surfaces correspond to fatigue crack region have been oxidized during high temperature fatigue cycling. During fatigue crack initiation and propagation, the fresh or newly formed crack surface is exposed to the oxidizing atmosphere and hence, the crack surface oxidizes and appears as bright. However, as the crack approaches critical crack size, the sample with reduced cross section thickness can no longer support the load, resulting in sudden fracture and hence, relatively appears as dark in comparison to the oxidized region.

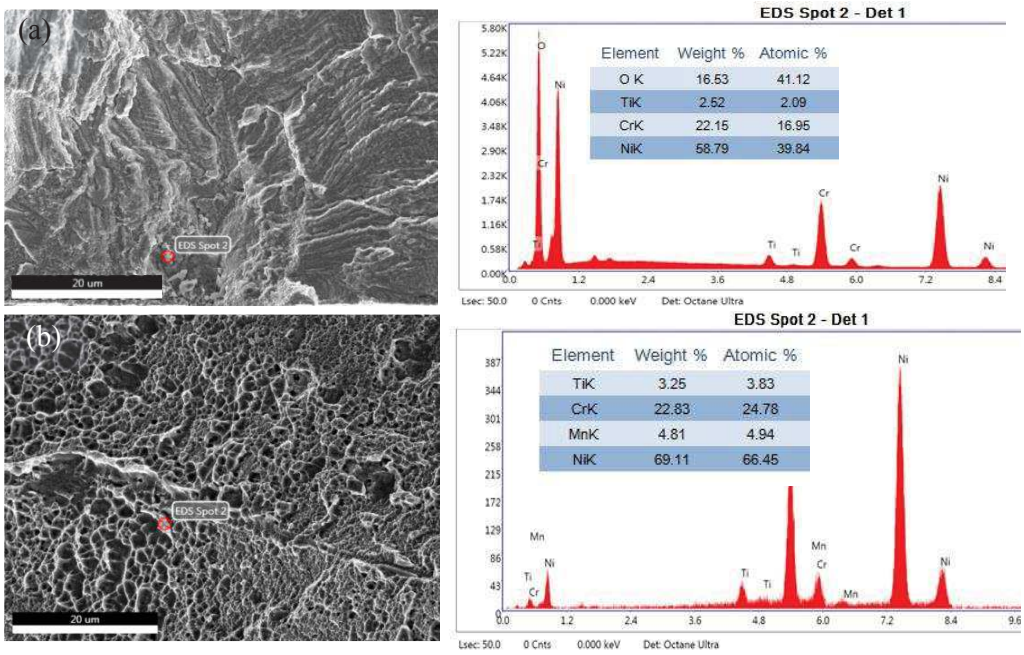

Figure 61: SEM micrograph and EDAX spectrum of (a) bright region and (b) dark region of the fracture surface

In order to compare and understand the effect of oxidation on crack lengths and widths, sample is also tested under vacuum condition.

Specimen tested under vacuum environment

Figure 62 gives the micrograph of the surface of the specimen showing the fatigue crack in the sample tested in vacuum. From Figure 62, it can be observed that two fatigue cracks with 0.30 mm and 0.12 mm surface crack length, respectively are present at the notch location. In addition, the total number of fatigue cycles required for initiating fatigue cracks

in vacuum is 3500 cycles which is 75% higher than that for air tested samples (~2000). This enhancement in the number of fatigue cycles for crack initiation is attributed to significant reduction in oxidation under vacuum which is known to aid material damage during fatigue [14, 15]. Figure 63 shows the EDS results carried out on the fatigue crack in the sample tested in vacuum. From Figure 63, it can be observed that crack surface or material surface does not show oxidation. Due to the absence of oxidation, the number of fatigue cycles for initiation and propagation of cracks is found to be higher in vacuum tested sample when compared with those of air tested samples. During the high temperature testing in air environment, oxidation drives the initiation and propagation of cracks resulting in lower number of fatigue cycles. Even though the sample is tested for higher number of fatigue cycles under vacuum, crack lengths observed are found to be lower in length (0.3 mm and 0.12 mm) when compared to the air tested samples. For example, compared to the overall crack length of the largest crack,(1.16 mm) in one of the air tested samples, the crack length in the vacuum tested sample is found to be lower (0.3 mm). It is mentioned that the comparative trends between high temperature fatigue cycled samples in air and vacuum environment cannot be associated with statistical significance due to disparity in the number of vacuum samples. Moreover, the crack width of the 0.3 mm surface fatigue crack in vacuum tested sample is found to be 0.60 μm only.

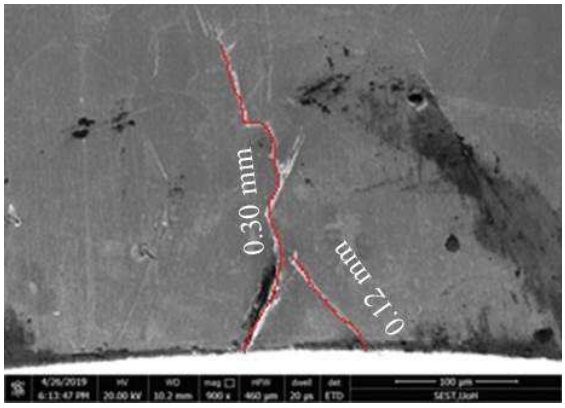

Figure 62: Micrograph of Fatigue crack in a sample tested under vacuum at 650°C

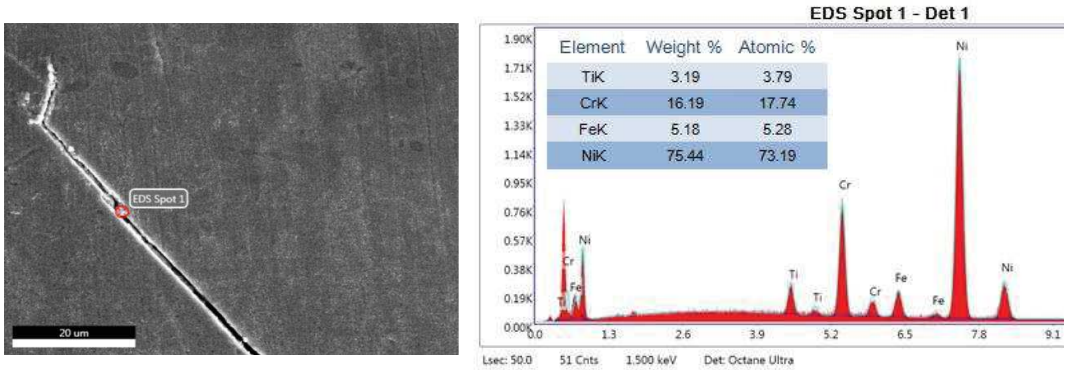

Figure 63: EDS analysis of fatigue crack generated in vacuum tested sample

5.1.3. NDT inspection of fatigue cracks

5.1.3.1 FLPT

5.1.3.1.1 Room temperature cracks

Table 4 shows the HIT/MISS defect indications obtained from inspection using FLPT technique. In Table 4, the HIT (defect detected) indications are represented with "H" whereas the MISS (defect undetected) indications are represented with "M". From Table 4, it can be observed that the total numbers of fatigue cracks detected are 13. In addition, the minimum crack size detected and the largest crack size missed by FLPT are 0.48 mm and 0.61 mm, respectively. This can be unrealistic in nature as the crack sizes larger than the minimum detectable crack size are found to be missed. Disparity in detectability of missing fatigue cracks can be attributed to their narrow widths (of less than 1μm) inspite of longer cracks [16]. Further, the HIT/MISS POD data obtained using FLPT is processed using log-odds distribution function for plotting the POD curves and hence the $a_{90/95}$ value.

Table 4: Crack Dimensions along with FLPT HIT/MISS indications.

ID	Side 1		FLPT	Side 2		FLPT
	L, mm	W, μm		L, mm	W, μm	
S2	0.61	1.1	H	1.59	1.65	H
S3	No Crack		-	0.31	0.68	M
S4	No Crack		-	0.24	0.76	M
S5	0.75	1.32	H	0.13	0.66	M

S6	0.65	2.65	H	1.66	3.17	H
S7	1.57	1.79	H	No Crack		-
S8	0.48	1.38	H	0.14	0.77	M
S9	0.31	0.64	M	0.17	0.51	M
S10	0.46	0.47	M	0.09	-	M
S12	0.43	0.41	M	0.61	0.53	M
S13	0.12	0.44	M	0.35	-	M
S14	No Crack		-	1.2	1.69	H
S15	0.26	0.68	M	0.57	2.28	H
S17	0.39	0.46	M	0.26	0.92	M
S18	0.48	0.55	M	0.61	0.99	H
S19	1.15	0.99	H	1.61	1.65	H
S21	0.53	0.2	M	1.04	1.13	H

Details on number of flaws at a site for applying different HIT/MISS POD approaches

As there are multiple cracks at a notch on many of the samples, the FLPT inspection data on room temperature samples is further processed with maximum flaw size approach and sum of flaw size approaches. This data is segregated according to the number of inspection sites, the number of flaws at a site and the corresponding flaw sizes along with FLPT inspection data. This data consists of 40 inspection sites and with a total of 52 fatigue cracks. The sizes of these fatigue cracks ranges from 0.1 mm to 1.66 mm. Out of the 40 inspection sites, 17 of them contain multiple fatigue cracks. For easy understanding, few of the segregated data is shown in Table 5. From Table 5, it can be observed that the maximum number of multiple fatigue cracks at a site is found to be 4 for site number 27. In addition, Table 5 also provides the FLPT inspection data in the form of H and M corresponding to HIT and MISS, respectively. As discussed in the experimental procedure (Section 3.6.1.1), the

FLPT HIT/MISS indications are segregated according to the three approaches and corresponding HIT and MISS indications are assigned for each individual flaw at a site.

Table 5: Details of inspection site number, number of flaws at a site and the corresponding flaw sizes along with FLPT indications.

Site No.	Number of flaws at a site	Flaw Sizes, mm	FLPT
1	3	0.09, 0.61, 0.61	H
2	1	1.59	H
3	1	0.68	M
5	1	0.75	M
7	2	0.65, 0.19	M
16	3	0.43, 0.11, 0.09	M
23	3	0.12, 0.39, 0.09	M
27	4	0.22, 0.19, 0.22, 1.15	H
30	2	0.47, 1.04	H
35	2	0.38, 0.30	M
40	1	1.78	H

5.1.3.1.2. High temperature cracks

Figure 64 shows the results observed from FLPT. From Figure 64, it can be observed that no crack is detected. Even though the crack lengths range from 0.01 mm to 1.16 mm and the crack widths range from 0.35 μm to 3.38 μm, none of the 69 cracks (among the 10 samples) are detected using FLPT. As discussed in the FLPT inspection of room temperature cracks, FLPT can detect fatigue cracks with average widths greater than 1 μm [16]. However, in the current study, fatigue cracks even with average widths greater than 1 μm (i.e., crack widths up to 3.38 μm) are not detected. Unlike the fatigue cracks generated under room temperature conditions, fatigue cracks generated at high temperature conditions in air environment are fully oxidized. Therefore, the crack openings are filled with oxides and thus restricting the capillary action of the penetrant to penetrate in to the defect, resulting in missing the detection of cracks. In general, FLPT occupies a predominant role in aero-industry for inspecting large number of turbine discs and blades. Absence of defect indications on oxidized fatigue cracks in those components using FLPT technique is misleading and could lead to catastrophic situations if the results are taken at their face value.

The FLPT of vacuum tested sample also could not detect the cracks (non-oxidized cracks) as the FLPT is not sensitive in detecting cracks with widths or openings below ~1 μm (i.e., width of fatigue crack in vacuum sample is 0.60 μm).

Figure 64: FLPT results captured under UV light in dark room

5.1.3.2. ECT inspection

5.1.3.2.1. ECT inspection of EDM notches

As discussed in the experimental procedure, EDM notches of different depths have been used for calibration of ECT before carrying out the actual inspection of fatigue cracks. Figures 65(a) and (b) show the ECT set up used for inspection of the calibration sample with EDM notches and its impedance plane response, respectively. Figure 66 shows the plot between the ECT signal amplitude and the EDM notch depth. From Figure 66, it can be observed that the ECT signal amplitude linearly increases with an increase in the EDM notch depth. Figure 66 also shows the data with linear regression fit equation as shown in Equation 15 and the correlation coefficient (adj.R^2) value of 97%. Using the parameters fixed for the calibration sample, the actual fatigue cracks generated in the current study are inspected.

$$\text{ECT amplitude} = 0.5201 + 12.07*(\text{EDM notch depth}) \quad (15)$$

Either in the fatigue cracks generated under room temperature or high temperature fatigue testing conditions, samples are not sectioned for measuring the depth of the fatigue cracks generated. Therefore, Equation 15 is used further to estimate equivalent crack depths in both room temperature fatigue cracks and high temperature fatigue cracks. The rationale in using Equation 15 for estimating equivalent crack depth will be discussed in Section

5.1.3.2.2. ECT signal amplitude obtained for room temperature and high temperature fatigue cracks is used to obtain equivalent crack depth from Equation 15.

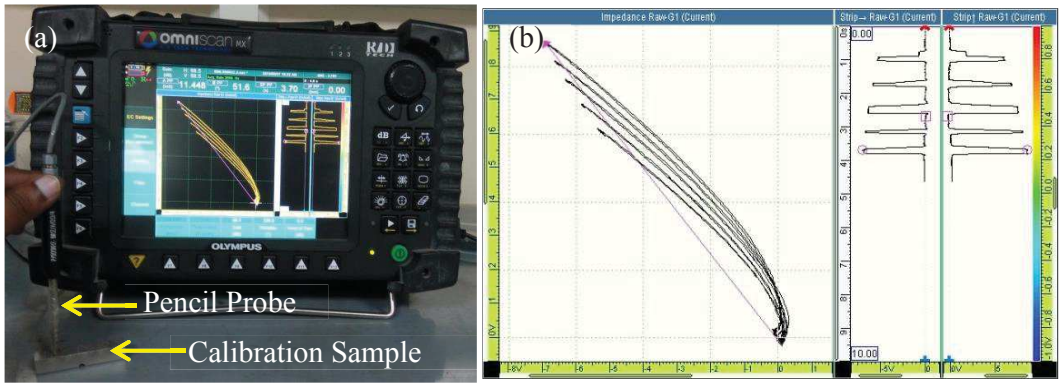

Figure 65: (a) ECT setup for inspection of calibration sample (b) Impedance plane of the EDM notches in calibration sample.

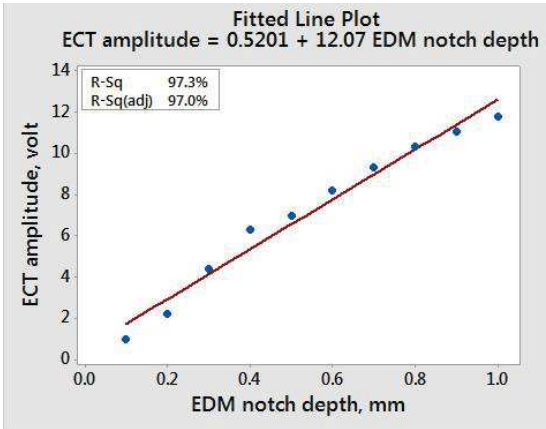

Figure 66: Linear regression of ECT amplitude data vs. EDM notch depth sizes

5.1.3.2.2. ECT Inspection of high temperature fatigue cracks

After calibrating the ECT inspection procedure using EDM notches, the high temperature fatigue cracks or oxidized fatigue cracks have been inspected using ECT. Figures 67(a) and (b) show the ECT impedance plane containing the eddy current signal obtained from inspection of EDM notch of size 1 mm and high temperature oxidized fatigue crack also with size of 1mm. From Figure 67, it can be observed that the ECT signal amplitude is higher for EDM notch than for an oxidized fatigue crack. In addition, it can also be observed that the ECT signal from high temperature crack is not as intense as the signal obtained from the EDM notch. This is attributed to the higher signal amplitude from EDM notch (larger crack volume due to the wider gap between the faces) compared to that of oxide cracks [17]. Even though multiple cracks are found at each of the notch locations in all the samples, considering

the contribution of all these crack indications at a particular site on the ECT signature, the crack length at a site is considered to be the sum of the lengths of all the cracks at that site. Burke [18] has demonstrated the applicability of swept frequency based methods for estimating crack depths using ECT. However, due to the lack of custom made air-cored coils for knowing precise coil geometry of the probe along with eddy current mathematical models for predicting the electromagnetic-flaw interactions, procedure adopted by Burke is not adopted in the current study. In addition, these swept frequency based methods are only good enough for estimating larger crack depths i.e., > 2 mm and has a tendency of underestimating crack depths below 2 mm [18]. Hence, equivalent crack depths are deduced from the ECT signal amplitude recorded at a particular inspection site by using the regression equation shown in Equation 15.

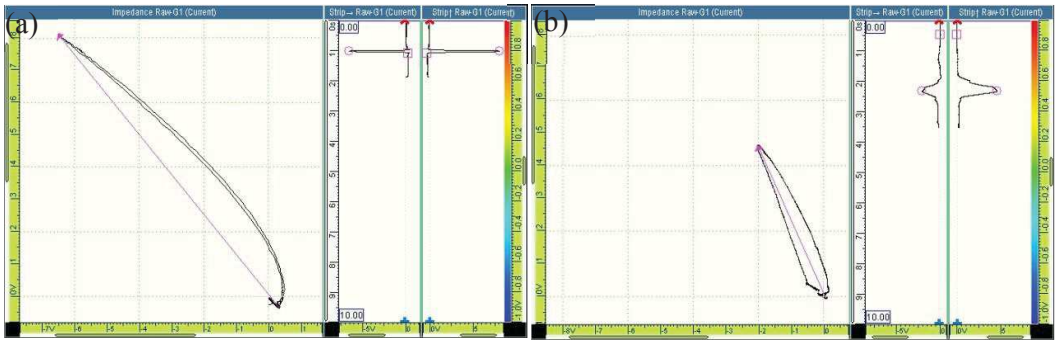

Figure 67: ECT impedance map 1 mm size defect (a) EDM notch (b) oxidized fatigue crack

Table 6 show the ECT HIT/MISS and signal response data of all the samples along with the average crack width, cumulative surface crack length and equivalent crack depth at each side of all high temperature tested samples. During the inspection of the samples, if any crack indication is observed in the ECT impedance plane, then it is considered as a HIT (defect detected) and the corresponding amplitude from the inspection site or notch location is noted. Otherwise, the response from the notch location is recorded as a MISS indication as shown in Table 6. In Table 6, 'H' indicates a HIT (defect detected) and 'M' indicated a MISS (defect not detected). From Table 6, it can be observed that, out of the 10 samples with cracks on both sides, i.e, 20 notch locations which are inspected using ECT, cracks at only 15 notch locations have been detected with ECT signals and hence, indicated with H (defect detected) and the remaining 5 notch locations are indicated with M (defect not detected). The range of cumulative surface crack length of oxidized fatigue cracks that are detected using ECT technique is from 0.27 to 1.16 mm whereas, the range of the surface crack length missed or undetected is from 0.11 mm to 0.37 mm. Hence, it can be understood that, among the

detected oxidized fatigue cracks, the smallest surface crack length detected is 0.27 mm whereas, the largest surface crack length missed by ECT is 0.37 mm. In addition, it can also be observed that the fatigue crack of length of 0.42 mm in the sample tested in vacuum is also not detected by the ECT inspection. However, the smallest crack length detected by the ECT inspection of high temperature cracks is 0.27 mm. Even though the crack length (0.42 mm) is larger in the sample tested in vacuum compared to that of crack length (0.27 mm) in high temperature air tested sample cracks, fatigue crack in vacuum sample is not detected by ECT inspection. This is due to the lower crack width (0.60 μm) of the fatigue crack in the sample tested in vacuum compared to that of the crack width (0.72 μm) of fatigue crack in high temperature air tested sample (from Table 6).

In addition, Table 6 also shows the ECT signal amplitude data of the corresponding 'H' indicated notch locations or sites. It can also be observed that ECT inspection did not detect fatigue cracks in the sample tested in vacuum. POD curve for ECT is usually plotted for depth [19]. However, as mentioned earlier, samples are not sectioned to measure crack depth. Hence, the POD curve considering ECT amplitude vs. depth could not have been plotted. As the ECT signal amplitude is a function of the crack volume which would affect the eddy currents, wider/deeper cracks would yield more signal amplitude (Figure 67) [19]. Comparing the ECT signal response from EDM notch and oxidized fatigue crack, (Figure 67), it can be observed that the response from the oxidized fatigue crack is found to be lesser indicating the effect of oxidation. This can also indicate that the effective crack volume in the case of high temperature fatigue cracks is lower compared to that of EDM notches. Hence, estimating the equivalent crack depths of oxidized fatigue cracks deduced from the ECT response of EDM notch depth as shown in Equation 15 would not result in error. Therefore, equivalent crack depths of the oxidized fatigue cracks are estimated by using the regression equation as shown in Equation 15.It is found that the range of equivalent crack depth sizes are from 0.07 mm to 0.57 mm. Figure 68 shows the goodness of fit test results along with histogram of log-normally distributed equivalent fatigue crack depths. From Figure 68, it can be observed that the crack sizes are log-normally distributed as the P- value (0.698) is found to be higher and the corresponding Anderson-Darling (AD) value (0.249) is lower compared to the all other 2-parameter distributions [2]. From Figure 68, it can be observed that the equivalent crack depth sizes also follow lognormal distribution. As the crack length (measured) is found to be lognormal in nature (Figure 53), it is imperative that crack depths also follow lognormal distribution as generally, it is assumed that, for a constant aspect ratio, longer and wider the cracks, deeper they are.

Table 6: ECT signal response data of all high temperature tested samples

Sample ID		Average crack width, µm	Cumulative crack length, mm	Equivalent crack depth, mm	ECT Response	
					HIT/ MISS	Amplitude, volt
Sample 1	side 1	0.56	0.24	-	M	-
	side 2	0.35	0.37	-	M	-
Sample 2	side 1	3.38	1.16	0.57	H	7.368
	side 2	3.09	0.65	0.45	H	5.980
Sample 3	side 1	0.54	0.27	0.07	H	1.410
	side 2	1.15	0.45	0.33	H	4.510
Sample 5	side 1	1.64	0.64	0.16	H	2.406
	side 2	1.13	0.42	0.22	H	3.132
Sample 6	side 1	-	0.11	-	M	-
	side 2	1.16	0.63	0.24	H	3.379
Sample 9	side 1	2.59	1.10	0.38	H	5.134
	side 2	2.09	0.97	0.32	H	4.400
Sample 10	side 1	-	0.14	-	M	-
	side 2	1.36	0.29	0.23	H	3.322
Sample 11	side 1	0.73	0.69	0.40	H	5.335
	side 2	0.60	0.84	0.21	H	2.997
Sample 12	side 1	1.94	0.39	0.25	H	3.484
	side 2	2.66	0.62	0.32	H	4.411
Sample 13	side 1	-	0.23	-	M	-
	side 2	3.12	0.56	0.26	H	3.682
Sample tested in vacuum	side 1	No crack			-	-
	side 2	0.60	0.42	-	M	-

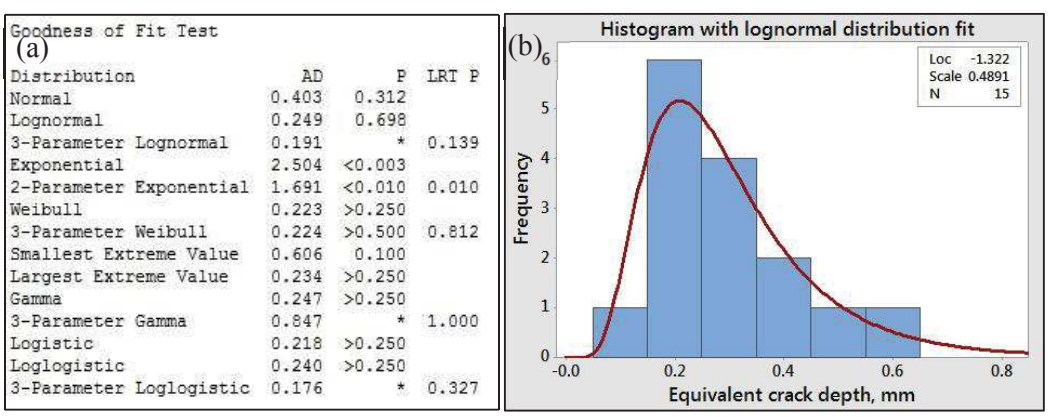

Figure 68: Histogram of equivalent crack depth sizes along with log-normal distribution fit.

5.1.3.2.3. ECT inspection of room temperature fatigue cracks

Further, similar to the ECT inspection of high temperature fatigue cracks or oxidized fatigue cracks, ECT inspection of room temperature fatigue cracks or non-oxidized fatigue cracks generated is also carried out. Hence, both HIT/MISS and ECT amplitude responses are recorded for all the samples. Table 7 show the ECT HIT/MISS and signal response data of all the samples along with the average crack width, cumulative surface crack length and equivalent crack depth at each side of all room temperature tested samples. From Table 7, it can be observed that, out of the 30 notch locations inspected using ECT, defects are detected only at 22 notch locations and hence, indicated with H (defect detected). The remaining 8 notch locations are indicated with M (defect not detected). From Table 7, the range in cumulative surface crack lengths of non-oxidized or room temperature fatigue cracks detected using ECT inspection are 0.14 to 1.95 mm and that of missed or undetected are 0.09 mm to 0.72 mm. This can be unrealistic as the maximum surface crack length (0.72 mm) missed in room temperature crack is higher than that of missed high temperature cracks (0.37 mm). In order to understand the reason for this observation, i.e. missing 0.72 mm length crack, the actual number of cracks at a particular location in one of the room temperature tested samples (sample 12 side 2) is considered. Two cracks with lengths of 0.61 mm and 0.11 mm are found in side 2 of sample 2 and hence, the cumulative surface crack length of 0.72 mm is observed. In addition, the average crack width of the largest among the 2 cracks i.e., 0.61 mm is found to be 0.53 μm (from Table 7). In order to understand the importance of average crack width on ECT detectability, similar cumulative surface crack lengths (0.69 mm) from sample 11 side 1 in high temperature cracks is used for comparison. This cumulative crack length of 0.69 mm is due to two high temperature cracks of lengths 0.47 mm and 0.22 mm. The average crack width of the largest (0.47 mm) among the two cracks in high temperature tested sample (sample 11 side 1) is 0.73 μm, as shown in Table 6. Hence, it can be clearly understood that even though the crack length (0.47 mm) in high temperature tested sample is less than (0.61 mm) the crack length in the room temperature tested sample, the average crack width for high temperature tested cracks (width of 0.73 μm for 0.47 mm crack) is higher compared to the crack width for room temperature cracks (width of 0.53 μm for 0.61 mm crack). From Table 7, it can also be observed that the range of average crack widths of room temperature or non-oxidized cracks is 0.40 μm to 3.17 μm. These minimum and maximum average crack widths correspond to surface crack lengths of dimensions 0.53 mm and 1.66 mm, respectively. However, the minimum and maximum of crack widths for high temperature or oxidized cracks is reported to be 0.35 μm to 3.38 μm corresponding to

surface crack lengths of 0.18 mm and 1.11 mm, respectively. Hence, it can be clearly observed that the average crack width is lower in room temperature cracks compared to that of high temperature cracks. Further, after removal of load, in addition to the crack surfaces to be under compression, there lies a probability for the crack surfaces to touch each other resulting in the closure of the crack. This leads to the electrical contact between the crack faces of a tight crack and will effectively short circuit the eddy-current flow generally leading to a smaller response from a crack compared to an EDM notch of wider gap between the faces [18]. In addition, the electrical conductivity of oxide (for example Nickel oxide=1.3 * 10^-5 mho/cm (i.e., 130 S/m)) is lower compared to the electrical conductivity of pure nickel (1.43 * 10^7 S/m) [20]. From these electrical conductivity values, it can be clearly understood that the oxides in the crack surfaces are highly insulating in nature. This would result in reduced or lack of impedance mismatch and hence, resulting in the miss indication by the technique for room temperature cracks. However, in the case of ECT inspection of high temperature cracks or oxidized fatigue cracks, dislodged oxide film acts as wedge and thus assists in maintaining higher crack width leading to the prevention of crack surfaces from touching each other [18].

In addition, Table 7 also shows the ECT signal amplitude data of the corresponding 'H' indicated notch locations. It is also observed that the ECT signal amplitude from room temperature cracks is lesser than that of EDM notch depth of similar length as shown in Figure 69. From Figure 69, it can also be observed that the ECT signal amplitude of room temperature fatigue crack is further lesser than that of high temperature crack. Fahr et al has observed that EDM slots generally produced larger magnitude eddy current signals (~20% higher) compared to service-induced cracks. Similarly, compared to laboratory-grown fatigue cracks, magnitudes of EDM slots were found to be 30-40% higher. The higher signal amplitude in EDM notches is attributed to the wider gap between the two faces which provides a higher electrical insulation. Similarly, the oxide layer often present in real cracks act as an insulator resulting in a larger magnitude eddy current signal as compared to the laboratory grown cracks. Similar result of higher ECT amplitudes for EDM notches and service cracks than that of laboratory cracks is shown by A.Fahr et.al [17].

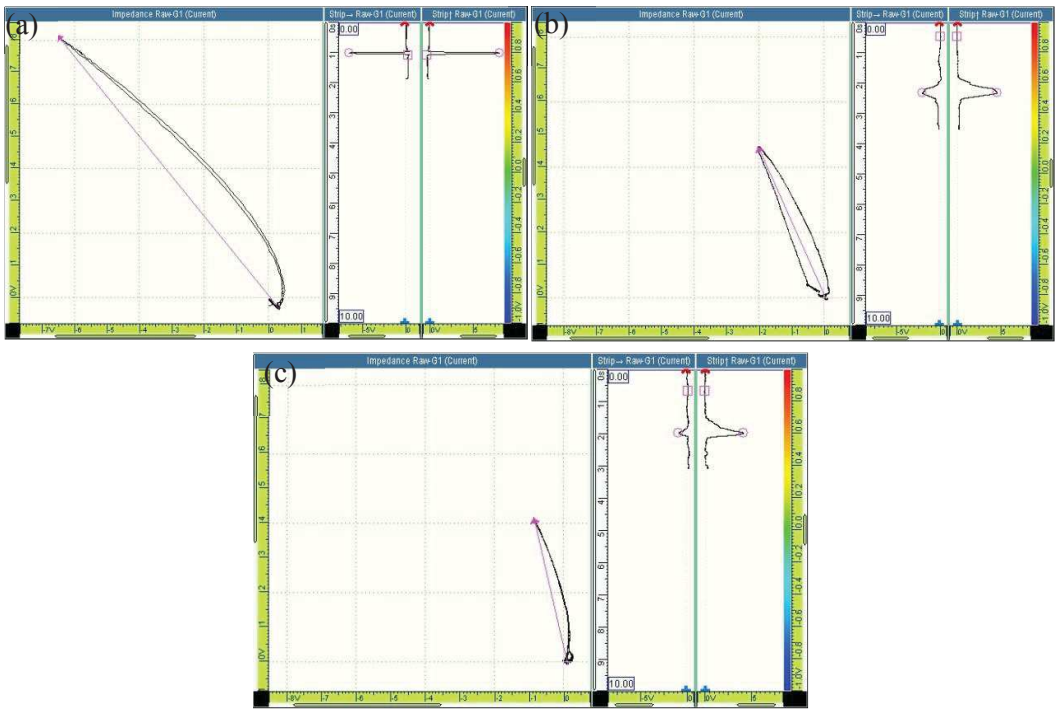

Figure 69: ECT impedance map 1 mm size defect (a) EDM notch (b) oxidized or high temperature fatigue cracks and (c) non-oxidized or room temperature fatigue crack.

Similar to the calculation of the equivalent crack depth sizes from oxidized cracks, equivalent crack depths of the non-oxidized or room temperature fatigue cracks is estimated using Equation 15. It is found that equivalent crack depth ranges from 0.12 mm to 0.77 mm. Figure 70 shows the goodness of fit test results along with histogram of log-normally distributed equivalent fatigue crack depths for room temperature fatigue cracks. As the P-value (0.507) is found to be higher and the corresponding Anderson-Darling (AD) value (0.323) is lower compared to the all other 2-parameter distributions [2], it can be observed that the crack sizes are log-normally distributed (Figure 70). From Figure 70, similar to Figure 68, it can be observed that the equivalent crack depths also follow lognormal distribution.

Table 7: ECT signal response data of all room temperature tested samples

Sample ID		**Average crack width, µm**	**cumulative crack length, mm**	**Equivalent crack depth, mm**	**ECT Response**	
					HIT/ MISS	**Amplitude, volt**
Sample 2	side 1	1.10	1.31	0.29	H	4.034
	side 2	1.65	1.59	0.52	H	6.839
Sample 3	side 1	No crack			-	-
	side 2	0.68	0.31	0.36	H	4.871

Sample 4	side 1	No crack			-	-
	side 2	0.76	0.24	0.32	H	4.345
Sample 5	side 1	1.32	0.75	0.24	H	3.412
	side 2	0.66	0.13	-	M	-
Sample 6	side 1	2.65	0.84	0.32	H	4.413
	side 2	3.17	1.66	0.77	H	9.807
Sample 7	side 1	1.79	1.57	0.73	H	9.376
	side 2	No crack			-	-
Sample 8	side 1	1.38	0.65	0.32	H	4.395
	side 2	0.77	0.14	0.23	H	3.256
Sample 9	side 1	0.64	0.31	-	M	-
	side 2	0.51	0.17	-	M	-
Sample 10	side 1	0.47	0.46	0.57	H	7.376
	side 2	-	0.09	-	M	-
Sample 12	side 1	0.41	0.63	0.66	H	8.434
	side 2	0.53	0.72	-	M	-
Sample 13	side 1	0.44	0.12	-	M	-
	side 2	-	0.53	-	M	-
Sample 14	side 1	No crack			-	-
	side 2	1.69	1.20	0.48	H	6.333
Sample 15	side 1	0.68	0.26	0.27	H	3.777
	side 2	2.28	0.57	0.37	H	4.924
Sample 17	side 1	0.46	0.60	0.12	H	1.950
	side 2	0.92	0.26	-	M	-
Sample 18	side 1	0.55	0.87	0.32	H	4.364
	side 2	0.99	0.77	0.46	H	6.035
Sample 19	side 1	0.99	1.78	0.40	H	5.232
	side 2	1.65	1.95	0.63	H	8.074
Sample 21	side 1	0.40	1.10	0.39	H	5.199
	side 2	1.13	1.51	0.33	H	4.495

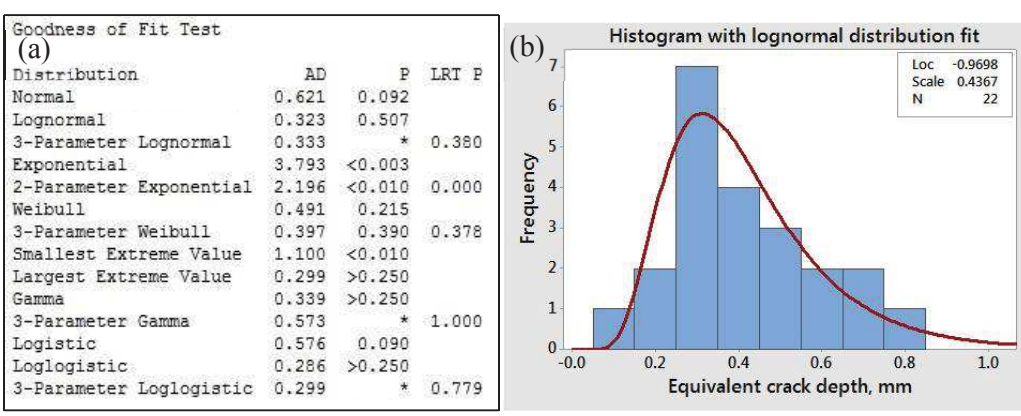

Figure 70: Histogram with lognormal distribution fit of equivalent crack depths of room temperature fatigue cracks

5.2. Part II-NDT response data generation using model based POD procedures

5.2.1 Validation of mathematical model

In order to validate the FEM model, ratio of successive peak to peak amplitudes and time of flight between successive backwall echoes are calculated for model based A-scan signal and compared with that of the experimentally obtained. From Table 8, it can be observed that for both experimentally obtained and 2D-axisymmetry model, ratios of peak to peak amplitude are approximately similar between 2nd & 3rd (1.66) and 3rd & 4th (1.69) back walls. However, the ratio of peak to peak amplitude between 1st & 2nd back wall echoes are completely different for both experimental signal (2.87) as well as the model generated signal (1.26). This major difference in ratio of peak to peak amplitudes can be attributed to the insertion losses [21, 22]. From Table 8, it can also be observed that the time of flight between successive back wall echoes for both experimental and numerically obtained A-scan signals are approximately similar. Hence, the 2D-axisymmetry model is considered to be validated and utilized for further simulations in predicting the ultrasonic response from defect.

Table 8: Peak to peak amplitudes of successive back wall echoes and the corresponding time difference and amplitude ratios of both experimental and modeling A-scan signals.

Back wall	Total Amplitude of back wall echo		Time Difference, Δt (μs)		Amplitude ratio	
	Experiment, volt	Model, mm	Experiment	Model	Experiment	Model
I	170.2	1.5E-06				
II	59.4	1.2E-06	6.45	6.20	2.86	1.26
III	35.60	7E-07	6.80	6.50	1.66	1.67
IV	21.01	4E-07	6.40	6.30	1.69	1.74

5.2.2 Generation of NDT response data from physics based numerical model

The validated FEM model for ultrasonic inspection is parameterized with random crack sizes generated using lognormal distribution. From the numerically obtained A-scans, automatic defect echo identification has been carried out by applying a Hilbert transform to the signal in Matlab program. The actual FBH sizes are considered as 'a' whereas the ultrasonic signal amplitude from the defect echo is considered as 'â'. Similar to the experimental procedure adopted for generating A-scan signal from a 0.5 mm FBH, the defect echo response in modeling is also set to 25 % full screen height (FSH) and the defect echo amplitudes of the remaining defects have been scaled assuming vertical linearity. Table 9

shows the some of the NDT response data generated using the validated ultrasonic numerical model.

Table 9: Representative NDT Response data generated using physics based numerical model

Flaw Size, a (mm)	0.36	0.42	0.54	0.55	0.64	0.81	0.96	1.00	1.27
Signal Response, â, %FSH	14.77	19.55	27.93	28.70	36.56	55.59	75.56	81.62	130.33

5.3. Part III - Statistical analysis of NDT response data

Detailed statistical analysis of the NDT response data obtained using both experimental and model based POD procedures is discussed in this section. This section provides the detailed statistical analysis for both â vs. a and HIT/MISS type NDT data. In this study, as the model based POD procedures yield quantitative ultrasonic NDT response data, â vs. a POD statistical procedure is applied for plotting model based POD curves. However, as the experimental based NDT response data obtained is both qualitative and quantitative (in case of ECT inspection) in nature, *â* vs. *a* and HIT/MISS statistical procedures are applied for generating experimental POD curves.

5.3.1. Statistical analysis for â vs. a data

5.3.1.1. POD using model based NDT data

Statistical analysis of data for POD curve generation involves in estimation of best linear fit between â vs. a. Subsequently, the best linear fit data is used for regression with censored data. From the censored regression, all the regression parameters are estimated using Maximum Likelihood Estimators (MLE) method. Further, the parameters of the parent distribution were calculated and the corresponding Cumulative Distribution Function (CDF) is plotted resulting in the POD curve. For the POD curve, 95 % lower confidence curve is also plotted so as to estimate the exact reliability of the NDT system by considering the crack size with 90% probability and 95% confidence limit ($a_{90/95}$) value.

5.3.1.1.1. Estimation of best linear fit between â vs. a

From Figure 71(a-d), it is observed that ln(â) vs. ln(a) data achieved the best linear fit as the R^2 value of ln(â) vs. ln(a) is 99.7% whereas for the â vs. a, â vs. ln(a) and ln(â) vs. a plots the R^2 values are 97.5%, 88.9% and 98.4%, respectively. Hence, 'ln(â) vs. ln(a)' is considered as the best fit for regression analysis. As mentioned above, MLE is considered

with censored data to perform regression analysis. Censoring of the data is performed in Minitab statistical software using "Regression with Life Data" condition such that signal amplitudes of less than 25 % FSH are left censored and greater than 80% FSH are right censored i.e. Signal assumed to be saturated. Table 10 shows â vs. a data for 9 out of 40 cracks for illustration purpose. From Table 10, it can be observed that the crack sizes 0.36 mm and 0.42 mm are left censored and 1.00 mm and 1.27 mm are right censored as the signal amplitudes are less than 25% FSH and greater than 80% FSH, respectively. 'L' is indicated for the left censored data and 'R' is indicated for right censored data in Table 10.

Table 10: â vs. a data along with left censoring (L) and right censoring (R)

a	0.36	0.42	0.54	0.55	0.64	0.81	0.96	1.00	1.27
â	14.77	19.55	27.93	28.70	36.56	55.59	75.56	81.62	130.33
Censor	L	L	27.93	28.70	36.56	55.59	75.56	R	R

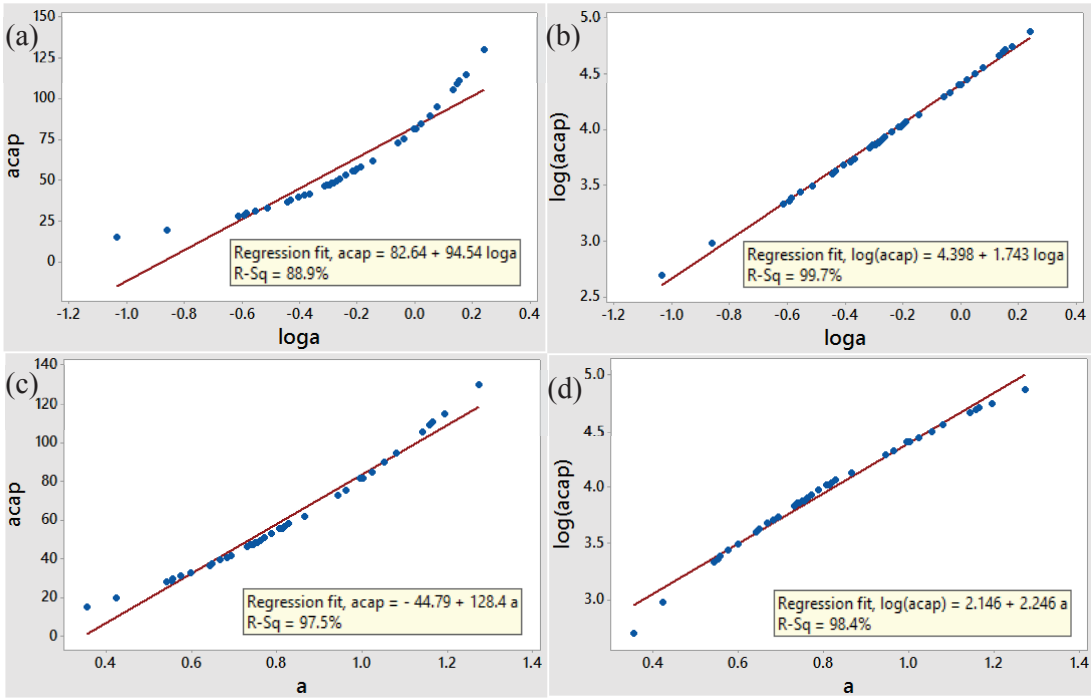

Figure 71: Linear regression of (a) â vs. ln(a) (b) ln(â) vs. ln(a) (c) â vs. a and (d) ln(â) vs. a

5.3.1.1.2. Regression with censoring data

Regression of the ln(â) vs. ln(a) data has to be performed with censoring option in order to calculate the mean and standard deviation and further to generate the POD curve. This regression of the censoring data is performed using "Regression with life data" option available in Minitab 17 statistical software. Figure 72 shows the result of the regression

performed between ln(â) and ln(a). From Figure 72, it can be observed that two left censored values (below 25 % FSH) and 10 right censored values (above 80 % FSH) exists in the data for 40 different crack sizes. Also from Figure 72, the coefficient of intercept also called as intercept and coefficient of ln(a) value (slope) of the regression line are obtained. Using these regression parameters (intercept and slope), mean and standard deviation are calculated according to Equation 8 and Equation 9, respectively. With these mean and standard deviation, the CDF of ln(a) is plotted. Further, the 95 % confidence curve is also plotted by estimating the 95 % confidence limits of the mean value using Equation 6.

Regression with Life Data: logacapL versus loga

```
Response Variable Start: logacapL  End: logacapR

Censoring Information  Count
Uncensored value          28
Right censored value      10
Left censored value        2

Estimation Method: Maximum Likelihood

Distribution:   Lognormal

Relationship with accelerating variable(s):   Linear


Regression Table

                       Standard                      95.0% Normal CI
Predictor       Coef      Error       Z      P      Lower      Upper
Intercept    4.41655  0.0052339  843.83  0.000    4.40629    4.42680
loga         1.82565  0.0151756  120.30  0.000    1.79591    1.85540
Scale      0.0190349  0.0026698                 0.0144598  0.0250576

Log-Likelihood = -41.718
```

Figure 72: Regression Table

Figure 73(a) shows the CDF of ln(a), which is actually the POD vs. ln(a) curve of 40 lognormally distributed FBH sizes. In Figure 73, the blue curve represents the POD curve whereas the red curve represents the 95 % LCL (Lower Confidence Limit) curve. From Figure 73, it can be observed that the $a_{90/95}$ value is the intersection point on the 95 % Lower Confidence Curve (LCL) curve at 90 % POD value. In addition, it can also be observed that the $\ln(a)_{90/95}$ value is -0.223, and the exponential of -0.223 results in $a_{90/95}$ value is 0.80 mm. Moreover, as the mean and standard deviation of the normal distribution is exactly equal to the location and scale of the lognormal distribution [2], the CDF of flaw sizes (a) is also plotted with the same mean and standard deviation values of ln(a). Figure 73(b) shows the plot of POD vs. 'a' of 40 lognormally distributed FBH sizes. From Figure 73(b), it can be observed that, the $a_{90/95}$ value (0.80 mm) is exactly equal to the $a_{90/95}$ value obtained from the

POD vs. ln(a) curve (Figure 73(a)). Apart from $a_{90/95}$ value, the a_{50} (flaw size with 50% probability of detection) and a_{90} (flaw size with 90% probability of detection) values are also found to be 0.5 mm and 0.73 mm, respectively. In addition, it can also be noted that the a_{50} value which is equal to 0.5 mm corresponds to the assumed decision threshold ($\hat{a}_{dec}$ = 25% FSH). As per the MIL-HDBK 1823A [19], the validity of the POD curve plotted can be ascertained when the observed a_{50} value equals to the flaw size corresponding to the assumed decision threshold ($\hat{a}_{dec}$) level selected for censoring. As the two values i.e., flaw size (0.5 mm) corresponding to the decision threshold ($\hat{a}_{dec}$) and a_{50} value match in this study, it can be concluded that the plotted POD curve is correct.

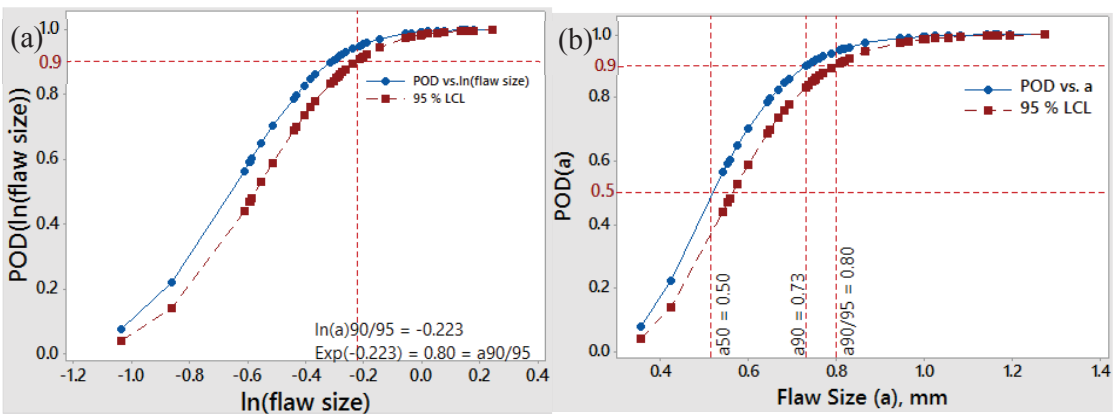

Figure 73: (a)POD vs. ln(a) for 40 lognormally distributed crack sizes indicating $a_{90/95}$ = 0.80 mm (b) POD vs. flaw size (a) indicating a_{50}, a_{90} and $a_{90/95}$ as 0.5 mm, 0.73 mm and 0.80 mm, respectively.

In order to understand the complexity related to selecting regression equation between natural logarithms of â and a or between logarithm to the base 10 of â and a, POD curves are also plotted using regression parameters obtained from $\log_{10}(\hat{a})$ vs. $\log_{10}(a)$ in addition to that of obtained from 'natural log of â' vs. 'a' (mentioned in previous discussion). Irrespective of the regression combination, the procedure adapted to plot POD curves is maintained constant. Figure 74 (a) shows the POD vs. $\log_{10}(a)$. From Figure 74(a), the $\log_{10}(a)_{90/95}$ value and its antilog ($\log_{10}(a)$) values are found to be -0.08 and 0.83, respectively. This $a_{90/95}$ value is approximately equal to $a_{90/95}$ value obtained above (Figure 73). Further, using mean and standard deviation obtained from regression, the CDF of flaw size, 'a' is also plotted. Figure 74(b) shows the POD vs. 'a' curve obtained from the mean and standard deviation of $\log_{10}(\hat{a})$ vs. $\log_{10}(a)$ regression. From Figure 74(b), it can be clearly observed that, the $a_{90/95}$ (0.91 mm) value obtained is different from the $a_{90/95}$ value obtained in Figure 74(a). Moreover, in this case, the observed a_{50} value (0.74 mm) is also not equal to the flaw size (0.5 mm)

corresponding to the $\hat{a}_{dec}$. Due to this reason, regression between natural ln(â) vs. ln(a) is considered for all analysis .

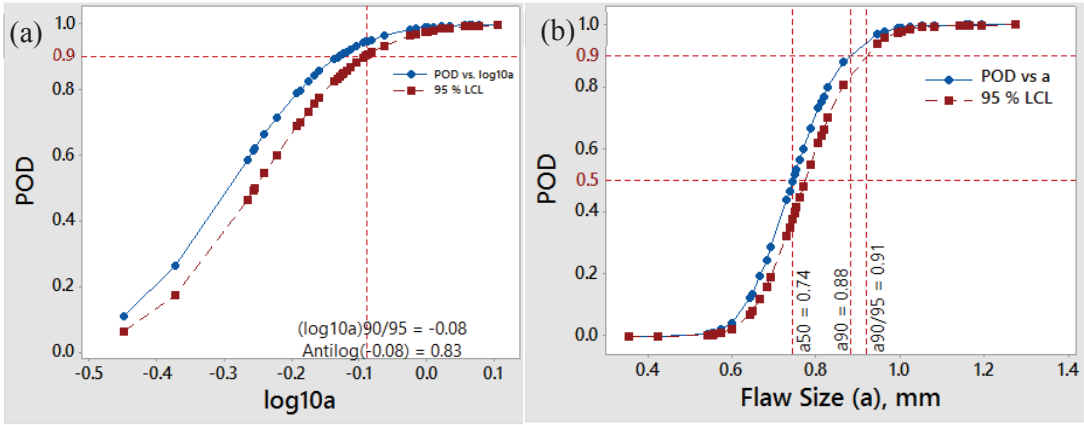

Figure 74: (a) POD vs. $\log_{10}$(a) plot for 40 lognormally distributed crack sizes indicating $a_{90/95}$ = 0.83 mm and (b) POD vs. flaw size plot indicating a_{50}, a_{90} and $a_{90/95}$ as 0.74 mm, 0.88 mm and 0.91 mm, respectively.

Similar procedure of plotting POD curves is adopted for 50, 100, 200, 300 and 500 cracks and the resulting POD curves for 50 and 500 cracks are shown in Figure 75 (a & b). Table 11 shows the number of censored and uncensored data for different number of defect sizes. In Table 11, the numbers of left censored and right censored data are defects with signal response less than 25 %FSH and greater than 80 %FSH, respectively. In addition from Table 11, it can be observed that the number of uncensored data is atleast 70 % of the total number of defects considered. Table 12 shows the $a_{90/95}$ values of 50, 100, 200 and 300 cracks for $\hat{a}_{dec}$ = 25 % FSH. From Figure 75 (a & b), it can be observed that $a_{90/95}$ obtained is 0.79 mm and 0.72 mm for 50 and 500 cracks, respectively. It can be observed that the $a_{90/95}$ value reduced with an increase in number of cracks from 50 to 500. A similar result of reduction in $a_{90/95}$ values with an increase in the number of crack sizes has been observed by Annis et al. [23]. In their study, Annis et al. [23] have concluded that $a_{90/95}$ value improved with an increase in the number of crack sizes from 30-60 and further saturated with an increase in number of crack sizes up to 120. This has been attributed to the enhancement in the confidence on the data and thereby reducing the confidence bound width in the POD curve. Due to this reason, the lower confidence curve will shift to the left with an increase in the number of crack sizes and thus reducing $a_{90/95}$ value. Moreover, it can be also observed that (Figure 75 (b)), the density of crack sizes in the transition zone of the POD curve increased with an increase in the number of crack sizes. In addition from Table 12, it can also be observed that the $a_{90/95}$ value is found to be 0.73 mm and 0.72 mm for 300 and 500 FBH sizes, respectively. Hence, it can be noted that the $a_{90/95}$ value gets saturated at 0.7 mm when

the number of defects are high. Therefore, enhancement in $a_{90/95}$ value is mainly attributed to reduction in confidence bound width and saturation of transition zone with the increase in number of cracks sizes.

Table 11: Number of censored and uncensored data with respect to the number of defect sizes

Number of defects	Left Censored (≤ 25 %FSH)	Right Censored (≥ 80 %FSH)	Uncensored
40	2	10	28
50	4	8	38
100	12	14	74
200	26	37	137
300	24	57	219
500	50	80	370

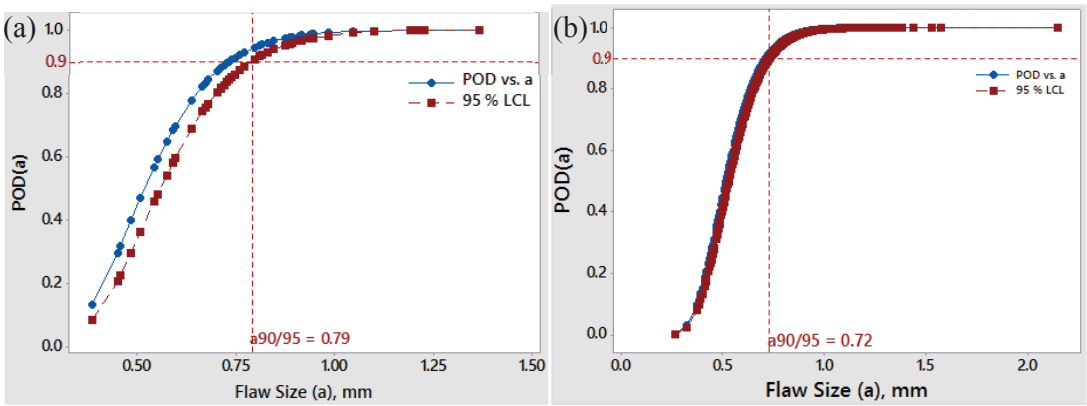

Figure 75: POD vs. flaw size plots for (a) 50 and (b) 500 lognormally distributed crack sizes indicating $a_{90/95}$ values as 0.79 and 0.72 mm, respectively.

5.3.1.1.3. Effect of $\hat{a}_{dec}$ (decision threshold) on $a_{90/95}$ values

In general, the decision threshold for processing â vs. a data for POD analysis usually depends on the signal noise level or the false call rate [24]. The signal noise levels are usually separated out by setting up the inspection threshold limit below which the NDT system cannot identify any response from the defect. Decision threshold is the one above/below which a crack/defect is considered to be detected/undetected and it completely depends on the false call rate. The decision threshold values should be higher if the false call rate is higher and vice-versa. Decision threshold is always greater than or equal to inspection threshold. Decision thresholds cannot be transferable between the different NDT systems due to differences in the probes, equipment type, etc. [24]. However, in the current study, as the noise/false call rate can be clearly differentiated from the signal response from the defect, results shown in Section 5.3.1.1.2 are plotted with the decision threshold selected as 25 %

FSH. It has to be noted that, if the decision threshold values are modified the corresponding variations in the $a_{90/95}$ values can be observed. Further if the $a_{90/95}$ values are modified, the detectability of the NDT system will also be varied. Hence, in the current study in order to study the effect of $\hat{a}_{dec}$ on $a_{90/95}$ values, two more decision threshold levels such as 35 % FSH and 45 % FSH are selected. Similar to the procedure adopted for plotting POD curves with a decision threshold of $\hat{a}_{dec}$ = 25 % FSH, POD curves are also plotted for 35 % FSH and 45 % FSH decision threshold levels. Figure 76 shows the $a_{90/95}$ data plotted against $\hat{a}_{dec}$ for different number of FBH defects. The corresponding values of $a_{90/95}$ are shown in Table 12. From Figure 76, it can be observed that $a_{90/95}$ values increased with an increase in decision threshold for all the crack sizes in this study. Similar results are also obtained in the literature [24-26]. Hence, the importance of carefully choosing the decision threshold levels while analyzing 'â vs. a' data can be established, in the absence of which the detectability (POD) of the NDT system could be wrongly estimated.

Table 12: Values of $a_{90/95}$ for various number of defects with different decision threshold levels

Decision Threshold ($\hat{a}_{dec}$) %FSH	**Number of defects**						
	40	**50**	**100**	**200**	**300**	**500**	
25	0.80	0.79	0.75	0.74	0.73	0.72	**$a_{90/95}$**
35	0.85	0.84	0.81	0.81	0.82	0.79	
45	0.92	0.91	0.90	0.91	0.90	0.89	

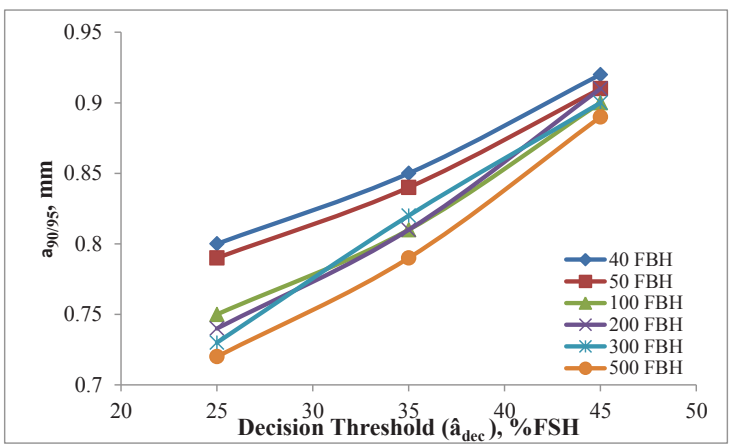

Figure 76: $a_{90/95}$ vs. $\hat{a}_{dec}$ values for different number of FBH defects

5.3.1.2. POD using experimental data

ECT signal response of high temperature and room temperature cracks

In addition to the ECT HIT/MISS response data, ECT signal amplitude data is also recorded at each inspection site for all the tested samples. Using this data, ECT signal amplitudes of all the fatigue cracks and equivalent crack depth data of both high temperature and room temperature fatigue cracks is statistically processed according to $\hat{a}$ vs. a type POD procedure for obtaining the POD curve of equivalent crack depth sizes. Tables 6 and 7 show the ECT amplitude and the corresponding equivalent crack depth data of all the fatigue cracks generated from both high temperature and room temperature tested samples, respectively. By using the ECT amplitude and the corresponding equivalent crack depth data, $\hat{a}$ vs. a type POD procedure is followed for obtaining the POD curve. As explained in Section 5.3.1.1, regression with censored data has been carried out between log(ECT amplitude) and log(equivalent crack depth sizes) data using maximum likelihood estimator method. Figure 77 show the regression between log(ECT amplitude) and log(equivalent crack depth sizes) data of high temperature oxidized fatigue cracks. From Figure 77, it can be observed that the correlation coefficient (adj.R^2) value of the linear fitting is 99.8%. Further, it can also be observed that the decision threshold ($\log(\hat{a}_{th})$) for processing $\hat{a}$ vs. a data for obtaining POD curves is maintained at 0.693 which is equivalent to 20% of the ECT signal amplitude i.e., 2 volt or log(2) = 0.693. ECT signal amplitude of 2 volt corresponds to the noise threshold, i.e., poor S/N ratio below 2 volt threshold. Figure 78 shows the regression table obtained from the regression with life data analysis between log(ECT amplitude) and log(equivalent crack depth sizes) data. From Figure 78, it can be observed that the regression with life data analysis is performed considering 14 uncensored and 1 censored data point. Data which is censored has an amplitude of 1.410 volt which is less than 2 volt for an equivalent crack depth size of 0.07 mm. In addition, it can also be observed that the coefficient values of intercept (2.40992) and loga (0.814078) i.e., log(equivalent crack depth) are the β_0 and β_1 values, respectively. By substituting these β_0 and β_1 values in Equation 8 and Equation 9, the mean, μ and the standard deviation, σ values of the distribution are calculated. Further, using μ and σ values, cumulative distribution function (CDF) of log-normal distribution function for each equivalent crack depth size is obtained. This CDF yields the probability of each equivalent crack depth value resulting in the POD curve of equivalent crack depth sizes. Similar procedure of CDF generation for room temperature cracks is also carried out to obtain the POD curve for room temperature crack depth data.

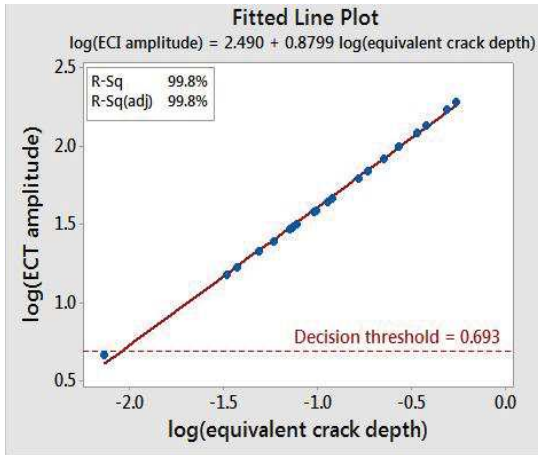

Figure 77: log-log plot with linear regression of ECT signal amplitude and the corresponding equivalent crack depth sizes data of high temperature oxidized fatigue cracks.

Regression with Life Data: log acap versus log a

```
Response Variable: log acap

Censoring Information  Count
Uncensored value          14
Right censored value       1

Censoring value: censor = C

Estimation Method: Maximum Likelihood

Distribution:   Normal

Relationship with accelerating variable(s):   Linear


Regression Table

                      Standard                    95.0% Normal CI
Predictor       Coef      Error       Z      P      Lower      Upper
Intercept    2.40992  0.0207235  116.29  0.000    2.36930    2.45053
log a       0.814078  0.0149130   54.59  0.000   0.784849   0.843307
Scale      0.0264542  0.0051338                 0.0180846  0.0386973
```

Figure 78: Regression with censored data using MLE method in Minitab statistical software

Figures 79(a) & (b) show the POD curves plotted using ECT amplitude data obtained for the fatigue cracks (equivalent crack depth sizes) generated under high temperature and room temperature conditions, respectively. From Figure 79(a) & (b), it can be observed that the a_{90} (detecting a crack with 90 % probability) values for ECT inspection of high

temperature and room temperature equivalent crack depth sizes are 0.45 mm and 0.58 mm, respectively. However, POD curves do not indicate the intersection point ($a_{90/95}$) between the POD curve and the 95% lower confidence curve at 90% probability value. Lack of $a_{90/95}$ value is attributed to the less number of data points available i.e., 15 and 22 cracks for oxidized and non-oxidized fatigue cracks, respectively for plotting the POD curves. This leads to the decrease in confidence probabilities and hence, wider gap between the POD curve and the 95% lower confidence curve resulting in the lack of $a_{90/95}$ value. However, due to the higher sensitivity of ECT for detection of the high temperature fatigue cracks when compared to room temperature fatigue cracks, the a_{90} value for oxidized fatigue cracks is found to be improved compared to that of the non-oxidized fatigue cracks.

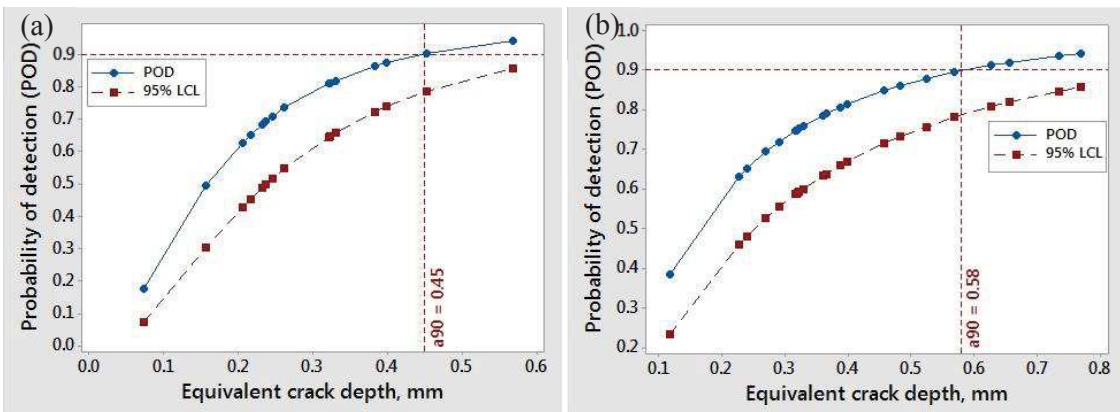

Figure 79: POD vs. equivalent crack depth for (a) oxidized cracks indicating a_{90} = 0.45 mm and (b) non-oxidized cracks indicating a_{90} = 0.58 mm

5.3.1.2.1. POD curves using higher number of random crack depth sizes

As mentioned earlier, POD curves obtained using equivalent crack depth data could not indicate $a_{90/95}$ value owing to the availability of lesser number of data points or cracks. As per MIL-HDBK-1823A [19], reliable POD crack generation demands at least 40 and 60 defect sizes for "*â* vs. *a*" and "*hit/miss*" type NDT data, respectively. Hence, in the current study, random crack sizes are generated for use in plotting the POD curves. In order to generate higher number of random crack sizes for use in NDT reliability studies, procedures as specified in MIL-HDBK 1823A [19] are followed according to the type of NDT outcome i.e., HIT/MISS and signal response data. In the current study, it is observed that the crack sizes generated under both high temperature and room temperature fatigue testing conditions follow lognormal distribution. Hence, the generation of the random crack sizes should also follow lognormal distribution with the same location and scale parameters as that of the

experimentally generated cracks (i.e, room temperature and high temperature conditions) [27]. In addition, the generation of the random cracks sizes also should be within the range of crack sizes obtained experimentally.

Random crack sizes for ECT signal response based POD curves

In the current study, initially 50 crack depths have been randomly generated by using similar values of distribution parameters i.e., around location of -1.322 and scale of 0.4891 of the lognormally distributed equivalent crack depth sizes for oxidized fatigue cracks. The range of these 50 random crack depth sizes obtained are from 0.07 mm to 0.84 mm. Figure 80 shows the histogram of 50 random lognormally distributed crack depth sizes. By using Equation 15, corresponding ECT signal amplitudes of all these 50 random crack depths are estimated. Further, by following the â vs. a POD procedure, the POD curves of all these 50 random crack depths are obtained. Figures 81(a) and (b) show the POD curves of the 50 lognormally distributed random crack depth sizes generated according to the probability distribution parameters of equivalent crack depth sizes obtained from both high temperature and room temperature tested samples, respectively. From Figure 81, it can be observed that the a_{90} and $a_{90/95}$ values of random crack depths generated using distribution parameters of equivalent crack depth from the high temperature cracks are 0.45 mm and 0.60 mm, respectively whereas, the a_{90} and $a_{90/95}$ values for random cracks generated using distribution parameters of equivalent crack depth from room temperature cracks are 0.58 mm and 0.75 mm, respectively.

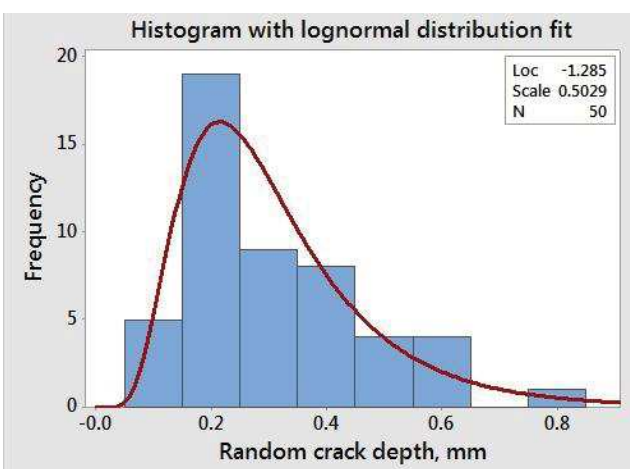

Figure 80: Histogram with lognormal distribution fit of 50 random crack sizes generated

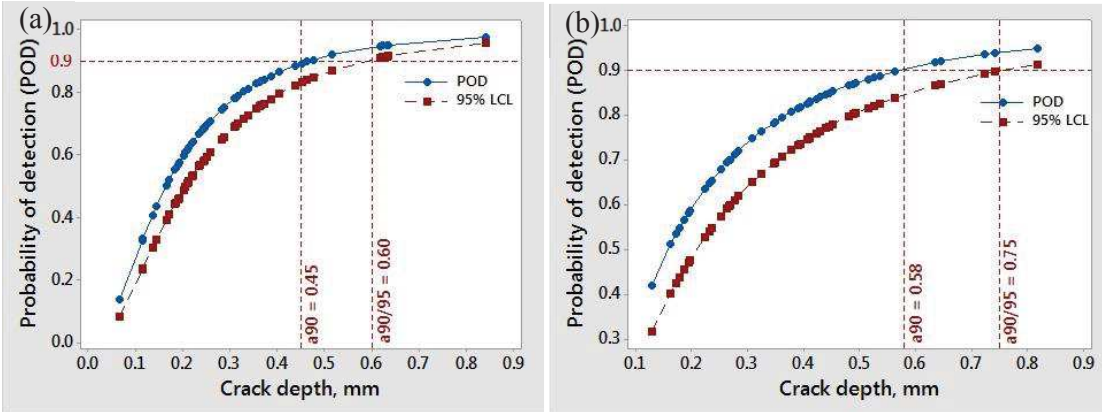

Figure 81: POD vs. 50 random crack depths generated according to the probability distribution parameters of (a) oxidized cracks indicating a_{90} = 0.45 mm and $a_{90/95}$ = 0.60 mm and (b) non-oxidized cracks indicating a_{90} = 0.58 mm and $a_{90/95}$ = 0.75 mm

Moreover, in order to understand the effect of increasing the number of randomly generated crack sizes on the $a_{90/95}$ value, 500 log-normally distributed random crack depths have also been generated and processed for POD analysis using the same analogy applied for obtaining POD curves using 50 random crack depths. Figure 82 shows the histogram of 500 lognormally distributed crack depths. The range of crack depth sizes generated is from 0.05 mm to 1.07 mm.

Further, statistically processing the equivalent signal response and 500 random crack depth sizes as per the procedures followed for POD curve processing using 50-random crack depths, the corresponding POD curves are obtained. Figures 83(a) and (b) show the POD curves of 500 lognormally distributed random crack depth sizes generated according to the probability distribution parameters of equivalent crack depths obtained from both high temperature and room temperature generated cracks, respectively. From Figure 83(a) and (b), it can be observed that a_{90}= $a_{90/95}$in both the high temperature and room temperature POD curves plotted for 500 random crack sizes. These values are in turn equivalent to a_{90}value of their respective POD curves (i.e., room temperature or high temperature) generated for 50 random crack depth sizes. This has been attributed to the enhancement in the confidence on the data and thereby reducing the confidence bound width in the POD curve. Due to this reason, the lower confidence curve will shift to the left and thus matches with the POD curve resulting in obtaining the same a_{90} and $a_{90/95}$ values [28]. It can be clearly observed that the $a_{90/95}$ values of the random crack depths generated using distribution parameters of equivalent crack depths from high temperature cracks improved compared to those random crack depths generated using distribution parameters of equivalent crack depths from room temperature cracks. Essentially, similar values of a_{90}, $a_{90/95}$ achieved for 500 cracks and its subsequent

equivalence to the a_{90} value achieved for 50 cracks for each of the high temperature and room temperature surface crack dimensions ascertain the validity of the statistical procedure proposed and adopted in this study [28]. When the number of cracks increases for POD analysis, there is an increase in the confidence in the data. In other words, physically, the confidence curves translate closer to the probability curve resulting in an overlap of POD and confidence curve. When both the curves overlap with each other, the a_{90} and $a_{90/95}$ values will be equal [28]. All this happens only if the adopted statistical procedures are correct for plotting POD curves. As the availability of the required number of cracks following Mil-HDBK 1823A [19] is often difficult to be generated, the proposed methodology can be adopted to extrapolate $a_{90/95}$ values obtained with limited data by including adequate number of random cracks.

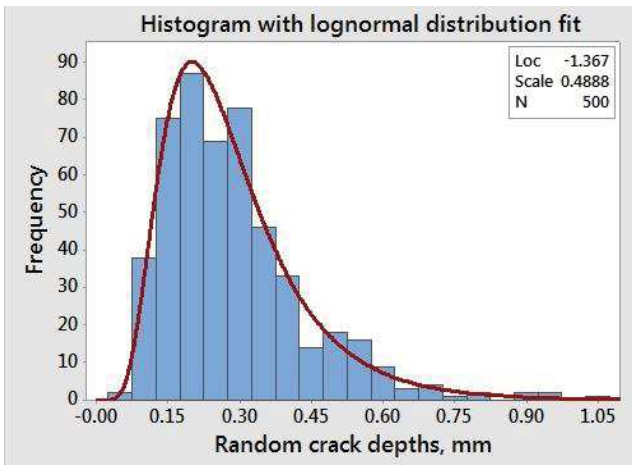

Figure 82: Histogram with lognormal distribution fit of 500 random crack sizes generated

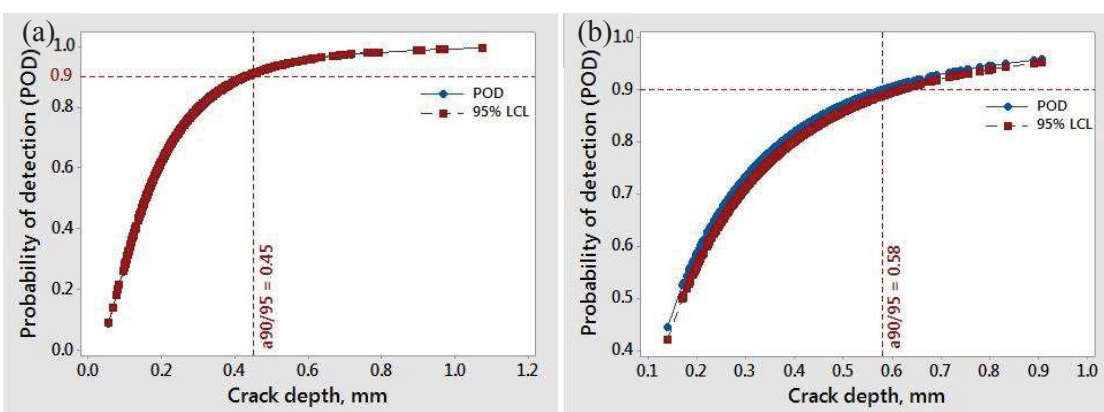

Figure 83: POD vs. 500 random crack depths generated according to the probability distribution parameters of (a) oxidized cracks indicating $a_{90/95}$ = 0.45 mm and (b) non-oxidized cracks indicating $a_{90/95}$ = 0.58 mm.

5.3.2. Statistical analysis using HIT/MISS data

5.3.2.1. FLPT data of room temperature cracks

As the FLPT inspection could only detect fatigue cracks in room temperature samples and not the fatigue cracks in high temperature samples due to the presence of oxide particles, POD of FLPT HIT/MISS data is only estimated for room temperature cracks. However, as discussed in Section 3.6.1.1, different HIT/MISS POD approaches [29] such as Type 1, modifies Type 1 and Type 2 approaches are applied for the FLPT HIT/MISS data of room temperature cracks. For all the HIT/MISS data obtained from FLPT inspection of room temperature cracks as demonstrated in Section 5.1.3.1, the POD is estimated using log-odds distribution function. Binary logistic regression is performed between NDT response and the log (crack size) using logit link function (discussed in detail in Section 3.6.1). Further, the regression parameters are substituted in the log-odds distribution function and the corresponding probabilities for each crack size are calculated. In addition, the 95% lower confidence limits are also calculated and the POD vs. flaw size (a) is plotted along with the 95% lower confidence curve.

Figure 84 shows the POD curves plotted using Type 1, modified Type 1 and Type 2 approaches for FLPT inspection of room temperature cracks data. From Figure 84, it can be observed that the $a_{90/95}$ values for Type 1 and modified Type 1 approaches for FLPT inspection data are 1.13 mm and 1.59 mm, respectively. In other words, modified Type 1 POD procedure makes the FLPT detectability slightly lower than Type 1. Figure 84(c) shows the POD curves plotted using Type 2 approach and the $a_{90/95}$ value obtained is 2.38 mm. In addition, it can also be observed that the $a_{90/95}$ value of the FLPT technique for Type 2 is greater (less sensitive) than the Type 1 and modified Type 1 approaches.

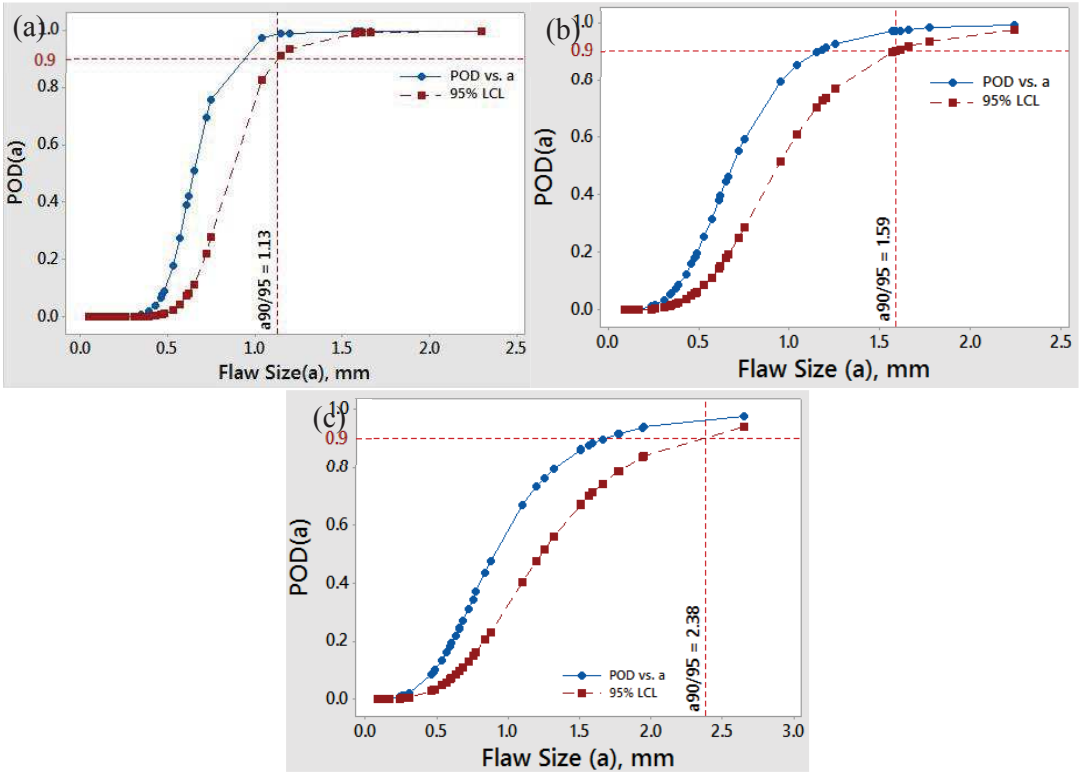

Figure 84: POD curves using three approaches for multiple cracks at a site for FLPT with (a) Type 1; (b) Modified Type 1 and (c) Type 2 approaches indicating $a_{90/95}$ values.

The effect of these $a_{90/95}$ values obtained using different HIT/MISS POD approaches on remnant life are discussed in the next part of results and discussion chapter i.e., (Section 5.4-Part IV). Figure 85(a) shows the POD curve plotted for NDT response data obtained from room temperature NDT response data using log-odds distribution function for FLPT technique. From Figure 85(a), it can be observed that the a_{90} (flaw detection with 90 % probability) and $a_{90/95}$ values are 0.94 and 1.13 mm, respectively. Further, in order to understand the effect of sample size and resulting number of cracks, the FLPT data of 5 samples with 17 cracks obtained from M.Tech thesis work [1] is also processed with log-odds distribution function. Figure 85(b) shows the POD curve obtained using lower number of samples comprising of lower number of crack sizes. From Figure 85(b), it can be observed that the a_{90} and $a_{90/95}$ values for FLPT technique are 1.77 mm and 2.23 mm, respectively. In addition, it can also be observed that the $a_{90/95}$ values of FLPT technique for 17 cracks data and 52 cracks data are 2.23 mm and 1.13 mm, respectively. Hence, it can be understood that the sensitivity of the NDT technique or its POD value improves with an increase in the number of cracks.

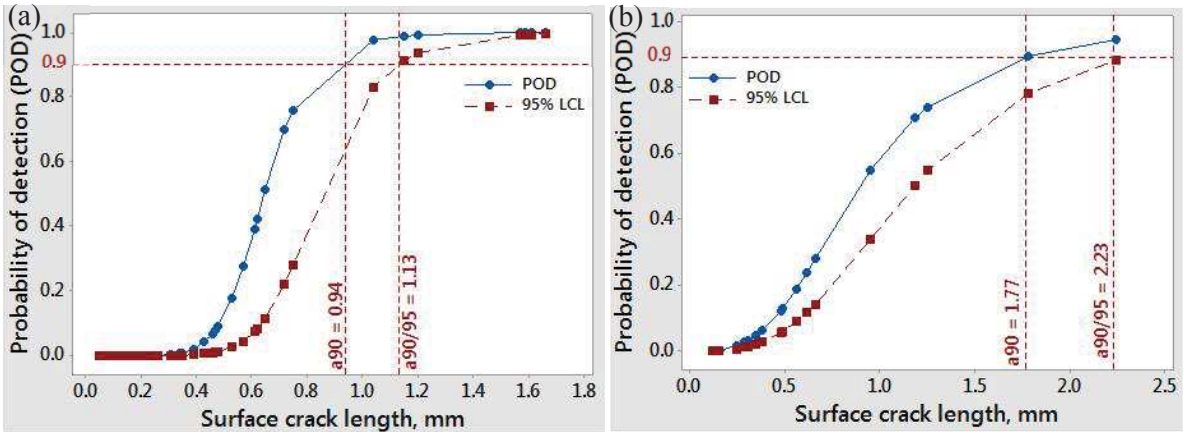

Figure 85: POD curves indicating a_{90} and $a_{90/95}$ values of FLPT data with (a) 52 cracks and (b) 17 cracks.

5.3.2.2. ECT inspection data

In the current work, surface crack lengths are obtained using microscopy tools whereas equivalent crack depths are estimated from the ECT signal amplitudes obtained from fatigue cracked samples using Equation 15. Moreover, the ECT inspection data is also available in both HIT/MISS and signal amplitude at an inspection site or notch location. Hence, in the current study, POD curves are plotted for both surface crack length and equivalent crack depth using HIT/MISS data.

The ECT HIT/MISS data shown in Tables 6 and 7 of both high temperature and room temperature generated fatigue cracks is processed statistically for plotting the POD curves. Figure 86 shows the binary logistic regression performed between the log (cumulative surface crack length) and the ECT HIT/MISS response data using logit link function. From Figure 86, it can be observed that the response of the ECT data is represented in terms of '1' for HIT indication and '0' for MISS indication. From the binary logistic regression, it can be observed that the intercept (7.71) and the slope (6.11) of the regression equation are identified as the 'α' and 'β' parameters, respectively to be used in the log-odds distribution function given in Equation (3).

Binary Logistic Regression: ni response versus ni loga

```
Method

Link function  Logit
Rows used      20


Response Information

Variable     Value  Count
ni response  1         15  (Event)
             0          5
             Total     20


Deviance Table

Source      DF  Adj Dev  Adj Mean  Chi-Square  P-Value
Regression   1   14.123   14.1225       14.12    0.000
  ni loga    1   14.123   14.1225       14.12    0.000
Error       18    8.371    0.4650
Total       19   22.493

Regression Equation

P(1)  =  exp(Y')/(1 + exp(Y'))


Y' = 7.71 + 6.11 ni loga
```

Figure 86: Binary logistic regression performed in Minitab software.

Figures 87(a) & (b) show the POD curves plotted using the ECT HIT/MISS data obtained from the inspection of fatigue cracks (cumulative surface crack length) generated under high temperature and room temperature conditions, respectively. From Figure 87, it can be observed that the $a_{90/95}$(flaw detection with 90 % probability and 95 % confidence) values for ECT inspection of high temperature and room temperature surface crack length sizes are 0.45 mm and 1.12 mm, respectively.

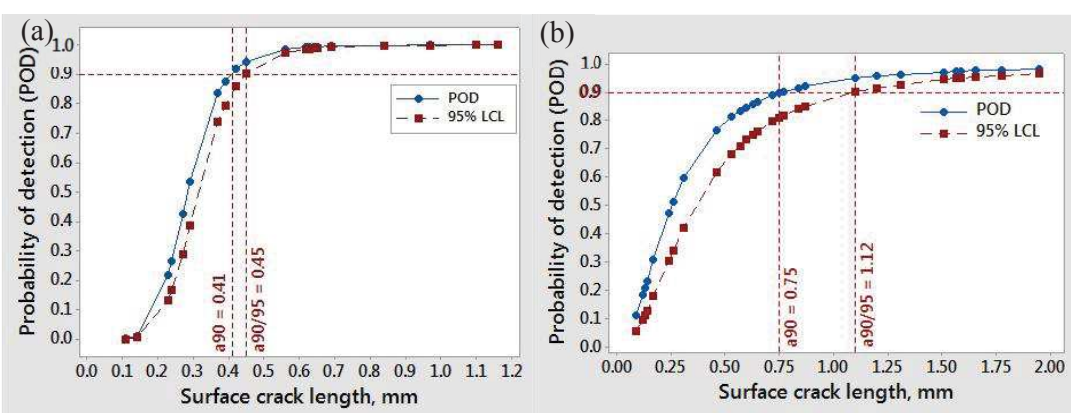

Figure 87: POD vs. surface crack length for (a) oxidized cracks indicating a_{90} = 0.41 mm and $a_{90/95}$ = 0.45 mm (b) non-oxidized cracks indicating a_{90} = 0.75 mm and $a_{90/95}$ = 1.12 mm

Similarly, HIT/MISS NDT data and the corresponding equivalent crack depth data of all the samples deduced from Equation 15 are processed for POD statistical analysis. Figure 88 shows the POD curves plotted using equivalent crack depth data of both oxidized and non-oxidized fatigue cracks. From Figure 88, it can be observed that the $a_{90/95}$ values for ECT inspection of high temperature and room temperature crack depth sizes are 0.35 mm and 0.76 mm, respectively. It can be noted that the $a_{90/95}$ value obtained by ECT inspection of high temperature cracks is improved (higher sensitivity) compared to that of room temperature cracks inspection in both cases i.e., POD plots using cumulative surface crack length and equivalent crack depth data. Hence, it can be understood that the oxidized fatigue cracks are more sensitive for ECT inspection than the room temperature cracks. This is attributed to the higher eddy current signal amplitudes obtained from the oxidized fatigue cracks (high temperature cracks) compared to that of non-oxidized cracks (room temperature cracks) [17]. This results in the sensitive $a_{90/95}$ value in the POD curve obtained using high temperature cracks, as compared to the room temperature cracks.

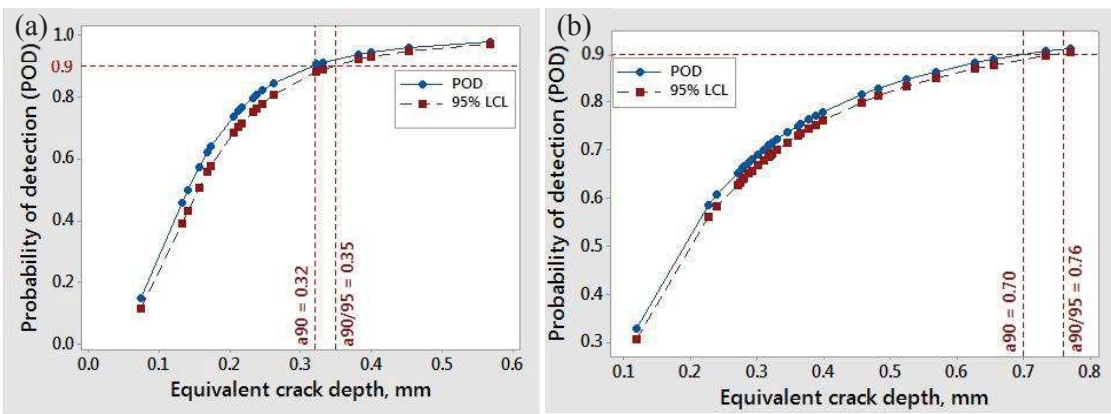

Figure 88: POD vs. equivalent crack depth for (a) oxidized cracks indicating a_{90} = 0.32 mm and $a_{90/95}$ = 0.35 mm (b) non-oxidized cracks indicating a_{90} = 0.70 mm and $a_{90/95}$ = 0.76 mm

Random crack sizes for HIT/MISS POD curves

Even though the $a_{90/95}$ values are obtained from the HIT/MISS POD analysis of FLPT and ECT inspection of fatigue cracks, in order to study the effect of higher number of cracks on HIT/MISS POD analysis, an attempt is made to generate random data. As the POD curves based on HIT/MISS NDT data depend on log-odds ratio, the assignment of HIT and MISS to the random crack sizes generated should also have the same log-odds ratio. For example, the total number of samples with oxidized fatigue cracks inspected with ECT technique is 20. Among these cracks, 15 were detected and 5 were not detected. Therefore, log(odds) ratio is

$$\text{Log(odds)} = \frac{Probability\ of\ success}{Probability\ of\ failure} = Log\left(\frac{15/20}{5/20}\right) = 0.478 \quad (16)$$

Hence, the random crack sizes generated should also be assigned with the suitable number of HIT and MISS such that the obtained log(odds) ratio should be same as that of the log(odds) ratio calculated from the limited number of experimental data. This assignment of HIT and MISS data to the random crack sizes can be carried out based on the information on the smallest crack size detected and the largest crack size missed by the ECI inspection of experimentally generated cracks. However, in order to statistically process any HIT/MISS NDT data for obtaining the POD curve, there should be intermittent MISS information of cracks. As this kind of information can never be logically included in the crack sizes generated, POD using log(odds) ratio for HIT/MISS methodology for higher number of crack sizes cannot be carried out.

Brief summary of ECT inspection of room temperature and high temperature cracks

In the current study, POD of cumulative surface crack lengths of both high temperature cracks ($a_{90/95}$ = 0.45 mm) and room temperature cracks ($a_{90/95}$ = 1.12 mm) are plotted using ECT HIT/MISS data. However, POD of equivalent crack depth data of both high temperature and room temperature cracks are plotted using both HIT/MISS ($a_{90/95}$ of oxidized cracks = 0.35 mm & $a_{90/95}$ of non-oxidized cracks = 0.76 mm) and signal response data (a_{90} of oxidized cracks = 0.45 mm & a_{90} of non-oxidized cracks = 0.58 mm) of ECT. As the ECT technique is more sensitive to crack depth rather than surface crack length, the $a_{90/95}$ values obtained from HIT/MISS POD of crack depth data of both high temperature ($a_{90/95}$ = 0.35 mm) and room temperature ($a_{90/95}$ = 0.76 mm) cracks is improved compared to that of surface crack length data ($a_{90/95}$ of oxidized cracks = 0.45 mm & $a_{90/95}$ of non-oxidized cracks = 1.12 mm) [17]. In all the types of POD curves plotted, the $a_{90/95}$ values using high temperature cracks are always found to be sensitive compared to room temperature cracks. This is attributed to the higher eddy current signal amplitudes obtained from the oxidized fatigue cracks (high temperature cracks) compared to that of non-oxidized cracks (room temperature cracks) [17]. Higher ECT signal amplitude is also observed for EDM cracked samples. The wider opening present in the samples with EDM notches acts as more insulating and thus, enhances signal amplitude. Similarly, oxides in the crack surface also act as insulators and thus generate higher eddy current signal amplitudes resulting in sensitive $a_{90/95}$ value. Moreover, as discussed earlier, compared to the high temperature fatigue cracks, lower

crack widths in room temperature cracks may enhance the probability for the crack surfaces to touch each other resulting in poor ECT detectability. This results in the sensitive $a_{90/95}$ value in the POD curve obtained using high temperature cracks, when compared to the room temperature cracks.

5.3.3. Summary of $a_{90/95}$ values obtained

Table 13 shows the summary of $a_{90/95}$ values obtained from FLPT and ECT inspection of both room temperature and high temperature cracks. In Table 13, 'RT' and 'HT' refers to room temperature and high temperature cracks. As the FLPT inspection could not detect any of the high temperature oxidized fatigue cracks, the $a_{90/95}$ values are only obtained for room temperature cracks with 3 different HIT/MISS POD approaches i.e., Type 1, Modified Type 1 and Type 2 approaches. Moreover, as the ECT response is always a cumulative response, only Type 2 approach is applied for both room temperature and high temperature cracks inspection data. From Table 13, it can be observed that the $a_{90/95}$ of ECT (1.12 mm) inspection of room temperature crack lengths is sensitive compared to the FLPT (2.38 mm) inspection due to the higher sensitivity of the ECT when compared with that of FLPT. However, the $a_{90/95}$ value of ECT (0.45 mm) inspection of high temperature crack length data is much sensitive when compared with ECT (1.12 mm) inspection of room temperature crack length due to the better detectability of oxidized cracks compared to the non-oxidized crack surfaces. Similarly, the $a_{90/95}$ values of ECT inspection of high temperature cumulative crack depth data are sensitive compared to the ECT inspection of room temperature cumulative crack depth data. As the $a_{90/95}$ values from ECT inspection of both room temperature and high temperature crack depth data processed using â vs. a POD method is not obtained, the $a_{90/95}$ values are shown from the ECT-POD curves obtained using higher number of random crack depth data. Even though the difference between all the $a_{90/95}$ values obtained is approximately less than 1 mm, the exact difference in the remnant fatigue cycles is not known. Hence, in order to understand the effect of $a_{90/95}$ values on remnant fatigue cycles, these $a_{90/95}$ values are further used for remnant life calculations using deterministic fracture mechanics approaches under the damage tolerance concept.

Table 13: Summary of $a_{90/95}$ values obtained using FLPT and ECT inspection of room temperature and high temperature cracks.

RT/HT - NDT		$a_{90/95}$, mm					
		H/M				â vs. a	
		Crack length, mm			Crack depth, mm	Crack depth, mm	
						50 cracks	500 cracks
		Type 1	Modified Type 1	Type 2	Type 2		
RT	FLPT	1.13	1.59	2.38	-	-	-
	ECT	-	-	1.12	0.76	0.75	0.58
HT	ECT	-	-	0.45	0.35	0.60	0.45

5.4. Part IV - Remnant life calculations using DT methodology

Under the damage tolerance based remnant life revision studies, irrespective of the POD procedures adopted, the $a_{90/95}$ values obtained are considered as the initial crack sizes detected by the NDT techniques for use in remnant life calculations. However, the actual manifestation of this $a_{90/95}$ on the remnant life is not addressed in the literature. With this view, the fourth part of the results and discussions from the thesis work demonstrates the importance of $a_{90/95}$ values obtained from FLPT and ECT inspection of both room temperature and high temperature cracks on remnant life analysis. However, the effect of this $a_{90/95}$ values on the remnant life calculations is studied using three-point bend geometry as the candidate testing protocol.

5.4.1 Theory on remnant life calculations using deterministic fracture mechanics approach

NDT reliability efforts results in estimating the standard metric $a_{90/95}$. This $a_{90/95}$ is in general used for damage tolerance based remnant life calculations using deterministic fracture mechanics approaches. Theoretically, damage tolerance life design methodology assumes that the failure prone locations of a component contain cracks. These cracks are assumed to grow during service and the crack growth rate can be found using Paris law as shown in Equation 17 [30],

$$\frac{da}{dN} = C(\Delta k)^n \tag{17}$$

On integrating the Paris law equation, remaining fatigue cycles required to grow a crack from initial size to critical size in a component can be calculated using Equation 18 [30]

$$N_c = \int_{a_i}^{a_c} \frac{da}{C(\Delta k)^n} \tag{18}$$

where,

N_c =Number of fatigue cycles to grow a crack from a_i to a_c

a_i= Initial crack size, mm = $a_{90/95}$ value obtained from the POD curve

a_c= Critical crack size, which can be estimated as shown in Equation 19 [30]

$$a_c = \frac{1}{\pi}\left(\frac{K_{IC}}{\sigma\lambda}\right)^2 \tag{19}$$

K_{IC} = Mode I fracture toughness of the material, MPa$\sqrt{m}$

$\Delta k =$ Stress intensity factor, MPa$\sqrt{m}$ = $\lambda\sigma\sqrt{\pi a}$

σ = Stress applied, MPa

$\lambda = f\left(\frac{a}{w}\right)$ = Specimen and crack geometrical factor

a = crack size or notch size in the specimen, mm

w = width of the specimen, mm

C and n are the material constants which can be determined from the fatigue crack growth rate (FCGR) testing. On substituting $\Delta k = \lambda\sigma\sqrt{\pi a}$, in Equation 18 and solving for N_c i.e., remnant fatigue cycles to grow a crack from initial size to critical size can be arrived at.

$$N_c = \frac{2}{(n-2)C\left(\lambda\sigma\sqrt{\pi a}\right)^n}\left(\frac{1}{a_i^{\left(\frac{n-2}{2}\right)}} - \frac{1}{a_c^{\left(\frac{n-2}{2}\right)}}\right) \tag{20}$$

In Equation 20 [31], λ or $f\left(\frac{a}{w}\right)$ is calculated for 3- point bend specimen design as shown in Figure 89 [32]. In Figure 89, 'P' is the load applied on the sample and 'S' is the span length between the supports.

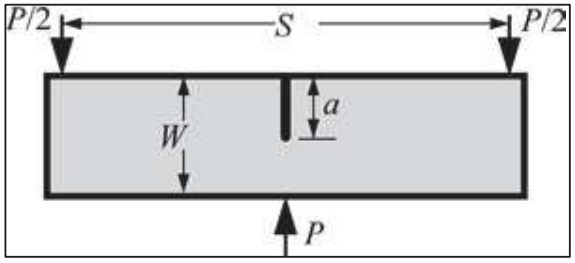

Figure 89: Schematic along with nomenclature of single edge notched bend (SENB) specimen [32]

The λ or $f\left(\frac{a}{w}\right)$ can be calculated using Equation 21 [32] as shown below

$$\lambda \; or \; f\left(\frac{a}{w}\right) = \left(\frac{3\left(\frac{s}{w}\right)\sqrt{\frac{a}{w}}}{2\left(1+2\frac{a}{w}\right)\left(1-\frac{a}{w}\right)^{3/2}}\right)\left[1.99 - \frac{a}{w}\left(1-\frac{a}{w}\right)\left\{2.15 - 3.93\left(\frac{a}{w}\right) + 2.7\left(\frac{a}{w}\right)^2\right\}\right] \tag{21}$$

5.4.2 Procedure for remnant life calculations

Even though Table 13 shows all the $a_{90/95}$ values obtained from the current work, the $a_{90/95}$ values obtained from HIT/MISS crack length data of both room temperature and high temperature cracks inspected using FLPT and ECT are only used for estimating remnant life calculations. As these lifing calculations are only estimated for the demonstration purpose, the $a_{90/95}$ values are selected such that these lifing calculations can be compared (1) between different HIT/MISS procedures for multiple cracks at a site condition, (2) between NDT techniques i.e., FLPT and ECT and (3) also between room temperature and high temperature cracks. Hence, the $a_{90/95}$ values of 1.13 mm, 1.59 mm and 2.38 mm corresponding to type I, modified type I and type II obtained from FLPT inspection of room temperature crack length data are selected for understanding the effect of different HIT/MISS procedures for multiple cracks at a site condition. In addition, the $a_{90/95}$ values of 2.38 mm and 1.12 mm corresponding to Type II obtained from FLPT and ECT inspection of room temperature crack length data are selected for understanding the effect of different NDT techniques on lifing calculations. Furthermore, the $a_{90/95}$ values of 1.12 mm and 0.45 mm corresponding to ECT inspection of both room temperature and high temperature crack length data are selected for understanding the effect of room temperature and high temperature cracks on lifing calculations. These $a_{90/95}$ values are substituted for the initial crack size values in Equation 20 for estimating the remnant fatigue cycles. The specimen geometric constant f(a/w) is calculated for the 3-point bend specimen for notch size equal to 2 mm and width of the

specimen equal to 10 mm using Equation 21. By substituting the stress corresponding to 30 % (193 MPa) of material yield stress (646 MPa) value at 650 ^{o}C in Equation 19, material fracture toughness K_{IC} (110 MPa$\sqrt{m}$ at 650 ^{o}C) obtained from K_{IC} testing of turbine disc material [33] and by calculating the λ or $f\left(\frac{a}{w}\right)$ = 5.87 of 3-point bend specimen, the critical crack size at which the sample fractures is calculated as (a_c = 3 mm). In addition, the material constants C (2 x 10^{-8}) and n (2.88) at 650 ^{o}C in the remnant life equation are obtained from the fatigue crack growth rate test of a compact tension (CT) specimen [33]. Further obtaining the values of all variables and the constants, the remaining fatigue cycles of the component are calculated using Equation 20. In order to convert these remaining fatigue cycles in to engine operating hours, these fatigue cycles are divided by a factor of 3 by considering at least 3 throttle excursions during the flight per hour of a military aircraft engine [34]. Finally, these fatigue cycles are further divided by a safety factor of 2 for obtaining the safe inspection intervals (SII) to be adopted in the damage tolerance lifing methodology [34].

5.4.3 Remnant life calculations using deterministic fracture mechanics approach

Table 14 shows the $a_{90/95}$ values and the corresponding remnant life in terms of fatigue cycles, engine operating hours and safe inspection intervals (SII) for FLPT and ECT NDT techniques inspection of both room temperature and high temperature cracks. From Table 14, it can be observed that ECT of room temperature cracks provides higher number of remaining fatigue cycles (4343 remnant fatigue cycles) and remnant engine operating hours than FLPT technique (290 remnant fatigue cycles) due to its higher sensitivity leading to lower or sensitive $a_{90/95}$. It can be understood that, even though the differences between the $a_{90/95}$ values between the 2 NDT techniques is 1.26 mm, the difference in remnant fatigue cycles stood at ~ 90%. However, the ECT inspection of high temperature cracks results in higher number of fatigue cycles (38793 remnant fatigue cycles) compared to the ECT inspection of room temperature cracks (4343 cycles). Similar to the percentage difference of ~90% in remaining fatigue cycles between FLPT and ECT inspection of room temperature cracks, the percentage of difference in remaining fatigue cycles between ECT inspection of room temperature and high temperature cracks is ~ 90% even though the difference in $a_{90/95}$ value is 0.67 mm. In addition, it can also be observed that sensitive $a_{90/95}$ values yields higher remnant life in the components. Further, the effect of $a_{90/95}$ values obtained from Type 1 and Type 2 approaches of FLPT data on remaining fatigue cycles and engine operating hours can be clearly observed. Figure 90 shows the remnant fatigue cycles corresponding to different

$a_{90/95}$ values of both the NDT techniques. From Figure 90, it can be observed that the remnant fatigue cycle decreases exponentially with an increase in the $a_{90/95}$ values (less sensitive). Moreover, it is beneficial to have higher SII values for better usability and reduced down time of aircrafts or airframe structures [34]. It is observed that the SII values are also higher for more sensitive $a_{90/95}$ values. The SII values should be in the range between 4000 to 8000 hours [34] in order to conclude that the proposed DFM approaches for these crack conditions in engine components are cost effective. Smaller SII values results in frequent maintenance and inspection schedules ultimately leading to higher costs and hence, it will not be cost effective for implementing damage tolerance lifing concept. However,higher SII values results in larger gaps between maintenance and inspection schedules. From Table 14, it can be observed that, except for the SII value of 6465 hours obtained from $a_{90/95}$ value corresponding to ECT inspection of high temperature cracks, the SII obtained from the other HIT/MISS methods or from the ECT inspection of room temperature cracks are not in the specified range i.e., between 4000 to 8000. Hence, it can be understood that depending on the room temperature cracks for carrying out NDT reliability studies would not yield successful results.

Table 14: Effect of $a_{90/95}$ on remnant life calculations

NDT Technique	Method	$a_{90/95}$, mm	N_d, Fatigue Cycles	Engine Operating Hours	SII, Hours
FLPT of room temperature cracks	Type 1	1.13	4241	1413	706
	Modified Type 1	1.59	1558	519	259
	Type 2	2.38	290	96	48
ECT of room temperature cracks	Type 2	1.12	4343	1447	723
ECT of high temperature cracks	Type 2	0.45	38793	12931	6465

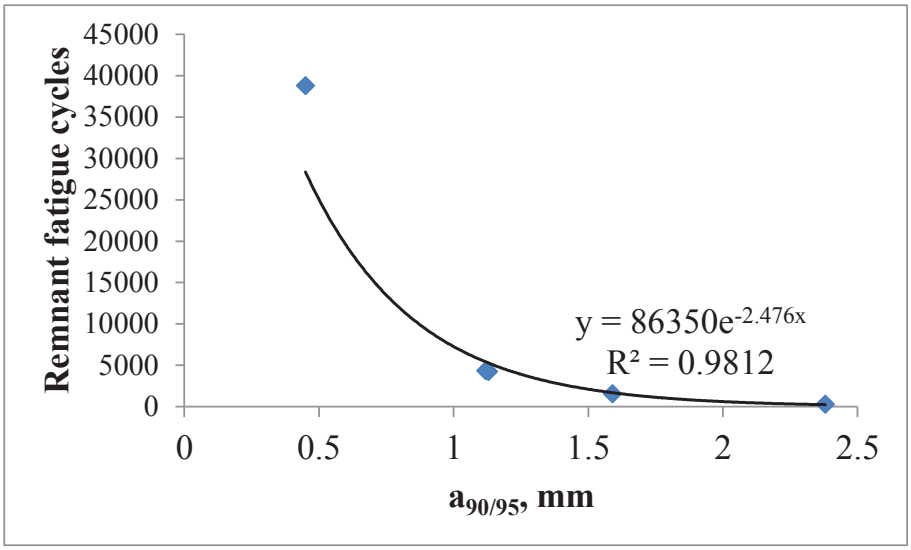

Figure 90: Effect of $a_{90/95}$ on remnant fatigue cycles

References

1. Vamsi Krishna Rentala, "Sensitivity Evaluation of NDT Techniques on Naturally Initiating Fatigue Cracks-an Experimental Approach for a POD Framework", M.Tech Thesis, University of Hyderabad, June 2014
2. W.Q.Meeker, L.A.Escobar, "Statistical methods for reliability data", wiley series in probability and statistics, text book, 1998.
3. D.A. Virkler, B.M. Hillberry, P.K. Goel, The statistical nature of fatigue crack propagation, J. Eng. Mater. Technol. 101 (1979) 148–153
4. Y. Liu, S. Mahadevan, Probabilistic fatigue life prediction using an equivalent initial flaw size distribution, Int. J. Fatigue 31 (2009) 476–487
5. Wåle, Ekström, 'Crack Characterisation for In-service Inspection Planning', SKI Projekt 14.4-940389, 94164 SAQ/FoU-Rapport 95/70, SAQ Kontroll AB, Sweden, pp 84, 1995.
6. Hänninen, Hakala, 'Pipe failure caused by thermal loading in BWR water conditions', Int. J. Pressure Vessel Piping, 9, 445–455, 1981.
7. M Kemppainen, I Virkkunen and H Hänninen, 'Advanced flaw production method for in-service inspection qualification mock-ups', Nuclear Eng and Design, Vol 224(1), pp 105-117, 2003.
8. A A Shanyavskiy and Y A Potapenko, 'In-service fatigue fracture mechanisms in covered disks of a TV3-117VK helicopter turbine engine', Strength of Materials, Vol 40(1), pp 158-161, 2008.

9. A A Shanyavskiy, 'Fatigue crack propagation in turbine disks of EI698 superalloy', Frattura ed Integritá Strutturale, Vol 24, pp 13, 2013.
10. Anand H.S. Iyer, Oxidation induced failure of superalloys-High temperature crack growth and oxide scale properties, THESIS FOR THE DEGREE OF LICENTIATE OF ENGINEERING, Chalmers University of Technology
Göteborg, Sweden 2017.
11. Chantal K. Sudbrack et.al, Oxidation And The Effects Of High Temperature Exposures On Notched Fatigue Life Of An Advanced Powder Metallurgy Disk Superalloy, 12th international symposium on superalloys, 2012.
12. S. Cruchley, H.E. Evans and M.P. Taylor, An overview of the oxidation of Ni-based superalloys for turbine disc applications: surface condition, applied load and mechanical performance, materials at High Temperatures, April 2016
13. E Wåle, 'Crack characterisation for in-service inspection planning', SKI Projekt 14.4-940389, 94164 SAQ/FoU-Rapport 95/70, SAQ Kontroll AB, Sweden, pp 84, 1995.
14. AndrePineau, Stephen D.Antolovich, "High temperature fatigue of nickel-base superalloys – A review with special emphasis on deformation modes and oxidation", Engineering Failure Analysis, Volume 16, Issue 8, December 2009, Pages 2668-2697
15. M.R.Bache, J.O'Hanlon, D.J.Child, M.C.Hardy, "High temperature fatigue behaviour in an advanced nickel based superalloy: The effects of oxidation and stress relaxation at notches", Theoretical and Applied Fracture Mechanics, Volume 84, August 2016, Pages 64-71.
16. B Larson, 'Study of the factors affecting the sensitivity of liquid penetrant inspections: review of literature published from 1970 to 1998', DTIC Document, 2002.
17. A.Fahr et al. Pod Assessment Using Real Aircraft Engine Components, NRC report Canada.
18. S K Burke, "Crack Depth Measurement using Eddy-Current NDE", ndt.net, APCNDT, 2001.
19. Department of Defense handbook, "Non-destructive evaluation system reliability assessment", MIL-HDBK-1823A (USA), April 2009.
20. Ahmed J. Hassan, "Study of Optical and Electrical Properties of Nickel Oxide (NiO) Thin Films Deposited by Using a Spray Pyrolysis Technique", Journal of Modern Physics, 2014, 5, 2184-2191
21. A.Vincent, influence of wear plate and coupling layer thickness on ultrasonic velocity measurements, Ultrasonics 25 (1985) 237–243.

22. Young H. Kim, Sung-jin Song, Sung-sik Lee, Joeng-ki Lee, A study on the couplant effects on contact ultrasonic testing, J. Korean Soc. Non-Destructive Test 22 (2002) 621–626.
23. Charles Annis, L. Gandossi, Influence of sample size and other factors on hit/miss probability of detection curves, in: ENIQ Report nr. 47, ENIQ TGR technical document, 2012,
24. Alan P. Berens, Probability of Detection (POD) analysis for the advanced retirement for cause (RFC)/engine structural integrity program (ENSIP) nondestructive evaluation (NDE) system development volume 1 – POD analysis, AFRL-ML-WP-TR-2001-4010, January 2000, pp-55.
25. David S. Forsyth, John C. Aldrin, Build Your Own POD, 4th Eur. Am. Work. Reliab. NDE, 2009.
26. Murat Yalçin, Hasan Ilker Yelbay, C. Hakan Gür, PoD Analysis of Phased Array and Conventional Ultrasonic Techniques, 19th World Conf. Non-Destructive Test. 2016.
27. Vamsi Krishna Rentala, PhaniMylavarapu, Jai PrakashGautam, "Issues in estimating probability of detection of NDT techniques – A model assisted approach", Ultrasonics 87, 59–70, 2018.
28. Charles Annis, L. Gandossi, Influence of sample size and other factors on hit/miss probability of detection curves, in: ENIQ Report nr. 47, ENIQ TGR technical document, 2012.
29. F W Spencer, 'Probability of detection estimation for HIT/MISS data when detection cannot be attributed to specific flaws: an exploratory data analysis', Review of Progress in Quantitative Nondestructive Evaluation, Portland, Oregon, USA, Vol 25, 20 July-4 August 2006.
30. George E.Dieter, "Mechanical Metallurgy", Third edition, Mc Graw Hill Publishers, 2013.
31. Afshin Motarjemi and Amir Shirzadi, "Structural Integrity Assessment of Engineering Components", University of Cambridge. https://www.phase-trans.msm.cam.ac.uk/2006/SI/SI.html
32. T. L. Anderson, "Fracture Mechanics, Fundamentals and Applications," 2nd Edition, CRC Press, Washington DC, 1994.
33. DMRL-DRDO project report - Classified

34. A K Koul, N C Bellinger and A Fahr, ‘Damage-tolerance-based life prediction of aeroengine compressor discs: I. A deterministic fracture mechanics approach’, Int J Fatigue, Vol 12, No 5, pp 379-387, 1990.

6. CONCLUSIONS

Successful implementation of damage tolerance methodology for aero-engines requires the estimation of safe inspection intervals. The estimation of safe inspection interval requires the details of initial and critical crack sizes of the component. In general, the critical crack size of a component can be calculated by applying fracture mechanics provided the information on material and best estimates of loads and other conditions during the service are known. However, the initial crack size present in a component can only be known under a non-destructive inspection as the usage component cannot be destroyed. Hence, it is highly important that the NDT techniques used for inspection should be highly reliable. Reliability estimation of NDT techniques are usually estimated by carrying out the POD studies. POD procedures involves in statistically processing the NDT response data from the defects. This NDT response data can be generated from both experimental and model based procedures. Considering the lack of procedures to perform POD analysis in India, this research work has successfully established both the experimental and model based POD procedures. In addition, efforts are also made in understanding the physical significance of $a_{90/95}$ in estimating the remnant life calculations under the DT methodology. Some of the noteworthy conclusions of the efforts put in both the experimental and model based POD procedures and their remnant life calculations are given below.

Summary and conclusions from room temperature experimental POD studies

- In the absence of service expired components required for POD curves, alternative methods of initiating fatigue cracks on nickel based superalloy laboratory specimens using 3-point bend fatigue testing for POD studies in a laboratory environment is demonstrated.
- Using this procedure, samples with representative in-service crack features such as crack tightness as low as 1 μm, crack tortuosity, trans-granular nature and multiple initiation sites of cracks are generated.
- These samples with representative cracks are used to estimate probability of detection of fluorescent liquid penetrant and eddy current inspection techniques with a qualitative defect response. ECT resulted in higher sensitivity of $a_{90/95}$ value (1.12 mm) compared to the FLPT technique (2.38 mm).

Summary and conclusions from high temperature experimental POD studies

Under the absence of service expired aero-engine components, several experimental based POD studies have been carried out using EDM notches and starter cracks grown under room temperature laboratory conditions. However, these approaches are considered to be unrealistic in nature due to the absence of morphological features of the fatigue cracks similar to those generated under service operating conditions. Therefore, an innovative approach discussed in this work suggests a viable methodology to generate fatigue cracks under simulated service conditions representing in-service fatigue cracks. A few noteworthy conclusions are as given below:

- An innovative methodology has been successfully employed to generate oxidized fatigue cracks with surface lengths ranging from 0.01 mm to 1.16 mm at 650°C using Gleeble® system, for the first time.
- Presence of oxides has been clearly observed at crack surfaces and slip bands using EDS analysis of high temperature fatigue cracks.
- FLPT inspection could not detect any of the oxidized fatigue cracks due to the closure of crack openings with oxide debris.
- The $a_{90/95}$ values obtained from POD curves plotted using ECT hit/miss data of cumulative surface crack lengths and equivalent crack depth data of high temperature cracks is 0.45 mm and 0.35 mm, respectively. However, the $a_{90/95}$ value obtained from POD of room temperature cracks for cumulative surface crack lengths and equivalent crack depth data is 1.12 mm and 0.76 mm, respectively.
- The a_{90} values obtained from POD curves plotted using ECT signal response data (of equivalent crack depth) is 0.45 mm for high temperature cracks and 0.58 mm for RT cracks. These values are exactly equal to the $a_{90/95}$ values obtained from POD curves plotted using higher number of random crack depths, following the procedure in MILHDBK-1823A standard.
- Due to the presence of oxide debris, ECT POD for fatigue cracks generated at higher temperatures is found to be higher compared to that of ECT POD for room temperature cracks.

Summary and conclusions from model assisted POD studies

- Owing to the challenges involved in experimental determination of POD, model assisted probability of detection (MAPOD) approach has been developed.

- POD curves of ultrasonic testing on volumetric defects with reflecting characteristics similar to that of flat bottom holes (calibration reflector) are considered as a model problem by addressing various issues involved in the whole statistical procedure.
- Some of the issues successfully addressed in the statistical procedure of â vs. a type POD data, include, selection of crack sizes distribution, challenges involved in censoring and regression, estimation of distribution parameters, selection of regression equation between natural logarithms or logarithms to the base 10.
- Ultrasonic physics based model is developed by validated against experimentally generated ultrasonic response.
- The $a_{90/95}$ values obtained for $\hat{a}_{dec}$ = 25 % FSH for lognormally distributed crack sizes of 40, 50, 100, 200, 300 and 500 are 0.80 mm, 0.79 mm, 0.75 mm, 0.74 mm, 0.73 mm and 0.72 mm, respectively. It is observed that there is an improvement and saturation of $a_{90/95}$ value to 0.70 mm with an increase in the number of crack sizes. This improvement and saturation of $a_{90/95}$ value is due to the reduction in confidence bound width with an increase in the number of crack sizes.

Summary and conclusions from remnant life calculations

- The physical significance of the $a_{90/95}$ values obtained from the reliability studies of NDT techniques on the remnant life calculations is demonstrated. In addition, the effect of $a_{90/95}$ values obtained from different POD approaches for multiple flaws at a site on SII are also addressed.
- Maximum flaw size approach for FLPT and sum of flaw sizes approach for ECT techniques yielded the more sensitive $a_{90/95}$ values. However, amongst the NDT techniques, ECT technique being highly sensitive compared to the FLPT technique resulted in the sensitive $a_{90/95}$ value for the same set of cracks inspected.
- Effect of $a_{90/95}$ values on the remnant life calculations is clearly observed for the FLPT inspection data and at least 90 % variation in the corresponding fatigue cycles and the engine operating hours is observed between Type 1 and Type 2 approaches. SII values are found to decrease exponentially with an increase in $a_{90/95}$ values. In addition, these DFM calculations obtained from ECT inspection of high temperature cracks are found to be cost effective as the obtained SII values are in line with the literature.

Appendix-I: Statistical analysis of HIT/MISS data using Minitab

In this Appendix-I, the step by step procedure followed in Minitab statistical software version 17 for processing the HIT/MISS data obtained from the FLPT inspection of room temperature crack length data is shown. This data consists of 52 cracks and the corresponding HIT and MISS data from the FLPT inspection technique. Table 15 shows the FLPT HIT/MISS response of the crack length sizes inspected. In Table 15, '0' and '1' in the H/M response column correspond to MISS (crack not detected) and HIT (crack detected), respectively. This data is processed with the Type I or maximum flaw size approach under the different HIT/MISS POD approaches for multiple cracks at a site.

Table 15: FLPT HIT/MISS response of room temperature crack length data

Crack length, mm	H/M Response	Log(crack length)	Crack length, mm	H/M Response	Log(crack length)
0.05	0	-2.9957	0.26	0	-1.3471
0.06	0	-2.8134	0.31	0	-1.1712
0.08	0	-2.5257	0.31	0	-1.1712
0.09	0	-2.4079	0.34	0	-1.0788
0.09	0	-2.4079	0.35	0	-1.0498
0.09	0	-2.4079	0.39	0	-0.9416
0.09	0	-2.4079	0.43	0	-0.8440
0.11	0	-2.2073	0.46	0	-0.7765
0.12	0	-2.1203	0.47	0	-0.7550
0.12	0	-2.1203	0.48	0	-0.7340
0.13	0	-2.0402	0.48	0	-0.7340
0.14	0	-1.9661	0.53	0	-0.6349
0.16	0	-1.8326	0.57	1	-0.5621
0.17	0	-1.7720	0.61	1	-0.4943
0.17	0	-1.7720	0.61	0	-0.4943
0.17	0	-1.7720	0.62	1	-0.4780
0.17	0	-1.7720	0.65	0	-0.4308
0.18	0	-1.7148	0.72	1	-0.3285
0.19	0	-1.6607	0.75	0	-0.2877
0.19	0	-1.6607	1.04	1	0.0392
0.2	0	-1.6094	1.15	1	0.1398
0.22	0	-1.5141	1.2	1	0.1823
0.22	0	-1.5141	1.57	1	0.4511
0.23	0	-1.4697	1.59	1	0.4637

0.24	0	-1.4271	1.61	1	0.4762
0.26	0	-1.3471	1.66	1	0.5068

The HIT/MISS data shown in Table 15 is further processed by performing binary logistic regression on binary HIT/MISS data. Figure 91 shows the screenshot of selecting binary logistic regression option in Minitab software. From Figure 91, it can be observed that under the 'stat' tab on the main menu bar of Minitab software, 'regression' option shows path for selecting 'binary logistic regression' and in turn the 'fit binary logistic model'.

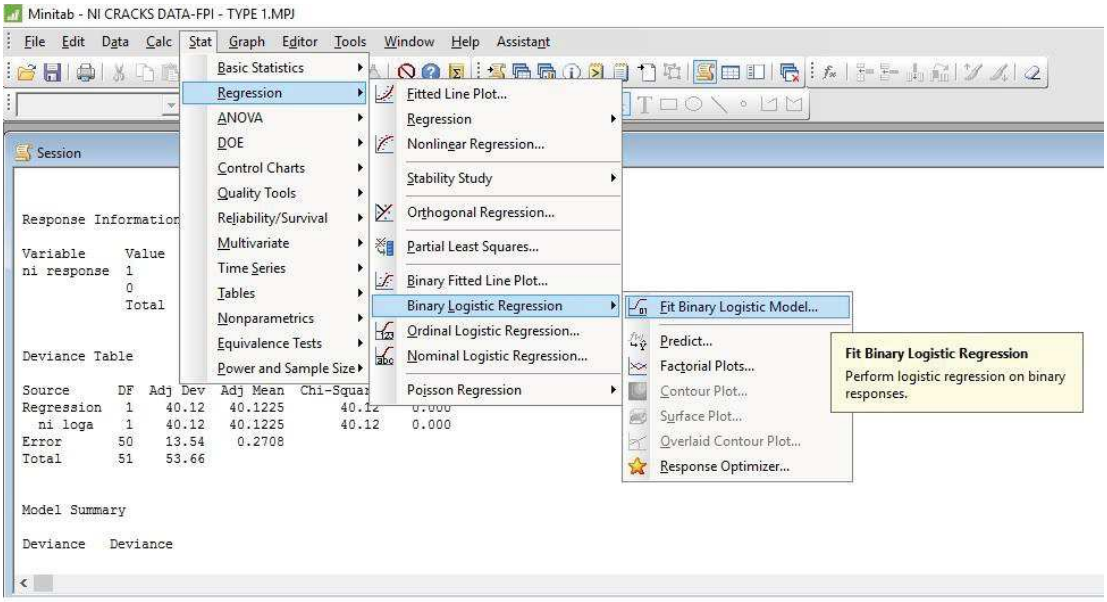

Figure 91: Screenshot showing the binary logistic regression option in Minitab software

As shown in Figure 92, a new window pops-up after selecting the 'fit binary logistic model' under the regression tab of main menu in Minitab software. In the new window, the column corresponding to the HIT/MISS response data is selected by mentioning the regression event as '1'. In addition, the continuous predictors i.e., column corresponding to the log(crack sizes) is chosen. However, in order to process the HIT/MISS data shown in Table 15, logit link function is selected as discussed earlier under the theory of HIT/MISS statistical procedure.

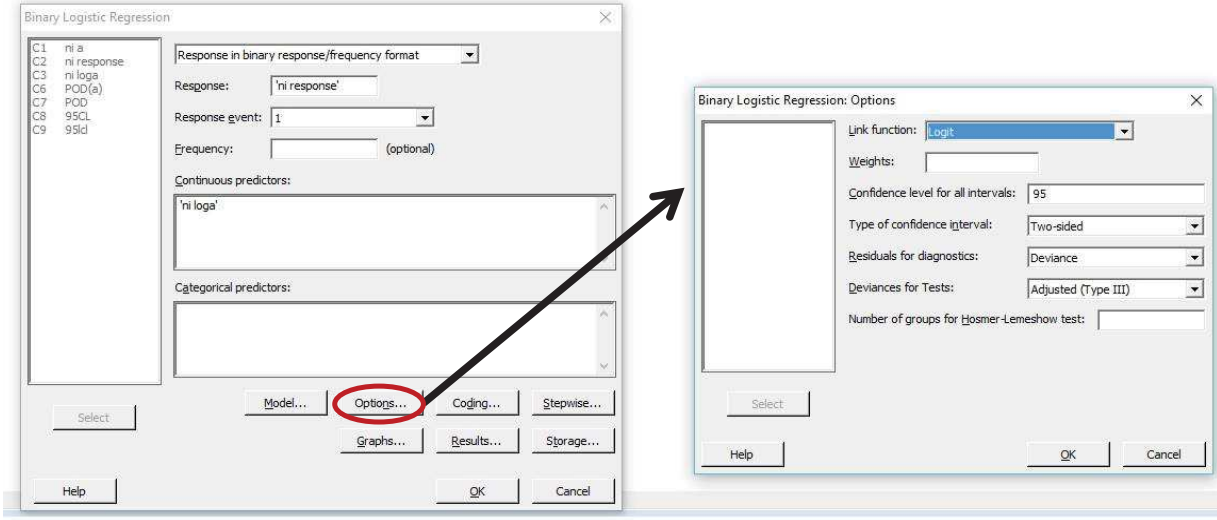

Figure 92: Screenshot showing the pop-up window of binary logistic regression

Further performing the binary logistic regression between the log(crack sizes) and the FLPT HIT/MISS response data, the result of the binary logistic regression is tabulated as shown in Figure 93. From Figure 93, the slope and intercept of the regression equation are substituted for β_0 and β_1 in the log-odds distribution function as shown in Equation 3.

Binary Logistic Regression: ni response versus ni loga

```
Method

Link function  Logit
Rows used      52


Response Information

Variable     Value  Count
ni response  1         11  (Event)
             0         41
             Total     52


Deviance Table

Source      DF  Adj Dev  Adj Mean  Chi-Square  P-Value
Regression   1    40.12   40.1225       40.12    0.000
  ni loga    1    40.12   40.1225       40.12    0.000
Error       50    13.54    0.2708
Total       51    53.66


Model Summary

Deviance   Deviance
    R-Sq  R-Sq(adj)    AIC
  74.77%     72.90%  17.54
```

```
Coefficients

Term      Coef  SE Coef   VIF
Constant  3.37     1.96
ni loga   7.71     3.61  1.00


Odds Ratios for Continuous Predictors

         Odds Ratio          95% CI
ni loga   2240.5210  (1.8796, 2.67076E+06)


Regression Equation

P(1)  =  exp(Y')/(1 + exp(Y'))


Y' = 3.37 + 7.71 ni loga


Goodness-of-Fit Tests

Test             DF  Chi-Square  P-Value
Deviance         50       13.54    1.000
Pearson          50       11.56    1.000
Hosmer-Lemeshow   8        2.46    0.964


Fits and Diagnostics for Unusual Observations

        Observed
Obs  Probability     Fit    Resid  Std Resid
 42       1.0000  0.4217   1.3142       1.40  X
 43       0.0000  0.5122  -1.1981      -1.29  X
 44       1.0000  0.6980   0.8480       0.94  X
 45       0.0000  0.7600  -1.6894      -1.89  X

X  Unusual X
```

Figure 93: Result of the binary logistic regression performed between log(crack sizes) and HIT/MISS response data

The probabilities of detecting each crack size by the FLPT inspection technique is obtained after solving the log-odds distribution function as shown in Equation 3 by substituting the β_0 and β_1 values obtained from the binary logistic regression equation shown in Figure 93. However, in order to estimate the $a_{90/95}$ value from the POD curve plotted, the lower 95% confidence limit of the β_0 is also obtained from the Equation 6. Hence, by calculating and substituting the lower 95% confidence limit of β_0 in the log-odds distribution function, the lower 95% confidence probabilities are also obtained. Table 16 shows the probabilities along with 95% lower confidence intervals of all the crack sizes inspected using FLPT inspection technique.

Table 16: Probabilities along with 95% confidence intervals of all the crack sizes inspected using FLPT

Crack length, mm	POD	95% LCL	Crack length, mm	POD	95% LCL
0.05	0.0000	0.0000	0.26	0.0009	0.0001
0.06	0.0000	0.0000	0.31	0.0035	0.0004
0.08	0.0000	0.0000	0.31	0.0035	0.0004
0.09	0.0000	0.0000	0.34	0.0071	0.0009
0.09	0.0000	0.0000	0.35	0.0088	0.0011
0.09	0.0000	0.0000	0.39	0.0200	0.0025
0.09	0.0000	0.0000	0.43	0.0416	0.0053
0.11	0.0000	0.0000	0.46	0.0680	0.0089
0.12	0.0000	0.0000	0.47	0.0793	0.0105
0.12	0.0000	0.0000	0.48	0.0920	0.0123
0.13	0.0000	0.0000	0.48	0.0920	0.0123
0.14	0.0000	0.0000	0.53	0.1787	0.0261
0.16	0.0000	0.0000	0.57	0.2761	0.0448
0.17	0.0000	0.0000	0.61	0.3915	0.0733
0.17	0.0000	0.0000	0.61	0.3915	0.0733
0.17	0.0000	0.0000	0.62	0.4217	0.0823
0.17	0.0000	0.0000	0.65	0.5122	0.1144
0.18	0.0001	0.0000	0.72	0.6979	0.2213
0.19	0.0001	0.0000	0.75	0.7599	0.2802
0.19	0.0001	0.0000	1.04	0.9752	0.8287
0.20	0.0001	0.0000	1.15	0.9884	0.9131
0.22	0.0002	0.0000	1.20	0.9916	0.9358
0.22	0.0002	0.0000	1.57	0.9989	0.9914
0.23	0.0003	0.0000	1.59	0.9990	0.9922
0.24	0.0005	0.0001	1.61	0.9991	0.9929
0.26	0.0009	0.0001	1.66	0.9993	0.9944

The crack sizes along with the probabilities and the 95% lower confidence intervals are plotted using the 'scatterplot' option under the main menu of Minitab statistical software to examine the relationship between the crack sizes and the probabilities. Figure 94 shows the screenshot of scatterplot option in Minitab software. Figure 95 shows the different options of the scatter plot in Minitab. From Figure 95, it can observed that 'with connect and groups' is selected under the scatterplot option inorder to plot the crack sizes along with both probabilities and 95% lower confidence intervals. Figure 96 shows the selection of x axis variable i.e., crack sizes and y axis variables i.e., probabilities for plotting POD curves.

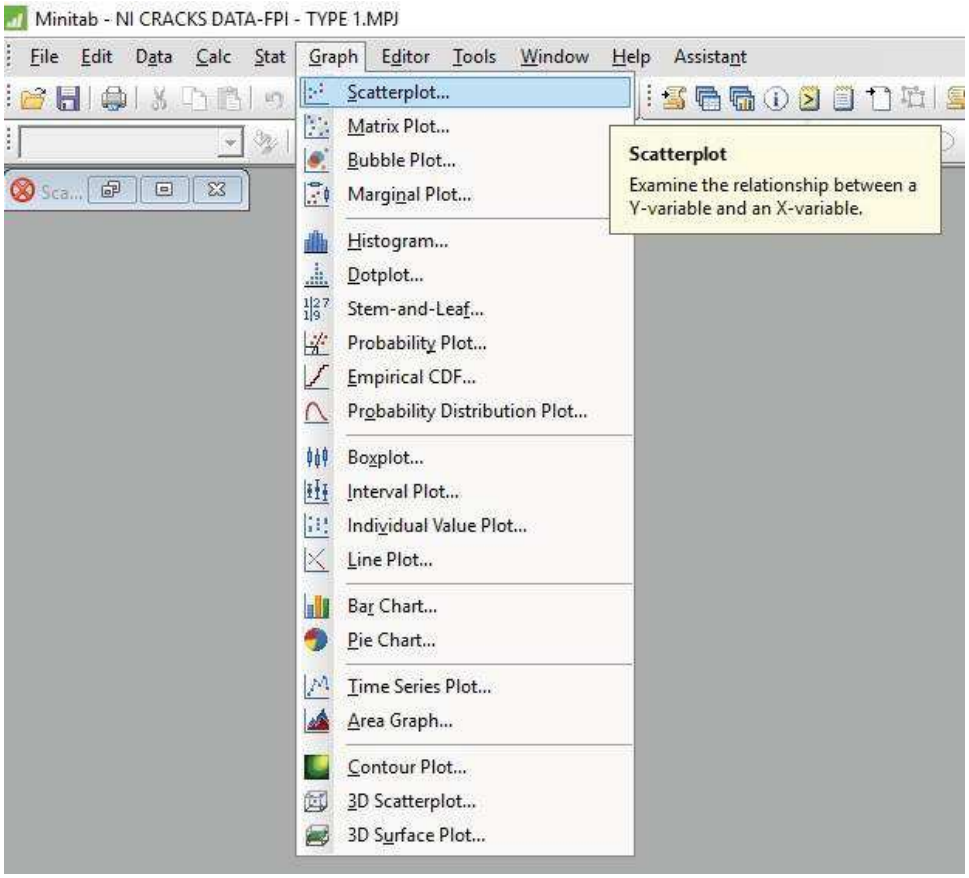

Figure 94: Screenshot showing the scatter plot option in Minitab software

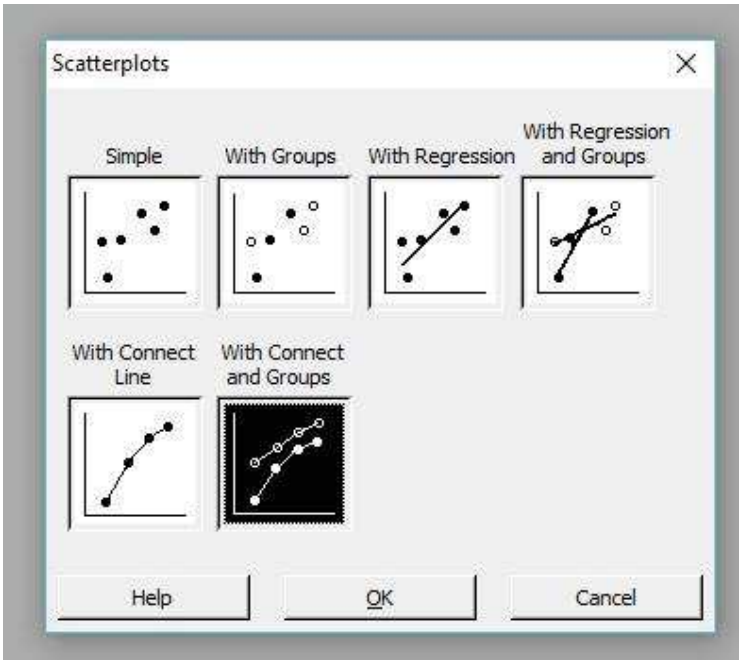

Figure 95: Screenshot showing the various modes of plotting scatter plot in Minitab software

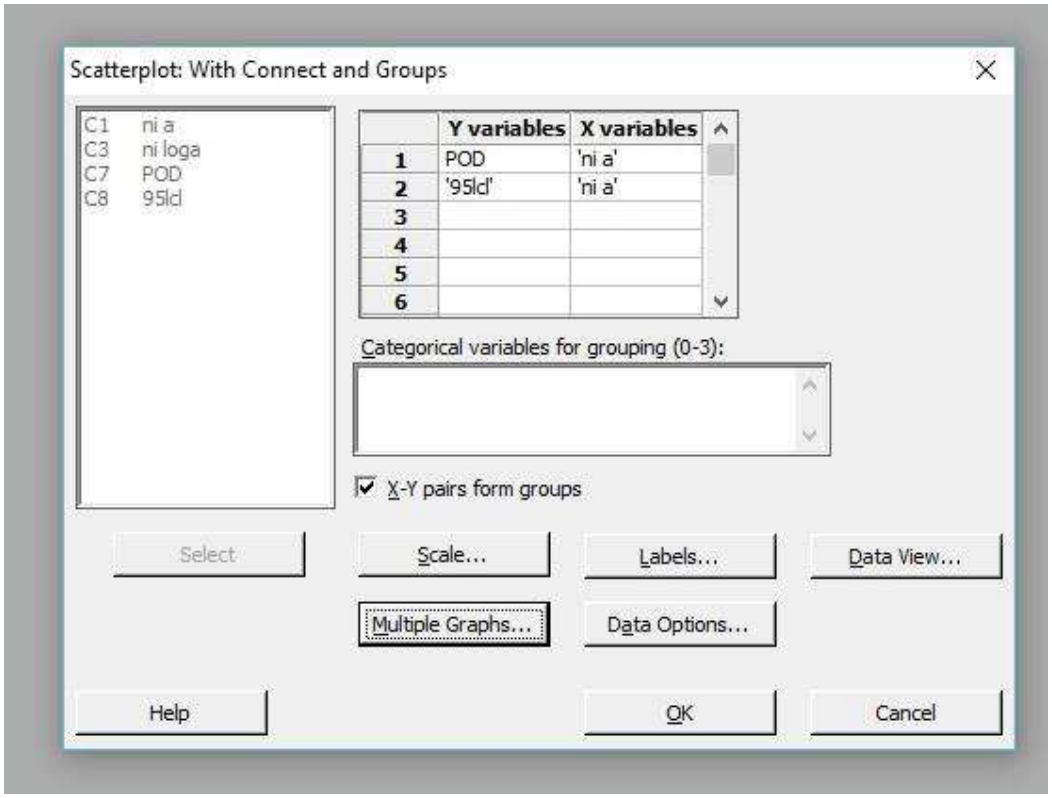

Figure 96: Screenshot showing the selection of x and y variables for plotting POD curves

Figure 97 shows the POD curve along with the 95% lower confidence curve of FLPT inspection of room temperature cracks. In Figure 97, the blue curve is the probability of detecting cracks whereas the red curve is the 95% lower confidence probability curve. From Figure 97, it can be observed that the a_{50}, a_{90} and $a_{90/95}$ values are 0.64 mm, 0.94 mm and 1.13 mm, respectively.

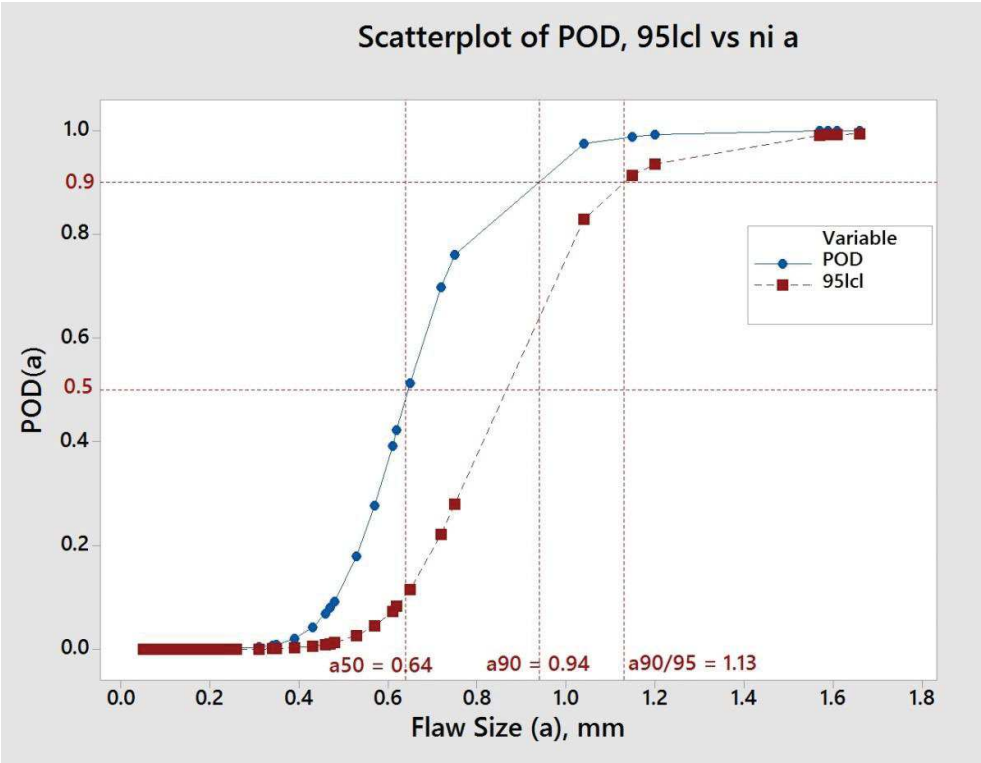

Figure 97: POD curve of FLPT inspection of room temperature cracks indicating a_{50}, a_{90} and $a_{90/95}$ values

Appendix- II – Statistical analysis for â vs. a data using Minitab

In this Appendix-II, the step by step procedure followed in Minitab statistical software version 17 for processing the *â* vs. *a* data obtained from the numerical model developed for ultrasonic inspection of flat bottom holes. This data consists of 40 defects and the corresponding ultrasonic signal amplitudes from physics based numerical model. Table 17 shows the lognormally distributed 40 defect sizes and the corresponding ultrasonic signal amplitudes. In Table 17, 'a', 'acapL', 'acapR' and 'loga' corresponds to crack/defect size, NDT signal response data with left censoring, NDT signal response data with right censoring and log(crack sizes), respectively. Censoring of this data is performed with 25% full screen height (FSH) and 80% FSH for left censored and right censored data, respectively.

Table 17: Lognormally distributed 40 FBH sizes and the corresponding ultrasonic signal amplitudes of defects

	a	acapL	acapR		loga		a	acapL	acapR		loga
1	0.36	*	14.7707		-1.03361	21	0.76	49.591	49.5908		-0.27268
2	0.42	*	19.5484		-0.85973	22	0.77	50.774	50.7738		-0.26112
3	0.54	27.931	27.9311		-0.61241	23	0.79	53.157	53.1569		-0.23882
4	0.55	28.704	28.7037		-0.59274	24	0.81	55.590	55.5899		-0.21552
5	0.55	28.704	28.7037		-0.59212	25	0.81	55.590	55.5899		-0.20769
6	0.56	29.501	29.5013		-0.58535	26	0.82	56.806	56.8063		-0.20093
7	0.58	31.127	31.1272		-0.55301	27	0.83	58.051	58.0514		-0.18798
8	0.60	32.839	32.8386		-0.51230	28	0.86	61.827	61.8274		-0.14511
9	0.64	36.560	36.5597		-0.44177	29	0.94	72.655	72.6551		-0.05712
10	0.65	37.550	37.5503		-0.43305	30	0.96	75.561	75.5614		-0.03745
11	0.67	39.595	39.5951		-0.40428	31	1.00	81.624	*		-0.00439
12	0.68	40.649	40.6489		-0.38213	32	1.00	81.624	*		0.00239
13	0.69	41.720	41.7201		-0.36572	33	1.02	84.787	*		0.02279
14	0.73	46.144	46.1438		-0.31413	34	1.05	89.735	*		0.05167
15	0.74	47.279	47.2795		-0.30489	35	1.08	94.851	*		0.07723
16	0.74	47.279	47.2795		-0.29564	36	1.14	105.508	*		0.13266
17	0.75	48.439	48.4392		-0.28827	37	1.16	109.202	*		0.14607
18	0.75	48.439	48.4392		-0.28786	38	1.17	111.038	*		0.15292
19	0.75	48.439	48.4392		-0.28262	39	1.19	114.773	*		0.17772
20	0.75	48.439	48.4392		-0.28242	40	1.27	130.333	*		0.24155

The $\hat{a}$ vs. a data shown in Table 17 is processed with regression with life data analysis for obtaining the regression parameters to be used in plotting the cumulative distributive function (CDF) of log-normal distribution. Figure shows the screenshot of 'regression with life data' analysis option in Minitab software.

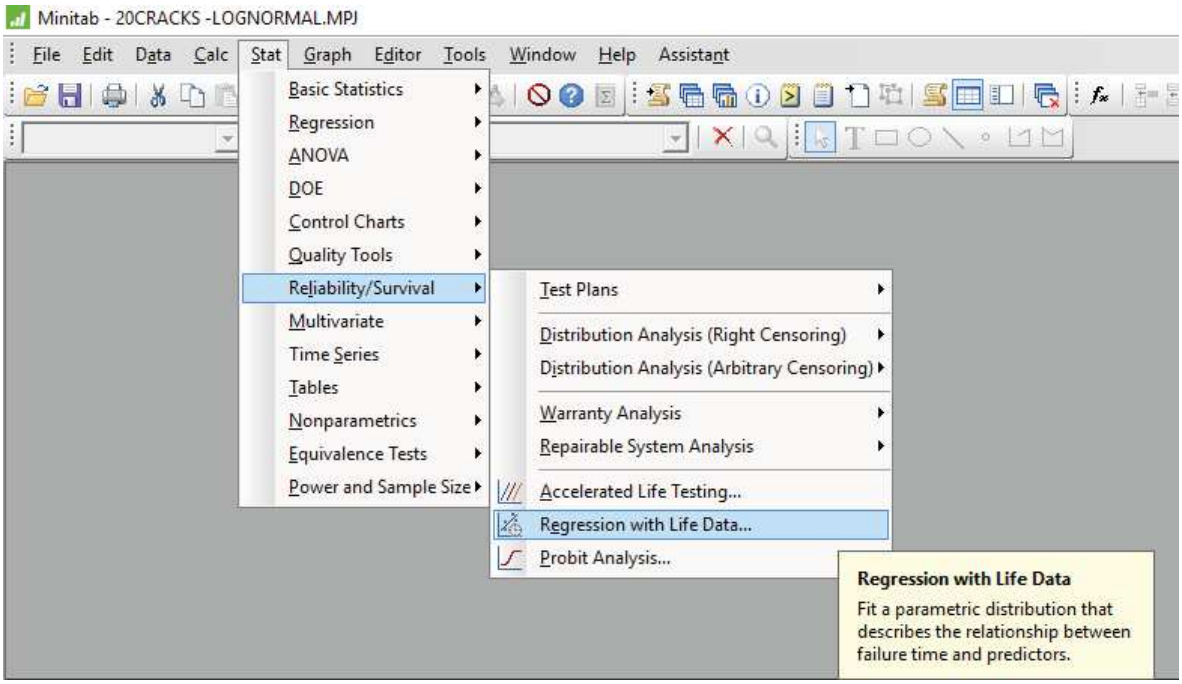

Figure 98: Screenshot showing regression with life data option in Minitab software

Further selecting the 'regression with life data' analysis option in Minitab, a new pop-up window opens as shown in Figure 99. From Figure 99, it can be observed that the start and end variables are selected according to the NDT signal response data with left censoring and right censoring, respectively. In addition, it can also be observed that the regression model is performed with logarithm of crack sizes followed by the selection of the suitable statistical distribution. In this case, it can be observed that the assumed distribution is selected as normal distribution as the cracks sizes 'a' is lognormally distributed and hence, the log(a) is assumed to be normally distributed.

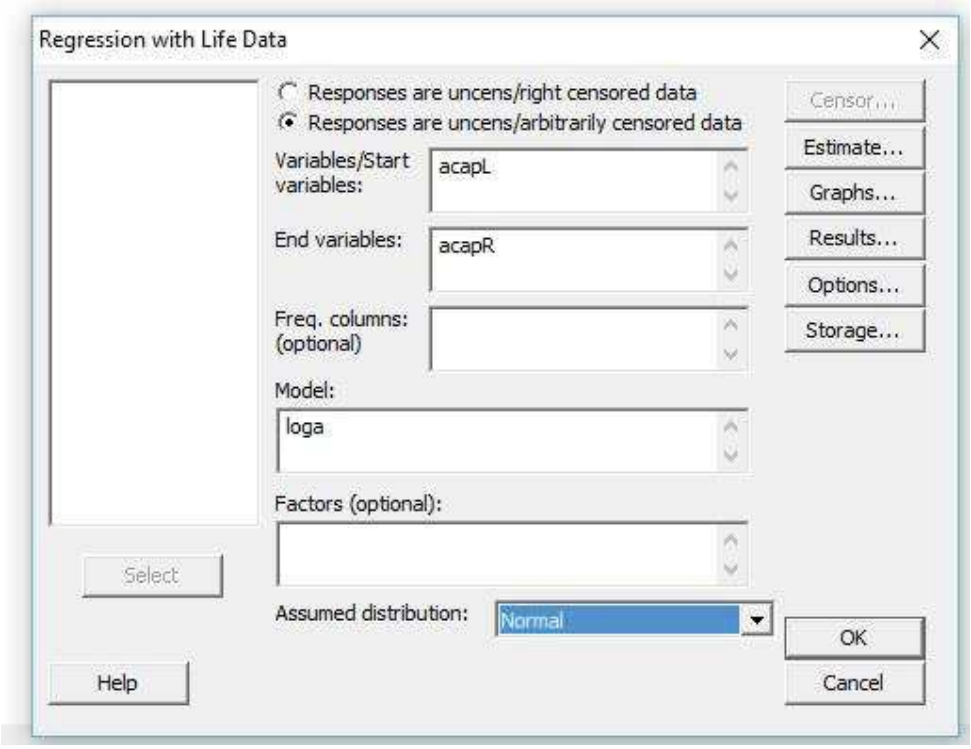

Figure 99: Screenshot showing the variables and model with distribution in Minitab software

Regression with Life Data: acapL versus loga

```
Response Variable Start: acapL  End: acapR

Censoring Information  Count
Uncensored value          28
Right censored value      10
Left censored value        2

Estimation Method: Maximum Likelihood

Distribution:   Normal

Relationship with accelerating variable(s):   Linear


Regression Table

                     Standard                  95.0% Normal CI
Predictor     Coef     Error       Z      P    Lower    Upper
Intercept  89.1720   2.17811   40.94  0.000  84.9029  93.4410
loga       121.377   6.30513   19.25  0.000  109.019  133.735
Scale      7.94829   1.11114                 6.04336  10.4537

Log-Likelihood = -104.238
```

Figure 100: Result of the regression with life data analysis

Figure 100 shows the result of the regression with life data analysis performed between the logarithm of crack sizes and the NDT response data with left and right censoring data. From Figure 100, the coefficients of the intercept and loga in the regression table are the mean and standard deviation of the normally distributed log(a). However, to plot the POD curves with respect to crack sizes 'a', which are log-normally distributed, the CDF parameters corresponding to the log-normal distribution function such as location and scale parameters are required. As it is known from the basics of probability distributions i.e., the distribution parameters (mean and standard deviation) of the normal distribution function are equal to the distribution parameters (location and scale) of the log-normal distribution function. Hence, the mean and standard deviation values obtained from the regression table of regression with life data analysis are used as the location and scale parameters for plotting the CDF of lognormally distributed (log(a)) values. Figure 101 shows the screenshot for identifying the location of 'CDF' of lognormal distribution function in Minitab.

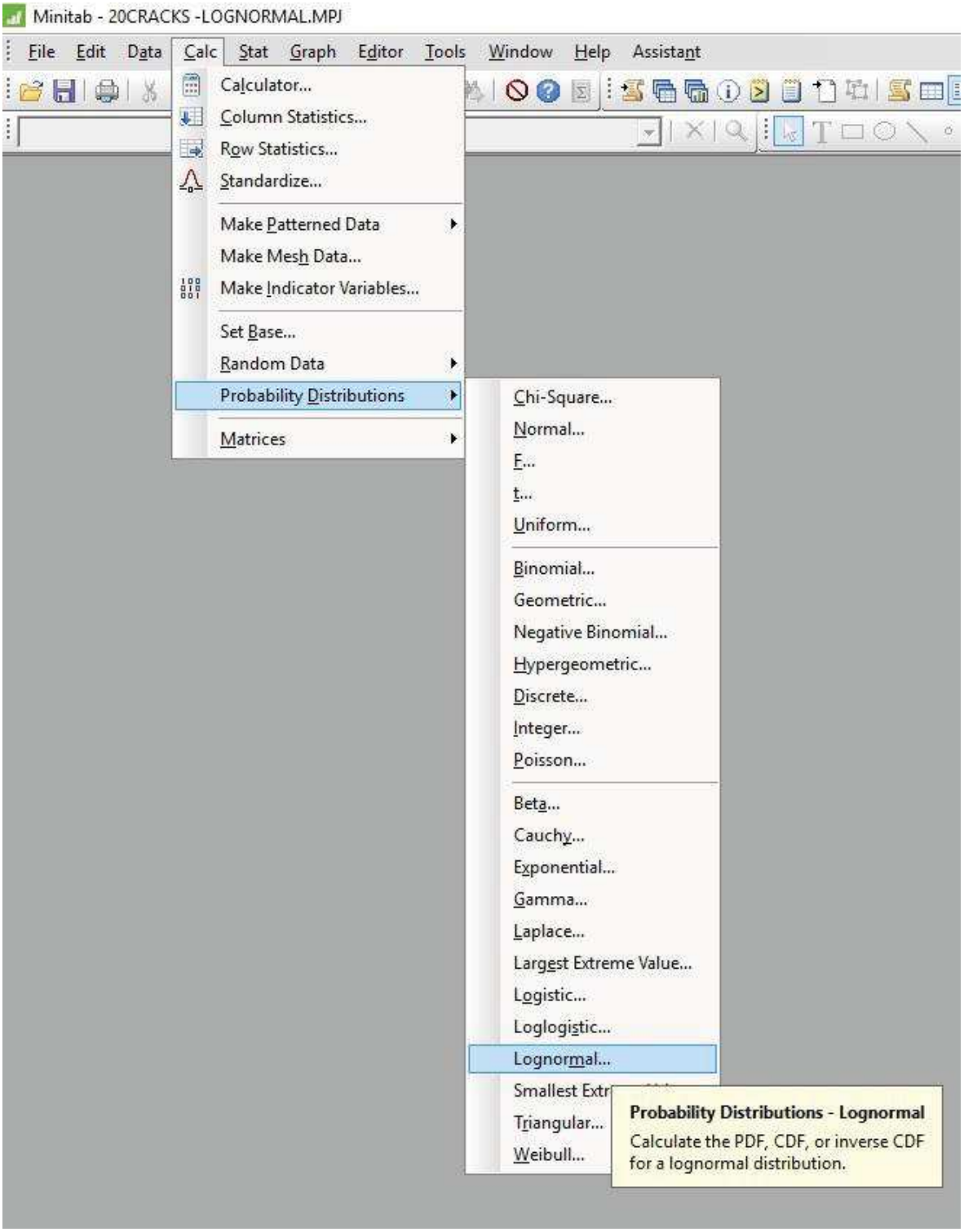

Figure 101: Screenshot showing the option for plotting CDF of lognormal distribution in Minitab software

Figure 102 shows the screenshot of plotting CDF of log-normal distribution function in Minitab software. Up on entering the corresponding location and scale parameters in the respective locations, CDF of the crack sizes 'a' can be obtained and stored in one of the columns in the minitab project worksheet.

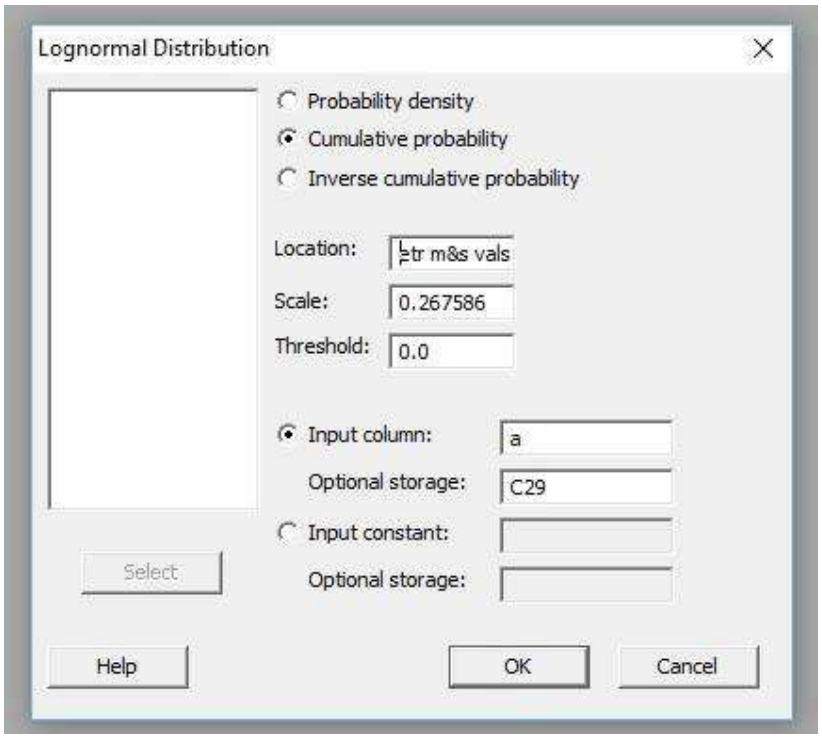

Figure 102: Screenshot showing the plotting of CDF of log-normal distribution function

Similar to the calculation of 95% lower confidence probabilities of FLPT H/M data in Appendix-I, the 95% lower confidence probabilities of the 40 lognormally distributed crack sizes are also calculated using Equation 6. Table 18 shows the probabilities and 95% lower confidence probabilities of detecting each crack size obtained from the CDF of log-normal distribution function.

Table 18: Probabilities and 95% lower confidence probabilities obtained from the CDF of log-normal distribution

POD	95cl	POD	95cl
0.079120	0.042633	0.924006	0.869205
0.223258	0.142053	0.929990	0.878156
0.564734	0.441598	0.940508	0.894194
0.593476	0.470741	0.950132	0.909263
0.594368	0.471656	0.953071	0.913949
0.604156	0.481741	0.955496	0.917850
0.649865	0.529914	0.959858	0.924944
0.704400	0.589864	0.971884	0.945127
0.788337	0.688202	0.987391	0.973082
0.797649	0.699635	0.989600	0.977340
0.826584	0.735930	0.992557	0.983216
0.846974	0.762274	0.993062	0.984244
0.861005	0.780813	0.994405	0.987019
0.899313	0.833413	0.995911	0.990220
0.905269	0.841894	0.996929	0.992455
0.910965	0.850090	0.998397	0.995822
0.915320	0.856417	0.998638	0.996400
0.915561	0.856769	0.998748	0.996667
0.918553	0.861150	0.999082	0.997490
0.918661	0.861309	0.999602	0.998834

Figure 103 shows the POD curve along with the 95% lower confidence curve of lognormally distributed 40 crack sizes. From Figure 103, it can be observed that the $a_{90/95}$ value is 0.80 mm.

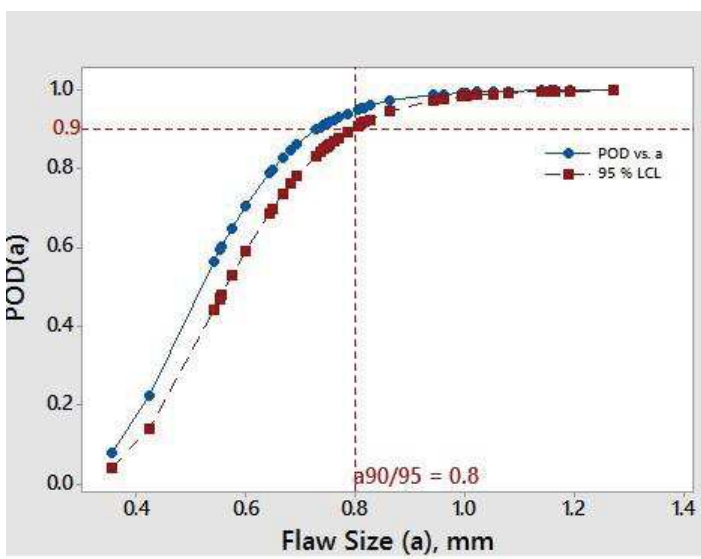

Figure 103: POD curve of 40 lognormally distributed crack sizes indicating a90/95 = 0.8 mm

Appendix- III – Matlab program for automatic defect identification using Hilbert transform from numerical A-scan signals

```
%% This code is to generate signal in time domain and to perform structural analysis in frequency domain
clc
clear all
close all
%% generating a signal
fo=5e6;
A=8e-7;
dt=20e-9;
fs=1/dt;
t=0:dt:6e-7;
y=A*cos(2*pi*fo*t);
L=length(y);
win1=hann(L)';
xw1=win1.*y;
figure;
plot(t,xw1);
xlabel('Time (s)');
ylabel('Amplitude')
```

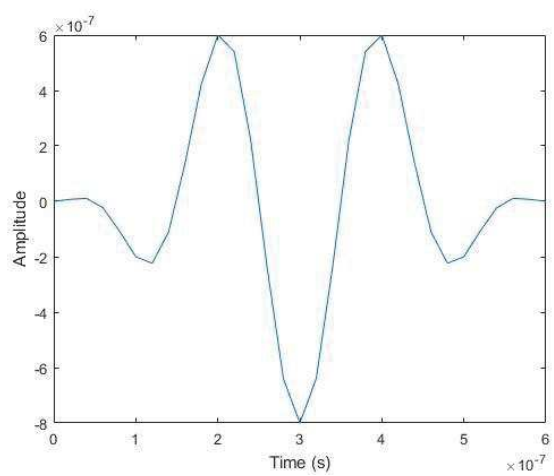

Figure 104: Generating initial signal in time domain

```
% initial signal length zero padded for 5e-6sec
rec_length=length(0:2e-8:5.1e-6);
NFFT=2^nextpow2(rec_length);% Next power of 2 from length of y
sig=[zeros(1,rec_length-L) xw1];
time=[0:2e-8:5.1e-6];
Y = fft(sig,NFFT);
Y(round(rec_length/2)+1:end)=[];
Y_norm=Y./max(abs(Y));
f=0:fs/rec_length:fs*rec_length/rec_length;
f=f';
count=1;
f(round(rec_length/2)+1:end)=[];
 Y_norm(round(rec_length/2)+1:end)=[];
for i=1:round(rec_length/2)
   if  abs(Y_norm(i))>0.07178
       fn(count)=f(i);
       weight(count)=Y_norm(i);
        ivec(count)=i;
       count=count+1;
   end
end
figure
plot(fn,abs(weight))

% Plot single-sided amplitude spectrum.
b=2*abs(Y_norm);
figure;
plot(f,b)
grid;
title('Single-Sided Amplitude Spectrum')
xlabel('Frequency (Hz)')
ylabel('|Y(f)|')
```

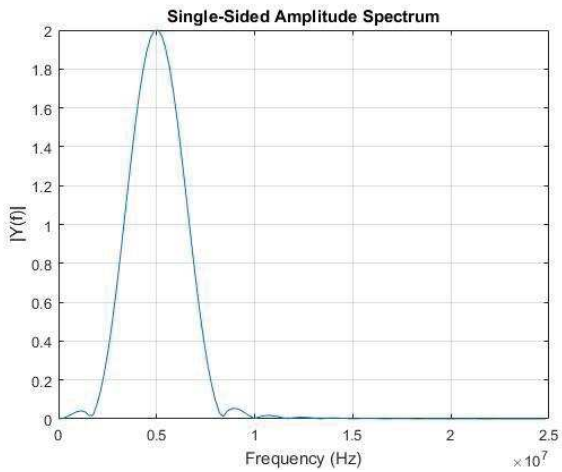

Figure 105: Generating 5 MHz signal

```
%% extracting data from frequency domain model%%
a=importdata('C:\Users\Kiran\Documents\MATLAB\Vamsi_Ph.D\20fbhlognor_freqdom.mat
');
n=19;
for i=0:n
a1=a(30*i+1:30*i+30,:);
Q=a1;
z12=[Q(1:11)*0;Q];
z1=[z12;zeros(128-length(z12),1)];
save 'z_freq.mat' z_total
z1=z1';
t=Y_norm.*z1;
flipt=conj(fliplr(t));
fecho=[t flipt];
echo=ifft(fecho,'symmetric');
echo=fliplr(echo);
echo_norm=echo/max(abs(echo));
t1=t./max(abs(t));
abs_comb=2*abs(t1);
figure
plot(f,b,'--b',f,abs_comb,'-*r');
figure(i+1)
plot(time,echo_norm,'-b.');
```

```
echo_norm_f=echo_norm(4:35);
echo_norm_d=echo_norm(136:174);
time_d=time(136:174);
h_f=hilbert(echo_norm_f);
h_d=hilbert(echo_norm_d);
p_f=abs(h_f);
p_d=abs(h_d);
figure(i+1);
plot(time_d,echo_norm_d,'-',time_d,p_d,'red');
M(i+1)=max(findpeaks(p_d));
N(i+1)=max(findpeaks(p_f));
M_norm(i+1)=M(i+1)*80/N(i+1);
i=i+1;
end
%% finding peaks-hilbert transform%
M=M';
N=N';
M_norm=M_norm';
a_true=xlsread('20fbh_lognor.xlsx');
xlswrite('20fbh_lognor_peaks.xls',a_true,'Sheet1','A1:A20');
xlswrite('20fbh_lognor_peaks.xls',N,'Sheet1','B1:B20');
xlswrite('20fbh_lognor_peaks.xls',M,'Sheet1','C1:C20');
xlswrite('20fbh_lognor_peaks.xls',M_norm,'Sheet1','D1:D20');
```

Effect of Fatigue Crack Surface Oxidation on Reliability of Non Destructive Testing Techniques

by Vamsi Krishna Rentala

Submission date: 16-Sep-2020 11:58AM (UTC+0530)
Submission ID: 1388371083
File name: Vamsi_Krishna_Rentala_12ETMM10_Ph.D_Thesis.pdf (5.44M)
Word count: 36170
Character count: 181756

Effect of Fatigue Crack Surface Oxidation on Reliability of Non Destructive Testing Techniques

ORIGINALITY REPORT

27 %	%	%	%
SIMILARITY INDEX	INTERNET SOURCES	PUBLICATIONS	STUDENT PAPERS

PRIMARY SOURCES

1	Vamsi Krishna Rentala, Phani Mylavarapu, Jai Prakash Gautam. "Issues in estimating probability of detection of NDT techniques – A model assisted approach", Ultrasonics, 2018 Publication	14%
2	Vamsi Krishna Rentala, Phani Mylavarapu, J.P. Gautam, Gp.Capt. B.V.N.Shiva, K Gopinath, Vikas Kumar. "Physical Manifestation of a90/95 in Remnant Life Revision Studies of Aero-engine Components", Procedia Structural Integrity, 2019 Publication	5%
3	www.nde-reliability.de Internet Source	2%
4	www.slideshare.net Internet Source	1%
5	www.jsm.or.jp Internet Source	1%

insights.ovid.com

Dr. JAI PRAKASH GAUTAM
Professor
School of Engineering Sciences & Technology
University of Hyderabad
Hyderabad-500 046.

Dr. JAI PRAKASH GAUTAM
Professor
School of Engineering Sciences & Technology
University of Hyderabad
Hyderabad-500 046.

6	Internet Source	<1 %
7	edoc.pub Internet Source	<1 %
8	www.asnt.net Internet Source	<1 %
9	lib.dr.iastate.edu Internet Source	<1 %
10	www.ndt.net Internet Source	<1 %
11	use.perl.asnt.org Internet Source	<1 %
12	www.statisticalengineering.com Internet Source	<1 %
13	Submitted to University of Johannsburg Student Paper	<1 %
14	www.sto.nato.int Internet Source	<1 %
15	Submitted to Middle East Technical University Student Paper	<1 %
16	worldwidescience.org Internet Source	<1 %
17	archive.org Internet Source	<1 %

18	Submitted to University of Houston System Student Paper	<1%
19	Review of Progress in Quantitative Nondestructive Evaluation, 1998. Publication	<1%
20	docplayer.net Internet Source	<1%
21	M S Safizadeh. "The effect of flaw size distribution on the estimation of POD", Insight - Non-Destructive Testing and Condition Monitoring, 06/2004 Publication	<1%
22	S Santhosh Kumar, V Seshu Bai, K V Rajkumar, G K Sharma, T Jayakumar, T Rajasekharan. "Elastic modulus of Al–Si/SiC metal matrix composites as a function of volume fraction", Journal of Physics D: Applied Physics, 2009 Publication	<1%
23	"ICAF 2019 – Structural Integrity in the Age of Additive Manufacturing", Springer Science and Business Media LLC, 2020 Publication	<1%
24	Fatigue under Thermal and Mechanical Loading Mechanisms Mechanics and Modelling, 1996. Publication	<1%

25	V K Rentala, P Mylavarapu, J Gautam, V Kumar. "Generation of POD curves in the absence of service-induced cracked components – an experimental approach", Insight - Non-Destructive Testing and Condition Monitoring, 2019 Publication	<1%
26	vdocuments.mx Internet Source	<1%
27	Submitted to National Institute of Technology, Rourkela Student Paper	<1%
28	www.ugc-inno-nehu.com Internet Source	<1%
29	C.O. Uemura, P.R. Underhill, T.W. Krause. "Estimating POD of a screening technique for cracks about ferrous fasteners without fastener removal", NDT & E International, 2019 Publication	<1%
30	Review of Progress in Quantitative Nondestructive Evaluation, 1989. Publication	<1%
31	U RAMAMURTY. "Fatigue in Ceramic Matrix Composites", Volume 4 Carbon/Carbon Cement and Ceramic Matrix Composites, 2003 Publication	<1%

Dr. JAI PRAKASH GAUTAM
Professor
School of Engineering Sciences & Technology
University of Hyderabad
Hyderabad-500 046.